TECTONICS AND VOLCANISM ON VENUS: CONSTRAINTS FROM TOPOGRAPHIC RELIEF, IMPACT CRATERING, AND DEGASSING

by

Noriyuki Namiki

B. S., Geophysics
Tokyo University, 1986

S. M., Geophysics
Tokyo University, 1988

SUBMITTED TO THE DEPARTMENT OF EARTH, ATMOSPHERIC, AND PLANETARY SCIENCES IN PARTIAL FULFILLMENT OF THE REQUIREMENTS FOR THE DEGREE OF

DOCTOR OF PHILOSOPHY IN GEOPHYSICS
AT THE
MASSACHUSETTS INSTITUTE OF TECHNOLOGY

SEPTEMBER 1995

Signature of Author: .....

Department of Earth, Atmospheric, and Planetary Sciences
July 20, 1995

Certified by: .....

Sean C. Solomon
Thesis Co-Supervisor

Certified by: .....

Bradford H. Hager
Thesis Co-Supervisor

Accepted by: .....

Thomas H. Jordan
Department Head

TECTONICS AND VOLCANISM ON VENUS: CONSTRAINTS FROM TOPOGRAPHIC RELIEF, IMPACT CRATERING, AND DEGASSING

by

Noriyuki Namiki

Submitted to the Department of Earth, Atmospheric, and Planetary Sciences on July 20, 1995, in partial fulfillment of the requirements for the Degree of Doctor of Philosophy in Geophysics

ABSTRACT

Radar images of the surface of Venus taken by the Magellan spacecraft have revealed styles of tectonics and volcanism remarkably different from those on Earth. To resolve the apparently complex history of geologic activity seen in the radar images is critical for an understanding of the planet's evolution. The small number of impact craters on the planet's surface, however, prevents the use of crater chronology to distinguish the ages of individual geological units. I attempt instead in this thesis to constrain the histories of tectonism and volcanism on Venus on the basis of three different data sets: topographic relief, the impact cratering record, and the atmospheric abundances of volcanic gasses. The high relief of the mountain belts of Ishtar Terra challenges a static view of topographic support, and may provide a constraint on rates of tectonic activity. Cratering records on volcanic features are integrated to yield information on rates of volcanic activity over the last several hundred million years. Volcanic gasses in the present atmosphere, in contrast, limit magmatic activity over the planet's history. The coupling of mantle degassing models for atmospheric species with different residence times constrain volatile abundances in the planetary interior. The new constraints obtained in this thesis sharpen our view of the tectonic and thermal evolution of Venus.

Maxwell Montes, standing up to 7 km above the adjacent highland plateaus, constitutes the highest mountain belt on Venus. Because the thickness of the crust is likely to be limited by the gabbro - garnet granulite - eclogite phase transitions, this relief is difficult to reconcile with the assumption of thermodynamic equilibrium and a standard Airy isostatic model. I explore the hypothesis that the crust-mantle boundary is not in phase equilibrium, but rather is rate-limited by the temperature-dependent volume diffusion of the slowest ionic species. Under the simplifying assumption that the mountains formed by uniform

horizontal shortening of the crust and lithospheric mantle at a constant rate, I solve the one-dimensional thermal evolution problem. The time-dependent density structure and surface elevation are calculated by assuming a temperature-dependent reaction rate and local Airy isostatic compensation. For a rate of horizontal strain of 10^{-15} s^{-1} or greater, the rise in temperature at the base of the crust during mountain formation is modest to negligible, the deepening lower crust is metastable, and surface elevation increases as the crust is thickened. For strain rates less than 10^{-16} s^{-1}, in contrast, crustal temperature increases with time because of internal heat production, and the lower crust is more readily transformed to the dense eclogite assemblage. For such models a maximum elevation is reached during crustal shortening. While this maximum relief is 7 km or more for some models, a smaller density contrast between crust and mantle than assumed here (500 kg m^{-3}) and incorporation of horizontal heat transport would lessen this value. I therefore favor formation of the mountain belt at a strain rate at least of order 10^{-15} s^{-1}.

The density of impact craters on large volcanoes on Venus is half the average crater density for the planet. The crater density on some classes of coronae is not significantly different from the global average density, but coronae with extensive associated volcanic deposits have lower crater densities. These results are inconsistent with both single-age and steady-state models for global resurfacing and suggest that volcanoes and coronae with associated volcanism have been active on Venus over the last 500 million years.

A new model of ^{40}Ar and ^{4}He degassing on Venus has been developed in order to sharpen constraints on the history of magmatism on the planet. The model incorporates catastrophic global resurfacing events and modest levels of magmatism between such events, consistent with recent analyses of the cratering record of the Venus surface. The model includes mantle, crustal, and atmospheric reservoirs, and the rate of magmatism between catastrophic events is assumed to be constant in time. Diffusive transfer of ^{40}Ar and ^{4}He from the crust to the atmosphere is taken into account. The ^{40}Ar abundance in the present atmosphere is directly related to the integrated degassing and magmatism over the planetary history. Whole-mantle degassing of ^{40}Ar limits the average crustal production rate to lie between 2 and 110 km^3 yr^{-1}; this upper bound increases as the mass of the degassed portion of the mantle decreases. Helium escapes from the planetary atmosphere within a characteristic residence time of 200 Myr to 1.8 Gyr, so the present atmospheric ^{4}He abundance is relevant to the volume of magma produced during the last global resurfacing event and the rate of the magmatism subsequent to that event. However, large uncertainties in mineral partition coefficients and in the He mixing ratio in the lower atmosphere of Venus prevent the use of ^{4}He, at least at present, as a tracer of planetary volcanism.

The fractional degree of melting and the K budget in the bulk silicate fraction of Venus are estimated on the basis of Venera and Vega γ-ray measurements of K, U, and Th concentrations in surface materials. For U and Th concentrations in the bulk silicate planet of between 18 and 29 ppb and 64 and 94 ppb, respectively, the degree of melting during the last catastrophic resurfacing event is calculated to be between 0.02 and 0.16. The degrees of melting calculated for materials from each landing site are combined with measurements of surface K concentration to estimate the K concentration in the bulk silicate planet at between 95 and 250 ppm.

The water abundance in a planetary interior is of special importance for the thermal and tectonic histories of the planet. The present atmospheric water abundance and D/H ratio on Venus as well as the estimated escape flux of hydrogen require a recent supply of water to the atmosphere by either volcanic outgassing or cometary impacts. Catastrophic global resurfacing of the planet 300 to 500 Myr ago postulated from analyses of the Venus cratering record must have had a significant influence on the present atmospheric water budget. Models in which the outgassing of mantle water by a catastrophic global

resurfacing event and subsequent steady magmatism have been responsible for the present atmospheric water abundance and D/H ratio lead to an upper bound on the water content in the present Venus mantle. I then develop a suite of models that combine outgassing of mantle ^{40}Ar and hydrogen escape over the planet's history, because the present atmospheric ^{40}Ar abundance constrains the integrated magmatism over the planet's history while the hydrogen escape flux limits the amount of past atmospheric water. These models not only constrain the water concentration in the present Venus mantle to be less than 15 ppm, an order of magnitude less than that of the MORB mantle of Earth, but also reveal that this depletion of water has characterized the Venus mantle over approximately the last 2.5 Gyr of the planet's history.

Thesis Co-Supervisor:	Sean C. Solomon
Title:	Director, Department of Terrestrial Magnetism Carnegie Institution of Washington
Thesis Co-Supervisor:	Bradford H. Hager
Title:	Cecil and Ida Green Professor of Earth Sciences

ACKNOWLEDGMENTS

I wish to thank Dr. Sean Solomon, now at the Carnegie Institution of Washington, for his continuous support and advice on this work. He has taught me the ABC of planetary science and research. I also thank Professor Brad Hager for intriguing discussions that have sharpened many issues in Chapters 2 and 6, and Professor Rick Binzel for his warm encouragement over my years at M.I.T.

I will always be grateful to my fellow students, Pat McGovern and Mark Simons, and my petrology teacher, Eiichi Takazawa. Their arguments have challenged my premature thoughts and have improved greatly this work. Libby Kurten, Marie Sénat, Deb Sykes, and Linda Meinke are appreciated for their administrative assistance and maintenance of the computer system.

Finally, I wish to thank my family. My son, Shigeru, deserves special thanks for waking me up every morning with a loud cry while I was finishing this work. And to my wife, Natsumi, I dedicate this work to you.

A-RI-GA-TOW.

This work was supported by the National Aeronautics and Space Administration under grants NAGW-1937, NAGW-3276, and NAGW-3425.

TABLE OF CONTENTS

Chapter 1:

Introduction

Radar images of Venus by the recent Magellan mission have revealed a planet with a wide variety of tectonic and volcanic features. Mountain belts, ridge belts, and compressive highland plateaus are the surface manifestations of lithospheric deformation driven by mantle convection. Large volcanoes, coronae, flood-type lava flows, shield fields, and canali are responses to magmatic activity on the planet and are also related to mantle dynamics. Global variations in the geoid/topography admittance measured by spacecraft indicate that much of the long-wavelength surface topography is supported by mantle convection, although highland plateaus and tessera terrain are likely to be products of an earlier regime of high crustal strain.

Details of the tectonic and volcanic histories of the planet, however, have been difficult to resolve. A total of about 1000 impact craters over the planet's surface limits the minimum area for a statistically meaningful crater chronology to be more than 1% of the surface, an area generally larger than the individual geological regions. Geophysical and geological scenarios advanced to account for these tectonic and volcanic features are complex, and the interpretations are frequently in conflict with one another. In this thesis, I attempt to address the tectonic and volcanic evolution of the planet from several independent directions: topographic relief, impact cratering density, and atmospheric abundances of volcanic gasses. New constraints on the history of the planet are obtained by combining these seemingly disparate elements of presently available information with the high-resolution radar images taken by the Magellan spacecraft.

Chapter 2 focuses on the dynamics and support mechanism of mountain belts in Ishtar Terra to constrain the nature of recent tectonic activity on the planet. Because the thickness of the crust is likely to be limited by the gabbro - garnet granulite - eclogite phase transitions, the characteristic relief of the belts is difficult to reconcile with the assumption of thermodynamic equilibrium and a standard Airy isostatic model. I have explored the hypothesis that the crust-mantle boundary is not in phase equilibrium, but rather is rate-limited by the temperature-dependent volume diffusion of the slowest ionic species. I

solved the one-dimensional thermal evolution problem under the simplifying assumption that the mountains formed by uniform horizontal shortening of the crust and lithospheric mantle at a constant rate. The time-dependent density structure and surface elevation were calculated by assuming a temperature-dependent reaction rate and local Airy isostatic compensation. I have shown that if the rate of horizontal strain is sufficiently large, the rise in temperature at the base of the crust during mountain formation is modest to negligible, the deepening lower crust is metastable, and surface elevation increases as the crust is thickened. If the strain rate is small, in contrast, crustal temperature increases with time because of internal heat production, and the lower crust is more readily transformed to the dense eclogite assemblage. For such models a maximum elevation is reached during crustal shortening. I conclude that crustal deformation at a high strain rate is favored.

In Chapter 3, I studied the impact crater density on volcanoes and coronae to constrain the history of volcanism and resurfacing on Venus over the last 300 to 500 Myr. While absolute age estimation for individual geological units is difficult to impossible, integrating areas for a given geologic terrain type enables us to estimate an average age for that particular terrain. The crater density on large volcanoes measured from the Magellan radar images is about half of the global average. From the measured area of large volcanoes and the population of embayed craters, I have estimated the volcanic resurfacing rate and the maximum volumetric magmatic flux. The crater density on coronae, on the other hand, is not significantly different from the global average. Detailed study of crater densities by corona class, however, suggests that coronae associated with extensive volcanic deposits have surfaces resolvably younger than the global average. These results are inconsistent with both single-age and steady-state models for global resurfacing, but they are consistent with scenarios calling for nearly global resurfacing followed by modest but finite levels of steady subsequent volcanic resurfacing.

The nature of the postulated global catastrophic resurfacing process that ended approximately 500 Myr ago is poorly constrained by Magellan radar images, because there

is an apparent lack of geological information significantly predating the end of the catastrophe. I therefore make use of ^{40}Ar and ^{4}He in Chapter 4 to constrain volcanic activity over the last 4.55 Gyr and the last several hundred million years, respectively. Because the half-life of ^{40}K is on the same order as the age of the planet, the abundance of its decay product ^{40}Ar provides a strong constraint on the total amount of degassing and magmatism over the planet's history. On the other hand, ^{4}He, a decay product of ^{235}, ^{238}U and ^{232}Th, can escape from the upper atmosphere because of its light atomic weight. An inferred residence time of ^{4}He in the atmosphere of from 200 million years to 2 billion years suggests that He abundance can potentially serve to constrain to estimate the rate of recent volcanic activity on Venus. I have developed a new degassing model in order to investigate further the episode of widespread volcanism postulated from geologic observations and the rate of volcanism implied by the cratering record in Chapter 3. A lower bound on an amount of volcanism integrated over the planet's history is obtained from ^{40}Ar degassing. Unfortunately, large uncertainties in the ^{4}He abundance in the lower atmosphere and in its partition coefficients between basaltic melt and mantle residuum prevent deriving useful constraints from ^{4}He degassing.

The lower bound on magmatism over the planet's history calculated in Chapter 4 is then used to constrain the water budget in Venus mantle. Water degassed from the mantle is dissociated in the atmosphere by ultraviolet radiation from the sun, and H atoms subsequently escape from the upper atmosphere. An integrated hydrogen escape flux over the planet's history therefore limits the amount of water degassed from the mantle. By dividing the estimated amount of degassed water by the above lower bound on a crustal production rate, an upper bound on the present water concentration in the Venus mantle is calculated to be an order of magnitude less than that of the MORB mantle on Earth. Further, this relatively anhydrous condition of the Venus mantle is shown to have held over the last several billion years.

Chapter 2 and 3 were co-authored by S. C. Solomon and were published in *J. Geophys. Res.*, *98*, 15,025-15,031, 1993 and *Science*, *265*, 929-933, 1994, respectively. Chapter 4, also written with S. C. Solomon, will be submitted to the *Journal of Geophysical Research.* Chapter 5, co-authored by S. C. Solomon and D. H. Grinspoon, will be submitted to *Icarus.*

Chapter 2:

The Gabbro - Eclogite Phase Transition and The Elevation of Mountain Belts on Venus

INTRODUCTION

The linear mountain belts of western Ishtar Terra on Venus are notable for their topographic relief and slope and for the intensity of surface deformation [*Barsukov et al.*, 1986; *Solomon et al.*, 1991, 1992]. These four mountain belts, including Akna, Freyja, Maxwell, and Danu Montes (Figure 2.1), are generally regarded as products of large-scale compression and horizontal shortening of the crust and lithosphere [*Pronin*, 1986; *Basilevsky*, 1986; *Crumpler et al.*, 1986; *Roberts and Head*, 1990; *Grimm and Phillips*, 1990; *Bindschadler and Parmentier*, 1990; *Solomon et al.*, 1991, 1992; *Kaula et al.*, 1992]. Among these mountain belts, Maxwell Montes is the highest and stands up to 11 km above mean planetary radius and 7 km above the highland plain Lakshmi Planum (Figure 2.1). Volcanism is rare to absent in Maxwell, Freyja, and Akna Montes, but a number of magmatic features are evident in Danu Montes [*Solomon et al.*, 1991; *Head et al.*, 1991; *Kaula et al.*, 1992], the mountain range least elevated above Lakshmi Planum.

The bulk composition and radioactive heat production of the crust on Venus, where measured, are similar to those of terrestrial basalts [*Surkov et al.*, 1984, 1987]. Because basalt transforms to eclogite at high pressure and because eclogite is likely to be denser than mantle material, the thickness of the crust may be limited by the gabbro - garnet granulite - eclogite phase transitions [*Anderson*, 1981; *Turcotte*, 1989]. The phase transition depth depends on the temperature structure of the crust beneath the mountains. If the thermal gradient is low and thermodynamic equilibrium is assumed, the phase changes would take place at shallow depth, and simple isostatic models underpredict the relief [*Vorder Bruegge and Head*, 1991]. If the thermal gradient is high, in contrast, the base of a crustal root sufficiently deep to support the mountains would exceed the melting temperature. Thus the 7-11 km maximum elevation of Maxwell Montes is difficult to understand under the assumptions of local isostasy and thermodynamic equilibrium except in the unlikely situation that the crust beneath the mountains contains a large volume of magma [*Vorder*

Bruegge and Head, 1991].

A possible explanation for the great relief of Maxwell Montes is that the base of the crust is not in phase equilibrium. Because of the high surface temperature on Venus (750 K) and the very low water abundance of the lower atmosphere [*von Zahn et al.*, 1983], the Venus crust is thought to contain negligible water [*Kaula*, 1990]. It has been suggested that under anhydrous conditions, the gabbro - eclogite phase transition takes place by solid-state diffusion and may require a geologically significant time to run to completion [*Ahrens and Schubert*, 1975]. Solid-state diffusion is a strongly temperature-dependent process, so that quantifying this suggestion for application to Venus requires the solution of a heat transport problem. In this chapter we develop simple models for the thermal evolution of the crust beneath mountain belts on Venus in an attempt to constrain the time-dependent depth of the gabbro - eclogite transition and thus to assess this hypothesis.

Because at long wavelengths the topography of western Ishtar Terra is correlated with the gravity field, at least partial dynamical support of the regional elevation of about 4 km is likely [e.g., *Grimm and Phillips*, 1991]. We therefore adopt the 7-km elevation of Maxwell Montes above the adjacent plateau as a conservative estimate of the relief attributable to local isostasy.

THERMAL MODEL

We assume that the crustal and mantle portions of the thermal boundary layer shorten horizontally and thicken vertically with time in the manner of pure shear. The thermal structure is then governed by the one-dimensional heat equation,

$$\frac{\partial T}{\partial t} + \dot{\gamma} z \frac{\partial T}{\partial z} = \kappa \frac{\partial^2 T}{\partial z^2} + \frac{A}{C_P} \qquad (1)$$

where T is temperature, t is time, $\dot{\gamma}$ is the horizontal strain rate, z is depth, κ is the thermal diffusivity, A is the crustal heat production, and C_P is the specific heat. Under the assumption that deformation is by pure shear, $\dot{\gamma}$ is constant and the vertical velocity is given by the product of $\dot{\gamma}$ and z. We solve equation (1) numerically by an explicit finite difference approximation. For a sufficiently small value of $\dot{\gamma}$, horizontal heat transfer can become comparable in importance to vertical transfer. In such a situation equation (1) underestimates the temperature increase in the crust. We discuss this point further below.

Model Parameters

The thermal diffusivity is assumed to be 1.0×10^{-6} m^2 s^{-1} in both crust and mantle. The crustal heat production is assumed to be uniformly distributed and to equal 1.0×10^{-10} W kg^{-1}, on the basis of the K, U, and Th concentrations determined by gamma ray spectrometry by Venera and Vega landers [*Surkov et al.*, 1987]. The specific heat is assumed to be 850 kJ kg^{-1} K^{-1}. The other physical properties of crustal and mantle materials are assumed to be those, respectively, of tholeiitic basalt and peridotite [*Basaltic Volcanism Study Project*, 1981]. Temperature at the surface and the bottom of the thermal boundary layer are fixed, respectively, at 750 K and at a value T_{bl}, a free parameter in numerical models. The initial temperature profile is determined by the assumption of steady-state conditions with zero strain rate. The increase in temperature with depth due to adiabatic compression is not considered here, because compressional heating is negligible compared with crustal heat production.

T_{bl} is interpreted as the temperature in an isothermal core of a thermal convection cell [*Turcotte and Schubert*, 1982] and is, thus, fixed at a constant. For a given T_{bl}, an initial temperature T_c at the base of the crust is determined. Since temperature at the base of the crust controls the elevation of the mountains, T_c has more importance than T_{bl}. *Zuber* [1987] analyzed wavelengths of tectonic features on Venus and found that the crustal thickness is less than about 15 km if the average vertical thermal gradient in the crust dT/dz is 25 K km^{-1}, and less than about 30 km if dT/dz is 10 K km^{-1}. The absence of significant viscous relaxation of impact crater relief also limits the crustal thickness in plains regions to be less than 10 km for dT/dz = 20 K km^{-1} and 20 km for dT/dz = 10 K km^{-1} [*Grimm and Solomon*, 1988]. These results give a maximum temperature difference across the crust of about 400 K. Therefore T_{bl} is given so that T_c initially satisfies this upper bound.

The phase diagram is assumed to be that of tholeiitic basalt [*Ito and Kennedy*, 1971], and the densities of gabbro and eclogite are taken to be 2900 and 3500 kg m^{-3}. The density of garnet granulite is assumed to increase linearly from that of gabbro to that of eclogite as pressure increases at a given temperature. The density of the mantle is assumed to be 3400 kg m^{-3}. The elevations calculated by an assumption of local Airy isostatic compensation are sensitive to the density difference between crust and mantle. We have adopted a relatively large value of 500 kg m^{-3}. Because a large density difference results in a higher elevation for a given root thickness, this assumption permits a conservative lower bound on horizontal strain rate. We discuss later the consequence of a lesser density contrast.

Diffusion Rates

The micromechanisms governing the gabbro - eclogite transition, which involves chemical as well as phase changes, are not well understood. A metamorphic reaction involves the nucleation of product crystals, the breakdown of reactant crystals, the

transport of materials between phases, and growth of the products; the rates of all of these processes will depend on temperature and perhaps on pressure [e.g., *Carlson*, 1989]. While laboratory experiments provide clues to the reaction rate of the gabbro - eclogite transformation [*Ito and Kennedy*, 1971], measurements reported to date were obtained from powdered samples and may be inapplicable to natural polycrystalline material where the transformation can occur by different mechanisms and at markedly slower rates [*Hacker et al.*, 1992]. In some terrestrial metamorphic environments, grain-boundary diffusion apparently controlled the governing nucleation and growth mechanisms [*Carlson*, 1989], but in the absence of an intergranular fluid, grain-boundary diffusion is likely a considerably less efficient process [*Ahrens and Schubert*, 1975]. Grain-boundary diffusion coefficients can be several orders of magnitude greater than those for volume diffusion, but such coefficients can be misleading, because mass transport by grain-boundary diffusion is confined to a thin layer [*Joesten*, 1991]. We consider this point further below.

We assume that under the anhydrous conditions likely to prevail in the crust of Venus, volume diffusion of cations is the process most likely to limit the rate of the gabbro - eclogite transformation [*Ahrens and Schubert*, 1975]. To accommodate our uncertainty in the validity of this assumption, however, we adopt a range of reaction rates by estimating upper and lower bounds on the limiting diffusion rate.

During volume diffusion the volume fraction of reacted components, ψ, is given by

$$\psi \frac{d\psi}{dt} = \frac{D}{r^2} \tag{2}$$

where r is the typical grain radius and D is the diffusion coefficient [*Ahrens and Schubert*, 1975]. For each parcel of shortening thermal lithosphere, ψ is obtained by integration over time. The density at a given depth is determined from the volume fractions of reacted and unreacted components.

There are several reactions occurring among constituent minerals in the garnet granulite

stability field [*Ringwood*, 1975]. The rate of each reaction is difficult to assess, because of a paucity of experimental data. We focus on the diffusion rates of ionic species in pyroxene, garnet, and olivine, because those minerals characterize the phase assemblages and therefore play important roles in the phase transitions. Plagioclase is possibly another important mineral for this assessment, but no data for self diffusion in plagioclase are available. The data for volume diffusion in silicates show that silicon and oxygen diffuse much more slowly than divalent and trivalent cations. Thus the Si-O groups provide a static framework through which the cations diffuse [*Freer*, 1981]. We examine the diffusion rates of four major cations, Mg^{2+}, Fe^{2+}, Ca^{2+}, and Al^{3+} (Figure 2.2). The slowest diffusion rate is likely to limit the reaction rate.

Diffusion rates of Fe^{2+} and Mg^{2+} in garnet and olivine [*Chakraborty and Ganguly*, 1991; *Morioka and Nagasawa*, 1991] and of Ca^{2+} in olivine [*Morioka and Nagasawa*, 1991] have been experimentally determined (Figure 2.2). Of these the diffusion rate of Mg^{2+} in garnet ($D_{Mg,\,Gt}$) is the lowest. Of course, if the diffusion rate of any unmeasured major species is slower than that of Mg^{2+} in garnet, then the phase change rate will be limited by this slower cation. We therefore take the diffusion coefficient $D_{Mg,\,Gt}$ for this process as an upper bound on D in equation (2).

Other diffusion rates, while not well-determined experimentally, have been estimated, either from measurements at a single temperature, or from observed compositional gradients. While all such estimates include large uncertainties, we take the minimum value of these estimates as a lower bound on D in equation (2). This minimum is for diffusion of Al^{3+} in orthopyroxene (Figure 2.2), estimated from an analysis of compositional gradients in natural assemblages [*Smith and Barron*, 1991]. The estimated rate depends on assumptions of cooling rate and pressure. While neither data nor estimates are available for the diffusion coefficients of Al^{3+} in olivine and garnet, cation diffusion in olivine and garnet is generally faster than in pyroxene [*Freer*, 1981; *Smith and Brown*, 1988], and thus is not likely to be rate-limiting. The diffusion of Ca^{2+} in garnet has been estimated by

numerical simulation only at 1200°C [*Chakraborty and Ganguly*, 1991] and is faster than that of Al^{3+} in orthopyroxene at that temperature (Figure 2.2). The mobilities of Ca^{2+} and Fe^{2+} are held to be comparable in garnet and pyroxene, because neither garnet nor pyroxene in natural assemblages is consistently homogeneous in those elements [*Smith and Barron*, 1991]. These considerations reinforce the view that $D_{Al,\,Opx}$ gives a reasonable lower bound on D in equation (2). The two bounds on D are

$$D \le D_{Mg,\,Gt} = 2.8\times10^{-8}\exp\left[-\left(270\text{ kJ} + 3.2\times10^{-6}P\right)/(RT)\right] \qquad (3a)$$

$$D \ge D_{Al,\,Opx} = 1.1\times10^{-5}\exp\left[-400\text{ kJ}/(RT)\right] \qquad (3b)$$

where P is in Pa [*Morioka and Nagasawa*, 1991; *Smith and Barron*, 1991].

There is some possibility that the assumed lower bound on D is too large. *Sautter et al.* [1988] and *Sautter and Harte* [1990] reported a diffusion rate of Al^{3+} in clinopyroxene less than the lower bound given above (Figure 2.2), while *Freer et al.* [1982] experimentally obtained a maximum diffusion rate as great as the upper bound given above (Figure 2.2). Further, the diffusion rates in plagioclase are generally less than in pyroxene [*Smith and Brown*, 1988], and interdiffusion of CaAl-NaSi in plagioclase is several orders of magnitude slower than the lower bound on D [*Grove et al.*, 1984]. If D is as low as suggested by these last results, no phase transition is expected to occur during the formation of mountains on Venus. However, the reaction rate is unlikely to be much slower than as given by the lower bound on D, because if volume diffusion is too slow, the reaction rate will be limited by grain-boundary diffusion.

It is important to estimate the relative importance of grain-boundary diffusion under anhydrous conditions, but grain-boundary diffusion data for the minerals involved in the gabbro - garnet granulite - eclogite reactions are few and generally not well determined [*Joesten*, 1991]. Reliable experimental data for grain-boundary diffusion of oxygen in forsterite, for instance, have been reported only at two temperatures [*Condit et al.*, 1985]. Under the assumption that the transport of O is rate-limiting for grain-boundary diffusion

[*Joesten and Fisher*, 1988], these measurements suggest that grain-boundary diffusion for grain sizes of 1-10 mm is no more efficient for bulk transport than the lower bound on volume diffusion adopted above (Figure 2.2). It is possible that the presence of carbon dioxide in the crust on Venus enhances grain-boundary diffusion, but experiments on Fe diffusion in dunite show that under conditions of chemical and mechanical equilibrium CO_2 exists as isolated pores and has no effect on diffusional transport [*Watson*, 1991].

NUMERICAL RESULTS

Temperatures in the thickening crust and mantle are calculated for rates of horizontal convergence of 10^{-15} (Figure 2.3a) and 10^{-16} s^{-1} (Figure 2.3b). For all models discussed here (Table 2.1), thicknesses of crust and thermal boundary layer are assumed to be initially 20 and 50 km, respectively, and to increase to 100 and 250 km, respectively. Temperature profiles for the strain rate of 10^{-15} s^{-1} are vertically stretched as the crust and mantle portion of the thermal boundary layer are thickened (Figure 2.3a). Temperatures do not increase significantly from initial values because heat is transferred mainly by advection and the contribution of crustal heat production is minor. Hence gabbro remains metastable for 50 My or more, and the elevation of shortened lithosphere can increase as much as 12 km above the surrounding area of undeformed lithosphere in that time interval (Model 1 in Figure 2.4a). Equation (2) shows that the reaction runs to completion in a shorter time for small grains than for larger grains. Also it is clear from equation (3) that a higher temperature increases the diffusion rate and promotes the reaction. For the slower diffusion rate ($D_{Al,\,Opx}$), however, a strain rate of 10^{-15} s^{-1} is sufficiently fast to suppress these effects (Model 2). The phase transition proceeds, i.e., elevation is limited, only if grains are small, diffusion is rapid, and temperature is high (Model 3).

For a strain rate of 10^{-16} s^{-1}, crustal heat production dominates advective heat transfer after the crust becomes as thick as 60-80 km (Figure 2.3b). The resulting increase in temperature hastens the phase transition, and the slower strain rate lengthens the formation time of the mountains. For larger grains (r = 10 mm) and a diffusion constant given by equation (3b) the elevation reaches 11 km or more even if the initial value of T_c is as great as 1120 K (Model 4 in Figure 2.4b). For the same initial value of T_c the elevation is at most 7 km for grains of 1 mm radius (Model 5). If initial T_c is greater than 1120 K, the model gives a maximum elevation lower than 7 km, that is, the model fails to explain the observed relief of Maxwell Montes. Therefore this result provides an upper bound on initial T_c for small grain size. If D is given by equation (3a), that upper bound is lowered

to 1030 K (Model 6). Thus the combination of the longer formation time due to the lesser value of $\dot{\gamma}$ and the faster reaction due to higher temperature constrains the range of parameters controlling the phase change if the elevation of the mountains is to reach 7 km or more above the adjacent plateaus.

DISCUSSION

The thermal model described above is simple, but significant constraints on the strain rate governing mountain building and the temperature at the base of the crust are nonetheless obtained. In this section, we first consider how the results would differ if key parameters were varied or the models were modified. We then discuss some implications of the numerical results given above.

The thermal evolution results are insensitive to the assumed initial thickness of the crust. At a strain rate of 10^{-15} s^{-1}, the advection-dominated thermal profile indicates that the temperature of each parcel of crust changes little as the parcel deepens. For a given value of initial T_c, the thermal structure at a given crustal thickness is not affected by initial crustal thickness, or, equivalently, initial thermal gradient. Only the time required for the crust to reach that thickness depends on the initial thickness. At a strain rate of 10^{-16} s^{-1}, in contrast, the thermal profile is close to steady state, that is, the geotherm is nearly the same as that for zero strain rate and thus does not depend on the initial crustal thickness. The initial crustal thickness is still important for the maximum relief, however, because by assumption it is identical to the crustal thickness beneath surrounding areas, taken here to be undergoing negligible rates of horizontal strain. By the assumption of Airy isostasy, at a given crustal thickness beneath the mountains a difference of 10 km in the thickness of the crust beneath surrounding areas results in a 1.5 km difference in relief.

Also important is the density difference between crust and mantle. If densities of 3000 and 3300 kg m^{-3} for crust and mantle are assumed, relative elevations are ~40% lower than the values presented here. At a strain rate of 10^{-15} s^{-1}, gabbroic lower crust remains metastable during the formation of mountains in most cases, as shown by models 1 and 2. Therefore a smaller density contrast simply requires thicker crust, i.e., greater duration of shortening, and does not otherwise constrain the model parameters. In contrast, at a strain rate of 10^{-16} s^{-1}, maximum elevations are limited in most cases by the gabbro - eclogite phase transition because of the high temperature at the base of the crust, as shown by

models 5 and 6. The lower relief resulting from a smaller density contrast lessens the upper bound on initial T_c. Thus such a lower density contrast constrains the models of thermal structure and phase transition depth more severely at low strain rates than do the density values adopted above.

At a strain rate of 10^{-16} s^{-1}, the thermal regime is dominated by crustal heat production and diffusion of heat. Horizontal heat transfer within the shortening thermal lithosphere therefore is probably not negligible. The maximum increase in temperature at the bottom of the crust due to horizontal heat transfer can be estimated from the solution for the instantaneous heating of the surface of a semi-infinite half-space [*Turcotte and Schubert*, 1982, p. 160],

$$\delta T = \Delta T \; erfc\left[\frac{L}{2\sqrt{\kappa\tau}}\right] \tag{4}$$

where δT is the increase in temperature, ΔT is the temperature difference between the base of the crust and an isothermal asthenosphere which surrounds the shortening lithosphere, L is the horizontal scale of the mountains, and τ is the formation time. In our problem, ΔT is given by T_{bl} - T_c, and L is ~100 km. Formation times of 50 My at a strain rate of 10^{-15} s^{-1} and of 500 My at a strain rate of 10^{-16} s^{-1} result in δT of 2 x 10^{-2} and 60 K, respectively. The assumption of one-dimensional heat transfer is therefore reasonable at the higher strain rate, but horizontal diffusion of heat increases temperature significantly at the lower strain rate. If horizontal heat transport were included in the thermal models at the lower strain rate, the reaction rate of the phase change would be faster, the maximum elevation would be less, and the corresponding upper bound on initial T_c would be lower.

These considerations favor the formation of Maxwell Montes at horizontal strain rates on the order of 10^{-15} s^{-1}. The implied age of the mountains is of order 50 My or less. Such an age is in agreement with a finite element model of viscoelastic deformation of regions of substantially thickened crust [*Smrekar and Solomon*, 1992], but young compared with the average crater retention age of the surface of Venus of about 500 My

[*Phillips et al.*, 1991]. An important question is whether such a young age is consistent with the presence of the 100-km diameter Cleopatra crater [*Basilevsky et al.*, 1987] (Figure 2.1) in Maxwell Montes, given that the crater appears to be undeformed in Magellan radar images [*Kaula et al.*, 1992]. The age of a single crater, of course, even a large one, is difficult to specify. The rate of formation of impact craters larger than 20 km in diameter on Venus has been estimated as $3.3 \pm 1.8 \times 10^{-15}$ km^{-2} yr^{-1} from the statistics of Earth-crossing and Venus-crossing asteroids and an assumed set of scaling laws [*Shoemaker et al.*, 1991]. If Maxwell Montes, 1000 km long and 500 km wide, formed in 50 My, the expected number of craters larger than 20 km in diameter is ~0.08. The probability that one and only one crater larger than 20 km diameter formed in Maxwell Montes in 50 My is thus ~8 %. This value indicates that the presence of a large impact crater is not likely if the mountains formed in only 50 My, but the figure is not so low as to reject the hypothesis at high confidence.

Although Danu Montes display compressional deformational features as extensive as the other mountain belts of Ishtar Terra, their maximum relief with respect to Lakshmi Planum is as little as 1 km (Figure 2.1). The presence of magmatic features within Danu Montes [*Solomon et al.*, 1991, 1992; *Head et al.*, 1991; *Kaula et al.*, 1992] indicates that temperature beneath the mountains exceeded the solidus of crustal or shallow mantle material at least locally. Given such evidence for relatively high temperature in the lower lithosphere, the reaction of sufficiently deep lower crustal material has probably gone nearly to completion, which may account for the comparatively modest topographic relief of these mountains. It is also noteworthy that even a small amount of melting can greatly enhance grain-boundary diffusion [*Condit et al.*, 1985; *Watson*, 1991]. Assessing the cause of higher temperatures beneath Danu Montes requires more detailed thermal models than the simple one-dimensional ones considered here.

The phase disequilibrium hypothesis explored in this study predicts that a deep root of metastable gabbroic crust is present beneath the mountain belt of Venus, particularly

Maxwell Montes. Circularization of the orbit of the Magellan spacecraft should yield gravity tracking data that can resolve anomalies at wavelengths as short as a few hundred kilometers, even at the high northern latitudes of Ishtar Terra. Such gravity measurements should thus provide a test of the validity of this hypothesis.

CONCLUSIONS

Taking into account the temperature-dependent reaction rate of the gabbro - eclogite phase transition, horizontal strain rates of 10^{-15} and 10^{-16} s^{-1} result in significant differences in the maximum elevation of mountains on Venus, not only because of the difference in the formation time for relief, but also because of the difference in the thermal regime from advection-dominated to crustal-heat-production dominated. For a strain rate of 10^{-15} s^{-1}, the observed maximum elevation of Maxwell Montes can be explained as a consequence of local isostasy and disequilibrium phase boundary depth for a wide range of physical parameters. For the lesser horizontal strain rate of 10^{-16} s^{-1}, only limited parameter values for thermal models are allowed, and this limitation becomes more difficult to satisfy when a smaller density contrast between the crust and mantle is assumed or when horizontal heat transport is considered. We favor the formation of Maxwell Montes at a strain rate of 10^{-15} s^{-1} or greater, although the likelihood that Cleopatra crater is younger than the implied age for Maxwell Montes (~50 My) is low. Magmatism within Danu Montes indicates higher temperatures in the crust or shallow mantle than beneath the other mountains. The modest elevation of Danu Montes relative to the other mountain belts of Ishtar Terra can be understood as a consequence of near completion of the phase transition.

REFERENCES

Ahrens, T. J., and G. Schubert, Gabbro - eclogite reaction rate and its geophysical significance, *Rev. Geophys. Space Phys.*, *13*, 383-400, 1975.

Anderson, D. L., Plate tectonics on Venus, *Geophys. Res. Lett.*, *8*, 309-311, 1981.

Barsukov, V. L., et al., The geology and geomorphology of the Venus surface as revealed by the radar images obtained by Venera 15 and 16, *Proc. Lunar Planet. Sci. Conf. 16th, J. Geophys. Res.*, *91*, D378-D398, 1986.

Basaltic Volcanism Study Project, *Basaltic Volcanism on the Terrestrial Planets*, 1286 pp., Pergamon, New York, 1981.

Basilevsky, A. T., Structure of central and eastern areas of Ishtar Terra and some problems of Venusian tectonics, *Geotectonics*, *20*, 282-288, 1986.

Basilevsky, A. T., B. A. Ivanov, G. A. Burba, I. M. Chernaya, V. P. Kryuchkov, O. V. Nikolaeva, D. B. Campbell, and L. B. Ronca, Impact cratering of Venus: A continuation of the analysis of data from Venera 15 and 16 spacecraft, *J. Geophys. Res.*, *92*, 12,869-12,901, 1987.

Bindschadler, D. L., and E. M. Parmentier, Mantle flow tectonics: The influence of ductile lower crust and implications for the formation of topographic uplands on Venus, *J. Geophys. Res.*, *95*, 21,329-21,344, 1990.

Carlson, W. D., The significance of intergranular diffusion to the mechanisms and kinetics of porphyroblast crystallization, *Contrib. Mineral. Petrol.*, *103*, 1-24, 1989.

Chakraborty, S., and J. Ganguly, Compositional zoning and cation diffusion in garnets, in *Diffusion, Atomic Ordering, and Mass Transport*, edited by J. Ganguly, pp. 120-175, Springer-Verlag, New York, 1991.

Condit, R. H., H. C. Weed, and A. J. Piwinskii, A technique for observing oxygen diffusion along grain boundary regions in synthetic forsterite, in *Point Defects in Minerals*, edited by R. N. Schrock, *Geophysical Monograph*, *31*, 97-105, Am.

Geophys. Union, Washington, D. C., 1985.

Crumpler, L. S., J. W. Head, and D. B. Campbell, Orogenic belts on Venus, *Geology, 14*, 1031-1034, 1986.

Freer, R., Diffusion in silicate minerals and glasses: A data digest and guide to the literature, *Contrib. Mineral. Petrol., 76*, 440-454, 1981.

Freer, R., M. A. Carpenter, J. V. P. Long, and S. J. B. Reed, "Null result" diffusion experiments with diopside: Implications for pyroxene equilibria, *Earth Planet. Sci. Lett., 58*, 285-292, 1982.

Grimm, R. E., and R. J. Phillips, Tectonics of Lakshmi Planum, Venus: Tests for Magellan, *Geophys. Res. Lett., 17*, 1349-1352, 1990.

Grimm, R. E., and R. J. Phillips, Gravity anomalies, compensation mechanisms, and the geodynamics of western Ishtar Terra, Venus, *J. Geophys. Res., 96*, 8305-8324, 1991.

Grimm, R. E., and S. C. Solomon, Viscous relaxation of impact crater relief on Venus: Constraints on crustal thickness and thermal gradient, *J. Geophys. Res., 93*, 11,911-11,929, 1988.

Grove, T. L., M. B. Baker, and R. J. Kinzler, Coupled CaAl-NaSi diffusion in plagioclase feldspar: Experiments and application to cooling rate speedometry, *Geochim. Cosmochim. Acta, 48*, 2113-2121, 1984.

Hacker, B. R., S. H. Kirby, and S. R. Bohlen, Time and metamorphic petrology: Calcite to aragonite experiments, *Science, 258*, 110-112, 1992.

Head, J. W., III, D. B. Campbell, C. Elachi, J. E. Guest, D. P. McKenzie, R. S. Saunders, G. G. Schaber, and G. Schubert, Venus volcanism: Initial analysis from Magellan data, *Science, 252*, 276-288, 1991.

Ito, K., and G. C. Kennedy, An experimental study of the basalt - garnet granulite - eclogite transition, in *The Structure and Physical Properties of the Earth's Crust*, edited by J. G. Heacock, *Geophysical Monograph, 14*, 303-314, Am. Geophys. Union, Washington, D. C., 1971.

Joesten, R., Grain-boundary diffusion kinetics in silicate and oxide minerals, in *Diffusion, Atomic Ordering, and Mass Transport*, edited by J. Ganguly, pp. 345-395, Springer-Verlag, New York, 1991.

Joesten, R., and G. Fisher, Kinetics of diffusion-controlled mineral growth in the Christmas Mountains (Texas) contact aureole, *Geol. Soc. Am. Bull., 100*, 714-732, 1988.

Kaula, W. M., Venus: A contrast in evolution to Earth, *Science, 247*, 1191-1196, 1990.

Kaula, W. M., D. L. Bindschadler, R. E. Grimm, V. L. Hansen, K. M. Roberts, and S. E. Smrekar, Styles of deformation in Ishtar Terra and their implications, *J. Geophys. Res., 97*, 16,085-16,120, 1992.

Morioka, M., and H. Nagasawa, Ionic diffusion in olivine, in *Diffusion, Atomic Ordering, and Mass Transport*, edited by J. Ganguly, pp. 176-197, Springer-Verlag, New York, 1991.

Phillips, R. J., R. E. Arvidson, J. M. Boyce, D. B. Campbell, J. E. Guest, G. G. Schaber, and L. A. Soderblem, Impact craters on Venus: Initial analysis from Magellan, *Science, 252*, 288-297, 1991.

Pronin, A. A., The structure of Lakshmi Planum, an indication of horizontal asthenospheric flow on Venus, *Geotectonics, 20*, 271-281, 1986.

Ringwood, A. E., *Composition and Petrology of the Earth's Mantle*, 618 pp., McGraw-Hill, New York, 1975.

Roberts, K. M., and J. W. Head, Western Ishtar Terra and Lakshmi Planum, Venus: Models of formation and evolution, *Geophys. Res. Lett., 17*, 1341-1344, 1990.

Sautter, V., and B. Harte, Diffusion gradients in an eclogite xenolith from the Roberts Victor kimberlite pipe: (2) kinetics and implications for petrogenesis, *Contrib. Mineral. Petrol., 105*, 637-649, 1990.

Sautter, V., O. Jaoul, and F. Abel, Aluminum diffusion in diopside using the $^{27}Al(p,r)^{28}Si$ nuclear reaction: Preliminary results, *Earth Planet. Sci. Lett., 89*, 109-114, 1988.

Shoemaker, E. M., R. F. Wolfe, and C. S. Shoemaker, Asteroid flux and impact cratering rate on Venus (abstract), *Lunar Planet. Sci., 22*, 1253-1254, 1991.

Smith, D., and B. Barron, Pyroxene - garnet equilibration during cooling in the mantle, *Am. Mineral., 76*, 1950-1963, 1991.

Smith, J. V., and W. L. Brown, *Feldspar Minerals*, 828 pp., Springer-Verlag, Berlin, 1988.

Smrekar, S. E., and S. C. Solomon, Gravitational spreading of high terrain in Ishtar Terra, Venus, *J. Geophys. Res., 97*, 16,121-16,148, 1992.

Solomon, S. C., J. W. Head, W. M. Kaula, D. McKenzie, B. Parsons, R. J. Phillips, G. Schubert, and M. Talwani, Venus tectonics: Initial analysis from Magellan, *Science, 252*, 297-312, 1991.

Solomon, S. C., et al., Venus tectonics: An overview of Magellan observation, *J. Geophys. Res., 97*, 13,199-13,255, 1992.

Surkov, Yu. A., V. L. Barsukov, L. P. Moskalyeva, V. P. Kharyukova, and A. L. Kemurdzhian, New data on the composition, structure, and properties of Venus rock obtained by Venera 13 and Venera 14, *Proc. Lunar Planet. Sci. Conf. 14th, J. Geophys. Res., 89*, B393-B402, 1984.

Surkov, Yu. A., F. F. Kirnozov, V. N. Glazov, A. G. Dunchenko, L. P. Tatsy, and O. P. Sobornov, Uranium, thorium, and potassium in the Venusian rocks at the landing sites of Vega 1 and 2, *Proc. Lunar Planet. Sci. Conf. 17th, J. Geophys. Res., 92*, E537-E540, 1987.

Turcotte, D. L., A heat pipe mechanism for volcanism and tectonics on Venus, *J. Geophys. Res., 94*, 2779-2785, 1989.

Turcotte, D. L., and G. Schubert, *Geodynamics: Applications of Continuum Physics to Geological Problems*, 450 pp., Wiley, New York, 1982.

von Zahn, U., S. Kumar, H. Niemann, and R. Prinn, Composition of the Venus atmosphere, in *Venus*, edited by D. M. Hunten, L. Colin, T. M. Donahue, and V. I.

Moroz, pp. 299-430, Univ. Arizona Press, Tucson, 1983.

Vorder Bruegge, R. W., and J. W. Head, Processes of formation and evolution of mountain belts on Venus, *Geology*, *19*, 885-888, 1991.

Watson, E. B., Diffusion in fluid-bearing and slightly-melted rocks: Experimental and numerical approaches illustrated by iron transport in dunite, *Contrib. Mineral. Petrol.*, *107*, 417-434, 1991.

Zuber, M. T., Constraints on lithospheric structure of Venus from mechanical models and tectonic surface features, *Proc. Lunar Planet. Sci. 17th, J. Geophys. Res.*, *92*, E541-E551, 1987.

Table 2.1. Parameters for Thermal Models

Model	r, mm	$\dot{\gamma}$, s^{-1}	D	initial T_c, K	T_{bl}, K
1	10	10^{-15}	$D_{Al,\ Opx}$	1050	1321
2	1	10^{-15}	$D_{Al,\ Opx}$	1120	1461
3	1	10^{-15}	$D_{Mg,\ Gt}$	1130	1481
4	10	10^{-16}	$D_{Al,\ Opx}$	1120	1461
5	1	10^{-16}	$D_{Al,\ Opx}$	1120	1461
6	10	10^{-16}	$D_{Mg,\ Gt}$	1030	1281

FIGURE CAPTIONS

Figure 2.1. Topographic map of western Ishtar Terra. Contour map of Magellan altimetry data gridded at 0.5° intervals of latitude and longitude; 1-km contour interval; polar stereographic projection. Cross symbol shows the location of Cleopatra crater (65.9°N 7.0°E).

Figure 2.2. Diffusion constants for ionic species in olivine, pyroxene, and garnet. Solid lines show diffusion constants that were experimentally determined (1 is for Fe in garnet [*Chakraborty and Ganguly*, 1991]; 2 is for Mg in garnet [*Chakraborty and Ganguly*, 1991]; 3 is for Fe in olivine [*Morioka and Nagasawa*, 1991]; 4 is for Mg in olivine [*Morioka and Nagasawa*, 1991]; and 5 is for Ca in olivine [*Morioka and Nagasawa*, 1991]). The shaded area shows the range of estimates for $D_{Al,\,Opx}$ including maximum and minimum (6) values [*Smith and Barron*, 1991]. Cross symbols show the values determined at a single temperature (7 is for Ca in garnet [*Chakraborty and Ganguly*, 1991]; 8 is an upper bound on the diffusion constant of Al^{3+} in clinopyroxene [*Freer et al.*, 1982]; 9 and 10 are values for Al^{3+} in clinopyroxene from *Sautter et al.* [1988] and *Sautter and Harte* [1990], respectively). The constants for grain-boundary diffusion of O in forsterite [*Condit et al.*, 1985] are converted to equivalent volume diffusion coefficients (11) by multiplying by the ratio of grain boundary width to grain diameter; the grain boundary width was taken to be 3 μm [*Condit et al.*, 1985], and the grain diameters were taken to be 1-10 mm.

Figure 2.3. Thermal evolution of crust (solid) and mantle (dashed) thickened at a uniform horizontal strain rate of (a) 10^{-15} and (b) 10^{-16} s^{-1}. The phase boundary of the gabbro (G), garnet granulite (GG), and eclogite (E) assemblages and the solidus (S) [*Ito and Kennedy*, 1971] are shown by dotted lines. The models shown correspond to models (a) 1 and (b) 4 and 5 in Table 2.1.

Figure 2.4. Temporal variation of elevation for the thermal models in Table 2.1.

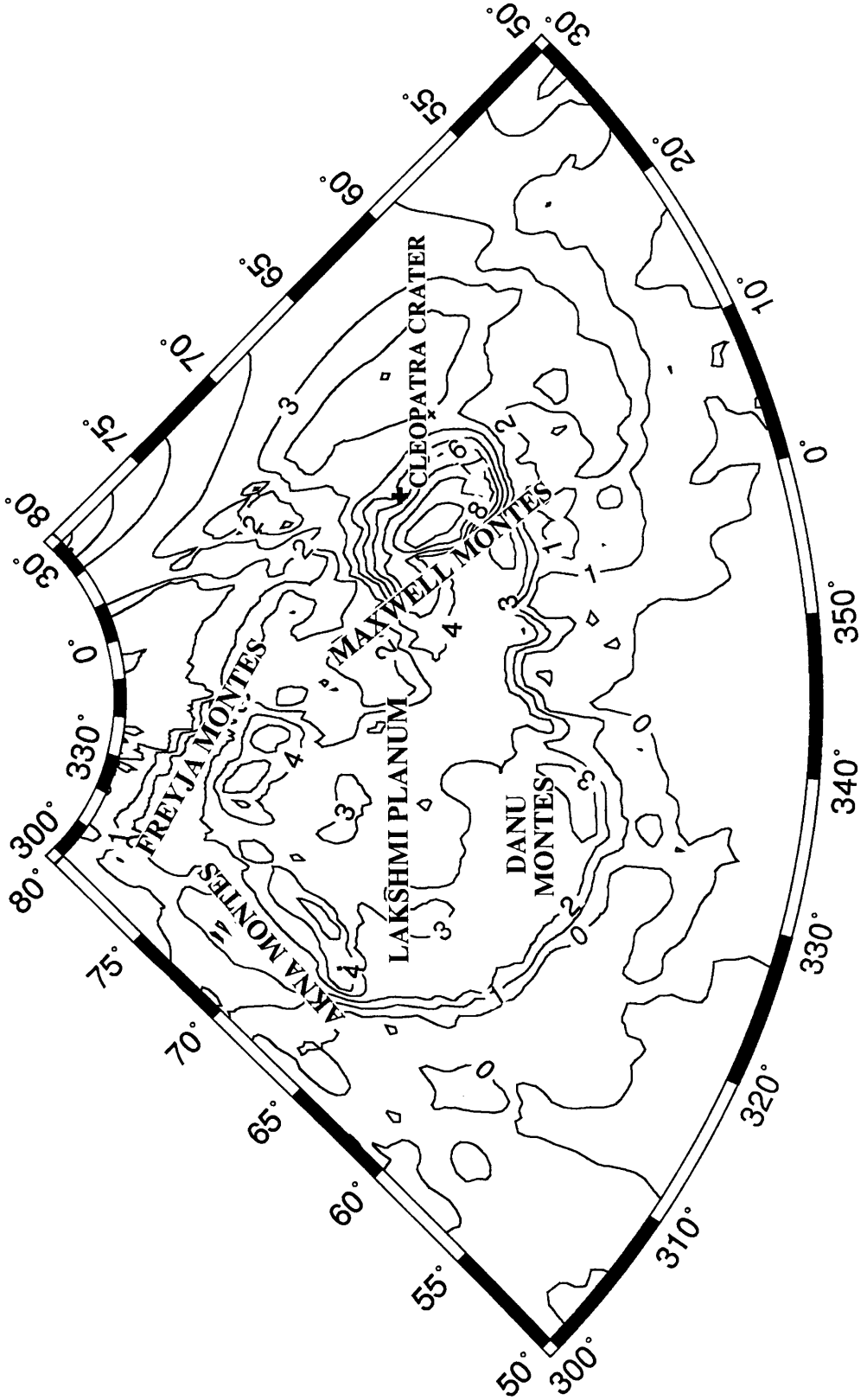
CLEOPATRA CRATER
MAXWELL MONTES
FREYJA MONTES
LAKSHMI PLANUM
AKNA MONTES
DANU MONTES

Figure 2.1

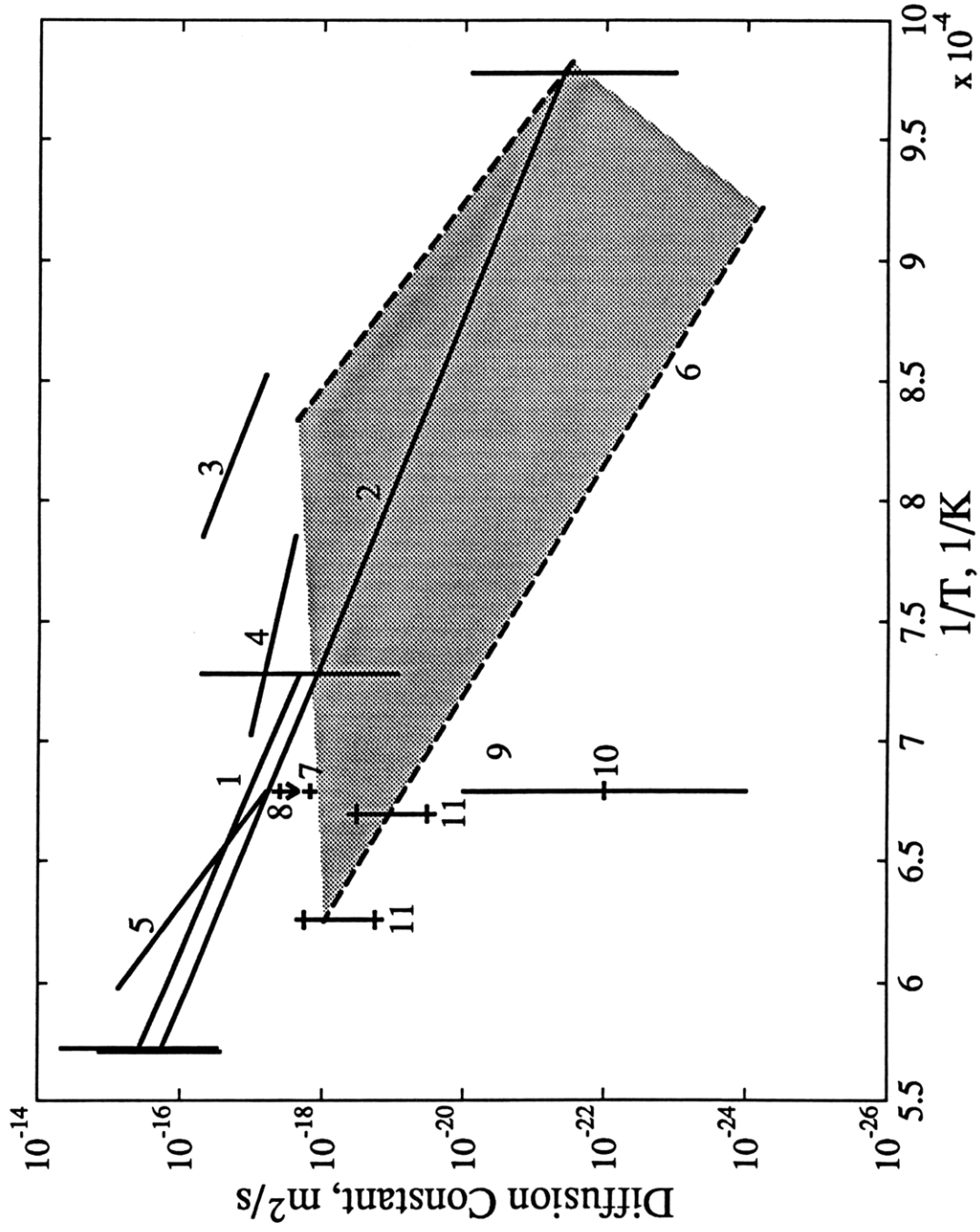
Diffusion Constant, m2/s
1/T, 1/K
x 10-4
10-14
10-16
10-18
10-20
10-22
10-24
10-26
5.5
6
6.5
7
7.5
8
8.5
9
9.5
10
1
2
3
4
5
6
7
8
9
10
11
11

Figure 2.2

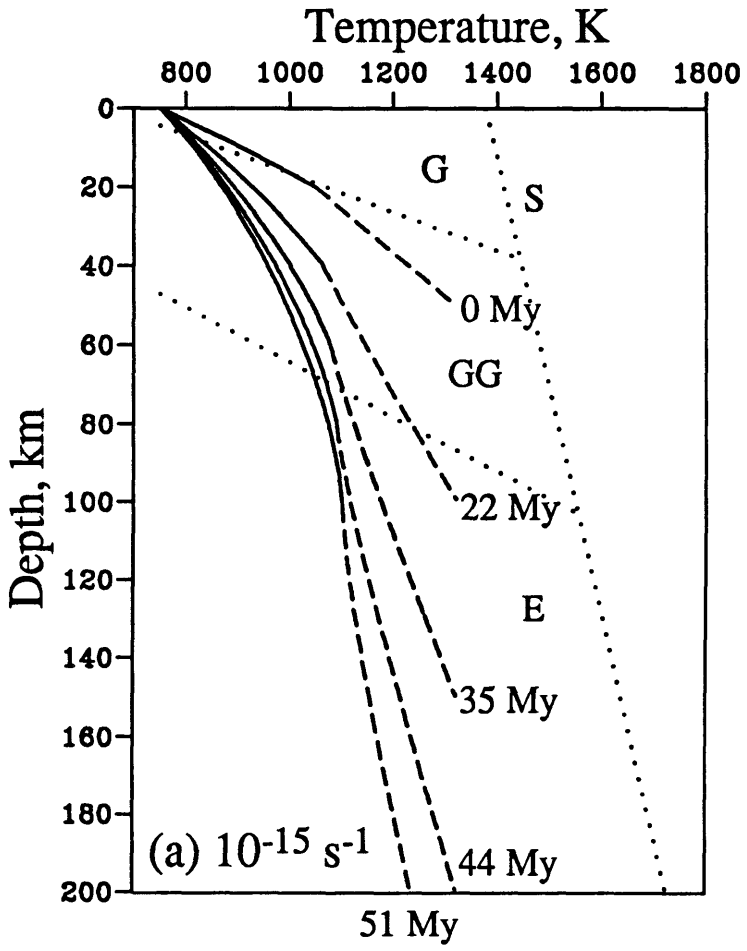
Temperature, K
800
1000
1200
1400
1600
1800
0
20
40
60
80
100
120
140
160
180
200
Depth, km
G
S
0 My
GG
22 My
E
35 My
(a) 10-15 s-1
44 My
51 My

Figure 2.3a

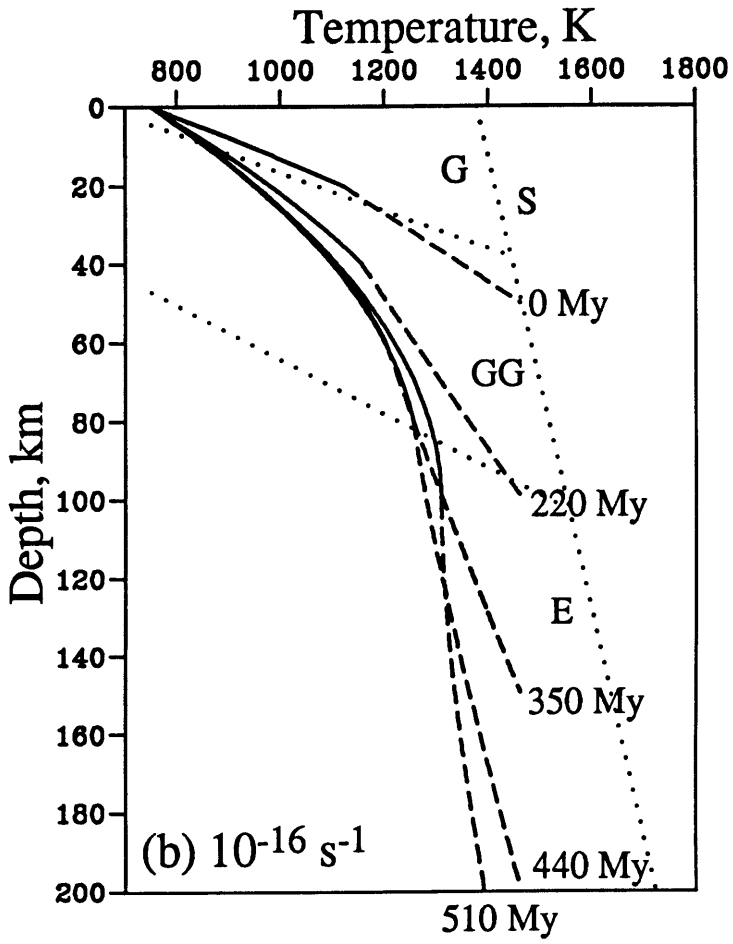
Temperature, K
800
1000
1200
1400
1600
1800
0
20
40
60
80
100
120
140
160
180
200
Depth, km
G
S
0 My
GG
220 My
E
350 My
(b) 10-16 s-1
440 My
510 My

Figure 2.3b

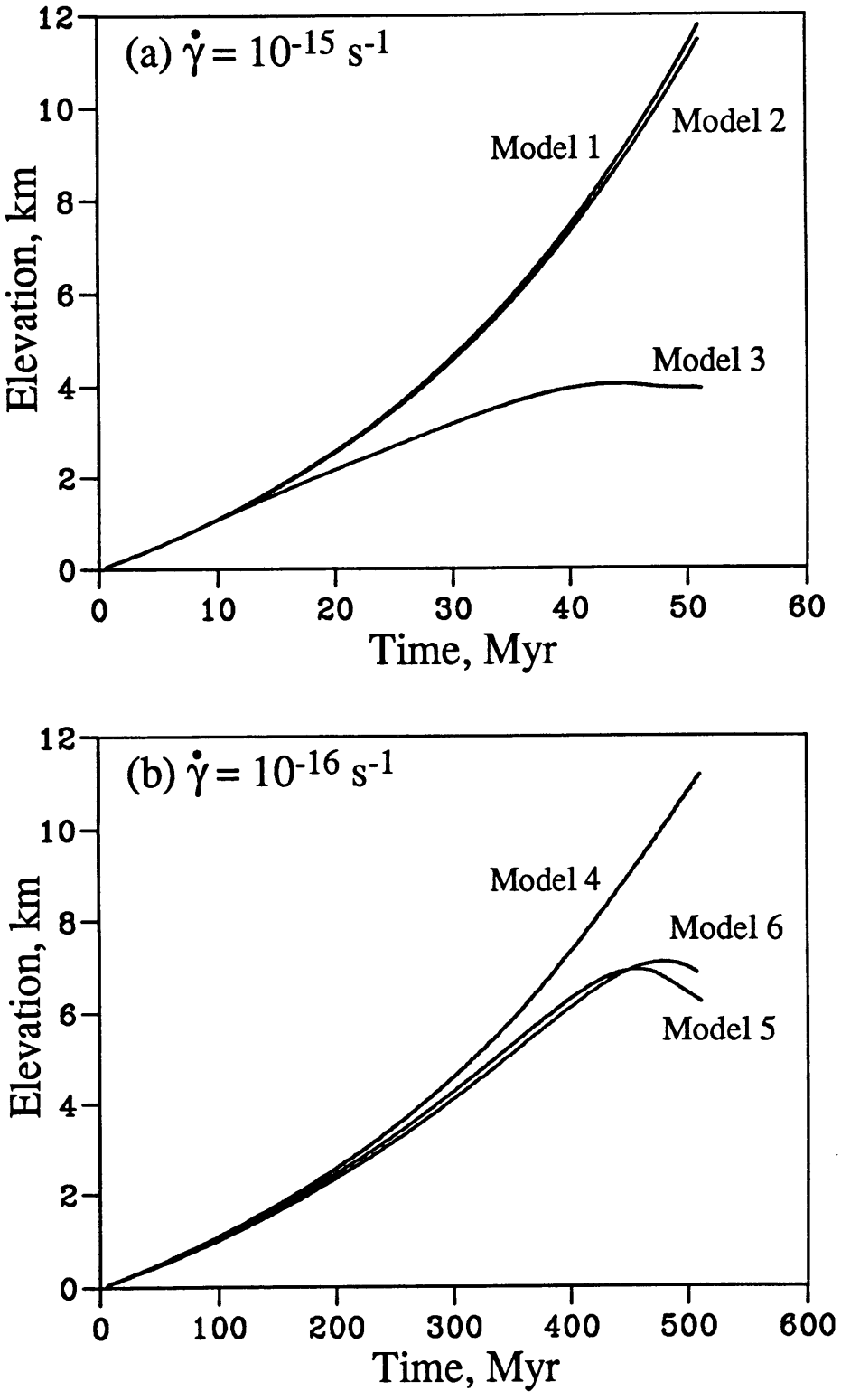
(a) $\dot{\gamma} = 10^{-15}$ s^{-1}
Model 1
Model 2
Model 3
Elevation, km
Time, Myr
0
2
4
6
8
10
12
0
10
20
30
40
50
60
(b) $\dot{\gamma} = 10^{-16}$ s^{-1}
Model 4
Model 6
Model 5
Elevation, km
Time, Myr
0
2
4
6
8
10
12
0
100
200
300
400
500
600

Figure 2.4

Chapter 3:

Impact Crater Densities on Volcanoes and Coronae on Venus: Implications for Volcanic Resurfacing

Volcanic features are widely distributed over the surface of Venus (1), and their ages provide critical information on the magmatic budget of the planet. However, the generally low density of impact craters on Venus, a result of atmospheric shielding (2, 3), has prevented a comparison of crater retention ages among small regions (4) and contributes to the controversy over whether a catastrophic (2) or an equilibrium model (3) better describes the global resurfacing history. The spatial diversity of the crater distribution has nonetheless been addressed by grouping areas by latitude or longitude (2), radar cross section (3), elevation (5), or terrain type (6). Following this practice, we have integrated the areas and cratering records for large volcanoes and for coronae (7) on Venus, and we assess here the implications of the results for volcanism and global resurfacing.

We made use of a data base of 841 impact craters classified according to the extent of tectonic deformation and of embayment or partial covering by volcanic material (5, 8). A data base for 175 volcanoes at least 50 km in diameter (9) compiled from Magellan images and a published map (1) includes radius and relief of the topographic edifice and the dimensions of the radial flow apron. A data base for 358 coronae (10) includes a classification by feature type and extent of interior volcanism. There are 51 features listed in both the volcano and corona data bases, because in many coronae there are associated volcanic centers.

For each large volcano, we ascertained from the data bases the presence of one or more impact craters on the edifice or flow apron, and from Magellan radar images we determined superposition relationships (Figure 3.1). We included the edifice and discernible radial flows in calculating the area of each volcano. All embayed craters associated with a large volcano are on plains units exterior to the volcanic edifice. We did not count those embayed craters because of the difficulty determining whether the impact occurred before or during the period of volcanic activity. Thus the crater density for large volcanoes measures the average time since major eruptions ceased. The lava

flow area for each volcano was measured from Magellan C1-MIDRs and F-MIDRs (11) using meshes of 53 x 53 km^2 and 18 x 18 km^2 grids, respectively. The sum of the measured flow areas, the observed total number of impact craters, and the average crater density are given in Table 3.1. Large volcanoes constitute 5% of the surface of Venus. Because the minimum area necessary to make an independent estimate of crater density on Venus is about 1% of the surface (4), the area covered by large volcanoes is sufficiently large to make such an estimate.

The distribution of the density of impact craters on large volcanoes with crater diameter is compared with the distribution for the planet as a whole in Figure 3.2a. Because we have included in our counts craters whose ejecta deposits barely overlap a volcano flow apron, the effective area of a volcano for a potentially superposed crater is larger than the actual area by an amount that depends on the crater dimensions. We corrected for this difference in the following manner. We determined a flow apron radius for each volcano by finding the circle having the same area as that of the edifice and radial lava flows. Then the effective area was taken equal to that of a circle whose radius is the sum of that of the flow apron, that of the crater, and the width of the crater ejecta deposits (12). The ratio of the measured area to the effective area provides a correction to the crater density at a given crater diameter.

The distribution of craters by size, so corrected, can be interpreted in one of two ways. On the basis of the similarity of densities of impact craters larger than 16 km on large volcanoes and on the planet as a whole, it might be argued that the surfaces of large volcanoes are the same average age as the planet overall (6), but that smaller craters have been preferentially removed by volcanic infilling. This explanation encounters a difficulty, however, when it is realized that we have excluded embayed craters in the counts. It is hard to conceive of a mechanism that would remove small craters but fail to embay the larger craters included in the counts. The second interpretation acknowledges the large uncertainties in the densities of the largest craters and makes use of the entire

distribution as an integrated measure of crater density. While the distribution of impact craters on large volcanoes can be distinguished from that for the entire planet, the hypothesis that the two distributions differ by a scalar multiple cannot be rejected at high confidence (13).

The corrected average density of impact craters of all diameters on large volcanoes, at $(0.9 \pm 0.2) \times 10^{-6}$ km^{-2}, is significantly less than the global average of $(2.0 \pm 0.1) \times 10^{-6}$ km^{-2} (2, 3). Further, the fraction of craters associated with large volcanoes embayed by volcanic deposits (33%) is much higher than the global fraction of embayed craters for the planet as a whole (6.5%). Thus the surfaces of large volcanoes are, on average, younger than the mean age for the planet of about 500 My (2, 3, 14). This result is consistent with the inference, but does not require, that large volcanoes as a class have relatively young ages. The age of initiation of volcanic activity at each center is, of course, greater than the age of the present volcano surface. On Earth, activity at intraplate hot spots and continental flood basalt provinces can last between several million years and 100 My (15, 16). The lifetimes of volcanoes on Venus, however, are poorly constrained. There is also a possibility that some old volcanoes may display a morphology sufficiently different from younger volcanoes that they have not yet been identified as volcanic centers. If so, then the crater densities obtained here are appropriate only to the youngest fraction of centers of volcanic construction.

For a global average surface age of 500 My (2, 3, 14), then from the total area of identified large volcanoes and associated radial flows we may infer an average rate of resurfacing by large volcanoes since that time of 0.05 km^2 yr^{-1}. This figure underestimates the overall volcanic resurfacing rate, of course, because many other types of volcanic landforms occur on Venus (1). If we assume that all embayed craters can be attributed to volcanic activity and that the density of partially embayed craters is a constant for all volcanic deposits younger than the mean crater retention age, then the area of volcanic flows capable of manifesting an embayment relationship in Magellan

images is estimated to be 1.0 x 10^8 km^2, or equivalently 22% of the surface, and the global volcanic resurfacing rate over the last 500 My is calculated as 0.2 km^2 yr^{-1}.

We may convert these areal resurfacing rates to volumetric fluxes by noting that large craters are more resistant to volcanic embayment than small craters and should therefore have a higher ratio of partially embayed craters. In Figure 3.3 we show the fraction of embayed craters versus crater diameter (5, 8). We suggest that the distinct increase in this fraction at a diameter near 30 km occurs because craters larger than this size tend to survive volcanic embayment. The depth and the rim height of a 30-km-diameter crater on Venus inferred from Magellan radar image measurements (12) are about 1.6 km and 0.5-0.8 km, respectively. We thus take 2 km as a conservative upper bound on the average thickness of embaying flow units. This value is comparable to average thicknesses of terrestrial continental flood basalt occurrences of 0.65 to 5 km (15). From the above estimate of the total area of lava flows capable of embaying craters, upper bounds on the volume of such flow units and the extrusive component of the magmatic flux over the last 500 My are 2.0 x 10^8 km^3 and 0.4 km^3 yr^{-1}, respectively. The latter bound is consistent with estimates of the volcanic flux obtained from 2-D and 3-D Monte Carlo resurfacing models (0.01-0.15 and 0.37 km^3 yr^{-1}, respectively) constrained to fit the observed global crater distribution and the fraction of partially embayed craters (17).

Magma reaching the surface as volcanic eruptions, of course, represents only a portion of the total amount of magma generated. A variety of intrusive volcanic landforms have been observed on Venus (1), and there is more intrusive than extrusive magmatism on Earth (18). However, little is known about the ratio of intrusive to extrusive magmatism on Venus. Such a ratio is likely controlled by the brittle strength of the crust and the ability of magma to propagate in dikes and sills (19). Estimates of the fracture toughness, or the resistance to fracture growth, and the maximum distance of shallow crustal magma propagation for Venus are not significantly different from terrestrial values (19, 20). Therefore, as a conservatively large estimate of the ratio of

intrusive to extrusive magmatism on Venus, we adopt the value 17, the maximum ratio documented on Earth (18). Upper bounds on the total volume of magmatic material and the magmatic flux over the last 500 My are then 3.6×10^9 km^3 and 7.2 km^3 yr^{-1}, respectively. The latter figure is within the range in estimates for the current rate of volcanism and near-surface magmatism on Venus (0.4 to 11 km^3 yr^{-1}) inferred from the rate of reaction of atmospheric SO_2 and surface carbonates (21).

For coronae, we determined the impact crater density within corona interiors (Figure 3.4); for most coronae the interior was taken to be the outer radius of the tectonic annulus. The area of each corona was taken from the dimensions given in the corona data base (10). The crater density on coronae and its distribution with crater diameter were corrected for effective area in the same manner as for craters on large volcanoes (Figure 3.2b and Table 3.1). The density of craters of diameter 8 km and greater is somewhat less than average for the planet, while the density of craters less than 8 km in diameter is somewhat greater than average. The small craters on coronae are not secondary craters, because no candidate primary craters are sufficiently near. Nor is the greater density of small craters due to a greater fractional coverage of full-resolution images of coronae than for the planet as a whole. Because of the small numbers of craters in each size range, we prefer, as with large volcanoes, to make use of the entire distribution of craters, rather than only a portion of the distribution, to assess crater density (22). Artemis, about 2200 km in diameter, and the largest corona on Venus (10), occupies nearly 15% of the total area of coronae and includes 5 craters. The crater density for coronae with Artemis excluded, however, is unchanged from that for all coronae (Table 3.1). Overall, the corrected average density of impact craters on coronae, at $(1.4 \pm 0.2) \times 10^{-6}$ km^{-2}, is midway between that for large volcanoes and the global average (Table 3.1). The significance of this result is illuminated by considering geological evidence for corona evolution.

A general sequence of corona development has been postulated from geological

studies of Venera 15/16 and Magellan images of individual coronae (10, 23). This evolutionary sequence consists of three stages (10). The first stage is characterized by uplift, interior deformation including extensive radial extensional faulting, and volcanic construction. In the second stage, formation of the tectonic annulus and trough occurs, along with continued volcanism. In the last stage coronae are no longer foci for activity but may be partially embayed by regional volcanic deposits or faulted during regional tectonic deformation (10, 23). On the basis of this scenario, coronae have been classified into five groups according to feature type, extent of associated volcanism, and extent of regional embayment by smooth plains material (10). The first group (termed radial, radial/concentric, and volcanic coronae) are held to correspond to the earliest stage of corona formation. The second to fourth groups (termed categories 1, 2, and 3) are distinguished by an increasing intensity of associated interior volcanism (10) and are held to represent successive evolution within the second stage of corona development. The last group (termed categories 2r and 3r) are older coronae no longer individually active.

The average crater density for each corona group is shown in Figure 3.5. While the small numbers of craters prevent quantitative discussion with high confidence, differences in crater density among corona groups can be recognized (24). The first (radial/volcanic) and second (category 1) groups have a combined crater density indistinguishable from the global average and, by implication, are comparable in average age. It is possible that some of the craters on such coronae predate the tectonic development of the corona structures. Older craters are likely to have been deformed during corona evolution. Three craters are classified as tectonically deformed among 13 craters on the first and second groups of coronae; the density of remaining craters is $(1.4 \pm 0.5) \times 10^{-6}$ km^{-2} for these two corona groups. This figure should be regarded as a lower bound, however, because the deformed craters may have formed during the interval of corona evolution or their deformation may have occurred as a result of regional tectonic modification after corona development. Regionally embayed coronae (categories

2r and 3r) also have a crater density similar to the global average. Only coronae with extensive associated volcanic deposits (categories 2 and 3) have crater densities clearly less than the average value for the planet.

The crater densities in Figure 3.5 are not those expected if coronae are distributed in age and if all coronae evolve from the radial or volcanic stages through the stages represented by corona categories 1-3. If all coronae evolve through the full postulated sequence of evolutionary stages, then those in early phases of evolution should be younger and thus have a lower crater density than those in later phases. The crater densities instead suggest that many coronae represent features that for the most part ceased to develop after a time near the global mean age of the surface. The lower crater densities of category 2 and 3 coronae, however, indicate that volcanic deposits in these features are considerably younger. This result is consistent with the observation that volcanism tends to become more concentrated within corona interiors as coronae evolve (25).

The crater densities obtained in this study provide a strong constraint on the history of resurfacing on Venus, one of the most fundamental questions raised by Magellan radar observations (2, 3). If the surface of Venus were uniform in age or if crater production and resurfacing were in equilibrium, then the crater density on volcanoes should equal the global average density regardless of the mix of global resurfacing mechanisms or the rate of volcanic activity (26). That crater densities on large volcanoes and on some coronae are significantly lower than the global average is inconsistent with both of these end-member models. Our results suggest that large volcanoes and coronae with voluminous associated volcanic deposits have been magmatically active during the past 500 My. Further, a crater density about half the global average is consistent with an age distribution for such features that is approximately uniform over that time interval. About 20% of the surface of Venus has been volcanically resurfaced during that time.

REFERENCES AND NOTES

1. J. W. Head, L. S. Crumpler, J. C. Aubele, J. E. Guest, R. S. Saunders, *J. Geophys. Res.* **97**, 13153 (1992).

2. G. G. Schaber et al., *ibid.* **97**, 13257 (1992).

3. R. J. Phillips et al., *ibid.* **97**, 15921 (1992).

4. J. J. Plaut and R. E. Arvidson, *ibid.* **93**, 15339 (1988).

5. R. R. Herrick and R. J. Phillips, *Icarus* **111**, 387 (1994).

6. M. A. Ivanov and A. T. Basilevsky, *Geophys. Res. Lett.* **20**, 2579 (1993).

7. Coronae are circular to ovate volcanotectonic structures 60 to more than 2000 km in diameter generally distinguished by an annulus of closely spaced deformational features.

8. The original data base includes 838 craters; we added 3 craters on the basis of recently distributed Magellan images. An independently compiled data base (2) lists impact craters but does not classify them by extent of tectonic deformation or exterior embayment. Using the latter data base increases the impact crater density on volcanoes and coronae by 14% and 13%, respectively, principally by the addition of craters less than 15 km in diameter.

9. P. J. McGovern, C. B. Siren, S. C. Solomon, unpublished material.

10. E. R. Stofan et al., *J. Geophys. Res.* **97**, 13347 (1992). We modified the original data base by removing 4 entries and adjusting the maximum widths of 5 features on the basis of Magellan images.

11. G. H. Pettengill, P. G. Ford, W. T. K. Johnson, R. K. Raney, L. A. Soderblom, *Science* **252**, 260 (1991). C1- and F-MIDRs are compressed-once and full-resolution Magellan image data records, respectively. Where the edges of lava flows are not clear in standard images, we applied high-pass and median filtering to measure flow area.

12. V. L. Sharpton, *Eos Trans. AGU* **73**, *Fall Meeting suppl.*, 331 (1992). We have assumed an ejecta width of 0.4 times the crater diameter.

13. On the basis of a χ^2 test, the probability that the two distributions are identical is 0.02%; the probability that the two are the same except for a scaling factor is 74%.

14. The average crater retention age of the surface on Venus has been estimated to lie between 210 and 720 My (2) and between 400 and 800 My (3). We take 500 My as a representative value (2, 3). The areal resurfacing rate and volcanic flux scale inversely with the assumed average age.

15. Basaltic Volcanism Study Project, *Basaltic Volcanism on the Terrestrial Planets* (Pergamon, New York, 1981); P. Cattermole, *Planetary Volcanism* (Ellis Horwood, Chichester, 1989).

16. T. Simkin, *Ann. Rev. Earth Planet. Sci.* **21**, 427 (1993).

17. M. A. Bullock, D. H. Grinspoon, J. W. Head, III, *Geophys. Res. Lett.* **19**, 2147 (1993); R. G. Strom, G. G. Schaber, D. D. Dawson, *J. Geophys. Res.*, **99**, 10899 (1994).

18. J. A. Crisp, *J. Volcan. Geotherm. Res.* **20**, 177 (1984); M. F. Coffin and O. Eldholm, *Rev. Geophys.* **32**, 1 (1994).

19. A. M. Rubin and D. D. Pollard, *Volcanism in Hawaii, U.S. Geol. Surv. Prof. Pap. 1350*, 1449, (1987); E. A. Parfitt, *J. Geophys. Res.* **96**, 10101 (1991); D. McKenzie, J. M. McKenzie, R. S. Saunders, *ibid.* **97**, 15977 (1992).

20. R. A. Schultz, *ibid.* **98**, 10883 (1993). Crustal pore pressure is negligible on Venus because of the absence of water, which may render the crust more resistant to dike propagation than on Earth. It should be noted, however, that there is a disagreement of two or more orders of magnitude between experimentally determined and field estimates of fracture toughness (19).

21. B. Fegley, Jr., and R. G. Prinn, *Nature* **337**, 55 (1989).

22. A χ^2 test yields a probability of 15% that the distribution of craters on coronae is identical to that for the entire planet; the probability that the two distributions are the same except for a scaling factor is 69%.

23. A. T. Basilevsky et al., *Proc. Lunar Planet. Sci. Conf. 16th, J. Geophys. Res.* **91**, D399 (1986); E. R. Stofan and J. W. Head, *Icarus* **83**, 216 (1990); A. A. Pronin and E. R. Stofan, *ibid.* **87**, 452 (1990); S. W. Squyres et al., *J. Geophys. Res.* **97**, 13611 (1992).

24. Areas covered by the different corona groups are 2.9, 3.5, 7.6, 6.7, and 5.6 x 10^6 km^2 for radial/volcanic, category 1, 2, 3, and 2r and 3r coronae, respectively. The areas of the first two groups are too small to estimate crater density reliably, but the last three groups cover sufficiently large areas (4). On the basis of a χ^2 test, the probability that crater densities in Figure 3.5 differ from random variations from an average is 68%.

25. K. M. Roberts and J. W. Head, *Geophys. Res. Lett.* **20**, 1111 (1993).

26. In the end-member equilibrium resurfacing model, the total number of impact craters on the surface, N^G, is described by

$$\frac{dN^G}{dt} = R_p S^G - u_r^G N^G$$

where R_p is the crater production rate per unit area, S^G is the surface area, and u_r^G is the fractional rate of removal of craters by global resurfacing. Similarly, the number of craters on volcanoes, N^V, is described by,

$$\frac{dN^V}{dt} = R_p S^V - u_r^G N^V$$

where S^V is the area of volcanoes. Under equilibrium, $dN/dt = 0$. If S^V is constant in time, the crater density on volcanoes is equal to the global average density, R_p/u_r^G.

27. Errors in crater counts are taken to equal the square root of the number of craters.

28. On the basis of the crater data base (5, 8), 18 large volcanoes have unmodified craters associated with them; 12 large volcanoes have associated embayed craters.

These two populations of volcanoes do not overlap. Four volcanoes each have an associated deformed crater; two of these craters are also embayed. A total of 143 (82%) of the identified large volcanoes lack any associated impact craters.

29. From (5, 8), 30 coronae have unmodified craters; 3 coronae have embayed craters; and 8 coronae have deformed craters. Artemis is the only corona displaying associated craters of different classes (1 unmodified, 2 deformed, and 2 embayed); the three subsets of coronae do not otherwise overlap. A total of 319 coronae (89%) lack any associated impact craters.

Table 3.1. Summary of crater counts on large volcanoes and coronae (27-29).

	Number of craters			Area,	Uncorrected (corrected) crater density,
	Unmodified	Embayed	Deformed	$x10^6$ km^2	$x10^{-6}$ km^{-2}
Volcanoes	26	14	4	25	1.0±0.2 (0.9±0.2)
Coronae	33	3	9	27	1.7±0.2 (1.4±0.2)
(excluding Artemis)	32	1	7	23	1.7±0.3 (1.4±0.2)

FIGURE CAPTIONS

Figure 3.1. Magellan radar image illustrating volcano-crater superposition relationships in southern Bell Regio. The image is centered at 29°N, 47°E, and is 1300 km wide. The impact crater Potanina (90-km diameter) at the upper right portion of the image overlies radar-dark lava flows emanating from an unnamed volcano near the center of the image. In the southwest portion of the image, radar-bright flows nearly completely embay a 60-km-diameter impact crater. This and following images are in sinusoidal equal-area projection; north is up; the radar illumination is from the left; and radar cross sections have been linearly stretched to enhance contrast. Black areas are data gaps.

Figure 3.2. Distribution of impact craters by crater diameter. Craters are binned into increments at intervals of a factor of 2 in diameter (the full crater density is the sum of these incremental densities). (a) Crater density on large volcanoes (circles). (b) Crater density on coronae (squares). Corrected densities are shown by filled symbols. The overall distribution for the planet is also shown (triangles). Error bars are indicated for the corrected densities and the global distribution (27).

Figure 3.3. Fraction of impact craters on Venus embayed by exterior lava flows versus crater diameter (27). Data from (5, 8).

Figure 3.4. Magellan images of coronae and associated impact craters. (a) Nishtigri Corona, centered at 24.5°S, 72°E, has a maximum width of 275 km. The image is 500 km wide. The corona has been assigned to volcanic category 2 (10). A deformed impact crater (6 km in diameter) is visible on the tectonic annulus in the southeastern quadrant. (b) Corona Lilinau, approximately 200 km in width. The image is centered at 33.5°N, 22.5°E, and is 400 km wide. This is an example of a radial corona (10), which consists of predominantly radial tectonic structures and generally lacks an

annulus of concentrated deformation. The "interior" of such a feature is less clear-cut than for traditional coronae, but for our study is taken from the radial dimensions. Two unmodified impact craters (18 and 29 km in diameter) are visible on the image. The crater nearest the corona center is counted in our statistics.

Figure 3.5. Crater densities on coronae by corona class (10, 27). Crater density is corrected for effective area as described in the text.

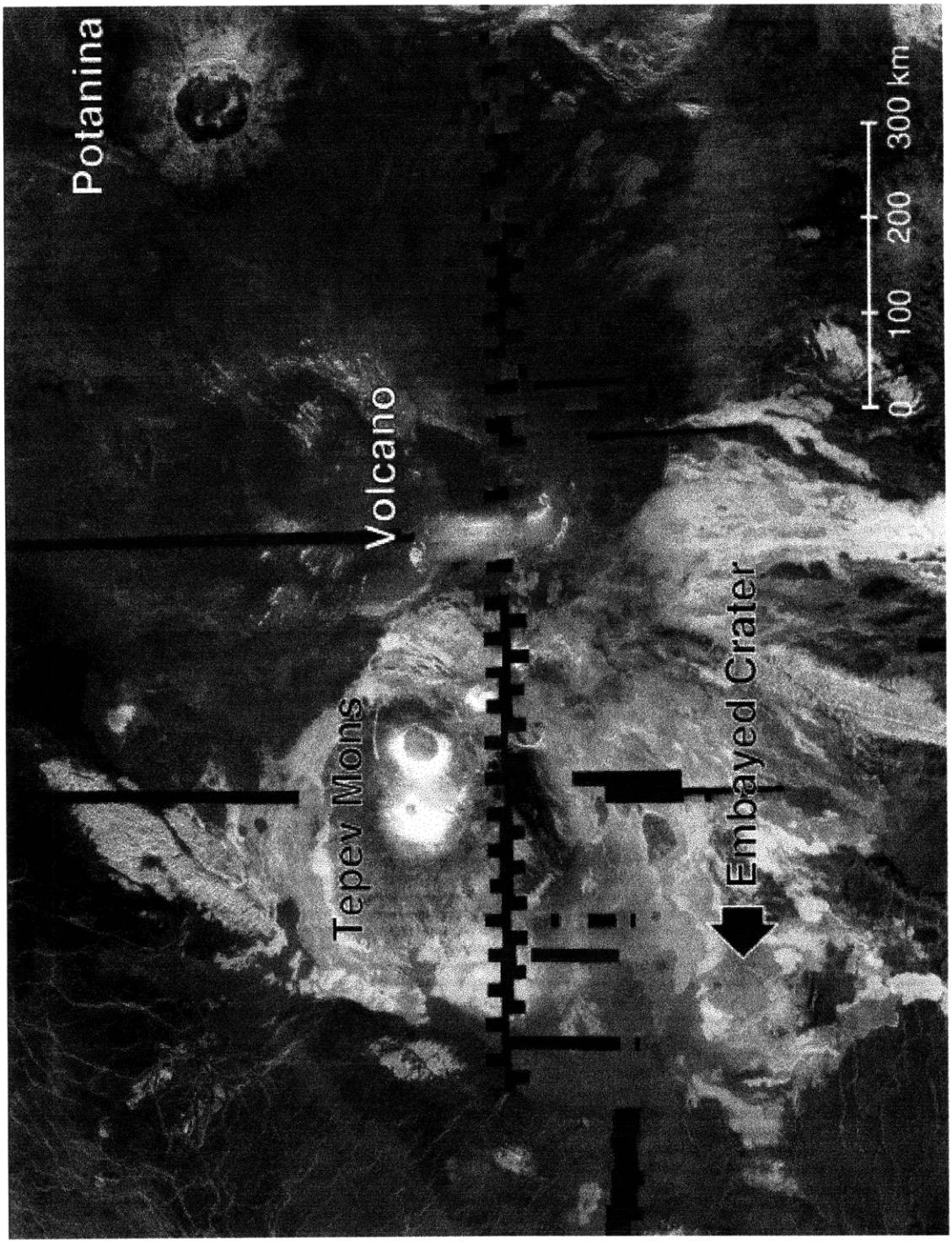

Figure 3.1

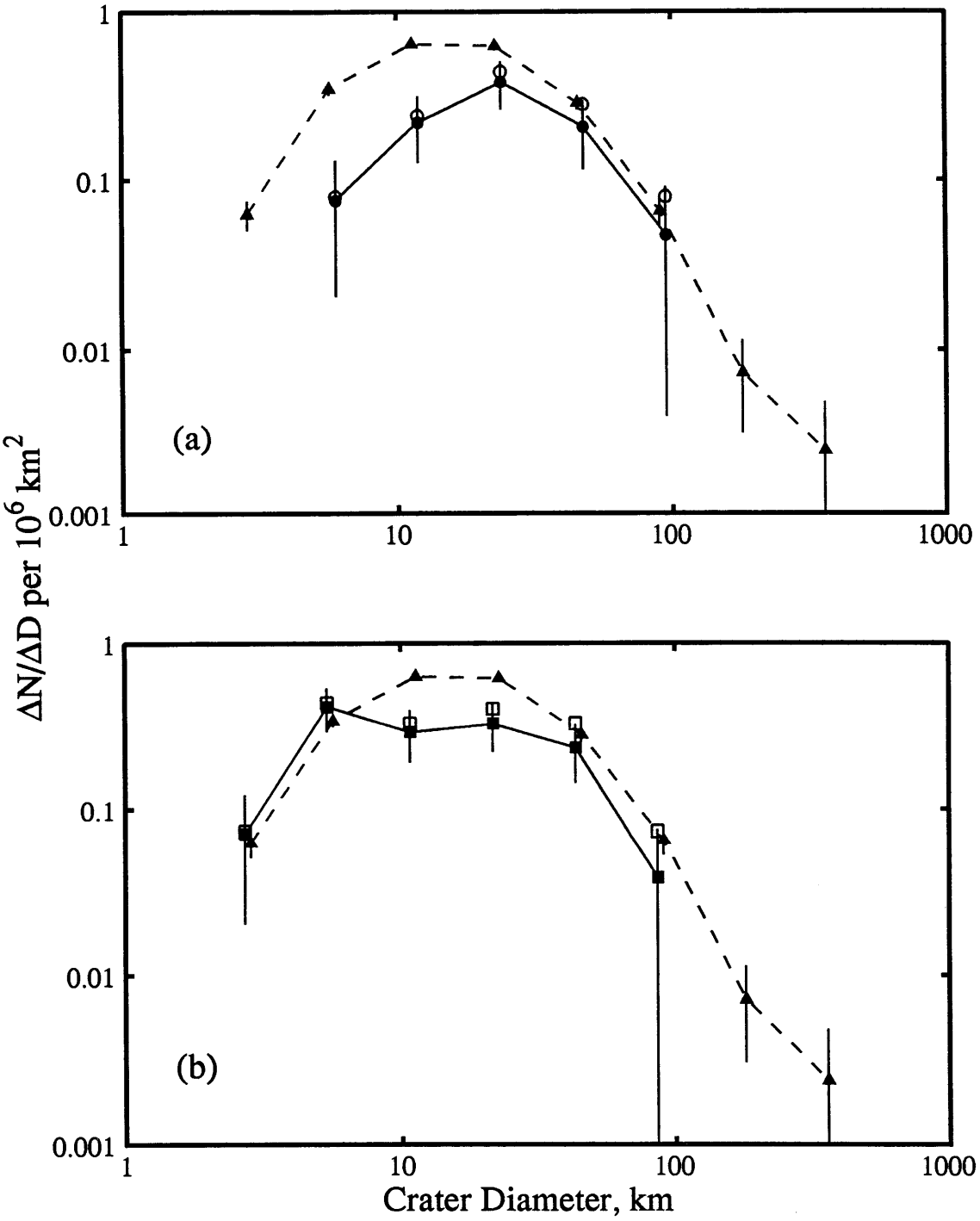
1
0.1
0.01
0.001
(a)
1
10
100
1000
ΔN/ΔD per 10^6 km^2
1
0.1
0.01
0.001
(b)
1
10
100
1000
Crater Diameter, km

Figure 3.2

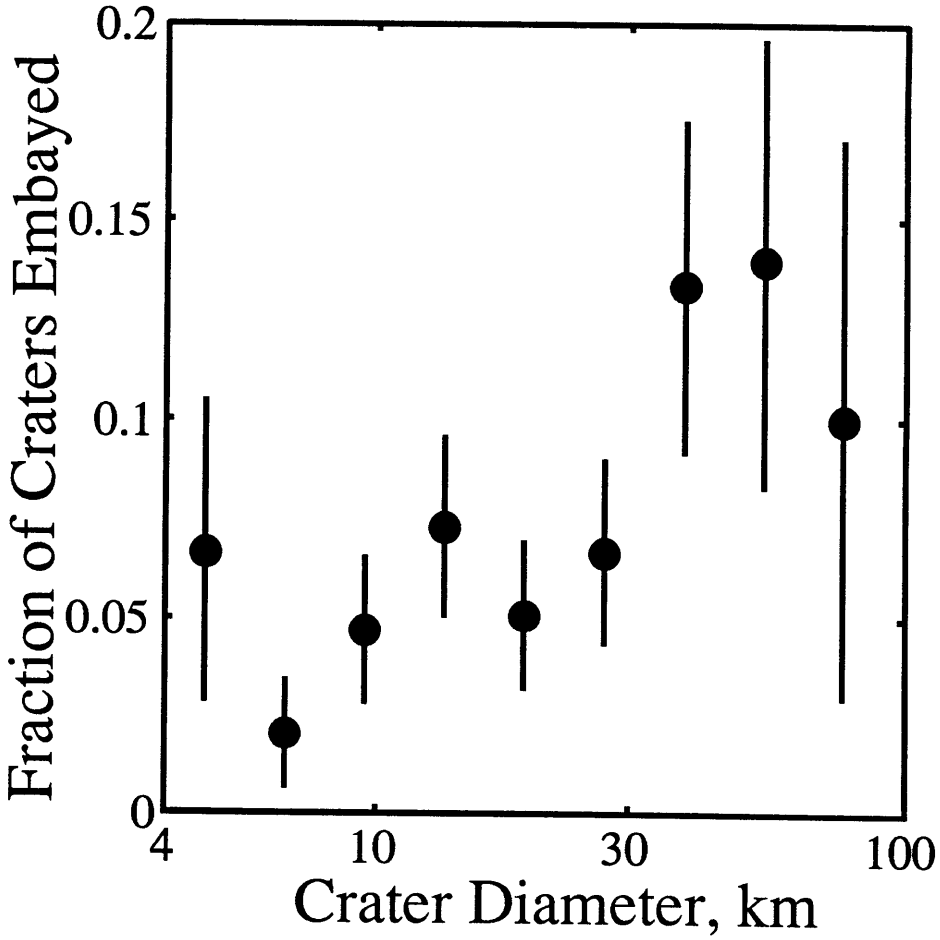
0.2
0.15
0.1
0.05
0
Fraction of Craters Embayed
4
10
30
100
Crater Diameter, km

Figure 3.3

Figure 3.4a

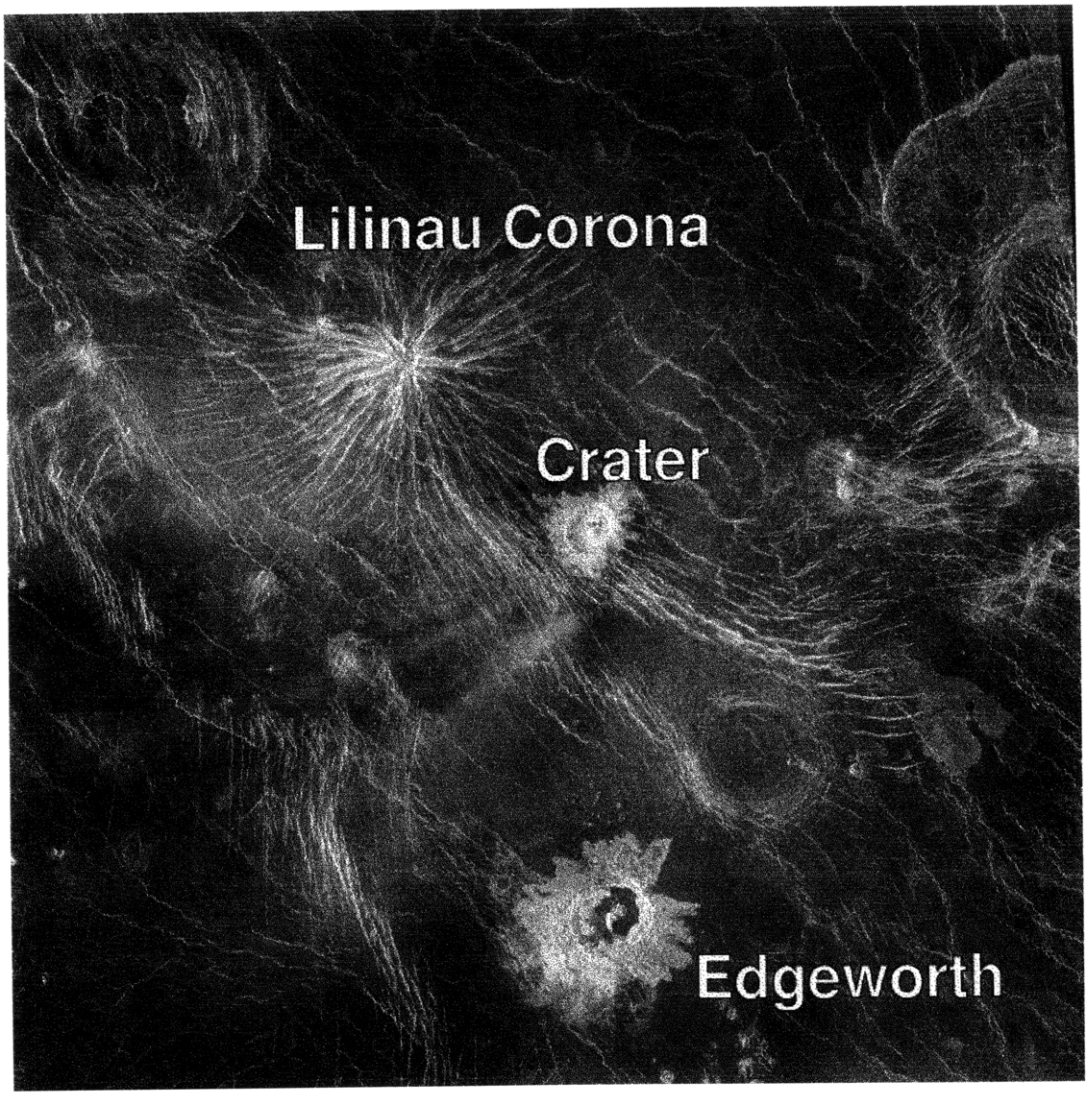

Figure 3.4b

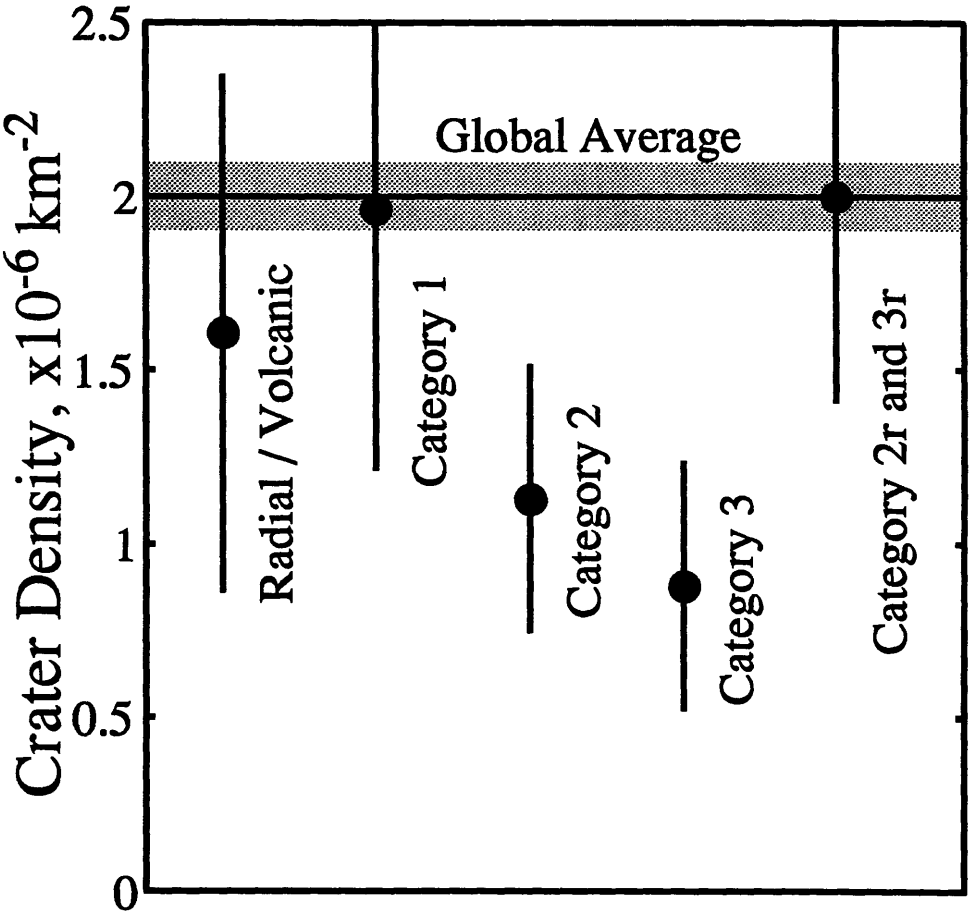
Crater Density, x10-6 km-2
2.5
2
1.5
1
0.5
0
Global Average
Radial / Volcanic
Category 1
Category 2
Category 3
Category 2r and 3r

Figure 3.5

Chapter 4:

Volcanic Degassing of Argon and Helium and the Nature of Crustal Production on Venus

INTRODUCTION

Radar images of the Venus surface obtained by the Magellan spacecraft revealed a surface approximately 500 million years old with widespread tectonic and volcanic features but no global plate tectonics [*Head et al.*, 1992; *Phillips et al.*, 1992; *Schaber et al.*, 1992; *Solomon et al.*, 1992]. The apparently random distribution of impact craters and the small fraction of modified craters [*Phillips et al.*, 1992; *Schaber et al.*, 1992; *Herrick and Phillips*, 1994; *Strom et al.*, 1994] led to two end-member hypotheses for the history of surface renewal: global resurfacing by a catastrophic event [*Schaber et al.*, 1992; *Strom et al.*, 1994] and approximately steady-state resurfacing [*Phillips et al.*, 1992]. More recent measurements of average crater densities on several types of volcanic and tectonic terrain, however, have revealed a spectrum of crater densities distinguishable from the global average, thus ruling out both end-member hypotheses [*Ivanov and Basilevsky*, 1993; *Namiki and Solomon*, 1994; *Price and Suppe*, 1994]. Analysis of the cratering records on volcanic terrains [*Namiki and Solomon*, 1994; *Price and Suppe*, 1994] as well as two- and three-dimensional Monte Carlo models of volcanic resurfacing [*Bullock et al.*, 1993; *Strom et al.*, 1994] have nonetheless shown that nearly global resurfacing 300 to 500 Myr ago [*Price*, 1995a] is strongly suggested as long as modest levels of volcanic resurfacing (affecting perhaps 20% of the surface) are postulated for subsequent times.

These geological observations thus suggest markedly different histories of heat loss and crustal production on Earth and Venus despite their similar mass, solar distance, and presumably bulk composition [*Basaltic Volcanism Study Project*, 1981; *Solomon and Head*, 1982, 1991; *Kaula*, 1990]. A variety of interior dynamical scenarios for Venus have been proposed to account for the postulated global resurfacing 300 to 500 Myr ago, either as a singular event or as the latest in a series of such events, and for modest levels of magmatic activity subsequent to 300-500 Myr ago, including (1) episodic development and subduction of a depleted mantle residuum layer [*Parmentier and Hess*, 1992], (2)

transition from layered- to whole-mantle convection driven by the sensitivity to the Rayleigh number of the tendency for layering in mantle convective flows [*Steinbach and Yuen*, 1992], (3) rapid cessation of mantle convection due to efficient cooling of the Venus mantle [*Arkani-Hamed et al.*, 1993], (4) episodic plate tectonics controlled by subduction of a conductively cooled and thickened lithosphere [*Turcotte*, 1993], (5) cessation of plate tectonics as a result of the lithospheric buoyancy driven to positive values by mantle cooling [*Herrick*, 1994], and (6) periodic overturn of a chemically denser upper mantle and a thermally buoyant lower mantle [*Herrick and Parmentier*, 1994]. These scenarios involve distinct histories of magmatism and chemical differentiation, yet no discriminating test has been proposed, partly because of an apparent lack of geological information significantly predating the most recent postulated global resurfacing event.

Magmatism transfers not only heat but also volatile species from the planetary interior. The present abundances of key atmospheric constituents can thus constrain the nature both of the postulated catastrophic resurfacing events and of magmatism during periods between such events [*Volkov and Frenkel*, 1993; *Matsui and Tajika*, 1995]. In this chapter, we focus on the species ^{40}Ar and ^{4}He. Noble gas abundances and their isotopic ratios in atmospheric, crustal, and mantle reservoirs have provided strong constraints on the degassing and thermal history of the Earth [*Hamano and Ozima*, 1978; *Sleep*, 1979; *Ozima and Podosek*, 1983; *Allègre et al.*, 1987; *Zhang and Zindler*, 1989; *Azbel and Tolstikhin*, 1990; *Tajika and Matsui*, 1993]. ^{40}Ar is generated in a planetary interior as a radioactive decay product of ^{40}K, which has a half life of 1.25 Gyr. In the absence of significant weathering and erosion on Venus, the principal mechanism for degassing ^{40}Ar is partial melting of mantle material and transport of magma to the surface or to near-surface reservoirs. Further, the inert nature of the noble gas prevents the return of Ar from the atmosphere to the mantle, the escape of Ar to space is negligible for planets the size of Venus and Earth, and ^{40}Ar has no significant non-radiogenic

component, so the ^{40}Ar abundance in the present atmosphere is directly related to the degassing and magmatic fluxes integrated over the planet's history [*Pollack and Black*, 1982; *Volkov and Frenkel*, 1993; *Matsui and Tajika*, 1995]. ^{4}He is a decay product of $^{235,238}U$ and ^{232}Th, which have half lives of 0.704, 4.47, and 14.0 Gyr, respectively. Unlike ^{40}Ar, however, ^{4}He escapes from the upper atmosphere at a significant rate over geological time scales because of its light atomic weight. An inferred residence time of ^{4}He in the atmosphere raging from 200 Myr to 2 Gyr [*Prather and McElroy*, 1983] enables us to estimate the rate of relatively recent magmatic activity on Venus.

Motivated by recent hypotheses for the history of resurfacing on Venus, we develop a new model for the degassing of ^{40}Ar and ^{4}He from Venus' interior and their escape from the atmosphere. In particular, we formulate the model in a manner that permits us to investigate the source volume for magma production for, and the characteristic time interval between, catastrophic resurfacing events [*Phillips et al.*, 1992; *Schaber et al.*, 1992; *Strom et al.*, 1994] as well as the rate of magmatism during intervals between catastrophic events [*Fegley and Prinn*, 1989; *Fegley and Treiman*, 1992; *Bullock et al.*, 1993; *Namiki and Solomon*, 1994; *Price and Suppe*, 1994; *Strom et al.*, 1994]. In contrast to previous work [*Ozima and Podosek*, 1983; *Volkov and Frenkel*, 1993; *Matsui and Tajika*, 1995], our model incorporates recent measurements of noble gas partition coefficients for several minerals [*Broadhurst et al.*, 1990, 1992] and of the extent of degassing during intrusive magmatism [*Westrich et al.*, 1988]. The model also addresses the diffusive transfer of noble gasses from the crust to the atmosphere [*Prather and McElroy*, 1983; *Turcotte and Schubert*, 1988]. All of these effects can significantly influence our estimates of crustal production on Venus. On the basis of this inquiry we attempt to develop new constraints on mechanistic models of catastrophic resurfacing [*Parmentier and Hess*, 1992; *Steinbach and Yuen*, 1992; *Arkani-Hamed et al.*, 1993; *Turcotte*, 1993; *Herrick and Parmentier*, 1994; *Herrick*, 1994].

MANTLE DEGASSING AND ATMOSPHERIC ESCAPE

An Overview of an Episodic Catastrophic Degassing Model

We model the history of crustal production on Venus as repeated cycles of two at least nominally distinct processes: episodic catastrophic resurfacing and steady magmatism between catastrophic resurfacing events. During a catastrophic resurfacing event, we presume that old crust is thoroughly recycled into the underlying mantle, and that this recycling transfers radioactive elements, K, U, and Th, and trapped noble gases, ^{40}Ar and ^{4}He. Accompanying the recycling of old crust is the formation of new crust generated by partial melting of the mantle. K, U, and Th in the crust and ^{40}Ar and ^{4}He in the atmosphere increase in proportion to the mass of this new crust and the corresponding species in the mantle decrease. Note that our use of the term "catastrophic resurfacing" follows the usage for Venus motivated by global analyses of the cratering record [*Phillips et al.*, 1992; *Schaber et al.*, 1992; *Strom et al.*, 1994] and denotes nearly global volcanic resurfacing ending 300 Myr [*Strom et al.*, 1994] to 500 Myr ago [*Phillips et al.*, 1992; *Schaber et al.*, 1992], over a time interval ranging from a few million [*Strom et al.*, 1994] to perhaps a hundred million years [*Price*, 1995a]. This terminology differs from that used in studies of Earth's degassing history, where "catastrophic degassing" generally refers to extensive outgassing postulated to have occurred within the first billion years of Earth's history on the basis of Ar isotopic ratios in the mantle and atmosphere [e.g., *Ozima and Podosek*, 1983].

After cessation of a catastrophic resurfacing event, steady magmatism is assumed to transfer radioactive elements and gases among the three reservoirs: mantle, crust, and atmosphere. Crater densities on several types of volcanic landforms have been interpreted as an indication of volcanic activity after the last global resurfacing event at the rate that is either indistinguishable from steady in time [*Namiki and Solomon*, 1994] or perhaps increasing with time [*Price and Suppe*, 1994]. For simplicity, we assume that

such magmatism takes place at a constant flux. Any crustal recycling during this interval is ignored because crustal ^{40}Ar and ^{4}He produced from the radioactive decay of crustal K, U, and Th are not important for the atmospheric reservoir, as discussed later. Noble gases produced and trapped in the crust are postulated to return to the mantle during episodic catastrophic resurfacing events, so our treatment amounts to an essentially two-reservoir model (mantle and atmosphere) for volatiles. We nonetheless include the crustal reservoir because its thickness [*Grimm*, 1994; *Konopliv and Sjogren*, 1994; *Simons et al.*, 1994] and observations of elemental abundances [*Surkov et al.*, 1987] can provide additional constraints on the numerical models.

Following a catastrophic resurfacing event, ^{4}He escapes from the atmosphere. We extrapolate the estimated escape flux of He at present [*Prather and McElroy*, 1983] to the past on the basis of previous work on escape mechanisms [*Hunten*, 1973; *Hunten and Donahue*, 1976; *McElroy et al.*, 1982; *Prather and McElroy*, 1983; *Hunten et al.*, 1989]. We assume that a rapid hydrodynamic outflow of hydrogen, or blow-off [*Kasting and Pollack*, 1983; *Pepin*, 1991; *Hunten*, 1993], ended at an arbitrarily chosen time between 0.5 and 1 Gyr after planetary formation [*Kasting and Pollack*, 1983; *Pepin*, 1991], and we calculate the subsequent evolution of atmospheric helium. Upward drag on He by hydrodynamic outflow is not considered as an important escape mechanism over the remainder of the planet's history because the total water abundance in the atmosphere has been small relative to major atmospheric components throughout this period (Chapter 5) [*Kumar et al.*, 1983; *Krasnopolsky*, 1985]. Escape of ^{40}Ar during the hydrodynamic outflow phase is ignored because ^{40}Ar is 10 times heavier than ^{4}He and is therefore more resistant to hydrodynamic escape. A model of hydrodynamic outflow on Venus, however, suggests that a considerable amount of ^{36}Ar in the primordial atmosphere was lost during the hydrodynamic out flow phase [*Pepin*, 1991]. If ^{40}Ar indeed escaped from the early atmosphere, the present atmospheric ^{40}Ar abundance provides only a lower bound on ^{40}Ar degassed over the planet's history. We discuss this point further below.

For the study of noble gas evolution on Earth, more detailed degassing models have been developed that include upper and lower mantle reservoirs, oceanic crust, a mixing zone, upper and lower continental crust, and an asthenosphere; such models have been motivated by a variety of measurements of isotopic ratios in materials thought to be representative of these reservoirs [*Hamano and Ozima*, 1978; *Ozima and Podosek*, 1983; *Allègre et al.*, 1987; *Zhang and Zindler*, 1989; *Azbel and Tolstikhin*, 1990; *Tajika and Matsui*, 1993]. We adopt only a simple three-reservoir model for Venus because of the lack of isotopic data on crustal and mantle reservoirs. The possible existence of an undegassed mantle on Venus' degassing history is considered further below by treating the mass of the degassed mantle as a free parameter. We do not include ^{36}Ar, ^{38}Ar, or ^{3}He in our degassing model, for several reasons. The observation that ^{36}Ar and ^{38}Ar in the Venus atmosphere are about 80 times more abundant than in the terrestrial atmosphere [e.g., *von Zahn et al.*, 1983] has been variously attributed to a greater level of solar wind implantation on the planetesimals that accreted to form Venus [*McElroy and Prather*, 1981; *Wetherill*, 1981], to a greater loss from Earth as a consequence of the giant impact responsible for the formation of Moon [*Cameron*, 1983], or to a greater contribution to the Venus atmosphere from a relatively late impact of a large comet [*Owen et al.*, 1992]. In contrast, it has been argued that terrestrial ^{3}He is primordial, i.e., retained in the interior since planetary formation [*Ozima and Podosek*, 1983; *Holland*, 1984; *Allègre et al.*, 1993]. For an assumed steady balance between atmospheric escape and mantle degassing, the current ^{3}He flux provides a constraint on the primordial He budget in the mantle. Unfortunately, a contamination of the Pioneer Venus gas spectrometer by terrestrial hydrogen [e.g., *von Zahn et al.*, 1983] prevents the use at present of ^{3}He as a tracer of mantle degassing on Venus.

K-Ar and U, Th-He Systematics

We solve for the transfer of K and Ar among mantle, crustal, and atmospheric reservoirs following *Hamano and Ozima* [1978]. The set of differential equations that govern mass transport by volcanism during intervals between resurfacing catastrophes are presented here. A corresponding set of finite difference equations govern mass transport during catastrophic resurfacing events. The transfer of K and Ar among mantle (subscript *M*), crustal (*C*), and atmospheric (*A*) reservoirs, and their radioactive decay and production in those reservoirs, are described by

$$\frac{d(^{40}K)_M}{dt} = -\lambda_{40}(^{40}K)_M - \pi^{K}_{M\rightarrow C}(^{40}K)_M \quad (1)$$

$$\frac{d(^{40}Ar)_M}{dt} = y_{40}\lambda_{40}(^{40}K)_M - \pi^{Ar}_{M\rightarrow C}(^{40}Ar)_M - \pi^{Ar}_{M\rightarrow A}(^{40}Ar)_M \quad (2)$$

$$\frac{d(^{40}K)_C}{dt} = -\lambda_{40}(^{40}K)_C + \pi^{K}_{M\rightarrow C}(^{40}K)_M \quad (3)$$

$$\frac{d(^{40}Ar)_C}{dt} = y_{40}\lambda_{40}(^{40}K)_C + \pi^{Ar}_{M\rightarrow C}(^{40}Ar)_M \quad (4)$$

$$\frac{d(^{40}Ar)_A}{dt} = \pi^{Ar}_{M\rightarrow A}(^{40}Ar)_M \quad (5)$$

where $(^{40}K)_M$, $(^{40}Ar)_M$, $(^{40}K)_C$, $(^{40}Ar)_C$, and $(^{40}Ar)_A$ are the mass of the designated isotope in each reservoir, t is the time since planet formation, λ_{40} and y_{40} are the decay constant (5.543×10^{-10} yr^{-1}) and yield of ^{40}Ar (0.1048 atom/atom) from the radioactive decay of ^{40}K [*McDougall and Harrison*, 1988], and $\pi^{K}_{M\rightarrow C}$, $\pi^{Ar}_{M\rightarrow C}$, and $\pi^{Ar}_{M\rightarrow A}$ are the degassing coefficients of K and Ar that describe mass transport from the mantle to crustal and atmospheric reservoirs. The physical mechanisms governing mantle degassing are partial melting of mantle material and the partitioning of volatiles between basaltic melt and residuum minerals. Degassing coefficients are derived in a later section. The estimated primordial ^{40}Ar/^{36}Ar ratio at $t = 0$ is so small that any primordial component to present atmospheric ^{40}Ar may be considered negligible [*Ozima and Podosek*, 1983]. We therefore assume zero primordial ^{40}Ar in both interior and atmospheric reservoirs, i.e., $(^{40}Ar)_M = (^{40}Ar)_C = (^{40}Ar)_A = 0$ at $t = 0$. Transfer of Ar from

crust to atmosphere is not included in equations (4) and (5) because Ar diffusion in the Venus crust is so slow that the contribution of crustal ^{40}Ar to the atmospheric reservoir is negligible. We discuss this point further below.

The isotope ^4He is a decay product of three radioactive elements, ^{235}U, ^{238}U, and ^{232}Th. Transfer of U, Th, and He among atmospheric, crustal, and mantle reservoirs, and their radioactive decay and production in those reservoirs, are described by

$$\frac{d(^{235}U)_M}{dt} = -\lambda_{235}(^{235}U)_M - \pi^U_{M\to C}(^{235}U)_M \tag{6a}$$

$$\frac{d(^{238}U)_M}{dt} = -\lambda_{238}(^{238}U)_M - \pi^U_{M\to C}(^{238}U)_M \tag{6b}$$

$$\frac{d(^{232}Th)_M}{dt} = -\lambda_{232}(^{232}Th)_M - \pi^{Th}_{M\to C}(^{232}Th)_M \tag{6c}$$

$$\begin{aligned}\frac{d(^4He)_M}{dt} = &\frac{4}{235}y_{235}\lambda_{235}(^{235}U)_M + \frac{4}{238}y_{238}\lambda_{238}(^{238}U)_M \\ &+\frac{4}{232}y_{232}\lambda_{232}(^{232}Th)_M - \pi^{He}_{M\to C}(^4He)_M - \pi^{He}_{M\to A}(^4He)_M\end{aligned} \tag{7}$$

$$\frac{d(^{235}U)_C}{dt} = -\lambda_{235}(^{235}U)_C + \pi^U_{M\to C}(^{235}U)_M \tag{8a}$$

$$\frac{d(^{238}U)_C}{dt} = -\lambda_{238}(^{238}U)_C + \pi^U_{M\to C}(^{238}U)_M \tag{8b}$$

$$\frac{d(^{232}Th)_C}{dt} = -\lambda_{232}(^{232}Th)_C + \pi^{Th}_{M\to C}(^{232}Th)_M \tag{8c}$$

$$\begin{aligned}\frac{d(^4He)_C}{dt} = &\frac{4}{235}y_{235}\lambda_{235}(^{235}U)_C + \frac{4}{238}y_{238}\lambda_{238}(^{238}U)_C \\ &+\frac{4}{232}y_{232}\lambda_{232}(^{232}Th)_C + \pi^{He}_{M\to C}(^4He)_M - F^{He}_{C\to A}\end{aligned} \tag{9}$$

$$\frac{d(^4He)_A}{dt} = \pi^{He}_{M\to A}(^4He)_M + F^{He}_{C\to A} - F^{He}_{A\to S} \tag{10}$$

where λ_{235}, λ_{238}, and λ_{232} are the decay constants of ^{235}U, ^{238}U, and ^{232}Th and are 9.849×10^{-10}, 1.551×10^{-10}, and 4.948×10^{-11} yr^{-1}, respectively [*Ozima and Podosek*, 1983], y_{235}, y_{238}, and y_{232} are the yields of ^4He from ^{235}U, ^{238}U, and ^{232}Th and are 7, 8, and 6, respectively [*Ozima and Podosek*, 1983], $F^{He}{}_{C\to A}$ is the mass flux of ^4He from crust to atmosphere, $F^{He}{}_{A\to S}$ is the He escape flux from the planetary atmosphere to

interplanetary space, and $\pi^{U}_{M\rightarrow C}$, $\pi^{Th}_{M\rightarrow C}$, and $\pi^{He}_{M\rightarrow A}$ are the degassing coefficients described in detail below.

Initial ^{4}He Abundances

Helium is the second most dominant gas species in the solar nebula [*Anders and Ebihara*, 1982; *Cameron*, 1982], so an initial atmosphere is likely to inherit a significant amount of ^{4}He from the primordial protoplanetary atmosphere remaining after the hydrodynamic outflow phase ceases several hundred million years after planetary formation [*Sasaki and Nakazawa*, 1988; *Pepin*, 1991]. The atmospheric ^{4}He abundance at the end of the hydrodynamic outflow phase ($t = t_{HO}$) can be calculated from the product of the atmospheric ^{4}He/^{20}Ne ratio and the atmospheric ^{20}Ne abundance estimated for that time. An upper bound on the atmospheric ^{20}Ne abundance at $t = t_{HO}$ is given by the present atmospheric ^{20}Ne abundance, i.e., by ignoring any contribution of mantle degassing to the present atmospheric budget. Because ^{20}Ne is too heavy to escape from the planetary atmosphere, loss of atmospheric ^{20}Ne after cessation of the hydrodynamic outflow phase can be neglected [*Ozima and Podosek*, 1983]. There is no well-posed lower bound, so we adopt zero atmospheric ^{20}Ne at $t = t_{HO}$ for simplicity. Regarding the ^{4}He/^{20}Ne ratio, *Ozima and Podosek* [1983] argue that the pattern of noble gas abundances in the Venus atmosphere is close to that measured in carbonaceous chondrites, or the "planetary" pattern, on the basis of a similarity of the ^{20}Ne/^{36}Ar ratio measured in the Venus atmosphere to that in chondrites. In contrast, *Pepin* [1991] suggests that noble gas abundances on Venus follow a "solar" pattern, i.e., the ratios calculated from solar abundances [*Anders and Ebihara*, 1982; *Cameron*, 1982], on the basis of the ^{36}Ar : ^{84}Kr : ^{132}Xe ratios. Because the atmospheric abundances of ^{20}Ne and ^{36}Ar on Venus are better determined than those of ^{84}Kr and ^{132}Xe [*von Zahn et al.*, 1983], we adopt a planetary ^{4}He/^{20}Ne ratio of between 220 and 350 [*Ozima and Podosek*, 1983] as appropriate to the Venus atmosphere at $t = t_{HO}$. For the present ^{20}Ne abundance

in the atmosphere, we adopt 7 ± 3 ppm [*von Zahn et al.*, 1983]. On the basis of these considerations, we assume that the value of $(^4He)_A$ at $t = t_{HO}$ is between 0 and 3500 ppm.

To constrain the ^{4}He abundance in the Venus mantle at $t = t_{HO}$, we adopt a value for the undegassed portion of the mantle on Earth. The existence of comparatively degassed and undegassed fractions of the mantle has been suggested on the basis of distinct isotopic compositions measured in various samples from the Earth's interior [e.g., *Allègre et al.*, 1987; *Azbel and Tolstikhin*, 1990]. Noble gas concentrations in the undegassed portion of the mantle are estimated by returning the present atmospheric constituents to the degassed portion of the mantle. Because the loss of noble gases during a hydrodynamic outflow phase has not been considered in the study of the Earth's degassing [*Ozima and Podosek*, 1983; *Allègre et al.*, 1987; *Azbel and Tolstikhin*, 1990], the noble gas abundances in the Earth's undegassed mantle are taken to correspond approximately to those in the Venus mantle at $t = t_{HO}$. *Azbel and Tolstikhin* [1990] calculate a ^{4}He concentration for the Earth of 4.5 ppb by weight by assuming that the primordial ^{4}He/^{20}Ne ratio (i.e., the ratio at $t = 0$) in the bulk silicate Earth is 500 and that all of the ^{20}Ne in the present atmosphere on Earth is attributable to degassing from 33% of the mantle. This figure may be an underestimate because the ^{20}Ne budget in the present mantle is not included. However, their analysis indicates that only 1% of primordial ^{3}He and 0.3% of primordial ^{36}Ar have been retained in the Earth's degassed portion of the mantle, so the effect of the ignored ^{20}Ne in the present mantle on their calculation of ^{4}He is likely to be minor. In contrast, the ignorance of the atmospheric ^{20}Ne abundance at $t = t_{HO}$ leads to an overestimate of the ^{4}He concentration in the bulk silicate Earth. Therefore we adopt this figure as an upper bound on $(^4He)_{M(t_{HO})}$ on Venus.

A different estimate of the Earth's primordial ^{4}He concentration has been derived from estimates of the ^{3}He abundance and the He isotopic ratios in the undegassed mantle. By assuming that all of the ^{36}Ar abundance in the present atmosphere is due to

outgassing from 46% of the mantle and that the $^{3}He/^{36}Ar$ ratio measured in basalt glasses from the Loihi seamount is representative of the undegassed mantle, *Allègre et al.* [1987] estimated the ^{3}He abundance in the undegassed mantle at 1.9×10^{-9} cm^3 STP g^{-1}. In this estimate, ^{36}Ar retained in the present degassed mantle is ignored because their analysis of $^{36}Ar/^{40}Ar$ ratios in MORB and Loihi glass samples shows that the degassed mantle has lost at least 99.6% of primordial ^{36}Ar until present. The ^{36}Ar abundance in the atmosphere after the cessation of the hydrodynamic outflow phase is also ignored in this estimate, but its contribution to the estimated ^{3}He concentration is minor because degassed ^{36}Ar is probably dominant in the present atmosphere on Earth [*Pepin*, 1991]. *Allègre et al.* [1987] have also estimated the primordial $^{4}He/^{3}He$ ratio in the undegassed mantle at 5200, but this figure is uncertain by more than factor of 4 due to variations in the $^{4}He/^{40}Ar$ ratio measured in Loihi samples [*Allègre et al.*, 1987]. Instead we adopt the solar $^{4}He/^{3}He$ ratio of 2500 obtained from isotopic measurements of He trapped in diamonds [*Ozima and Zashu*, 1983]. The terrestrial ^{4}He abundance in the undegassed mantle is then 0.84 ppb, and we use this figure as a lower bound.

Degassing Coefficients

Two-Stage Degassing Model. Mass transfer of radioactive elements and noble gases are governed by partial melting of mantle material and the partitioning of these elements between melt and residual solid. Therefore the degassing coefficients in equations (1) to (10) may be derived from equations for elemental partitioning during melting. We adopt a two-stage degassing model of radioactive elements and noble gases from mantle material following previous investigations of terrestrial degassing [*Hamano and Ozima*, 1978; *Ozima and Podosek*, 1983; *Allègre et al.*, 1987]. We assume that the first stage consists of pressure-release partial melting of mantle material, and that radioactive elements and noble gases are partitioned between liquid and solid phases according to

$$C_L = \frac{C_0}{K_{mode} + f_{melt}(1 - K_{stoi})} \tag{11}$$

where C_L is the mass concentration in the melt, C_0 is the mass concentration in mantle material prior to partial melting, f_{melt} is the fractional degree of melting, and K_{mode} and K_{stoi} are bulk partition coefficients between solid and melt [*Kinzler and Grove*, 1992a]. K_{mode} is an average of mineral partition coefficient weighted by the modal abundances of mantle material prior to partial melting, and K_{stoi} is an average of mineral partition coefficients weighted by the stoichiometric coefficients of the melting reaction [*Kinzler and Grove*, 1992a]. The stoichiometric coefficient is the weight fraction of a major mineral consumed to produce one unit mass of basaltic melt [*Kinzler and Grove*, 1992a]. The assumed modal abundances of mantle material, stoichiometric coefficients, and mineral partition coefficients are discussed further below. It is assumed in equation (11) that melt remains with the residual solid as mantle material rises through the melting regime and that the partitioning between melt and residual solid is in equilibrium until the final removal of melt to a shallow crustal magma chamber (equilibrium batch melting) [*Kinzler and Grove*, 1992b]. If melts segregate from the rising residual solid (fractional melting), equation (11) can be applied only to the equilibrium mass balance between melt and residual solid when melts are produced. We discuss further below the influence of this assumption of equilibrium batch melting on the estimate of f_{melt}.

The value of f_{melt} is assumed to be constant in time, and in particular to be the same during catastrophic resurfacing events and during the time intervals between such events. While this assumption is an oversimplification, we incorporate a wide range of values for f_{melt} to assess at least partially the possible effects of temporal variation and to constrain conservatively upper and lower bounds on the average crustal production rate over the planet's history. We discuss this point further below.

The second stage of our degassing model is taken to be the transfer of radioactive elements and noble gases from shallow magma chambers to the crust and atmosphere. Radioactive elements and noble gases are thus assumed in the model to ascend without modification during melt transport from the mantle to magma chambers beneath volcanic

centers. We assume that the crust on Venus formed by this magmatism and that the rate of magma production equals the rate of crustal production, Q_C. Then the mass flux of radioactive elements and noble gases from mantle to magma chamber is

$$Q_{gas} = C_L Q_C = \frac{Q_C}{K_{mode} + f_{melt}(1 - K_{stoi})} C_0 \tag{12}$$

Since all K in the magma chamber is retained in igneous rocks as the magma solidifies, transfer of K from mantle to crust is simply described by

$$\frac{\Delta(^{40}K)_C}{\Delta t} = \frac{Q_C}{K^K_{mode} + f_{melt}(1 - K^K_{stoi})} \frac{(^{40}K)_M}{M_M} \tag{13}$$

where M_M is the mass of the mantle. The degassing coefficient of K from mantle to crust is thus given by

$$\pi^K_{M \to C} = \frac{1}{K^K_{mode} + f_{melt}(1 - K^K_{stoi})} \frac{Q_C}{M_M} \tag{14}$$

[*Ozima and Podosek*, 1983]. Similarly, the degassing coefficients of U and Th are given by

$$\pi^U_{M \to C} = \frac{1}{K^U_{mode} + f_{melt}(1 - K^U_{stoi})} \frac{Q_C}{M_M} \tag{15}$$

and

$$\pi^{Th}_{M \to C} = \frac{1}{K^{Th}_{mode} + f_{melt}(1 - K^{Th}_{stoi})} \frac{Q_C}{M_M} \tag{16}$$

For Ar and He degassing, we assume that magma chambers release all noble gases to atmosphere during the eruption or subsurface solidification of magma. Therefore

$$\pi^{Ar}_{M \to A} = \frac{1}{K^{Ar}_{mode} + f_{melt}(1 - K^{Ar}_{stoi})} \frac{Q_C}{M_M} \tag{17}$$

$$\pi^{He}_{M \to A} = \frac{1}{K^{He}_{mode} + f_{melt}(1 - K^{He}_{stoi})} \frac{Q_C}{M_M} \tag{18}$$

$$\pi^{Ar}_{M \to C} = \pi^{He}_{M \to C} = 0 \tag{19}$$

Strictly stated, Q_C represents only the supply of magma that releases noble gases to the atmosphere. While it is generally accepted that extrusive eruption releases almost all volcanic gasses, the fraction of volatiles degassed from intrusions is not well understood, and more intrusive than extrusive magmatism occurs on Earth [*Crisp*, 1984; *Coffin and*

Eldholm, 1994]. Therefore in order to convert Q_C to a full crustal production rate, we must examine the degassing efficiency from intrusions.

Degassing from Intrusions. Measurement of volatile content in drill core samples from a terrestrial rhyolitic dome has revealed two primary processes of volatile loss from magma: isothermal decompression and isobaric crystallization, or second boiling [*Westrich et al.*, 1988]. Isothermal decompression is a degassing mechanism driven by the decreasing solubility in magma with decreasing confining pressure during ascent. A comparison of water contents in glass samples from different depths indicates that the magma had lost 97% of its original water by decompression even before the extrusion of the dome had begun [*Westrich et al.*, 1988]. As magma subsequently solidifies at the surface or subsurface, volatiles are forced out of the system by the phase change of the volatile-bearing magma to a nonvolatile-bearing crystalline assemblage (isobaric crystallization). The interior of the intrusion loses nearly 100% of the water remaining after decompression by crystallization [*Westrich et al.*, 1988].

For Ar degassing, a similar extent of volatile loss from mid-ocean ridge basalt (MORB) magma prior to eruption has been suggested on the basis of variable ^{40}Ar concentrations in MORB glasses from a common magma source [*Fisher and Perfit*, 1990; *Hilton et al.*, 1993]. *Allègre et al.* [1987] estimated the efficiency of Ar degassing of MORB glass as 98.3% under the assumptions that both K_{mode} and K_{stoi} for K and Ar are negligible relative to f_{melt} and that the isotopic ratios measured in Loihi sample are representative of those in the undegassed portion of the mantle. The isobaric crystallization of MORB leads to further degassing from MORB lava, so an efficiency close to 100% is implied.

An independent constraint on Ar retention in intrusive rocks can be obtained from measurements of excess Ar. Excess argon is the component of ^{40}Ar incorporated into samples by processes other than *in situ* radioactive decay of ^{40}K [*McDougall and*

Harrison, 1988]. While the source of excess Ar is usually difficult to identify, measurements of its abundance in intrusive igneous rocks allow us to estimate an upper bound on the noble gas abundances retained in intrusive rocks. For example, typical MORB glass contains less than 2.5×10^{-6} cm^3 STP g^{-1}, or 4.5 ppb by weight, of ^{40}Ar [*Fisher*, 1986; *Sano et al.*, 1986; *Allègre et al.*, 1987; *Fisher and Perfit*, 1990]. For continental and island arc intrusive rocks, analyses of ^{40}Ar/^{39}Ar ratios show excess Ar in amphibole minerals of less than 3.2 ppb [*Gilbert and Foland*, 1985; *Landoll et al.*, 1989; *Onstott et al.*, 1989]. These values can be regarded as upper bounds because the crystalline MORB rocks contain less Ar than glasses [*Fisher*, 1986; *Azbel and Tolstikhin*, 1990], and because the concentration of excess Ar is generally highest in amphibole and pyroxene among the major minerals [*Gilbert and Foland*, 1985].

These upper bounds on ^{40}Ar retention can be used to calculate a lower bound on the degassing efficiency by comparison with estimates of ^{40}Ar abundances in mantle-derived melts. We note that noble gas concentrations measured in MORB glasses should not be applied to concentrations in mantle-derived melts because MORB magma is likely to have degassed prior to eruption [*Allègre et al.*, 1987; *Fisher and Perfit*, 1990; *Hilton et al.*, 1993]. *Azbel and Tolstikhin* [1990] have obtained $C_0(^{40}\mathrm{Ar}) = 11$ ppb for their terrestrial degassing model under the assumptions $f_{melt} = 0.1$ and $K^{Ar}_{mode} = K^{Ar}_{stoi} = 0.1$. By substituting these parameters into equation (11), $C_L(^{40}\mathrm{Ar})$ in mantle-derived melts is calculated as 57 ppb. Separately *Tajika* [1992] has estimated that the current Ar degassing rate from the terrestrial mantle is 2.5×10^8 mol yr^{-1}. For a present crustal production rate of 26 to 34 km^3 yr^{-1} [*Crisp*, 1984], or 0.86 to 1.1×10^{14} kg yr^{-1}, *Tajika*'s estimate corresponds to an average ^{40}Ar concentration in mantle-derived melts of 91 to 120 ppb. Thus the measurements of excess Ar and theoretical estimates of ^{40}Ar abundance in mantle-derived melts suggest that at most 3 to 8% of mantle-derived noble gases can remain in intrusive rocks, or that the efficiency of ^{40}Ar degassing during the solidification of intrusions is at least 92%.

Obtaining an estimate of the degassing efficiency of ^{4}He from intrusions is not as straightforward as for ^{40}Ar. Excess ^{4}He has been measured in MORB glasses and rocks [*Fisher*, 1986; *Sano et al.*, 1986; *Allègre et al.*, 1987; *Fisher and Perfit*, 1990], but the ^{4}He concentration in mantle-derived melts has not been estimated. We therefore employ ^{3}He as a tracer of He degassing efficiency from both extrusive and intrusive rocks. Abundances of excess ^{4}He and ^{3}He/^{4}He ratios in continental plutonic rocks have been measured to be 7.5×10^{-5} cm^3 STP g^{-1} and 2.6×10^{-7} [*Tolstikhin et al.*, 1992], respectively, and yield a ^{3}He concentration of 2.6×10^{-15} by weight. While such excess ^{3}He is not necessarily a residue of noble gases partitioned into melt in the mantle [*Tolstikhin et al.*, 1992; *Hilton et al.*, 1993], the measurement provides an estimate of the amount of ^{3}He trapped in intrusive rocks. The ^{3}He concentration in mantle-derived melts, on the other hand, is estimated to be 1.3×10^{-13} by weight for $f_{melt} = 0.1$ [*Tolstikhin et al.*, 1992]. An estimate of the present ^{3}He degassing rate from the terrestrial mantle of 1.067×10^3 mol yr^{-1} [*Tajika*, 1992] yields an average ^{3}He concentration in mantle-derived melts of 2.8×10^{-14} by weight, for a current crustal production rate of 1.1×10^{14} kg yr^{-1}. Thus the degassing efficiency of ^{3}He is 91 - 98%. Such lower bounds on the degassing efficiency of Ar and He as well as the above argument on the efficient loss of H_2O from magma supports our assumption of complete degassing from both extrusive and intrusive magmas, and indicates that Q_C is likely to be close to the full crustal production rate for the planet.

Other Degassing Models. Other than the two-stage, steady-degassing-coefficient model adopted here, a variety of alternative models have been developed for the study of atmospheric and mantle evolution on Earth. For example, recent numerical models include time-variable degassing coefficients that are governed by the vigor of parameterized convection [*McGovern and Schubert*, 1989; *Williams and Pan*, 1992; *Tajika and Matsui*, 1993]. We have adopted time-independent degassing coefficients in

this study, partly out of a desire for simplicity and partly because parameterized convection models are not likely to be good representations of internal evolution and crustal formation on Venus, whose evolution appears to have been much more strongly variable in time than in parameterized convection models. It is also worth noting that additional degassing mechanisms have been proposed for the Earth's mantle, particularly those involving gas-liquid equilibrium in degassing from near-surface magma reservoirs. *Zhang and Zindler* [1989, 1993] have pointed out that the $^{4}He/^{3}He$ and $^{40}Ar/^{36}Ar$ isotopic ratios in Earth's degassed and undegassed mantle are not consistent with an assumption that both ^{3}He and ^{36}Ar degassed under the control of solid-liquid partitioning, and they instead proposed a degassing model controlled by the solubility between liquid and gas phases. *Azbel and Tolstikhin* [1990] advocated a model in which equilibrium partitioning between solid and liquid phases is assumed at the first stage and equilibrium between liquid and gas phases is assumed at the second stage. *Tajika and Matsui* [1992] have developed a degassing model for equilibrium partitioning of volatiles among coexisting solid, liquid and gas phases. Solubility-controlled degassing [*Zhang and Zindler*, 1989, 1993] of primordial noble gases such as ^{36}Ar and ^{3}He is consistent with the hypothesis of extensive degassing early in Earth's history [*Hamano and Ozima*, 1978], if a magma ocean existed on Earth as indicated by some scenarios for planetary accretion [*Safronov*, 1978; *Kaula*, 1979, 1980], and if the atmosphere at the time of planetary formation is in solubility equilibrium with the magma ocean as suggested for the origin of the terrestrial atmosphere and ocean [*Holland*, 1984; *Abe and Matsui*, 1986; *Matsui and Abe*, 1986]. However, the noble gas isotopic ratios in terrestrial degassed and undegassed mantle portions do not require that subsequent degassing of radiogenic noble gases is also governed by solubility equilibrium. On the contrary, because geologic studies of terrestrial magma degassing imply that volatiles dissolved in the melt are eventually released by isobaric crystallization as magma solidifies, solubility equilibrium is not a governing mechanism for modern volatile degassing [*Westrich et al.*, 1988]. On

these grounds we argue that the two-stage model for mantle degassing, under the assumption that melt-solid partitioning governs the degassing mechanism [*Hamano and Ozima*, 1978; *Ozima and Podosek*, 1983; *Allègre et al.*, 1987], is adequate for Venus.

Bulk Partition Coefficients of K, Ar, U, Th and He

For calculations of K_{mode} and K_{stoi} in equations (11) to (18), we assume that Venus' mantle consists of peridotite, on the basis of the similar bulk densities of Venus and Earth [*Basaltic Volcanism Study Project*, 1981; *Solomon and Head*, 1982, 1991; *Kaula*, 1990] and the similarity of several Venus surface samples to tholeiitic basalt [*Surkov et al.*, 1984; *Surkov et al.*, 1987; *McKenzie et al.*, 1992; *Kargel et al.*, 1993]. We adopt four sets of mineral compositions for modal abundances of mantle material prior to melting on Venus; primitive spinel lherzolite, depleted spinel lherzolite, primitive plagioclase lherzolite, and depleted plagioclase lherzolite [*Kinzler and Grove*, 1993] (Table 4.1). Spinel lherzolite represents the stable peridotite assemblage at pressures between 0.9 and 2.5 GPa, while plagioclase lherzolite represents the stable assemblage at pressures $\leq$ 0.9 GPa [*Kinzler and Grove*, 1992a]. We adopt the coefficients for partial melting of spinel and plagioclase lherzolites from *Kinzler and Grove* [1992a] (Table 4.1). Negative values of the stoichiometric coefficient for olivine imply that the mineral crystallizes from the melt at the expense of other minerals [*Kinzler and Grove*, 1992a]. At pressures $\geq$ 2.5 GPa, garnet lherzolite represents the stable assemblage of peridotite [e.g., *Takahashi*, 1986]. However, because partition coefficients of noble gases between garnet and basaltic melt have not yet been measured, we do not consider garnet lherzolite for the calculations of bulk partition coefficients for K, Ar, and He.

Partition coefficients of K between major minerals and silicate melts are compiled from the literature [*Yurimoto and Sueno*, 1984; *Yurimoto and Sueno*, 1987; *Kinzler and Grove*, 1992a; *Hart and Dunn*, 1993] (Table 4.2). Because of the uncertainties in the mantle composition (Table 4.1) and of the individual mineral partition coefficients (Table

4.2), ranges of K^K_{mode} and K^K_{stoi} are allowed. In order to constrain upper and lower bounds on the differentiation efficiency of K from mantle to crust, we determine the pairs of K^K_{mode} and K^K_{stoi} that maximize and minimize $\pi^K_{M\rightarrow C}$ as a function of f_{melt} (Appendix A, Table 4.3). For $\pi^{Ar}_{M\rightarrow A}$ in equation (17), pairs of K^{Ar}_{mode} and K^{Ar}_{stoi} are calculated in the same manner as for $\pi^K_{M\rightarrow C}$ to constrain upper and lower bounds on Ar degassing from the mantle to the atmosphere (Appendix A). Partition coefficients of Ar between clinopyroxene, olivine, spinel, and plagioclase and silicate melt are taken from *Hiyagon and Ozima* [1986] and *Broadhurst et al.* [1990, 1992] (Table 4.4). While the partition coefficient between orthopyroxene and silicate melt has not yet been measured, we assume that $K^{Ar}_{Opx} \leq K^{Ar}_{Cpx}$ because partition coefficients of trace elements are usually smaller for orthopyroxene than for clinopyroxene [*Ayers*, 1993]. Calculated values of K^{Ar}_{mode} and K^{Ar}_{stoi} for maximum and minimum $\pi^{Ar}_{M\rightarrow A}$ are listed in Table 4.3.

It should be stressed that mineral partition coefficients, in particular those for olivine, are not well constrained in spite of their importance for the study of planetary degassing. There is a discrepancy of nearly two orders of magnitude between two different sets of measurements of the Ar partition coefficient for olivine [*Hiyagon and Ozima*, 1986; *Broadhurst et al.*, 1992]. We adopt the coefficient measured by *Hiyagon and Ozima* [1986] because their results generally agree with other partition coefficients for clinopyroxene, spinel, and plagioclase and also because the results given by *Broadhurst et al.* [1992] include uncertain corrections for the solubility of Ar measured in forsterite. We note, however, that a much higher partition coefficient for Ar between olivine and silicate melt reported by *Broadhurst et al.* [1992] decreases the efficiency of Ar degassing from the mantle to the atmosphere and hence increases significantly the estimated rate of crustal production. Another controversy over the partition coefficient of Ar for olivine has arisen because the coefficient between a natural olivine-glass pair is considerably smaller than those measured in synthetic rock [*Marty and Lussiez*, 1993, 1994; *Hiyagon*,

1994]. Because the lower limit on the coefficient measured by *Hiyagon and Ozima* [1986] is small relative to f_{melt} (Table 4.4), a decrease in the Ar partition coefficient for olivine from the values assumed here is not important for the estimate of C_L (equation (11)) for Ar and thus for our numerical models.

We do not consider the bulk partition coefficients of U and Th for plagioclase lherzolite because the mineral partition coefficients for plagioclase have not been well determined [*Dostal and Capedri*, 1975; *Wörner et al.*, 1983]. The bulk partition coefficients of U and Th for spinel lherzolite and garnet lherzolite, in contrast, have been estimated on the basis of measurements of mineral partition coefficients [*LaTourrette and Burnett*, 1992; *Beattie*, 1993a, b; *LaTourrette et al.*, 1993]. We adopt values for K^U_{mode} and K^{Th}_{mode} of 1.2×10^{-3} and 2.9×10^{-4}, respectively [*Beattie*, 1993b], and we assume $K^U_{stoi} = K^U_{mode}$ and $K^{Th}_{stoi} = K^{Th}_{mode}$ (Table 4.3). Because both U and Th are highly incompatible, numerical results are little dependent on the assumed bulk partition coefficients.

Partition coefficients for He have been measured only between olivine and basaltic melt [*Hiyagon and Ozima*, 1986; *Marty and Lussiez*, 1993]. In order to constrain the partition coefficients of He for clinopyroxene and spinel, we adopt the partition coefficients of Ne as upper bounds [*Broadhurst et al.*, 1992] because the partition coefficient increases with increasing atomic number [*Hiyagon and Ozima*, 1986; *Broadhurst et al.*, 1992]. Also we assume $D^{He}_{Opx} \leq D^{He}_{Cpx}$, as discussed above for D^{Ar}_{Opx}. For lower bounds on He partition coefficients, we assume zero values in the limit of highly incompatible elements (Table 5). Bulk partition coefficients for maximum and minimum degassing cases for He are listed in Table 4.3 (Appendix A).

Helium Escape Flux

For the purpose of describing atmospheric escape processes, it is convenient to divide an atmosphere into three regions with increasing altitude: the homosphere, heterosphere,

and exosphere [*Hunten and Donahue*, 1976; *Houghton*, 1986]. The homosphere is the lowermost region of the atmosphere where atmospheric constituents are uniformly mixed and most of the atmospheric mass is concentrated. Above the homosphere is the heterosphere, where both molecular and heat transfer are dominated by diffusive equilibrium. The exosphere is the uppermost region of the atmosphere where the density is so low that molecular collisions can be ignored and atmospheric escape of fast moving particles occurs. The boundaries between the homosphere and the heterosphere and between the heterosphere and the exosphere are called the homopause and the exobase, respectively [*Hunten and Donahue*, 1976; *Houghton*, 1986].

Atmospheric escape of He occurs by diffusive transfer of helium in the heterosphere and loss of helium from the exosphere. In brief, the He escape flux is proportional to the He number density and ionization rate in the exosphere [*McElroy et al.*, 1982; *Prather and McElroy*, 1983]. The helium number density in the exosphere is, in turn, proportional to the He mixing ratio in the homosphere because of the linearity of the diffusion equation for He transfer in the heterosphere [*Hunten*, 1973; *Hunten and Donahue*, 1976; *Hunten et al.*, 1989]. Therefore $F^{He}_{A\rightarrow S}$ is taken to be proportional to the He mixing ratio at the homopause, X^{He}_{homo}. We also must consider the effect of the solar extreme ultraviolet (EUV) flux on the ionization rate. On the basis of the observed UV fluxes from sun-like stars, *Zahnle and Walker* [1982] have postulated that the solar EUV flux has been steadily decreasing with time. Because an enhanced EUV flux increases the He ionization rate [*Banks and Kockarts*, 1973], $F^{He}_{A\rightarrow S}$ must also have been greater in the past than at present. We assume that the temporal variation of EUV intensity is given by *Hunten et al.* [1989],

$$F^{He}_{A\rightarrow S} \propto t^{-5/6} X^{He}_{homo} \tag{20}$$

The proportional constant in equation (20) can be determined by taking the present values of X^{He}_{homo} and $F^{He}_{A\rightarrow S}$.

The He abundance in the present atmosphere has been measured only at altitudes above 130 km [*Niemann et al.*, 1980; *von Zahn et al.*, 1980]; therefore a best fit curve of helium measurements between 130 and 200 km altitude has been extrapolated downward into the well-mixed homosphere, and a constant He mixing ratio of 12 ppm below 100 km altitude has been obtained with an uncertainty of a factor of 3 [*Massie et al.*, 1983; *von Zahn et al.*, 1983]. The present ^{4}He escape rate has been estimated to be $(9.6 \pm 2.9) \times 10^5$ kg yr^{-1} on the basis of the current ionization rate and the measured concentration of ^{4}He in the exosphere [*Prather and McElroy*, 1983]. We assume a present escape flux of 9.6×10^5 kg yr^{-1} in the following discussion for simplicity. Thus the helium escape flux is described by

$$F^{He}_{A\rightarrow S} = 9.6\times10^5\left(\frac{t}{t_P}\right)^{-5/6}\frac{X^{He}_{homo}(t)}{X^{He}_{homo}(t_P)}, \text{ kg yr}^{-1} \qquad (21)$$

where t_P is the age of the planet (4.55 Gyr) and $X^{He}{}_{homo}(t_P)$ is the present helium mixing ratio in the homosphere and is assumed to be between 4 and 36 ppm. $X^{He}(t_P)$ is equivalent to $(^4He)_A(t_P)$ because atmospheric mass is concentrated in the lower atmosphere.

Strictly, equation (20) allows an infinitely high escape rate at the beginning of planetary history. There is a limit on He escape flux, however, as a result of the slow rate of diffusion of He through the heterosphere at times after the end of any hydrodynamic outflow phase [*Hunten*, 1973; *Hunten et al.*, 1989]. This limit on the He escape flux is termed the diffusion limit and can be estimated by using the experimentally-determined bimolecular diffusion coefficient. Under the assumption of a background CO_2 atmosphere at an exospheric temperature of 275 K [*Kasting and Pollack*, 1983], a binary collision parameter for the He-CO_2 system [*Masson and Marrero*, 1970] and a scale height of 5.9 km constrain an upper bound on the helium escape flux to be $1.7 \times 10^{13}\, X^{He}{}_{homo}$ atoms cm^{-2} s^{-1}, or

$$F^{He}_{A\rightarrow S} \le 1.6\times10^{13} X^{He}_{homo} \text{ kg yr}^{-1} \qquad (22)$$

By comparing equations (21) and (22), the time when diffusion through the heterosphere limits He loss can be calculated to be before the first 40 Myr of planetary history. Inasmuch as we have assumed that the hydrodynamic outflow phase has a duration greater than 40 Myr [*Kasting and Pollack*, 1983; *Kasting*, 1988; *Pepin*, 1991; *Hunten*, 1993], the diffusion limit on the He escape flux can be neglected for our problem.

Diffusive Transfer of Ar and He from Crust to Atmosphere

Transfer of Ar from the crust to the atmosphere is not included in equations (4) and (5). This omission is despite the inference that the degassing coefficient of Ar from the Earth's continental crust to the atmosphere is estimated to be 3.71×10^{-10} yr^{-1} on the basis of differences between K-Ar mineral ages and Rb-Sr rock ages [*Hamano and Ozima*, 1978]. The mechanism of transfer of Ar within the crust on Venus is likely to be different from that on Earth because of the high surface temperature and the absence of water and hydrous phases [*Fegley and Treiman*, 1992]. For example, *Turcotte and Schubert* [1988] argue that Ar diffusion in the crust is faster on Venus than on Earth because of higher surface temperature, and therefore that more ^{40}Ar is transferred from the crust to the atmosphere on Venus than Earth. Also *Head and Swindle* [1995] discuss a contribution of crustal ^{40}Ar to the atmospheric reservoir under the assumption of instant transport of Ar along grain boundaries. Degassing of excess ^{40}Ar under anhydrous conditions is significantly slower than under hydrous conditions, however, even at high temperature [*Zeitler*, 1987]. We examine the influence of both volume and grain-boundary diffusion and crustal deformation on the transfer of *in situ* ^{40}Ar from the crust to the atmosphere.

Diffusion is a strongly temperature-dependent process. We adopt the surface temperature of 750 K as a diffusion temperature in the crust because the thermally controlled diffusive flux will be slowest near the surface where the temperature is minimum. An experimentally determined rate of volume diffusion for Ar in K-feldspars is 1.8×10^{-19} m^2 s^{-1} at 750 K [*Smith and Brown*, 1988]. Assuming a typical grain

diameter of 20 mm, an upper bound on grain size observed from panorama pictures taken by Venera 13 and 14 [*Surkov et al.*, 1984], this volume diffusion coefficient yields 18 Myr as an upper bound on the characteristic time for Ar transfer within a mineral grain. Thus ^{40}Ar produced in minerals from the radioactive decay of ^{40}K should be transported to grain boundaries within a geologically short period, and bulk Ar transfer in the crust is governed by grain-boundary diffusion.

Grain-boundary diffusion has been proposed as an Ar loss mechanism for submarine volcanic rocks on the basis of a low measured activation energy of 50 to 84 kJ mol^{-1} [*Ozima and Takigami*, 1979]. Unfortunately, *Ozima and Takigami* [1979] did not reveal the pre-exponential factor of their grain-boundary diffusion coefficient, so their measurements cannot be applied to estimate grain-boundary diffusion rates on Venus. The study of Ar loss from lunar basalts shows an activation energy of about 120 kJ mol^{-1} for diffusion under anhydrous conditions, but again the pre-exponential factor was not measured [*McDougall and Harrison*, 1988]. We adopt Arrhenius parameters for K-feldspar (sanidine), a mineral that shows a similarly low activation energy [*Freer*, 1981]. An activation energy of 103.3 kJ mol^{-1} and a pre-exponential factor of 2.2×10^{-10} m^2 s^{-1} yield a diffusion coefficient of 1.4×10^{-17} m^2 s^{-1} at 750 K and a diffusion length of 0.66 m for 1 Gyr. Such a diffusion length is much smaller than the crustal thickness of 20 - 50 km [*Grimm*, 1994; *Konopliv and Sjogren*, 1994; *Simons et al.*, 1994], and the total Ar produced within this skin depth is negligible compared with $(^{40}Ar)_A$. Further, temperature variations with depth within this skin depth are so small that depth-dependent diffusivity is not significant for Ar diffusive transfer.

Of course, it is possible that the numerous fractures within the crust observed in Magellan radar images [*Solomon et al.*, 1991, 1992] may have enhanced the diffusive transfer of Ar from deeper parts of the crust. However, the small population (~ 12%) of tectonically fractured craters [*Phillips et al.*, 1992; *Strom et al.*, 1994] indicates that crustal deformation has been limited in either time or space, at least over the last 0.5 Gyr.

Also fracturing experiments on basaltic rocks show little release of *in situ* ^{40}Ar by cracking [*Honda et al.*, 1982]. Thus the diffusive transfer of Ar from the crust to the atmosphere can be ignored for both the crustal and atmospheric reservoirs in equations (4) and (5).

From the atmospheric ^4He abundance of 12 ppm and the escape rate of 9.6×10^5 kg yr^{-1}, the atmospheric residence time of ^4He may be estimated to be 600 Myr [*Prather and McElroy*, 1983]. Because this residence time is considerably smaller than the age of the planet, *Prather and McElroy* [1983] suggested that thermally enhanced diffusion of radiogenic ^4He from the crust serves to supply atmospheric ^4He. This contribution of crustal ^4He to the atmospheric reservoir, $F^{He}_{C\rightarrow A}$ in equations (9) and (10), can be examined quantitatively from the experimentally determined diffusion rate of He. Following the procedure described above for Ar, we adopt the diffusion parameters of the silica mineral tridymite from a compilation of helium diffusivity in minerals [*Freer*, 1981], under the assumption that the lowest activation energy corresponds to grain-boundary diffusion. The pre-exponential factor and the activation energy are 7.7×10^{-8} and 50.2 kJ mol^{-1}, respectively. Helium diffusivity at 750 K is thus calculated to be 2.5×10^{-11} m^2 s^{-1}, and the diffusive length scale is 0.88 km in 1 Gyr, the approximate time since the last global resurfacing event [*Phillips et al.*, 1992; *Schaber et al.*, 1992; *Strom et al.*, 1994]. This length scale is small relative to the thickness of the Venus crust. Unlike Ar, however, He production within this skin depth can account for a significant fraction of the present He escape rate [*Prather and McElroy*, 1983]. Further the calculation of $F^{He}_{C\rightarrow A}$ becomes complicated when the thermal structure of the crust is taken into account. We assume a one-dimensional mass transfer of He with depth, and we solve $F^{He}_{C\rightarrow A}$ as a function of time since the most recent catastrophic resurfacing event. The algebraic treatment of the diffusion equation with a depth-variable diffusion coefficient is discussed in detail in Appendix B. Temporal variation of $F^{He}_{C\rightarrow A}$ is calculated for allowable ranges of crustal U and Th concentrations, the thermal gradient

in the crust, crustal thickness, and the age of the crust. An upper bound on the present $F^{He}_{C \rightarrow A}$ so calculated, however, is still about an order of magnitude less than the present ^{4}He escape flux from the atmosphere. The contribution of crustal ^{4}He on the present atmospheric budget is thus likely to be insignificant relative to mantle outgassing.

Fractional Degree of Melting and the K Budget of the Venus Mantle

Constraints on the degree f_{melt} of partial melting and the K budget in the Venus mantle may be derived from the *in situ* γ-ray measurements of U, Th, and K concentrations in Venus surface materials. *Kargel et al.* [1993] estimated f_{melt} during the last catastrophic resurfacing event by substituting the K concentration estimated from X-ray analysis of Venera 13 and 14 and Vega 2 samples into C_L in equation (11). By assuming that the K concentration in the Venus mantle and in the bulk silicate Earth are the same, *Kargel et al.* [1993] calculated f_{melt} to be from a few thousandths to 0.2 depending on the K_2O content of Venera 13 and 14 samples. The assumption of equal K concentrations in both planets is supported by the similarity of the K/U and K/Th ratios measured by Venera and Vega landers to those in terrestrial igneous rocks [*Pollack and Black*, 1982] and from theoretical analyses of gravitational mixing of planetesimals during planetary accretion [*Wetherill*, 1980, 1994; *Wetherill and Stewart*, 1989]. We note, however, that these premises are worth a re-examination. The K/U and K/Th ratios vary over orders of magnitude because of large uncertainties in the γ-ray measurements. In addition, the K concentrations in the bulk silicate portions of Venus and Earth may differ because K is a moderately volatile element. A smaller heliocentric distance for Venus may lead to condensation of protoplanetary materials at generally higher temperature for Venus than Earth, and volatile abundances in Earth in particular may be considerably higher than in Venus [*Kargel et al.*, 1993]. On the other hand, it has been suggested that the giant impact held to be responsible for the formation of the Moon [*Hartmann*, 1986; *Melosh and Sonett*, 1986; *Benz et al.*, 1987] may have resulted in substantial depletion of volatile elements on Earth, and an enrichment of K in Venus relative to Earth [*Kargel et al.*, 1993], but recently reported measurements of potassium isotope abundances in meteorites and lunar and terrestrial rocks strongly limit volatile

depletion by evaporation during the formation of the Earth and the Moon [*Humayun and Clayton*, 1995a, b].

We constrain f_{melt} from U and Th concentrations rather than those of K. Because U and Th are highly refractory elements, depletion or enrichment of these radioactive elements during planetary accretion is likely to be negligible. We assume U and Th concentrations in Venus mantle between 18 and 29 ppb and between 64 and 94 ppb, respectively, on the basis of estimates for the bulk silicate Earth [*Dreibus and Wänke*, 1989; *McDonough et al.*, 1992; *Kargel and Lewis*, 1993] and for the bulk silicate portion of Venus [*Basaltic Volcanism Study Project*, 1981]. The concentrations of U and Th in the mantle are likely about a few tens of percent lower than that in the bulk silicate planet because U and Th are enriched in the crust. We discuss this point further below. The C_L values for U and Th in equation (11) are taken from γ-ray measurements by Venera and Vega landers and are listed in Table 4.6 [*Surkov et al.*, 1987]. Partition coefficients for U and Th are listed in Table 4.3.

Calculated ranges of f_{melt} are shown in Figure 4.1a. Uncertainties both in the γ-ray measurements [*Surkov et al.*, 1987] and in the mantle concentrations of U and Th are taken into account. Total uncertainties are shown by horizontal lines and range from factors of 2 to 10. Because the difference between the concentrations of U and Th in the mantle and the corresponding values for the bulk silicate Venus are small compared with these total uncertainties, we neglect the effect of crustal enrichment of U and Th on f_{melt}. The estimated fractional degree of melting is different for each sample. We assume, however, that both U and Th in each sample are partitioned by the same process of partial melting. Therefore a plausible range for f_{melt} during the magma genesis leading to each sample is the overlap between the calculated ranges of f_{melt} for U and Th. We do not take the measurements by Venera 8 into further consideration because the observed high concentration of radioactive elements in the sample (Table 4.6) is indicative of an involvement of material enriched in trace elements [*Basilevsky et al.*, 1992]. The smallest

value of f_{melt} is then 0.021, obtained from Vega 2, and the largest value, obtained from Vega 1, is 0.16 (Figure 4.1a). If we take mean values of respective γ-ray measurements and average values of mantle concentrations of U and Th, the calculated value for f_{melt} is constrained to lie between 0.022 and 0.06 except that derived from Th at Venera 10 (Figure 4.1a).

Vega 1 and 2 landed in northeastern Rusalka Planitia and Venera 9 and 10 landed on the eastern flank of Beta Regio [*Weitz and Basilevsky*, 1993]. All landing sites are dominated by radar-dark flow units that are associated with either the surrounding plains or lava flows from Beta Regio [*Kargel et al.*, 1993; *Weitz and Basilevsky*, 1993]. Therefore these estimates are appropriate to f_{melt} during or after the last catastrophic resurfacing event; f_{melt} before the last catastrophic event remains unconstrained. Also, it should be remembered that these estimates are based on an assumption of equilibrium batch melting (equation (11)). If melts segregated from the residual solid as they were produced (fractional melting), radioactive elements originally contained in the mantle material would concentrate in the first melt, because these elements are incompatible with the residual solid. As melting proceeds, concentrations of U and Th in the melt decrease, resulting in an overestimate of f_{melt} if equation (11) is employed.

Crystallization of olivine, plagioclase, and pyroxene during gradual cooling of mantle-derived magma prior to eruption (fractional crystallization) has not been considered here, because rock compositions estimated from X-ray analyses at the Venera 13 and 14 and Vega 2 landing sites show low TiO_2 and high MgO contents [*Surkov et al.*, 1986; *Barsukov*, 1992; *Kargel et al.*, 1993], suggesting insignificant fractionation of the mantle-derived magmas from which the surface materials were derived [*Barsukov*, 1992; *Grove et al.*, 1992; *Kargel et al.*, 1993]. If the surface materials sampled by Vega 1 and 2 and Venera 9 and 10 nevertheless did not form from primary liquids, then the measured concentrations of U and Th lead will yield underestimates of f_{melt} because both radioactive elements are highly incompatible with the primary crystallized phases (Table

4.3) [*Dostal and Capedri*, 1975; *Wörner et al.*, 1983; *LaTourrette and Burnett*, 1992; *Beattie*, 1993a, b; *LaTourrette et al.*, 1993]. Melting experiments on MORB glasses under a variety of P-T conditions show that fractional crystallization decreases the weight of the melt 10 to 70% by removal of the crystallized minerals [*Grove et al.*, 1992]. The measured concentrations of U and Th may therefore be higher than the concentrations in the primary magma by a factor of as much as 3, resulting in an underestimate of f_{melt} by the same factor.

Without further knowledge of partial melting and melt modification processes on Venus, including the uncertain and perhaps partly counteracting effects of fractional melting and fractional crystallization, we should thus allow a generous range of f_{melt} for the numerical calculations to follow. We therefore take 0.02 and 0.16 as upper and lower bounds on f_{melt}, and we adopt 0.04 as a nominal value.

We then make use of the calculated f_{melt} for each sample to estimate the K concentration in the present bulk silicate fraction of Venus, $(K)_{bulk}$. Again we utilize equation (11), and we substitute γ-ray measurements of the surface K concentration into C_L for K, including experimental errors (Table 4.6). The K^K_{mode} and K^K_{stoi} for maximum and minimum differentiation (Table 4.3) are substituted into equation (11) so that uncertainties related to mantle composition and mineral partition coefficients for K are taken into account as well. The neglect of the enrichment of U and Th in the crust is largely offset by ignoring the crustal enrichment of K, because the calculated value for $(K)_{bulk}$ is principally determined by the K/U and K/Th ratios in each sample and the U and Th abundances in the bulk silicate planet. We show the range of calculated $(K)_{bulk}$ for each sample as a function of f_{melt} in Figure 4.1b. A wide range of $(K)_{bulk}$ values is allowed for each sample. However, a plausible inference is that the average K concentrations in the present bulk silicate Venus must lie within each calculated range shown in Figure 4.1b (except that for the Venera 8 sample). It is clear from the figure that the estimated ranges of bulk silicate K concentration for Vega 1, 2 and Venera 10

samples overlap the range for the Venera 9 sample. Therefore we assume that the K budget in the bulk silicate Venus is constrained by the Venera 9 sample and is between 95 and 250 ppm (Figure 4.1b).

There are some uncertainties involved in the above estimate. The assumption of equilibrium batch melting (equation (11)) is likely to add insignificant error because we calculate individual K abundances using f_{melt} determined from U and Th concentrations in the same sample. An overestimate of f_{melt} is thus compensated. We adopt nominal values of experimental errors for the γ-ray measurement provided by *Surkov et al.* [1987], but a full assessment of the errors, particularly those for the 50-minute-long experiment conducted by the Venera 9 lander [*Surkov et al.*, 1977], is critical for constraining a plausible range for the average K abundance. The modal abundance of plagioclase in the Venus mantle (Table 4.1) is also important for this estimate because the partition coefficient of K for plagioclase is orders of magnitude higher than the other mineral partition coefficients (Table 4.2). Spatial and temporal variations in the plagioclase abundance in the mantle source region, however, are difficult to assess, even for Earth [*Basaltic Volcanism Study Project*, 1981; *Hart and Zindler*, 1986]. Because a range in mantle compositions (Table 4.1) and in the partition coefficient for plagioclase (Table 4.2), both taken into account in K^K_{mode} and K^K_{stoi}, allow a considerably wide range of K differentiation (Appendix A), our estimate is likely to be insensitive to variations in the plagioclase content in the mantle source region of each sample.

The effect of possible fractional crystallization on our estimate of $(K)_{bulk}$ is small, because K is as incompatible as U and Th in olivine and pyroxene (Tables 4.2 and 4.3). The K/U and K/Th ratios therefore do not change significantly by the crystallization of these minerals. While K is relatively compatible with plagioclase compared with olivine and pyroxene, the partition coefficient of K for plagioclase is still smaller than unity (Table 4.2), indicating that K is partitioned mostly into the melt rather than into the plagioclase during feldspar crystallization. Melting experiments on MORB glasses show

that at least 80% of the K in mantle-derived magmas is retained in the melt after plagioclase has been removed from the liquid by crystallization [*Grove et al.*, 1992]. Thus any correction in our estimate for $(K)_{bulk}$ due to the fractional crystallization is less than 20%.

In spite of these uncertainties, the estimate of $(K)_{bulk}$ of 100 to 250 ppm is in good agreement with the K abundance in the bulk silicate Earth. *Allègre et al.* [1987] calculated a K concentration in the bulk silicate Earth of 280 ppm under the assumption that 46% of the mantle degassed the ^{40}Ar in the present atmosphere on Earth. *Azbel and Tolstikhin* [1990] calculated a terrestrial $(K)_{bulk}$ of 480 ppm from the present atmospheric ^{40}Ar by assuming that only 33% of the mantle degassed, but this value exceeds an upper limit of 360 ppm obtained from an assumed global average heat flow of 70 mW m^{-2} [*Kargel and Lewis*, 1993]. This upper limit increases by 17% if a more carefully developed value for the average terrestrial heat flow of 82 mW m^{-2} [*Sclater et al.*, 1980] is adopted, but the estimate of $(K)_{bulk}$ by *Azbel and Tolstikhin* [1990] is still higher than the increased upper limit. Compositional models provide an estimate for K concentration in the bulk silicate Earth between 130 and 260 ppm [*Dreibus and Wänke*, 1989; *McDonough et al.*, 1992; *Kargel and Lewis*, 1993]. The K concentration in the bulk silicate fraction of Venus calculated from an equilibrium condensation model is more than 5 times higher than our upper bound [*Basaltic Volcanism Study Project*, 1981], but other models based on chondritic meteorite compositions yield $(K)_{bulk}$ of 130 to 220 ppm [*Basaltic Volcanism Study Project*, 1981], in good agreement with our estimate.

Evaluation of the K Concentration in the Bulk Silicate Planet from Ar Degassing

In order to clarify constraints on the resurfacing history of Venus, we classify model parameters into those related to volcanic resurfacing in general and those relevant only to Ar degassing. The first group is common to both Ar and He degassing models and consists of the characteristic time interval between catastrophic resurfacing events, the

age of the last catastrophic resurfacing event, the volume of crust produced during each catastrophic resurfacing event, the rate of magmatism during time intervals between catastrophic events, and f_{melt}. We term this group the crustal production parameters. The second group includes the bulk partition coefficients of Ar and K, the present $(^{40}Ar)_A$ and crustal K concentration, and $(K)_{bulk}$. This group we term the Ar degassing parameters. A third group of parameters, relevant only to the degassing and escape of He, consists of the bulk partition coefficients of He, U, and Th, the present $(^4He)_A$, the present U and Th abundances in the crust and in the bulk silicate Venus, $F^{He}_{C\rightarrow A}$, and $F^{He}_{A\rightarrow S}$. These we term the He degassing parameters.

For given crustal production parameters, $\pi^K_{M\rightarrow C}$ and $\pi^{Ar}_{M\rightarrow A}$, the absolute abundances of K and ^{40}Ar in each reservoir are calculated from $(^{40}K)_M(t=0)$ (equations (1) to (5)). The K concentrations in the crust and in the bulk silicate planet follow from the masses of crust and mantle (Figure 4.2). The calculated K concentration in the crust and the Ar abundance in the atmosphere are compared with *in situ* measurements by Venera, Vega, and Pioneer Venus [*von Zahn et al.*, 1983; *Surkov et al.*, 1987] to constrain the crustal production parameters. For a given $(^{40}K)_M$ at $t = 0$, the calculated K concentration in present crust is highest when a maximum of K differentiation efficiency from mantle to crust (Table 4.3) is assumed. Such a calculated upper limit on the crustal K abundance must be higher than 0.14%, a lower bound on the γ-ray measurements of K by Vega 1 and 2 and Venera 9 and 10 (Table 4.6) [*Surkov et al.*, 1987]. Otherwise the assumed crustal production parameters fail to satisfy the constraint on crustal K abundances within a range of K differentiation efficiency (Table 4.3). Thus a lower limit on $(^{40}K)_M(t=0)$ is obtained. Because of the assumption of zero $(^{40}K)_C$ at $t = 0$, this lower limit on $(^{40}K)_M(t=0)$ can be immediately converted to a lower limit on $(K)_{bulk}$ by taking into account the radioactive decay of ^{40}K over 4.55 Gyr and the K isotopic ratio at present. For a characteristic time interval between catastrophic resurfacing events of 500 Myr, an age of the last catastrophic resurfacing event of 300 Myr, a value for f_{melt} of

0.04, a volume of new magmatism during each catastrophic event of 2.3×10^9 km^3 (equivalent to an average thickness over the planetary surface of 5 km), and a rate of magmatism between catastrophic events of 1 km^3 yr^{-1} (Figure 4.2), this lower limit on $(K)_{bulk}$ at present is 62 ppm by weight. Similarly an upper limit on $(K)_{bulk}$ is obtained at 380 ppm by taking a minimum K differentiation efficiency from mantle to crust (Table 4.3) and a crustal K concentration of 0.67%, the upper bound on the γ-ray measurements by Vega 1 and 2 and Venera 9 and 10 (Table 4.6) [*Surkov et al.*, 1987].

A different constraint on $(K)_{bulk}$ is derived also from Figure 4.2 by taking the Ar abundance in the present atmosphere of 70 ± 25 ppm [*von Zahn et al.*, 1983]. The ^{40}Ar/Ar ratio of 0.472 [*von Zahn et al.*, 1983] yields lower and upper bounds on present atmospheric ^{40}Ar of 21 and 45 ppm, respectively. For a given $(K)_{bulk}$, the calculated $(^{40}Ar)_A$ at present is highest when both the K abundance in the mantle and the Ar degassing from mantle to atmosphere are highest. Alternatively, a lower limit on the present $(K)_{bulk}$ is constrained by taking a lower bound on the present $(^{40}Ar)_A$, a minimum K differentiation efficiency, and a maximum Ar degassing efficiency (Table 4.3). Similarly, for an upper limit on present $(K)_{bulk}$, we adopt an upper bound on present $(^{40}Ar)_A$, a maximum K differentiation efficiency, and a minimum Ar degassing efficiency (Table 4.3). The calculated lower and upper limits on $(K)_{bulk}$ are 120 and 1400 ppm, respectively, for the crustal production parameters adopted in Figure 4.2. A successful Ar degassing model, of course, must satisfy the constraints of both crustal K concentration and atmospheric Ar abundance at the same time. Therefore a plausible range for $(K)_{bulk}$ is between 120 and 380 ppm. This calculated range of $(K)_{bulk}$ overlaps with our estimate of 100 to 250 ppm in Figure 4.1b, and thus satisfies γ-ray measurements of crustal K, U, and Th concentrations as well. As discussed above, the ignorance of ^{40}Ar escape during the hydrodynamic outflow phase results in an underestimate of mantle outgassing. Therefore the lower limit on $(K)_{bulk}$ is conservative while the upper limit includes an uncertainty.

For the above lower limit on $(K)_{bulk}$ from present $(^{40}Ar)_A$, we assume a minimum K differentiation efficiency, in contrast to the maximum K differentiation efficiency assumed for the lower limit calculated from the crustal K concentration. These two apparently opposite assumptions do not contradict one another because the obtained upper and lower limits on $(K)_{bulk}$ of 120 to 380 ppm are necessary, but not sufficient, to satisfy simultaneously the constraints both of the crustal K concentration and the atmospheric Ar abundance. If the calculated K concentration in the present crust were less than 0.14% for minimum K differentiation efficiency and a $(K)_{bulk}$ of 120 ppm, then a necessary and sufficient lower bound on $(K)_{bulk}$ is greater than 120 ppm. However, we do not attempt to obtain the lower limit necessary and sufficient to satisfy simultaneously both the crustal K and the atmospheric Ar abundances, but rather adopt the above lower limit on $(K)_{bulk}$ for the discussion below because the total K and Ar abundances in the crust are minor compared with those in the mantle (Figure 4.2). The calculated $(^{40}Ar)_A$ at present depends little on the crustal K abundance, and therefore any increase in the lower limit on $(K)_{bulk}$ due to higher K differentiation is insignificant.

Constraints on Average Crustal Production Rate

The above procedure has been repeated for a series of crustal production models that are parameterized by the volume of magmatism during each catastrophic resurfacing event and the rate of magmatism between catastrophic events. In Figure 4.3a, we show contours of the lower and upper limits on $(K)_{bulk}$ (dashed and solid lines, respectively) calculated by assuming a characteristic time interval between catastrophic resurfacing events of 500 Myr, an age of the last catastrophic resurfacing event of 300 Myr, and an f_{melt} of 0.04. In the shaded area, volcanic degassing by catastrophic resurfacing events and magmatism between catastrophic events are so small that a present $(K)_{bulk}$ higher than 250 ppm is required to supply more atmospheric ^{40}Ar than the observed lower bound (21 ppm). Such Ar degassing models are not consistent with the observed K, U,

and Th concentrations in the Venus crust (Figure 4.1b). Therefore in Figure 4.3a, crustal production is constrained by the calculated lower limit on $(K)_{bulk}$ and the 250-ppm upper bound derived from crustal K, U, and Th concentrations.

A trade off between the volume of magmatism during each catastrophic resurfacing event and the rate of magmatism between catastrophic events is evident in Figure 4.3a. This is because the present $(^{40}Ar)_A$ depends principally on the total crustal volume produced over the planet's history and is not sensitive to the manner in which the crust forms. Therefore we cannot distinguish the contributions from episodic catastrophic resurfacing and magmatism between catastrophic events from ^{40}Ar degassing alone.

In Figure 4.3b, the upper and lower limits on $(K)_{bulk}$ at every point outside the shaded area in Figure 4.3a are projected as functions of average crustal production rate over the planet's history, i.e., over resurfacing events as well as intervening periods. For an average crustal production rate less than 12 $km^3\ yr^{-1}$, the lower limit on $(K)_{bulk}$ is constrained to afford sufficient atmospheric ^{40}Ar for given magmatic flux. For a crustal production rate higher than 12 $km^3\ yr^{-1}$, the lower bound on crustal K concentration limits the amount of K in the mantle and thus the total K budget on Venus. Similarly the upper limit on $(K)_{bulk}$ is constrained by the upper bound on crustal K concentration for an average crustal production rate less than 19 $km^3\ yr^{-1}$, and by the upper bound on the present $(^{40}Ar)_A$ for a crustal production rate higher than 19 $km^3\ yr^{-1}$ (Figure 4.3b). Taking into account the limits on $(K)_{bulk}$ of 95 and 250 ppm estimated in the previous section from crustal K, U, and Th concentrations (Figure 4.1b), the allowable ranges in $(K)_{bulk}$ and average crustal production rate are shown by the shaded area in Figure 4.3b.

Because of the trade off between the volume of magmatism during each catastrophic event and the rate of magmatism between catastrophic events (Figure 4.3a), ^{40}Ar degassing is insensitive to the assumed characteristic time interval between catastrophic resurfacing events. In Figures 4.4a and 4.4b, we show calculated upper and lower bounds on $(K)_{bulk}$ as functions of average crustal production rate for characteristic time intervals

between catastrophic resurfacing events of 200 Myr and 1 Gyr, respectively. The assumed values for f_{melt} and the age of the last catastrophic resurfacing event are same as in Figure 4.3b, 0.04 and 300 Myr, respectively. If the calculated lower limit on $(K)_{bulk}$ is higher than 250 ppm or if the upper limit is less than 95 ppm, the adopted crustal production parameters are inconsistent with the observed crustal K, U, and Th concentrations and thus are not included in Figures 4.4a and 4.4b. K abundances in the crust and mantle are determined by equation (11) and mass conservation. The crustal K concentration is therefore dependent not only on partition coefficients and f_{melt} but also on crustal mass. Because the crustal mass is a product of the crustal production rate and the characteristic time interval between catastrophic events, the upper and lower limits on $(K)_{bulk}$ constrained from the crustal K concentration are slightly dependent on the characteristic time interval between catastrophic resurfacing events (Figures 4.3b, 4.4a, and 4.4b). In contrast, upper and lower limits on $(K)_{bulk}$ constrained by the present $(^{40}Ar)_A$ depend little on the assumed manner of crustal formation or the characteristic time interval between catastrophic resurfacing events, but rather on the average crustal production rate, because the present $(^{40}Ar)_A$ is a manifestation of integrated magmatism over 4.55 Gyr. By the same reasoning, these upper and lower limits on $(K)_{bulk}$ are independent of the age of the last catastrophic resurfacing event. Therefore the lower bound on the average crustal production rate determined by a calculated lower limit on $(K)_{bulk}$ less than 250 ppm is nearly identical for all Ar degassing models shown in Figures 4.3b, 4.4a, and 4.4b and is 2.6 $km^3\ yr^{-1}$. Similarly the upper bound on average crustal production rate is determined at 110 $km^3\ yr^{-1}$ when the calculated upper limit on $(K)_{bulk}$ is more than 95 ppm at $f_{melt} = 0.04$ (Figure 4.4a) regardless of the manner of crustal formation, the characteristic time interval between catastrophic resurfacing events, or the age of the last catastrophic event.

Such lower and upper bounds on average crustal production rate depend on f_{melt}, as is evident in equation (12). As f_{melt} decreases, the efficiency of both Ar degassing and K

differentiation increases. Enhanced degassing efficiency of Ar decreases the calculated $(K)_{bulk}$ for a given $(^{40}Ar)_A$ at present, while an enhanced differentiation efficiency of K increases the calculated $(K)_{bulk}$ because enrichment of K in the crust increases $(K)_{bulk}$ for a given $(^{40}K)_M$. Thus whether calculated $(K)_{bulk}$ increases or decreases as f_{melt} increases depends on the relative significance of Ar degassing and K differentiation to $(^{40}Ar)_A$. For a lower bound on the average crustal production rate, the variation of f_{melt} controls the Ar degassing efficiency because f_{melt} is comparable to K^{Ar}_{mode} for maximum Ar degassing (Table 4.3), while $(^{40}Ar)_A$ is little dependent on K differentiation as discussed above. Therefore an allowable minimum average crustal production rate for any Ar degassing model is obtained when a lower bound on f_{melt} of 0.02 is adopted; this lower bound is 2.0 $km^3\ yr^{-1}$ (Figure 4.4c). For an upper bound on the average crustal production rate, in contrast, a variation in f_{melt} is significant for K differentiation efficiency because K^K_{mode} for maximum K differentiation is small compared with f_{melt} (Table 4.3). On the other hand, Ar degassing is nearly independent of a variation in f_{melt} because K^{Ar}_{mode} for minimum Ar degassing is much greater than f_{melt} (Table 4.3). An allowable maximum average crustal production rate for any Ar degassing model is obtained again as the lower bound on f_{melt} of 0.02 is adopted, and is 110 $km^3\ yr^{-1}$ (Figure 4.4c), a figure indistinguishable from the upper bound calculated above with the nominal value for f_{melt} of 0.04 (Figure 4.4a).

On the basis of flow morphologies seen in Magellan radar images, it has been suggested that plains volcanism was characterized by voluminous sources and high degree of partial melting [*Head et al.*, 1995]. The average value for f_{melt} during the catastrophic resurfacing events is not well constrained (Figure 4.1a), but the largest estimate of f_{melt} (0.16) is derived from the U and Th concentrations measured by Vega 1 (Figure 4.1a), which landed in northeastern Rusalka Planitia [*Kargel et al.*, 1993; *Weitz and Basilevsky*, 1993]. We then adopt $f_{melt} = 0.16$ as a basis for a comparison between our Ar degassing model and such radar observations (Figures 4.5a and 4.5b). A

characteristic time interval between catastrophic resurfacing events of 500 Myr and an age of the last catastrophic event of 300 Myr are assumed. The lower bound on $(K)_{bulk}$ is greatly increased for such high a value of f_{melt} because of the decreased K differentiation efficiency. Accordingly, the upper bound on $(K)_{bulk}$ of 250 ppm given by the crustal U, Th and K concentrations (Figure 4.1b) yields not only a lower bound but also an upper bound on average crustal production rate (Figures 4.5a and 4.5b). Thus strong constraints on average crustal production rate are provided for high values of f_{melt}.

Evaluation of He Degassing/Escape Models

For He degassing/escape models, we first adopt a value for $X^{He}_{homo}(t_P)$ in equation (21) in order to fix $F^{He}_{A\rightarrow S}$ in the past. The calculated present value of $(^4He)_A$ must satisfy this assumed value, of course, within allowable ranges of He degassing parameters. We use this criterion to constrain crustal production parameters. For example, the calculated present value of $(^4He)_A$ increases as $(^4He)_A(t_{HO})$ increases. Also increases in $(^4He)_M(t_{HO})$, in the current U and Th concentrations in the bulk silicate planet ($(U)_{bulk}$ and $(Th)_{bulk}$), in $F^{He}_{C\rightarrow A}$ (Appendix B), and in the He degassing efficiency (Table 4.3) result in an increased calculated $(^4He)_A(t_P)$. Therefore a maximum value for calculated $(^4He)_A(t_P)$ is obtained when upper bounds on these He degassing parameters are adopted. The upper bounds on $(U)_{bulk}$ and $(Th)_{bulk}$ are also constrained by U and Th concentrations in the crust. We adopt the lower of two upper bounds on $(U)_{bulk}$: either 29 ppb or the quantity corresponding to a crustal U concentration of 1.11 ppm (Table 4.6). The upper bound on $(Th)_{bulk}$ is similarly either 94 ppb or that satisfying a crustal Th concentration of 4.07 ppm (Table 4.6). If this maximum calculated $(^4He)_A(t_P)$ is lower than the value assumed before calculation, the adopted crustal production parameters fail to reproduce an internally consistent volcanic history within the allowable ranges of He degassing parameters and thus should be rejected. Similarly a minimum of $(^4He)_A(t_P)$ may be calculated if lower bounds on these He degassing

parameters are adopted, and this calculated minimum must be lower than the value assumed before the calculation.

The calculated He degassing/escape evolution is illustrated in Figure 4.6a. The ^{4}He abundances in the mantle (diagonally hatched area), crust (horizontally hatched area), and atmosphere (shaded area) are calculated under the assumptions that $(^4He)_A(t_P)$ is 12 ppm, the characteristic time interval between catastrophic resurfacing events is 500 Myr, the age of the last catastrophic resurfacing is 300 Myr, f_{melt} is 0.04, t_{HO} is 500 Myr, the magmatism during each catastrophic event is equivalent to a thickness of 5 km, and the rate of magmatism between catastrophic events is 1 km^3 yr^{-1}. Calculated abundances corresponding to minimum and maximum $(^4He)_A(t_P)$ are shown by solid and dashed lines, respectively. These calculated maximum and minimum values for present $(^4He)_A(t_P)$ are 33 and 3.3 ppm, respectively, and include the assumed value of 12 ppm permitting an internally consistent He degassing/escape model within the ranges of He degassing parameters.

The residence time of ^{4}He in the atmosphere is calculated by dividing the atmospheric ^{4}He abundance by $F^{He}_{A\rightarrow S}$. Thus ^{4}He escape is faster for smaller $(^4He)_A(t_P)$. For $(^4He)_A(t_P)$ equal to 4, 12 , and 36 ppm, the residence times are 0.2, 0.6, and 1.8 Gyr, respectively [*Prather and McElroy*, 1983]. For comparison, we show in Figure 4.6b the atmospheric evolution of ^{4}He for the same He degassing parameters as in Figure 4.6a but with $(^4He)_A(t_P)$ equal to 4 and 36 ppm (shaded and diagonally hatched areas, respectively). Because ^{4}He abundances in the crust and mantle are independent of the assumed $(^4He)_A(t_P)$, the results for $(^4He)_C$ and $(^4He)_M$ for these models are the same as in Figure 4.6a. The calculated maximum and minimum values for $(^4He)_A(t_P)$ are 0.87 and 8.4 ppm and 8.3 and 110 ppm for $(^4He)_A(t_P)$ equal to 4 and 36 ppm, respectively (Figure 4.6b). The assumed crustal production parameters are thus also consistent with a present atmospheric ^{4}He abundance of either 4 or 36 ppm.

The effects of He degassing parameters on the calculated maximum and minimum values of $(^4He)_A(t_P)$ are also illustrated in Figures 4.6a and 4.6b. First, $(^4He)_C$ is negligible relative to $(^4He)_M$. Thus $(^4He)_A$ is dominated by degassing from the mantle, and diffusive transfer of crustal ^{4}He to the atmosphere does not affect atmospheric evolution of ^{4}He unless the mantle reservoir is isolated from the crust and atmosphere. The atmospheric ^{4}He available at $t = t_{HO}$ escapes from the atmosphere within 1 to 2 Gyr when $(^4He)_A(t_P)$ is assumed to be 4 ppm (Figure 4.6b) and 12 ppm (Figure 4.6a), respectively. Therefore neither $(^4He)_A(t_P)$ nor t_{HO} is important for a present atmospheric ^{4}He abundance less than 12 ppm. In contrast, the residence time of 1.8 Gyr for $(^4He)_A(t_P) = 36$ ppm is comparable to t_P, so a considerable portion of the present atmospheric ^{4}He budget of 36 ppm can be attributed to $(^4He)_A(t_{HO})$ (Figure 4.6b).

We repeat the above procedure for a series of models parameterized by the volume of magmatism during each catastrophic event and the rate of magmatism between catastrophic events as we did for Ar degassing in Figure 4.3a. Upper and lower limits on planetary magmatism are constrained for each model so that calculated maximum and minimum values for $(^4He)_A(t_P)$ are consistent with the assumed $(^4He)_A(t_P)$. In Figure 4.7a, we show ranges of crustal production that satisfy these criteria for assumed $(^4He)_A(t_P)$ of 4, 12, and 36 ppm. Other crustal production parameters (f_{melt}, the characteristic time interval between catastrophic resurfacing, the age of the last catastrophic resurfacing event, and t_{HO}) are the same as in Figure 4.6. Solid lines correspond to crustal production models for which the calculated maximum $(^4He)_A(t_P)$ equals the assumed value, and dashed lines correspond to crustal production models for which the calculated minimum $(^4He)_A(t_P)$ equals the assumed value. Crustal production models above the dashed lines or below the solid lines (shaded areas) are unable to reproduce an internally consistent ^{4}He degassing/escape history within the ranges of He degassing parameters, and therefore should be rejected.

Constraints on Scenarios for Crustal Production from He Degassing/Escape

Figure 4.7a demonstrates that a greater $(^4He)_A$ at present does not necessarily indicate a higher rate of planetary magmatism in the past, because the total amount of mantle outgassing also depends on $F^{He}_{C\rightarrow A}$, which decreases as $(^4He)_A(t_P)$ increases. A longer residence time increases the contribution of $(^4He)_A(t_{HO})$ to the present atmospheric ^{4}He budget (Figure 4.6b) and hence less mantle degassing is required. This effect of $(^4He)_A(t_P)$ on required mantle degassing is most pronounced for the lower bound on crustal production (solid lines in Figure 4.7a), for which an upper bound on $(^4He)_A(t_{HO})$ is assumed. Thus a constraint on minimum crustal production is obtained with $(^4He)_A(t_P)$ = 36 ppm (Figure 4.7a). A longer hydrodynamic outflow phase enhances this effect of $(^4He)_A(t_P)$ on the minimum crustal production constraint by increasing the contribution of $(^4He)_A(t_{HO})$ to the present atmosphere. In Figure 4.7b, we show results for He degassing models with t_{HO} = 1 Gyr but with the other He degassing parameters as in Figure 4.7a. The greater contribution of $(^4He)_A(t_{HO})$ can match a $(^4He)_A(t_P)$ of 36 ppm with no mantle outgassing, so any model in Figure 4.7b satisfies the constraint on minimum crustal production.

For the upper bounds on crustal production (dashed lines in Figure 4.7a), $(^4He)_A(t_{HO})$ is assumed to be zero and all present $(^4He)_A$ is attributed to degassing from the mantle. For a rate of magmatism between catastrophic events of less than 9 km^3 yr^{-1}, a constraint on maximum crustal production is obtained by $(^4He)_A(t_P)$ = 4 ppm because the short residence time of ^{4}He requires considerable outgassing during the last catastrophic event. For a rate of magmatism between catastrophic events more than 9 km^3 yr^{-1}, in contrast, $(^4He)_A$ is in a nearly steady balance between recent mantle degassing and atmospheric escape. Because the contribution to the present atmospheric ^{4}He budget from degassing by magmatism after the last catastrophic event surpasses that from degassing during the last catastrophic event in this parameter range, this upper bound on the rate of magmatism between catastrophic events is nearly constant regardless of the volume of magmatism

during each catastrophic event (see upper bound for $(^4He)_A(t_P)$ = 4 ppm in Figure 4.7a). This dependence on the rate of magmatism between catastrophic events and independence of the volume of magmatism during such events is better illustrated for a He degassing model with an older age for the last catastrophic resurfacing event. In Figure 4.7c, we show results for He degassing models with the same He degassing parameters as in Figure 4.7a but with the age of the last catastrophic resurfacing event at 500 Myr. It is clear from Figure 4.7c that for $(^4He)_A(t_P)$ = 4 ppm He degassing models depend only on recent magmatism and are not sensitive to magmatic activity before the last few hundred million years because the residence time is short relative to the age of the last catastrophic event. The volume of magmatism during each catastrophic event is thus not constrained from above He degassing/escape models unless the present ^{4}He budget in the atmosphere and the age of the last catastrophic event are better constrained.

Increasing f_{melt} decreases the allowable range of crustal production models, as discussed above for Ar degassing models (Figures 4.5a and 4.5b), because the uncertainty in the bulk partition coefficients (Table 4.3) becomes insignificant as f_{melt} increases. In Figure 4.7d, we show results for He degassing models with the same He degassing parameters as in Figure 4.7a but with f_{melt} = 0.16. An increase in f_{melt} introduces a new constraint on crustal production parameters from the U concentration in the crust. The U concentration in the crust and mantle are determined by equation (11) and mass balance between the two reservoirs. As f_{melt} increases, the U concentration in the crust decreases. The calculated U concentration decreases further for greater crustal production due to mass balance between the crust and mantle because U is enriched in the crust. Therefore too great a crustal production for high f_{melt} results in a calculated concentration of crustal U less than 0.17 ppm, the lower bound given by γ-ray measurements (Table 4.6) [*Surkov et al.*, 1987]. This constraint on maximum crustal production rate is also shown in Figure 4.7d.

The characteristic time interval between catastrophic resurfacing events also has an effect on model predictions. In Figure 4.7e, results are shown for He degassing models with the same He degassing parameters as in Figure 4.7a but with a characteristic time interval between catastrophic events of 200 Myr. More frequent catastrophic resurfacing greatly promotes degassing from the mantle. For an $(^4He)_A(t_P)$ of 12 and 36 ppm, the residence times of 0.6 and 1.8 Gyr are too long to remove accumulated outgassed ^{4}He from the atmosphere in the time intervals between events. The present atmospheric ^{4}He contains contributions from the mantle over the full planetary history. For a $(^4He)_A(t_P)$ of 4 ppm, in contrast, most of the present $(^4He)_A$ degassed in the last few hundred million years. The ^{4}He flux from the mantle decreases with time for this set of parameters because the production of ^{4}He by radioactive decay in the mantle cannot compensate for the loss of helium by frequent degassing. Therefore the amount of magmatism during the last catastrophic event for $(^4He)(t_P) = 4$ ppm is larger in Figure 4.7e than in Figure 4.7a.

In summary, ^{4}He degassing/escape is more sensitive to the manner of recent crustal production than ^{40}Ar degassing because its residence time is less than the planetary age. Therefore ^{4}He has the potential for disclosing some of the characteristics of catastrophic resurfacing, including the time interval between catastrophic resurfacing episodes and the age and volume of the last catastrophic resurfacing event. However, large uncertainties in the bulk partition coefficients and in the present ^{4}He abundance in the lower atmosphere permit a wide range of scenarios (Figures 4.7a-e). Until these uncertainties are significantly reduced, ^{4}He provides no strong constraint on the nature of catastrophic resurfacing.

DISCUSSION

Comparison of Ar and He Degassing/Escape Results with Previous Work

The combined application of ^{40}Ar and ^{4}He degassing models (e.g., Figures 4.3a and 4.7a, or Figures 4.5a and 4.7d) appears to allow improved constraints on crustal production parameters. However, we must be cautious in mixing constraints on crustal production appropriate to different time scales. The present $(^{40}Ar)_A$ is an integral of mantle degassing over the planet's entire history, as discussed above. While the convective vigor of the planetary mantle was likely to have been considerably higher in the first several hundred million years after planetary accretion [e.g., *Schubert et al.*, 1989], the total amount of ^{40}Ar degassed is insensitive to magmatism in the first billion years of the planet's history [*Pollack and Black*, 1982] because of the long half life of ^{40}K (1.25 Gyr) and because the ^{40}Ar abundance at $t = 0$ is negligible relative to the present atmospheric budget [*Ozima and Zashu*, 1983]. Thus the upper and lower bounds on crustal production rate obtained from ^{40}Ar degassing should be considered as averages over approximately the last 3.5 Gyr.

Results on ^{4}He degassing/escape illustrated in Figures 4.5 to 4.7 constrain crustal production on the scale of the atmospheric residence time, i.e., ranging from 200 Myr to 1.8 Gyr depending on the assumed ^{4}He mixing ratio in the homosphere. If the ^{4}He abundance in the present atmosphere is as low as 4 ppm, the observed $(^{4}He)_{A(tP)}$ is sensitive to volcanic activity over the last several hundred million years and may constrain the rate of magmatism after the last catastrophic event (Figure 4.7c). If the ^{4}He abundance in the present atmosphere is as high as 36 ppm, in contrast, then ^{4}He degassing/escape provides independent constraints on crustal production on a time scale similar to that of ^{40}Ar degassing. Thus an improvement in the estimate of the atmospheric ^{4}He abundance by theoretical studies of the structure of the lower atmosphere [*Hoffman et al.*, 1980; *Massie et al.*, 1983; *von Zahn et al.*, 1983] or by direct

measurement on future planetary missions would have a significant influence on our understanding of recent volcanic activity on Venus.

The range in the average crustal production rate on Venus of between 2.0 and 114 $km^3\ yr^{-1}$ is wide compared with the modern crustal production rate on the Earth, estimated to be 26 to 34 $km^3\ yr^{-1}$ [*Crisp*, 1984]. These rates are equivalent to a total thickness of crust produced over the last 4.55 Gyr of 20 to 1100 km. The lower bound on the crustal production rate is thus barely sufficient to yield the present crustal thickness [*Grimm*, 1994; *Konopliv and Sjogren*, 1994; *Simons et al.*, 1994], while the upper bound would require continual crustal recycling in the past as often as once every hundred million years. Thus Ar degassing alone neither requires nor excludes lithospheric recycling during catastrophic resurfacing events [*Parmentier and Hess*, 1992; *Turcotte*, 1993]. While we have assumed a temporally constant f_{melt}, a time-dependent f_{melt} would not change the estimated range in average crustal production because the effect of a variable f_{melt} is taken into account by the above procedure aimed at estimating minimum and maximum values (Figure 4.4c).

The atmospheric ^{40}Ar abundance normalized by planetary mass is about 3 to 6 times less on Venus than Earth [*Ozima and Podosek*, 1983; *von Zahn et al.*, 1983]. The simplest inference is that either the magmatic flux or the time period of magmatism is 3 to 6 times less on Venus than Earth, assuming similar K budgets and degassing mechanisms on both planets. In particular, previous estimates of average crustal production rates on Venus of less than 5 $km^3\ yr^{-1}$ by *Volkov and Frenkel* [1993] and of 3.6 $km^3\ yr^{-1}$ by *Matsui and Tajika* [1995], or estimates of the time interval of magmatism of 1 Gyr by *Pollack and Black* [1982] and of 2 Gyr by *Matsui and Tajika* [1991], all based on ^{40}Ar degassing, are certainly consistent with our results. By taking into account the potential differences in planetary K budgets (Figure 4.1b) and degassing mechanisms between Venus and Earth, however, our numerical results allow a wider range of crustal production rates. The upper bound on crustal production rate in Figure 4.4a is

considerably higher than others reported, due to the adopted lower bound on $(K)_{bulk}$ of 95 ppm and the upper bounds on Ar partition coefficients (Table 4.4). Thus thermal and chemical evolution scenarios, such as that of *Parmentier and Hess* [1992], that predict crustal production rates more than a factor of 2 greater than the current rate on Earth may not be rejected at present [cf. *Matsui and Tajika*, 1995]. Further experimental studies of mineral partition coefficients, particularly for clinopyroxene and orthopyroxene, can significantly reduce the uncertainties in these estimates.

The current rate of magmatism on Venus has been estimated to be between 0.4 and 11 $km^3\ yr^{-1}$ on the basis of the rate of reaction of atmospheric SO_2 and surface carbonates [*Fegley and Prinn*, 1989; *Fegley and Treiman*, 1992]. A time scale for the reaction of 1.9 Myr [*Fegley and Prinn*, 1989] ensures that the estimated rate represents the crustal production rate after the last catastrophic event. Two- and three-dimensional Monte Carlo models of volcanic resurfacing indicate volcanic resurfacing rates over the last 500 Myr of 0.01 - 0.15 and 0.37 $km^3\ yr^{-1}$, respectively [*Bullock et al.*, 1993; *Strom et al.*, 1994]. Because crustal production by intrusions is not taken into account in such volcanic resurfacing models, these figures should be regarded as lower bounds on the rate of magmatism after the last catastrophic resurfacing event. Analysis of the cratering record on volcanic terrains also constrains the rate of volcanic resurfacing [*Namiki and Solomon*, 1994; *Price and Suppe*, 1994]. For a terrestrial volumetric ratio of intrusive and extrusive volcanism between 10 and 17, the rate of crustal production is suggested to be nearly constant over the last several hundred million years at 2 to 7.2 $km^3\ yr^{-1}$ [*Namiki and Solomon*, 1994; *Price*, 1995]. By subtracting this rate from the average rate of crustal production, the relative importance of catastrophic resurfacing and magmatism between catastrophic events could, in principle, be evaluated. However, because our results from ^{40}Ar degassing and these estimates overlap and because both involve large uncertainties, none of the postulated scenarios for catastrophic resurfacing can presently

be excluded [*Parmentier and Hess*, 1992; *Steinbach and Yuen*, 1992; *Arkani-Hamed et al.*, 1993; *Turcotte*, 1993; *Herrick and Parmentier*, 1994; *Herrick*, 1994].

Degassing from a Differentiated Mantle

Distinct isotopic compositions of various samples from the Earth's interior have led those studying the degassing history of the Earth to postulate at least two different mantle reservoirs, i.e., degassed and undegassed mantle [e.g., *Allègre et al.*, 1987; *Azbel and Tolstikhin*, 1990]. Of course, there is no evidence for or against the existence of an undegassed mantle on Venus, or for its association with a lower mantle layer, but the implications for the thermal and magmatic history of the planet of convectively distinct mantle layers have been argued in literature [e.g., *Steinbach and Yuen*, 1992; *Herrick and Parmentier*, 1994; *Phillips and Hansen*, 1994]. A lower bound on the mass of degassed mantle, or equivalently an upper bound on that of undegassed mantle, on Venus can be calculated from the present value for $(^{40}Ar)_A$ and the K concentration in the degassed mantle. A lower bound on present $(^{40}Ar)_A$ of 21 ppm and an upper bound on mantle K concentration of 250 ppm yield a mass for the degassed mantle of 2.6×10^{23} kg, or 8% of the total mass of the bulk silicate planet.

Such a lower bound on the mass of the degassed mantle presumes that no ^{40}Ar is left in the degassed mantle, in other words, that the outgassing rate from the degassed mantle is infinitely high. Thus no upper bound on crustal production rate is obtained if the possibility of distinct degassed and undegassed mantle reservoirs on Venus is considered. For demonstrating the influence of an undegassed mantle on crustal production rate, it is sufficient to show an example of Ar degassing from a degassed mantle which occupies one third of the mass of the bulk silicate planet, after some models of degassing on Earth [*Azbel and Tolstikhin*, 1990] (Figures 4.8a and 4.8b). The time interval between catastrophic resurfacing events is assumed to be 70 Myr in order to achieve a high average crustal production rate. The age of the last catastrophic resurfacing and f_{melt} are

assumed to be 300 Myr and 0.04, respectively. An assumed time interval less than the age of the last catastrophic resurfacing event can be interpreted as indicating either more frequent or more voluminous catastrophic resurfacing events in the past. The upper bound on crustal production rate exceeds 200 $km^3\ yr^{-1}$ in Figure 4.8b, and this upper bound increases as the mass of the degassed mantle decreases. The lower bound on crustal production rate is also raised to 2.9 $km^3\ yr^{-1}$. The depths of the phase transitions marking the mantle transition zone are deeper in Venus than Earth because of lower pressure at a given depth in the smaller planet [*Basaltic Volcanism Study Project*, 1981; *Steinbach and Yuen*, 1992]. If a lower bound on the mass of the degassed mantle on Venus can be taken form the scaled mass of Earth's upper mantle, an upper bound on crustal production rate is obtained. However, the equivalence of the degassed mantle and the upper mantle is by no means certain, even for Earth [e.g., *Allègre et al.*, 1987; *Zhang and Zindler*, 1989].

CONCLUSIONS

A series of magmatic evolution models incorporating episodic catastrophic resurfacing events and modest levels of magmatism between catastrophic episodes is investigated on the basis of outgassing of ^{40}Ar and ^{4}He and the abundances of these species in the present atmosphere of Venus. The fractional degree of melting during the last resurfacing event and the K budget in the bulk silicate planet are estimated to be between 0.02 and 0.16 and between 95 and 250 ppm, respectively, from an analysis of γ-ray measurements of K, U, and Th in Venus surface materials. The atmospheric ^{40}Ar abundance provides an average crustal production rate over approximately the last 3.5 Gyr independent of the relative significance of catastrophic resurfacing episodes and intervening magmatism. Lower and upper bounds on the crustal production rate are 2 and 110 $km^3\ yr^{-1}$ for whole-mantle degassing. However, this upper bound is removed if the Venus mantle has distinct degassed and undegassed portions. The ^{4}He abundance in the present atmosphere is sensitive to the nature of crustal production over the last several hundred million to several billion years because He escapes from the planetary atmosphere. However, further experimental determination of mineral partition coefficients and better estimates of the present ^{4}He abundance in the lower atmosphere are necessary to constrain the recent degassing history on Venus sufficiently well to yield useful constraints from ^{4}He degassing.

APPENDIX A: BULK PARTITION COEFFICIENTS FOR MAXIMUM AND MINIMUM DEGASSING COEFFICIENTS

The bulk coefficients K_{mode} and K_{stoi} in equations (11-18) are described by

$$K_{mode} = \sum_n K_n \xi_n \tag{A1}$$

$$K_{stoi} = \sum_n K_n \eta_n \tag{A2}$$

where K_n is the partition coefficient between the n th mineral and basaltic melt (Tables 4.2, 4.4, and 4.5), and ξ_n and η_n are the modal abundances of mantle material prior to partial melting [*Kinzler and Grove*, 1993] and the stoichiometric coefficient [*Kinzler and Grove*, 1992a] of the n th mineral (Table 4.1), respectively. To derive bulk partition coefficients for maximum and minimum degassing cases, we take partial derivatives of equation (11) with respect to the mineral partition coefficients K_m

$$\frac{\partial C_L}{\partial K_m} = \frac{C_0}{\{\sum_n K_n \xi_n + (1 - \sum_n K_n \eta_n) f_{melt}\}^2} (\eta_m f_{melt} - \xi_m) \tag{A3}$$

For olivine, $\eta_{Ol} < 0$ (Table 4.1), so C_L decreases as K_{Ol} increases. For clinopyroxene, orthopyroxene, and spinel, we make use of an upper bound on f_{melt} estimated at 0.16 from the measured U and Th concentrations in the crust and assumed U and Th abundances in the bulk silicate planet (see text). Because $\eta_n > 0$ and $f_{melt} \leq 0.16 < \xi_n/\eta_n$ for those minerals (Table 4.1), C_L decreases as K_{Cpx}, K_{Opx}, and K_{Sp} increase. For both primitive and depleted spinel lherzolites, C_L is thus lowest when upper bounds on K_{Cpx}, K_{Opx}, K_{Ol} and K_{Sp} are assumed; and C_L is highest when the lower bounds on the partition coefficients are assumed.

For primitive plagioclase lherzolite, ξ_{Plag}/η_{Plag} is 0.121, and for depleted plagioclase lherzolite, ξ_{Plag}/η_{Plag} is 0.112 (Table 4.1). Thus the set of partition coefficients that yield highest or lowest C_L depends on f_{melt}. If $f_{melt} < 0.121$, C_L for primitive plagioclase lherzolite is lowest when upper bounds on K_{Cpx}, K_{Opx}, K_{Ol}, and K_{Plag} are assumed. If $f_{melt} \geq 0.121$, C_L for primitive plagioclase lherzolite is lowest when upper bounds on

K_{Cpx}, K_{Opx}, and K_{Ol}, and a lower bound on K_{Plag}, are assumed. Similarly, two sets of K_{Cpx}, K_{Opx}, K_{Ol}, and K_{Plag} that yield highest C_L for primitive plagioclase lherzolite are obtained depending on whether $f_{melt} < 0.121$ or not. An analogous logic yields highest and lowest C_L for depleted plagioclase lherzolite depending on whether $f_{melt} < 0.112$ or not.

By taking K^K_{mode} and K^K_{stoi} determined from the above procedures, we calculate highest and lowest C_L/C_0 ratios for primitive spinel lherzolite, depleted spinel lherzolite, primitive plagioclase lherzolite, and depleted plagioclase lherzolite as functions of f_{melt} (Figure 4.A1). It is clear from the figure that neither the mantle composition nor the mineral partition coefficients are important for the efficiency of K differentiation for $f_{melt} > 0.05$, because K acts as an incompatible element. For $f_{melt} < 0.05$, melting of both primitive and depleted plagioclase lherzolites result in lower C_L/C_0 ratio than that of spinel lherzolite because K^K_{Plag} is orders of magnitude higher than other mineral partition coefficients (Table 4.2). The calculated C_L/C_0 ratio is less for primitive plagioclase lherzolite than for depleted plagioclase lherzolite (Figure 4.A1). We therefore use the set of partition coefficients for primitive plagioclase lherzolite giving the lowest value of C_L for the case of minimum K differentiation (Table 4.3). The C_L/C_0 ratios calculated for primitive and depleted spinel lherzolite are nearly identical because the mineral partition coefficients are negligible relative to f_{melt} (Figure 4.A1), but that for depleted spinel lherzolite is slightly higher than that for primitive spinel lherzolite. Therefore we adopt the set of partition coefficients for depleted spinel lherzolite giving the highest value of C_L for the case of maximum K differentiation (Table 4.3).

For Ar degassing, we calculate the highest and lowest C_L/C_0 ratios for the four mantle compositions by taking the mineral partition coefficients of Ar from Table 4.4 (Figure 4.A2). Ar is a moderately incompatible element (Table 4.4), so the efficiency of Ar degassing is dependent on the adopted partition coefficients (Figure 4.A2). For a maximum Ar degassing case, we adopt the set of partition coefficients for depleted

plagioclase lherzolite giving the highest value of C_L. For a minimum Ar degassing case, the set for primitive spinel lherzolite giving the lowest value of C_L are adopted (Table 4.3).

For He degassing, only the partition coefficient between olivine and silicate melt has been measured [*Hiyagon and Ozima*, 1986]. For other minerals, we have taken the partition coefficients for Ne [*Broadhurst et al.*, 1992] to be upper bounds on those for He, and we adopt zero lower bounds (Table 4.5). Because there is no measurement of the He or Ne partition coefficient for plagioclase, bulk partition coefficients are estimated here only for spinel lherzolite. C_L is highest when $K^{He}_{mode} = K^{He}_{stoi} = 0$, of course, and C_L is lowest when a primitive spinel lherzolite composition and upper bounds on K_{Cpx}, K_{Opx}, K_{Ol}, and K_{Sp} are assumed (Table 4.3).

APPENDIX B: DIFFUSIVE TRANSFER OF HE WITH A DEPTH-VARIABLE DIFFUSION COEFFICIENT

Production and mass transfer of He in the crust between catastrophic resurfacing events is described by the one-dimensional diffusion equation with depth-variable diffusivity,

$$\frac{\partial C^{He}(t,z)}{\partial t} = \frac{\partial}{\partial z}\left(D^{He}(z)\frac{\partial C^{He}(t,z)}{\partial z}\right) + \frac{4}{238} y^{238}\lambda^{238} C^{238}(t_0)\exp(-\lambda^{238}(t-t_0)) \tag{B1}$$

where z is the depth, C^{He} and C^{238} are the mass concentrations of He and ^{238}U in the crust, respectively, and D^{He} is the depth-variable diffusion coefficient

$$D^{He}(z) = 7.7\times10^{-8}\exp\left(-\frac{50.2\ kJ\ mol^{-1}}{RT(z)}\right),\ \mathrm{m^2\ s^{-1}} \tag{B2}$$

where R is the gas constant (8.314 J K^{-1} mol^{-1}) and $T(z)$ is the crustal temperature profile. Because of the linearity of the diffusion equation, we can treat the three radioactive production terms separately by means of the above equation and superpose the results at

the end. As initial conditions, we assume that catastrophic resurfacing ends at $t = t_0$, that both extrusive and intrusive magma completely degas ^{4}He at the time of catastrophic resurfacing as discussed in the text, i.e., $C^{He}(t_0) = 0$, and that U and Th are uniformly distributed with depth. The boundary conditions $C^{He}(z = 0) = 0$ and $\partial C^{He}/\partial z(z = L) = 0$ are assumed, where L is the crustal thickness.

First we normalize equation (B1) by introducing the non-dimensional variables $t' = \lambda^{235}(t-t_0)$ and $Lz' = z$. By taking the Fourier transform with respect to z' of the normalized equation (B1)

$$\frac{1}{2}\frac{d\mathbf{c}}{dt'} = -\bar{D}\mathbf{d}\mathbf{c} + \frac{4}{238}y^{238}\left[\frac{\exp(-t')}{\left(n-\frac{1}{2}\right)\pi}\right] \tag{B3}$$

where $\mathbf{c}$ is a vector of Fourier coefficients of $C^{He}(t, z)$ normalized by $C^{235}(t_0)$, $\bar{D}$ is the normalized diffusion constant, $\mathbf{d}$ is a matrix representing a convolution of Fourier coefficients of $D^{He}(z)$ and $C^{He}(t, z)$, and the last term is a vector of Fourier coefficients of the production term in equation (B1),

$$c_n = 2\int_0^1 dz' \frac{C^{He}(t', z')}{C^{238}(t_0)}\sin\left(\left(n-\frac{1}{2}\right)\pi z'\right) \tag{B4}$$

$$d_{nm} = \left(n-\frac{1}{2}\right)\left(m-\frac{1}{2}\right)\pi^2 \times\int_0^1 dz' \cos\left(\left(n-\frac{1}{2}\right)\pi z'\right)\exp\left(-\frac{50.2\ kJ\ mol^{-1}}{RT(z')}\right)\cos\left(\left(m-\frac{1}{2}\right)\pi z'\right) \tag{B5}$$

$$\bar{D} = \frac{7.7\times10^{-8}\ m^2\ s^{-1}}{\lambda^{238}L^2} \tag{B6}$$

and

$$C^{He}(t', z') = C^{238}(t_0)\sum_n c_n(t')\sin\left(\left(n-\frac{1}{2}\right)\pi z'\right) \tag{B7}$$

We integrate equation (B5) numerically and approximate the infinite matrix $\mathbf{d}$ by a finite matrix. Equation (B3) is easily solved by taking eigenvalues, μ_k, and eigenvectors, $\mathbf{e}_k$, of the finite matrix, respectively. Equation (B3) is reduced to

$$\frac{1}{2}\frac{d\alpha_k}{dt'} = -\overline{D}\mu_k\alpha_k + \beta_k \exp(-t') \tag{B8}$$

where

$$\alpha_k = \mathbf{c}\cdot\mathbf{e}_k \tag{B9}$$

$$\beta_k = \frac{4y^{238}}{238}\left[\frac{1}{\left(n-\frac{1}{2}\right)\pi}\right]\cdot\mathbf{e}_k \tag{B10}$$

The dots in equations (B8) and (B9) denote inner products. Since $C^{He}(t' = 0) = 0$ for any z', $\mathbf{c} = \mathbf{0}$ and therefore $\alpha_k = 0$ at $t' = 0$. Then equation (B7) can be integrated to yield

$$\alpha_k = \frac{2\beta_k}{\pi}\frac{\exp(-t') - \exp(-2\overline{D}\mu_k t')}{2\overline{D}\mu_k - 1} \tag{B11}$$

Thus

$$\mathbf{c} = \frac{2}{\pi}\sum_k \beta_k \frac{\exp(-t') - \exp(-2\overline{D}\mu_k t')}{2\overline{D}\mu_k - 1}\mathbf{e}_k \tag{B12}$$

The rate of ^{4}He transfer from the crust to the atmosphere, $F^{He}{}_{C\to A}$, is then calculated as a product of $D^{He}(z = 0)$ and $\partial C^{He}/\partial z(z = 0)$,

$$F^{He}_{C\to A} = D^{He}(z=0)\,\mathbf{c}\cdot\left[\left(n-\frac{1}{2}\right)\frac{\pi}{L}\cos\left(\left(n-\frac{1}{2}\right)\pi\frac{z}{L}\right)\right]\times(\textit{surface area}) \tag{B13}$$

Because only the uppermost 1 km or so is important for the diffusive loss of He, as discussed in the text, and because the variation in the diffusion coefficient due to the increase in temperature with depth is small within this depth range, $F^{He}{}_{C\to A}$ does not depend strongly on crustal temperature beneath this skin depth. Therefore we assume a constant linear thermal gradient in the crust, dT/dz, so that

$$T(z) = 750\ \mathrm{K} + \left(\frac{dT}{dz}\right)z \tag{B14}$$

for equations (B2) and (B5). Any effect of spatial and temporal variations in the thermal gradient is negligible because the thermal diffusion coefficient of crustal material is several orders of magnitude greater than the He diffusion coefficient. Further, the ^{4}He

abundance in the crust is zero after catastrophic resurfacing by assumption and the half-life for radioactive production of ^{4}He is considerably longer than the time scale for lithospheric cooling. Therefore the effect of high crustal temperatures after catastrophic resurfacing is also minor. $F^{He}_{C\rightarrow A}$ increases as dT/dz increases, of course. Thus for upper and lower bounds on $F^{He}_{C\rightarrow A}$, we take dT/dz values of 50 and 0 K/km, respectively [*Zuber*, 1987; *Grimm and Solomon*, 1988]. L is assumed to be 50 and 20 km for upper and lower bounds on $F^{He}_{C\rightarrow A}$, but this parameter has little effect on the diffusive flux because diffusive loss occurs only within the uppermost 1 km or so of the crust (see text).

Examples of $F^{He}_{C\rightarrow A}$ so calculated are shown in Figure 4.B1. $F^{He}_{C\rightarrow A}$ increases with time so that a maximum $F^{He}_{C\rightarrow A}$ is achieved by assuming that crust formed 4.55 Gyr ago and that no catastrophic resurfacing occurred subsequently (light shaded area). The calculated values of $F^{He}_{C\rightarrow A}$ are more than about an order of magnitude less than the estimated He escape flux at present (arrow).

REFERENCES

Abe, Y., and T. Matsui, Early evolution of the Earth: Accretion, atmosphere formation, and thermal history, *Proc. Lunar Planet. Sci. Conf. 17th, J. Geophys. Res., 91*, E291-E302, 1986.

Allègre, C. J., T. Staudacher, and P. Sarda, Rare gas systematics: Formation of the atmosphere, evolution and structure of the Earth's mantle, *Earth Planet. Sci. Lett., 81*, 127-150, 1987.

Allègre, C. J., P. Sarda, and T. Staudacher, Speculations about the cosmic origin of He and Ne in the interior of the Earth, *Earth Planet. Sci. Lett., 117*, 229-233, 1993.

Anders, E., and M. Ebihara, Solar-system abundances of the elements, *Geochim. Cosmochim. Acta, 46*, 927-955, 1982.

Arkani-Hamed, J., G. G. Schaber, and R. G. Strom, Constraints on the thermal evolution of Venus inferred from Magellan data, *J. Geophys. Res., 98*, 5309-5315, 1993.

Ayers, J. C., Partitioning and mass-balance relations in lherzolites, *Chem. Geology, 107*, 19-27, 1993.

Azbel, I. Y., and I. N. Tolstikhin, Geodynamics, magmatism, and degassing of the Earth, *Geochim. Cosmochim. Acta, 54*, 139-154, 1990.

Banks, P. M., and G. Kockarts, *Aeronomy*, 430 pp., Academic Press, New York, 1973.

Barsukov, V. L., Venusian igneous rocks, in *Venus Geology, Geochemistry, and Geophysics*, edited by V. L. Barsukov, A. T. Basilevsky, V. P. Volkov, and V. N. Zharkov, pp. 165-176, Univ. Arizona Press, Tucson, 1992.

Basaltic Volcanism Study Project, *Basaltic Volcanism on the Terrestrial Planets*, 1286 pp., Pergamon, New York, 1981.

Basilevsky, A. T., O. V. Nikolaeva, and C. M. Weitz, Geology of the Venera 8 landing site region from Magellan Data: Morphological and geochemical considerations, *J. Geophys. Res., 97*, 16,315-16,355, 1992.

Beattie, P., The generation of uranium series disequilibria by partial melting of spinel peridotite: Constraints from partitioning studies, *Earth Planet. Sci. Lett.*, *117*, 379-391, 1993a.

Beattie, P., Uranium-thorium disequilibria and partitioning on melting of garnet peridotite, *Nature*, *363*, 63-65, 1993b.

Benz, W., W. L. Slattery, and A. G. W. Cameron, The origin of the Moon and the single-impact hypothesis, II, *Icarus*, *71*, 30-45, 1987.

Broadhurst, C. L., M. J. Drake, B. E. Hagee, and T. J. Bernatowicz, Solubility and partitioning of Ar in anorthite, diopside, forsterite, spinel, and synthetic basaltic liquids, *Geochim. Cosmochim. Acta*, *54*, 299-309, 1990.

Broadhurst, C. L., M. J. Drake, B. E. Hagee, and T. J. Bernatowicz, Solubility and partitioning of Ne, Ar, Kr, and Xe in minerals and synthetic basaltic melts, *Geochim. Cosmochim. Acta*, *56*, 709-723, 1992.

Bullock, M. A., D. H. Grinspoon, and J. W. Head III, Venus resurfacing rates: Constraints provided by 3-D Monte Carlo simulation, *Geophys. Res. Lett.*, *19*, 2147-2150, 1993.

Cameron, A. G. W., Elemental and nuclidic abundances in the solar system, in *Essays in Nuclear Astrophysics*, edited by C. Barnes, D. Clayton, and D. Schramm, pp. 23-43, Cambridge Univ. Press, 1982.

Cameron, A. G. W., Origin of the atmospheres of the terrestrial planets, *Icarus*, *56*, 195-201, 1983.

Coffin, M. F., and O. Eldholm, Large igneous provinces: Crustal structure, dimensions, and external consequences, *Rev. Geophys.*, *32*, 1-36, 1994.

Crisp, J. A., Rates of magma emplacement and volcanic output, *J. Volcan. Geotherm. Res.*, *20*, 177-211, 1984.

Dostal, J., and S. Capedri, Partition coefficients of uranium for some rock forming minerals, *Chem. Geology*, *15*, 285-294, 1975.

Dreibus, G., and H. Wänke, Supply and loss of volatile constituents during the accretion of terrestrial planets, in *Origin and Evolution of Planetary and Satellite Atmospheres*, edited by S. K. Atreya, J. B. Pollack, and M. S. Matthews, pp. 268-288, Univ. Arizona Press, Tucson, 1989.

Fegley, B., Jr., and R. G. Prinn, Estimation of the rate of volcanism on Venus from reaction rate measurements, *Nature*, *337*, 55-58, 1989.

Fegley, B., Jr., and A. H. Treiman, Chemistry of atmosphere - surface interactions on Venus and Mars, in *Venus and Mars: Atmospheres, Ionospheres, and Solar Wind Interactions*, edited by J. G. Luhmann, M. Tatrallyay, and R. O. Pepin, *Geophysical Monograph*, *66*, pp. 7-71, Am. Geophys. Union, Washington, D. C., 1992.

Fisher, D. E., Rare gas abundances in MORB, *Geochim. Cosmochim. Acta*, *50*, 2531-2541, 1986.

Fisher, D. E., and M. R. Perfit, Evidence from rare gases for magma-chamber degassing of highly evolved mid-ocean-ridge basalt, *Nature*, *343*, 450-452, 1990.

Freer, R., Diffusion in silicate minerals and glasses: A data digest and guide to the literature, *Contrib. Mineral. Petrol.*, *76*, 440-454, 1981.

Gilbert, L. A., and K. A. Foland, The Mont Saint Hilaire plutonic complex: Occurrence of excess ^{40}Ar and short intrusion history, *Can. J. Earth Sci.*, *23*, 948-958, 1985.

Grimm, R. E., The deep structure of Venusian plateau highlands, *Icarus*, *112*, 89-103, 1994.

Grimm, R. E., and S. C. Solomon, Viscous relaxation of impact crater relief on Venus: Constraints on crustal thickness and thermal gradient, *J. Geophys. Res.*, *93*, 11,911-11,929, 1988.

Grove, T. L., R. J. Kinzler, and W. B. Bryan, Fractionation of mid-ocean ridge basalt (MORB), in *Mantle Flow and Melt Generation at Mid-Ocean Ridges*, edited by J. P. Morgan, D. K. Blackman, and J. M. Sinton, *Geophysical Monograph*, *71*, pp. 281-310, Am. Geophys. Union, Washington, D. C., 1992.

Hamano, Y., and M. Ozima, Earth-atmosphere evolution model based on Ar isotopic data, in *Terrestrial Rare Gases*, edited by E. C. Alexander and M. Ozima, pp. 155-171, Japan Sci. Soc. Press, Tokyo, 1978.

Hart, S. R., and T. Dunn, Experimental cpx/melt partitioning of 24 trace elements, *Contrib. Mineral. Petrol., 113*, 1-8, 1993.

Hart, S. R., and A. Zindler, In search of a bulk-earth composition, *Chem. Geology, 57*, 247-267, 1986.

Hartmann, W. K., Moon Origin: The impact-trigger hypothesis, in *Origin of the Moon*, edited by W. K. Hartmann, R. J. Phillips, and G. J. Taylor, pp. 579-608, Lunar and Planetary Institute, Houston, 1986.

Head, J., A. Basilevsky, and L. Wilson, Evolution of volcanic styles on Venus (abstract), *Eos Trans. AGU, 76*, S191, 1995.

Head, J. N., and T. D. Swindle, Argon diffusion: Implications for meteorites from Venus and Mercury and for Venus degassing history (abstract), *Lunar Planet Sci., 26*, 571-572, 1995.

Head, J. W., L. S. Crumpler, J. C. Aubele, J. E. Guest, and R. S. Saunders, Venus volcanism: Classification of volcanic features and structures, associations, and global distribution from Magellan data, *J. Geophys. Res., 97*, 13,153-13,197, 1992.

Herrick, D. L., and E. M. Parmentier, Episodic large-scale overturn of two-layer mantles in terrestrial planets, *J. Geophys. Res., 99*, 2053-2062, 1994.

Herrick, R. R., Resurfacing history of Venus, *Geology, 22*, 703-706, 1994.

Herrick, R. R., and R. J. Phillips, Implications of a global survey of Venusian impact craters, *Icarus, 111*, 387-416, 1994.

Hilton, D. R., K. Hammerschmidt, G. Loock, and H. Friedrichsen, Helium and argon isotope systematics of the central Lau Basin and Valu Fa Ridge: Evidence of crust/mantle interactions in a back-arc basin., *Geochim. Cosmochim. Acta, 57*, 2819-2841, 1993.

Hiyagon, H., Constraints on rare gas partition coefficients from analysis of olivine-glass from a picritic mid-ocean ridge basalt — Comments, *Chem. Geology, 112*, 119-122, 1994.

Hiyagon, H., and M. Ozima, Partition of noble gases between olivine and basalt melt, *Geochim. Cosmochim. Acta, 50*, 2045-2057, 1986.

Hoffman, J. H., R. R. Hodges, T. M. Donahue, and M. B. McElroy, Composition of the Venus lower atmosphere from the Pioneer Venus mass spectrometer, *J. Geophys. Res., 85*, 7882-7890, 1980.

Holland, H. D., *The Chemical Evolution of the Atmosphere and Oceans*, 582 pp., Princeton Univ. Press, 1984.

Honda, M., K. Kurita, Y. Hamano, and M. Ozima, Experimental studies of He and Ar degassing during rock fracturing, *Earth Planet. Sci. Lett., 59*, 429-436, 1982.

Houghton, J. T., *The Physics of Atmospheres*, 271 pp., Cambridge Univ. Press, 1986.

Humayun, M., and R. N. Clayton, Precise determination of the isotopic composition of potassium: Application to terrestrial rocks and lunar soils, *Geochim. Cosmochim. Acta, 59*, 2115-2130, 1995a.

Humayun, M., and R. N. Clayton, Potassium isotope cosmochemistry: Genetic implications of volatile element depletion, *Geochim. Cosmochim. Acta, 59*, 2131-2148, 1995b.

Hunten, D. M., The escape of light gases from planetary atmospheres, *J. Atmos. Sci., 30*, 1481-1494, 1973.

Hunten, D. M., Atmospheric evolution of the terrestrial planets, *Science, 259*, 915-920, 1993.

Hunten, D. M., and T. M. Donahue, Hydrogen loss from the terrestrial planets, *Ann. Rev. Earth Plant. Sci., 4*, 265-292, 1976.

Hunten, D. M., T. M. Donahue, J. C. G. Walker, and J. F. Kasting, Escape of atmospheres and loss of water, in *Origin and Evolution of Planetary and Satellite*

Atmospheres, edited by S. K. Atreya, J. B. Pollack, and M. S. Matthews, pp. 386-422, Univ. Arizona Press, Tucson, 1989.

Ivanov, M. A., and A. T. Basilevsky, Density and morphology of impact craters on tessera terrain, Venus, *Geophys. Res. Lett.*, *20*, 2579-2582, 1993.

Kargel, J. S., and J. S. Lewis, The composition and early evolution of Earth, *Icarus*, *105*, 1-25, 1993.

Kargel, J. S., G. Komatsu, V. R. Baker, and R. G. Strom, The volcanology of Venera and VEGA landing sites and the geochemistry of Venus, *Icarus*, *103*, 253-275, 1993.

Kasting, J. F., Runaway and moist greenhouse atmosphere and the evolution of Earth and Venus, *Icarus*, *74*, 472-494, 1988.

Kasting, J. F., and J. B. Pollack, Loss of water from Venus. I. Hydrodynamic escape of hydrogen, *Icarus*, *53*, 479-508, 1983.

Kaula, W. M., Thermal evolution of Earth and Moon growing by planetesimal impacts, *J. Geophys. Res.*, *84*, 999-1008, 1979.

Kaula, W. M., The beginning of the Earth's thermal evolution, in *The Continental Crust and Its Mineral Deposits*, edited by D. W. Strangway, pp. 25-34, Geol. Assoc. Can. Spec. Pap. 20, Waterloo, Ont., 1980.

Kaula, W. M., Venus: A contrast in evolution to Earth, *Science*, *247*, 1191-1196, 1990.

Kinzler, R. J., and T. L. Grove, Primary magmas of mid-ocean ridges basalts 1. Experiments and methods, *J. Geophys. Res.*, *97*, 6885-6906, 1992a.

Kinzler, R. J., and T. L. Grove, Primary magmas of mid-ocean ridges basalts 2. Applications, *J. Geophys. Res.*, *97*, 6907-6926, 1992b.

Kinzler, R. J., and T. L. Grove, Corrections and further discussion of the primary magmas of mid-ocean ridge basalts, 1 and 2, *J. Geophys. Res.*, *98*, 22,339-22,347, 1993.

Konopliv, A. S., and W. L. Sjogren, Venus spherical harmonic gravity model to degree and order 60, *Icarus*, *112*, 42-54, 1994.

Krasnopolsky, V. A., Total injection of water vapor into Venus atmosphere, *Icarus*, *62*, 221-229, 1985.

Kumar, S., D. M. Hunten, and J. B. Pollack, Nonthermal escape of hydrogen and deuterium from Venus and implications for loss of water, *Icarus*, *55*, 369-389, 1983.

Landoll, J. D., K. A. Foland, and C. M. B. Henderson, Excess argon in amphiboles from fluid interaction and short intrusion interval at the epizonal Maranguzi complex, Zimbabwe, *J. Geophys. Res.*, *94*, 4053-4069, 1989.

LaTourrette, T. Z., and D. S. Burnett, Experimental determination of U and Th partitioning between clinopyroxene and natural and synthetic basaltic liquid, *Earth Planet. Sci. Lett.*, *110*, 227-244, 1992.

LaTourrette, T. Z., A. K. Kennedy, and G. J. Wasserburg, Thorium-uranium fractionation by garnet: Evidence for a deep source and rapid rise of oceanic basalts, *Science*, *261*, 739-742, 1993.

Marty, B., and P. Lussiez, Constraints on rare gas partition coefficients from analysis of olivine-glass from a picritic mid-ocean ridge basalt, *Chem. Geology*, *106*, 1-7, 1993.

Marty, B., and P. Lussiez, Constraints on rare gas partition coefficients from analysis of olivine-glass from a picritic mid-ocean ridge basalt — Reply, *Chem. Geology*, *112*, 122-127, 1994.

Massie, S. T., D. M. Hunten, and D. R. Sowell, Day and night models of the Venus thermosphere, *J. Geophys. Res.*, *88*, 3955-3969, 1983.

Masson, E. A., and T. R. Marrero, The diffusion of atoms and molecules, in *Advances in Atomic and Molecular Physics*, edited by D. R. Bates and I. Esterman, *6*, pp. 155-232, Academic Press, New York, 1970.

Matsui, T., and Y. Abe, Impact-induced atmospheres and oceans on Earth and Venus, *Nature*, *322*, 526-528, 1986.

Matsui, T., and E. Tajika, Early environmental evolution of Venus (abstract), *Lunar Planet. Sci.*, *22*, 863-864, 1991.

Matsui, T., and E. Tajika, Comparative study of crustal production rates of Mars, Venus, and the Earth (abstract), *Lunar Planet. Sci., 26*, 909-910, 1995.

McDonough, W. F., S.-S. Sun, A. E. Ringwood, E. Jagoutz, and A. W. Hofmann, Potassium, rubidium, and cesium in the Earth and Moon and the evolution of the mantle of the Earth, *Geochim. Cosmochim. Acta, 56*, 1001-1012, 1992.

McDougall, I., and T. M. Harrison, *Geochronology and Thermochronology by the $^{40}Ar/^{39}Ar$ Method*, 212 pp., Oxford University Press, New York, 1988.

McElroy, M. B., and M. J. Prather, Noble gases in the terrestrial planets, *Nature, 293*, 535-539, 1981.

McElroy, M. B., M. J. Prather, and J. M. Rodriguez, Loss of oxygen from Venus, *Geophys. Res. Lett., 9*, 649-651, 1982.

McGovern, P. J., and G. Schubert, Thermal evolution of the Earth: Effects of volatile exchange between atmosphere and interior, *Earth Planet. Sci. Lett., 96*, 27-37, 1989.

McKenzie, D., P. G. Ford, C. Johnson, B. Parsons, D. Sandwell, S. Saunders, and S. C. Solomon, Features on Venus generated by plate boundary processes, *J. Geophys. Res., 97*, 13,533-13,544, 1992.

Melosh, H., and C. P. Sonett, When worlds collide: Jetted vapor plumes and Moon's origin, in *Origin of the Moon*, edited by W. K. Hartmann, P. R. J., and G. J. Taylor, pp. 621-642, Lunar and Planetary Science Institute, Houston, 1986.

Namiki, N., and S. C. Solomon, Impact crater densities on volcanoes and coronae on Venus: Implications for volcanic resurfacing, *Science, 265*, 929-933, 1994.

Niemann, H. B., W. T. Kasprzak, A. E. Hedin, D. M. Hunten, and N. W. Spencer, Mass spectrometric measurements of the neutral gas composition of the thermosphere and exosphere of Venus, *J. Geophys. Res., 85*, 7817-7827, 1980.

Onstott, T. C., V. B. Sisson, and D. L. Turner, Initial argon in amphibole from the Chugach mountains, southern Alaska, *J. Geophys. Res., 94*, 4361-4372, 1989.

Owen, T., A. Bar-Nun, and I. Kleinfeld, Possible cometary origin of heavy noble gases in the atmospheres of Venus, Earth and Mars, *Nature, 358*, 43-46, 1992.

Ozima, M., and F. A. Podosek, *Noble Gas Chemistry*, 367 pp., Cambridge Univ. Press, 1983.

Ozima, M., and Y. Takigami, Activation energy for thermal release of Ar from some DSDP submarine rocks, *Geochim. Cosmochim. Acta, 44*, 141-144, 1979.

Ozima, M., and S. Zashu, Primitive helium in diamonds, *Science, 219*, 1067-1068, 1983.

Parmentier, E. M., and P. C. Hess, Chemical differentiation of a convective planetary interior: Consequences for a one plate planet such as Venus, *Geophys. Res. Lett., 20*, 2015-2018, 1992.

Pepin, R. O., On the origin and early evolution of terrestrial planet atmospheres and meteoritic volatiles, *Icarus, 92*, 2-79, 1991.

Phillips, R. J., and V. L. Hansen, Tectonic and magmatic evolution of Venus, *Ann. Rev. Earth Planet. Sci., 22*, 597-654, 1994.

Phillips, R. J., R. F. Raubertas, R. E. Arvidson, I. C. Sarkar, R. R. Herrick, N. Izenberg, and R. E. Grimm, Impact craters and Venus resurfacing history, *J. Geophys. Res., 97*, 15,921-15,948, 1992.

Pollack, J. B., and D. C. Black, Noble gases in planetary atmospheres: Implications for the origin and evolution of atmospheres, *Icarus, 51*, 169-198, 1982.

Prather, M. J., and M. B. McElroy, Helium on Venus: Implications for uranium and thorium, *Science, 220*, 410-411, 1983.

Price, M., Resurfacing history of the Venusian plains based on distribution of impact craters (abstract), *Lunar Planet. Sci., 26*, 1143-1144, 1995a.

Price, M. H., Estimates of global magmatic flux on Venus based on geologic mapping and dating of volcanism (abstract), *Eos Trans. AGU, 76*, S190-S191, 1995b.

Price, M., and J. Suppe, Mean age of rifting and volcanism on Venus deduced from impact crater densities, *Nature, 372*, 756-759, 1994.

Safronov, V. S., The heating of the Earth during its formation, *Icarus*, *33*, 3-12, 1978.

Sano, Y., Y. Nakamura, H. Wakita, and T. Ishii, Light noble gasses in basalt glass from Mariana Trough, *Geochim. Cosmochim. Acta*, *50*, 2429-2432, 1986.

Sasaki, S., and K. Nakazawa, Origin of isotopic fractionation of terrestrial Xe: Hydrodynamic fractionation during escape of the primordial H_2-He atmosphere, *Earth Planet. Sci. Lett.*, *89*, 323-334, 1988.

Schaber, G. G., R. G. Strom, H. J. Moore, L. A. Soderblom, R. L. Kirk, D. J. Chadwick, D. D. Dawson, L. R. Gaddis, J. M. Boyce, and J. Russell, Geology and distribution of impact craters on Venus: What are they telling us?, *J. Geophys. Res.*, *97*, 13,257-13,301, 1992.

Schubert, G., D. L. Turcotte, S. C. Solomon, and N. H. Sleep, Coupled evolution of the atmospheres and interiors of planets and satellites, in *Origin and Evolution of Planetary and Satellite Atmospheres*, edited by S. K. Atreya, J. B. Pollack, and M. S. Matthews, pp. 450-483, Univ. Arizona Press, Tucson, 1989.

Sclater, J. G., C. Jaupart, and D. Galson, The heat flow through oceanic and continental crust and heat loss of the Earth, *Rev. Geophys. Space Phys.*, *18*, 269-311, 1980.

Simons, M., B. H. Hager, and S. C. Solomon, Global variations in the geoid/topography admittance of Venus, *Science*, *264*, 798-803, 1994.

Sleep, N. H., Thermal history and degassing of the Earth: Some simple calculations, *J. Geology*, *87*, 671-686, 1979.

Smith, J. V., and W. L. Brown, *Feldspar Minerals*, 828 pp., Springer-Verlag, Berlin, 1988.

Solomon, S. C., and J. W. Head, Mechanisms for lithospheric heat transport on Venus: Implications for tectonics and volcanism, *J. Geophys. Res.*, *87*, 9236-9246, 1982.

Solomon, S. C., and J. W. Head, Fundamental issues in the geology and geophysics of Venus, *Science*, *252*, 252-260, 1991.

Solomon, S. C., J. W. Head, W. M. Kaula, D. McKenzie, B. Parsons, R. J. Phillips, G. Schubert, and M. Talwani, Venus tectonics: Initial analysis from Magellan, *Science*, *252*, 297-312, 1991.

Solomon, S. C., S. E. Smrekar, D. L. Bindschadler, R. E. Grimm, W. M. Kaula, G. E. McGill, R. J. Phillips, R. S. Saunders, G. Schubert, S. W. Squyres, and E. R. Stofan, Venus tectonics: An overview of Magellan observations, *J. Geophys. Res.*, *97*, 13,199-13,255, 1992.

Steinbach, V., and D. A. Yuen, The effects of multiple phase transitions on venusian mantle convection, *Geophys. Res. Lett.*, *19*, 2243-2246, 1992.

Strom, R. G., G. G. Schaber, and D. D. Dawson, The global resurfacing of Venus, *J. Geophys. Res.*, *99*, 10,899-10,926, 1994.

Surkov, Yu. A., F. F. Kirnozov, V. N. Glazov, A. G. Dunchenko, and L. P. Tatsii, The content of natural radioactive elements in Venusian rock as determined by Venera 9 and Venera 10, *Kosmich. Issled.*, Engl. Transl., *14*, 618-622, 1977.

Surkov, Yu. A., V. L. Barsukov, L. P. Moskalyeva, V. P. Kharyukova, and A. L. Kemurdzhian, New data on the composition, structure, and properties of Venus rock obtained by Venera 13 and Venera 14, *Proc. Lunar Planet. Sci. Conf. 14th, J. Geophys. Res.*, *89*, B393-B402, 1984.

Surkov, Yu. A., L. P. Moskalyova, V. P. Kharyukova, A. D. Dudin, G. G. Smirnov, and S. Y. Zaitseva, Venus rock composition at the Vega 2 landing site, *Proc. Lunar Planet. Sci. Conf. 17th, J. Geophys. Res.*, *91*, E215-218, 1986.

Surkov, Yu. A., F. F. Kirnozov, V. N. Glazov, A. G. Dunchenko, L. P. Tatsy, and O. P. Sobornov, Uranium, thorium, and potassium in the Venusian rocks at the landing sites of Vega 1 and 2, *Proc. Lunar Planet. Sci. Conf. 17th, J. Geophys. Res.*, *92*, E537-E540, 1987.

Tajika, E., Evolution of the atmosphere and ocean of the Earth: Global geochemical cycles of C, H, O, N, and S, and degassing history coupled with thermal history, Ph. D. thesis, Univ. Tokyo, 416 pp., 1992.

Tajika, E., and T. Matsui, Evolution of terrestrial proto-CO_2 atmosphere coupled with thermal history of the earth, *Earth Planet. Sci. Lett.*, *113*, 251-266, 1992.

Tajika, E., and T. Matsui, Evolution of seafloor spreading rate based on ^{40}Ar degassing history, *Geophys. Res. Lett.*, *20*, 851-854, 1993.

Takahashi, E., Melting of a dry peridotite KLB-1 up to 14 Gpa: Implications on the origin of peridotitic upper mantle, *J. Geophys. Res.*, *91*, 9367-9382, 1986.

Tolstikhin, I. N., V. S. Dokuchaeva, I. L. Kamenskt, and Y. V. Amelin, Juvenile helium in ancient rocks: II. U-He, K-Ar, Sm-Nd, and Rb-Sr systematics in the Monche Pliton. $^3He/^4He$ ratios frozen in uranium-free ultramafic rocks, *Geochim. Cosmochim. Acta*, *56*, 987-999, 1992.

Turcotte, D. L., An episodic hypothesis for Venusian tectonics, *J. Geophys. Res.*, *98*, 17,061-17,068, 1993.

Turcotte, D. L., and G. Schubert, Tectonic implications of radiogenic noble gases in planetary atmospheres, *Icarus*, *74*, 36-46, 1988.

Volkov, V. P., and M. Y. Frenkel, The modeling of Venus' degassing in terms of K-Ar system, *Earth Moon Planets*, *62*, 117-129, 1993.

von Zahn, U., K. H. Fricke, D. M. Hunten, D. Krankowsky, K. Mauersberger, and A. O. Nier, The upper atmosphere of Venus during morning conditions, *J. Geophys. Res.*, *85*, 7829-7840, 1980.

von Zahn, U., S. Kumar, H. Niemann, and R. Prinn, Composition of the Venus atmosphere, in *Venus*, edited by D. M. Hunten, L. Colin, T. M. Donahue, and V. I. Moroz, pp. 299-430, Univ. Arizona Press, Tucson, 1983.

Weitz, C. M., and A. T. Basilevsky, Magellan observations of the Venera and Vega landing site regions, *J. Geophys. Res.*, *98*, 17,069-17,097, 1993.

Westrich, H. R., H. W. Stockman, and J. C. Eichelberger, Degassing of rhyolitic magma during ascent and emplacement, *J. Geophys. Res.*, *93*, 6503-6511, 1988.

Wetherill, G. W., Numerical calculations relevant to the accumulation of the terrestrial planets, in *The Continental Crust and Its Mineral Deposits*, edited by D. W. Strangway, pp. 3-24, Geol. Assoc. Can. Spec. Pap. 20, 1980.

Wetherill, G. W., Solar wind origin of ^{36}Ar on Venus, *Icarus*, *46*, 70-80, 1981.

Wetherill, G. W., Provenance of the terrestrial planets, *Geochim. Cosmochim. Acta*, *58*, 4513-4520, 1994.

Wetherill, G. W., and G. R. Stewart, Accumulation of a swarm of small planetesimals, *Icarus*, *77*, 330-357, 1989.

Williams, D. R., and V. Pan, Internally heated mantle convection and the thermal and degassing history of the Earth, *J. Geophys. Res.*, *97*, 8937-8950, 1992.

Wörner, G., J. Beusen, N. Duchateau, R. Gijbels, and H. Schmincke, Trace element abundances and mineral/melt distribution coefficients in phonolites from Laacher See volcano (Germany), *Contrib. Mineral. Petrol.*, *84*, 152-173, 1983.

Yurimoto, H., and S. Sueno, Anion and cation partitioning between olivine, plagioclase phenocrysts and the host magma: A new application of ion microprobe study, *Geochem. J.*, *18*, 85-94, 1984.

Yurimoto, H., and S. Sueno, Anion and cation partitioning between three pyroxenes, chrome spinel phenocrysts and the host boninite magma: An ion microprobe study, *Geochem. J.*, *21*, 85-104, 1987.

Zahnle, K. J., and J. C. G. Walker, The evolution of solar ultraviolet luminosity, *Rev. Geophys. Space Phys.*, *20*, 280-292, 1982.

Zeitler, P. K., Argon diffusion in partially outgassed alkali feldspars: Insights for $^{40}Ar/^{39}Ar$ analysis, *Chem. Geology*, *65*, 167-181, 1987.

Zhang, Y., and A. Zindler, Noble gas constraints on the evolution of the Earth's atmosphere, *J. Geophys. Res.*, *94*, 13,719-13,737, 1989.

Zhang, Y., and A. Zindler, Distribution and evolution of carbon and nitrogen in Earth, *Earth Planet. Sci. Lett.*, *117*, 331-345, 1993.

Zuber, M. T., Constraints on lithospheric structure of Venus from mechanical models and tectonic surface features, *Proc. Lunar Planet. Sci. Conf. 17th, J. Geophys. Res.*, *92*, E541-E551, 1987.

Table 4.1. Mantle modal abundances and stoichiometric coefficients [after *Kinzler and Grove*, 1992a, 1993].

Mineral§	Mantle Composition				Stoichiometric Coefficient†	
	Spinel Lherzolite		Plagioclase Lherzolite		Spinel	Plagioclase
	Primitive	Depleted	Primitive	Depleted	Lherzolite	Lherzolite
Cpx	0.19	0.182	0.13	0.128	0.82	0.28
Opx	0.28	0.28	0.26	0.261	0.4	0.19
Ol	0.5	0.508	0.54	0.546	-0.3	-0.05
Sp	0.03	0.03	—	—	0.08	—
Plag	—	—	0.07	0.065	—	0.58

§ Cpx, clinopyroxene; Opx, orthopyroxene; Ol, olivine; Plag, plagioclase; Sp, spinel.

† Stoichiometric coefficients are same for both primitive and depleted mantle compositions.

Table 4.2. Measured partition coefficients for K between major minerals and silicate melt.

Mineral	K^K	References
Cpx	$3.67 - 7.2 \times 10^{-3}$	*Yurimoto and Sueno* [1987], *Hart and Dunn* [1992]
Opx	$2.96 - 6.48 \times 10^{-4}$	*Yurimoto and Sueno* [1987]
Ol	2.47×10^{-3}	*Yurimoto and Sueno* [1984]
Plag	0.123 - 0.27	*Yurimoto and Sueno* [1984], *Kinzler and Grove* [1992a]
Sp	3.66×10^{-5}	*Yurimoto and Sueno* [1987]

Table 4.3. Bulk partition coefficients for maximum and minimum degassing models.

		f_{melt}	K_{mode}	K_{stoi}
K	max		0.002	0.0024
	min	≤ 0.121	0.021	0.16
		> 0.121	0.011	0.073
Ar	max	≤ 0.112	0.053	0.098
		> 0.112	0.12	0.68
	min		0.51	1.1
He	max		0.0	0.0
	min		0.21	0.44
U			0.0012	0.0012
Th			0.00029	0.00029

Table 4.4. Measured or inferred partition coefficients for Ar between major minerals and silicate melt.

Mineral	K^{Ar}	References
Cpx	0.15 - 0.84	*Broadhurst et al.* [1992]
Opx	0 - 0.84	See text.
Ol	0.05 - 0.15	*Hiyagon and Ozima* [1986]
Plag	0.1 - 1.1	*Broadhurst et al.* [1990]
Sp	0.04 - 1.3	*Broadhurst et al.* [1992]

Table 4.5. Measured or inferred partition coefficients for He between major minerals and silicate melt.

Mineral	K^{He}	References
Cpx	0 - 0.37	D^{Ne}_{Cpx} in *Broadhurst et al.* [1992]
Opx	0 - 0.37	See text.
Ol	0 - 0.07	*Hiyagon and Ozima* [1986]
Plag	—	—
Sp	0 - 0.088	D^{Ne}_{Sp} in *Broadhurst et al.* [1992]

Table 4.6. Concentrations of radioactive elements at the surface of Venus measured by Venera and Vega landers [after *Surkov et al.*, 1987].

	K, wt %	U, ppm	Th, ppm
Vega 1 (1984)	0.45 ± 0.22	0.64 ± 0.47	1.5 ± 1.2
Vega 2 (1984)	0.40 ± 0.20	0.68 ± 0.38	2.0 ± 1.0
Venera 8 (1972)	4.0 ± 1.2	2.2 ± 0.7	6.5 ± 0.2
Venera 9 (1975)	0.47 ± 0.08	0.60 ± 0.16	3.65 ± 0.42
Venera 10 (1975)	0.30 ± 0.16	0.46 ± 0.26	0.70 ± 0.34

FIGURE CAPTIONS

Figure 4.1. (a) Nominal estimates of fractional degree of mantle melting calculated from γ-ray measurements of U (filled circles) and Th (crosses) in Venus surface materials (Table 4.6) [*Surkov et al.*, 1987] and assumed mantle concentrations of the radioactive elements. Uncertainties both in the γ-ray measurements [*Surkov et al.*, 1987] and in the mantle concentrations of U and Th (see text) are taken into account. (b) Estimates of the K concentration in the bulk silicate fraction of Venus for each sample in (a) and from γ-ray measurements of the K concentration in the surface materials (Table 4.6) [*Surkov et al.*, 1987]. The range of f_{melt} indicated for each sample corresponds to the overlap of the two horizontal lines for U and Th in (a). Line type agrees with (a): Vega 1 (dotted lines), Vega 2 (thin solid lines), Venera 8 (dot-dash lines), Venera 9 (thick solid lines), and Venera 10 (dashed lines).

Figure 4.2. Evolution of K and Ar abundances in mantle, crustal, and atmospheric reservoirs. The assumed crustal production parameters are given in the text. For a lower limit on $(K)_{bulk}$, a present $(^{40}Ar)_A$ abundance of 21 ppm, a maximum of Ar degassing and a minimum of K differentiation (Table 4.3) are assumed (thick dashed lines); for an upper limit on $(K)_{bulk}$, a present crustal K concentration of 0.67% and minimum K differentiation (Table 4.3) are assumed (thick solid lines). Allowable ranges of $(^{40}K)_M$ (vertically hatched area), $(^{40}Ar)_M$ (light shaded area), $(^{40}K)_C$ (diagonally hatched area), $(^{40}Ar)_C$ (horizontally hatched area), and $(^{40}Ar)_A$ (dark shaded area) are also shown. Values of K^{Ar}_{mode} of 0.098 and K^{Ar}_{stoi} of 0.1 are assumed for the upper limit on $(K)_{bulk}$ (thick solid lines) so that the present $(^{40}Ar)_A$ does not exceed an observed upper bound of 45 ppm.

Figure 4.3. (a) Contours of lower (dashed lines) and upper (solid lines) limits on present $(K)_{bulk}$ calculated from Ar degassing models parameterized by the volume of magmatism during each catastrophic resurfacing event averaged over the planetary

surface (ordinate) and the rate of magmatism between catastrophic events (abscissa). Other crustal production parameters are assumed to be the same as in Figure 4.2. The shaded area represents crustal production models rejected because the calculated minimum $(K)_{bulk}$ is higher than 250 ppm, an upper bound derived from crustal K, U, and Th concentrations (Figure 4.1b). (b) Upper and lower limits on $(K)_{bulk}$ as functions of average crustal production rate. Allowable ranges of $(K)_{bulk}$ and average crustal production rate are shown by the shaded area.

Figure 4.4. Upper and lower limits on $(K)_{bulk}$ as functions of average crustal production rate. Crustal production parameters are assumed to be the same as in Figure 4.3, but the characteristic time interval of catastrophic resurfacing events is (a) 200 Myr, or (b) 1 Gyr, or (c) $f_{melt} = 0.02$. Allowable ranges of $(K)_{bulk}$ and average crustal production rate are shown by shaded areas.

Figure 4.5. (a) Contours of lower (dashed lines) and upper (solid lines) limits on $(K)_{bulk}$ for Ar degassing models parameterized by the volume of magmatism during each catastrophic resurfacing event averaged over the planetary surface (ordinate) and the rate of magmatism between catastrophic events (abscissa) and (b) upper and lower limits on $(K)_{bulk}$ as functions of average crustal production rate. Crustal production parameters are the same as in Figures 3a and 3b except f_{melt} is assumed to be 0.16. Ar degassing models with calculated lower bounds on $(K)_{bulk}$ higher than 250 ppm are shown by shaded areas in (a) and are not included in (b).

Figure 4.6. (a) Upper (solid lines) and lower (dashed lines) limits on ^{4}He abundances in the mantle (diagonally hatched area), crust (horizontally hatched area), and atmosphere (shaded area) calculated by assuming $(^4He)_A(t_P) = 12$ ppm. (b) Upper (solid lines) and lower (dashed lines) limits on atmospheric ^{4}He for $(^4He)_A(t_P)$ equal to 4 ppm (diagonally hatched area) and 36 ppm (shaded area). The assumed value for $(^4He)_A(t_P)$ for each atmospheric evolution set is indicated by arrows on the right.

Figure 4.7. Ranges of plausible crustal production models calculated from ^{4}He degassing/escape. Upper and lower limits on crustal production are shown by dashed and solid lines, respectively, for a present ^{4}He abundance of 4, 12, and 36 ppm. Shaded areas represent crustal production models that fail to yield an internally consistent ^{4}He degassing/escape history within acceptable ranges of He degassing parameters. Models are as follows: (a) crustal production parameters as in Figure 4.3a; (b) similar parameters except t_{HO} = 1 Gyr; (c) same as in (a) except the age of the last catastrophic resurfacing event is 500 Myr; (d) same as in (a) except f_{melt} = 0.16; (e) same as in (a) except the characteristic time interval between catastrophic resurfacing events is 200 Myr. The dotted line in (d) denotes a constraint on maximum crustal production from the crustal U concentration (see text).

Figure 4.8. (a) Contours of lower (dashed lines) and upper (solid lines) bounds on $(K)_{bulk}$ for Ar degassing models parameterized by the volume of magmatism during each catastrophic resurfacing event averaged over the planetary surface (ordinate) and rate of magmatism between catastrophic events (abscissa). (b) Upper and lower bounds on $(K)_{bulk}$ as functions of average crustal production rate. The mass of the degassed mantle is assumed to be one third of that of the bulk silicate planet.

Figure 4.A1. Highest and lowest C_L/C_0 ratios for K differentiation as functions of f_{melt}. Assumed mantle compositions are primitive spinel lherzolite (dashed lines), depleted spinel lherzolite (dash-dot lines), primitive plagioclase lherzolite (dotted lines), and depleted plagioclase lherzolite (solid lines). Results for primitive and depleted spinel lherzolites are so close that they are indistinguishable in this figure.

Figure 4.A2. Highest and lowest C_L/C_0 ratios for Ar degassing as functions of f_{melt}. Assumed mantle compositions are primitive spinel lherzolite (dashed lines), depleted

spinel lherzolite (dash-dot lines), primitive plagioclase lherzolite (dotted lines), and depleted plagioclase lherzolite (solid lines).

Figure 4.B1. Maximum and minimum diffusive fluxes (solid and dashed lines, respectively) of ^{4}He from crust to atmosphere. Crust is assumed to have formed 4.55 Gyr ago (light shaded area) or 300 Myr ago (dark shaded area). For the maximum diffusive flux, a thermal gradient dT/dz of 50 K km^{-1}, a crustal thickness L of 50 km, and crustal concentrations of U and Th of 1.11 and 4.07 ppm, respectively (Table 4.6), are assumed. For the minimum diffusive flux, dT/dz = 0 K km^{-1}, L = 20 km, and crustal concentrations of U and Th of 0.17 and 0.30 ppm, respectively (Table 4.6), are assumed. The arrow denotes the present escape flux of ^{4}He.

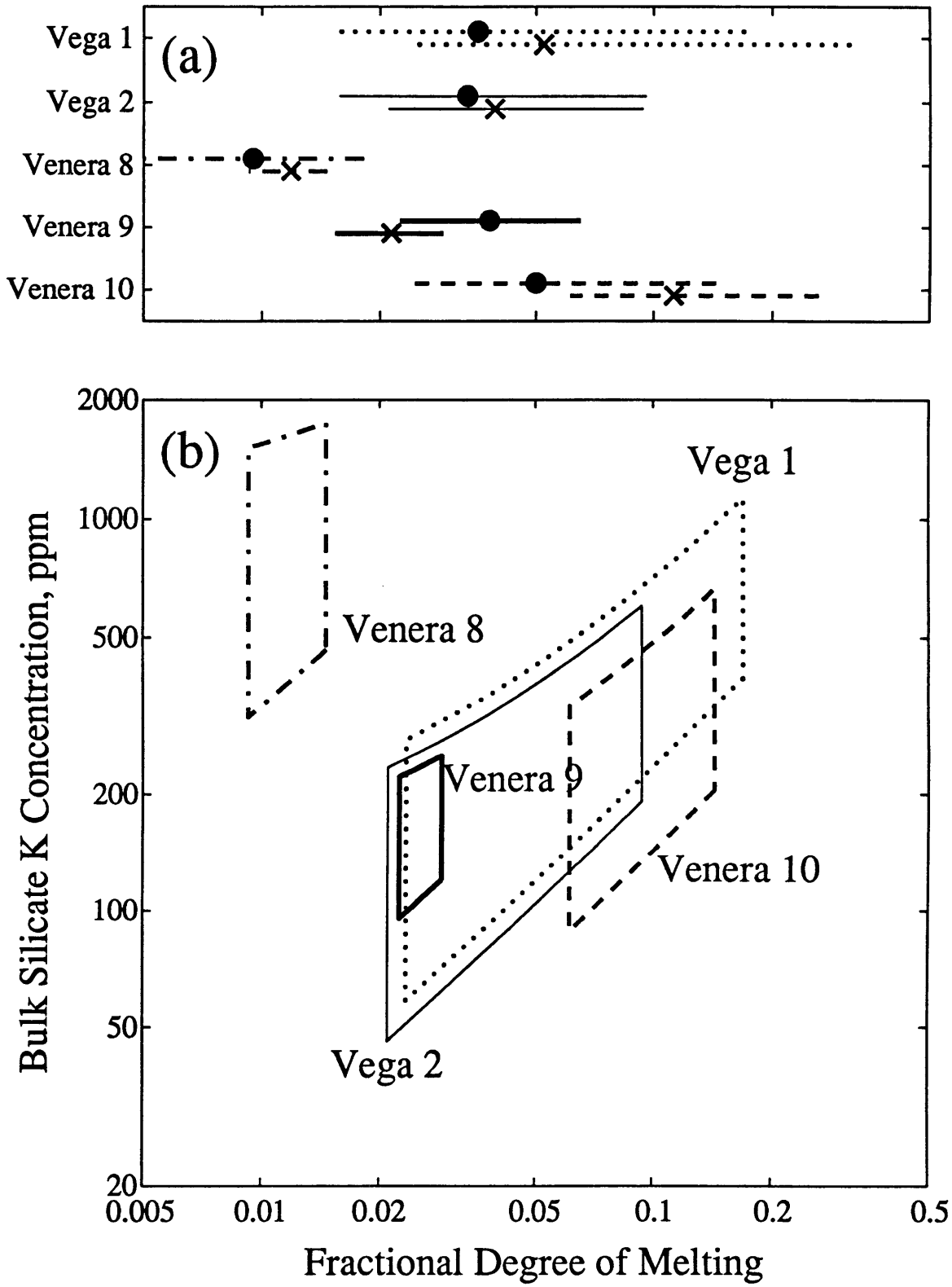
(a)
Vega 1
Vega 2
Venera 8
Venera 9
Venera 10
(b)
Vega 1
Venera 8
Venera 9
Venera 10
Vega 2
Bulk Silicate K Concentration, ppm
2000
1000
500
200
100
50
20
0.005
0.01
0.02
0.05
0.1
0.2
0.5
Fractional Degree of Melting

Figure 4.1

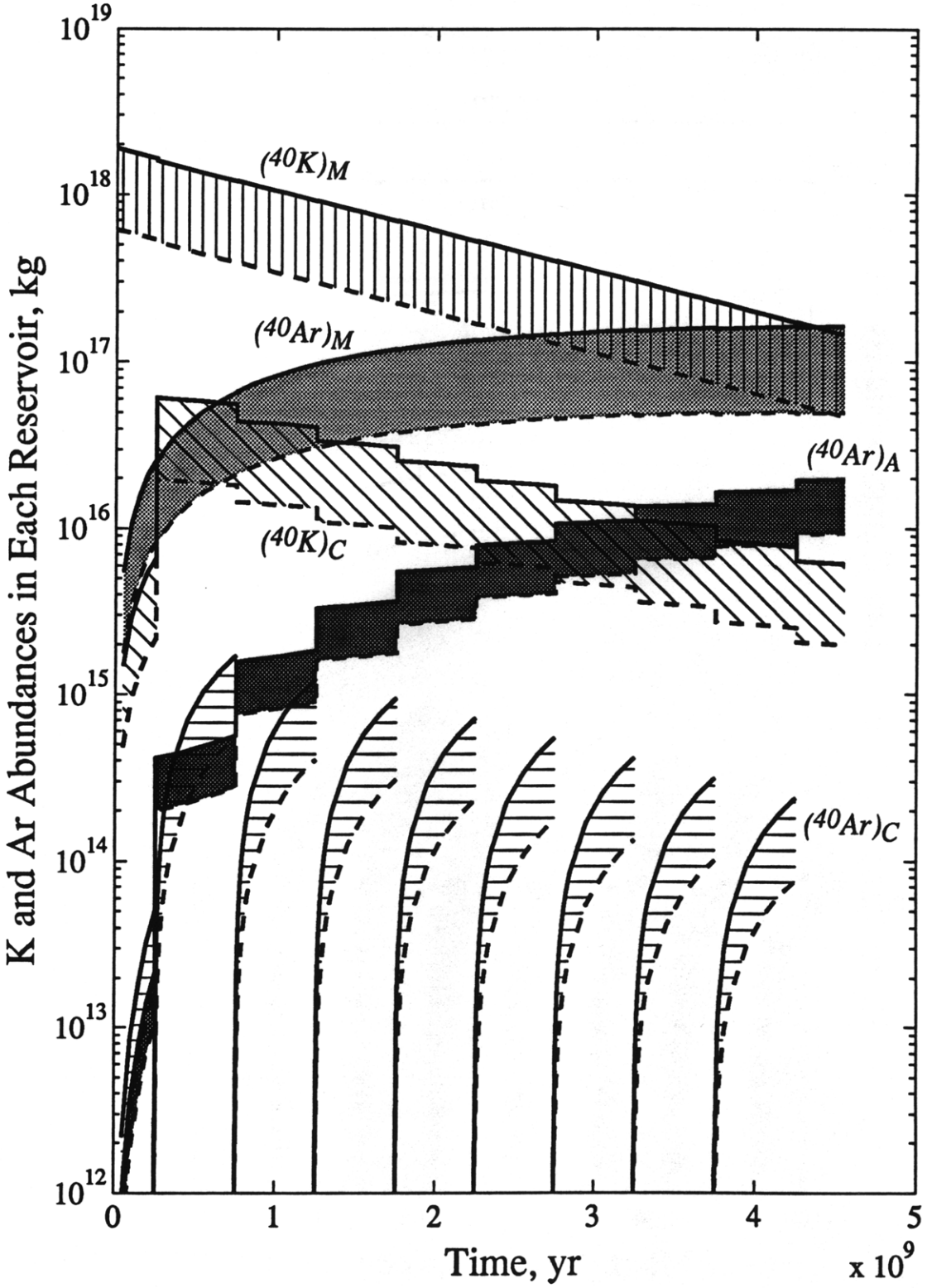
10^{19}
10^{18}
10^{17}
10^{16}
10^{15}
10^{14}
10^{13}
10^{12}
K and Ar Abundances in Each Reservoir, kg
$(^{40}K)_M$
$(^{40}Ar)_M$
$(^{40}Ar)_A$
$(^{40}K)_C$
$(^{40}Ar)_C$
0
1
2
3
4
5
Time, yr
x 10^9

Figure 4.2

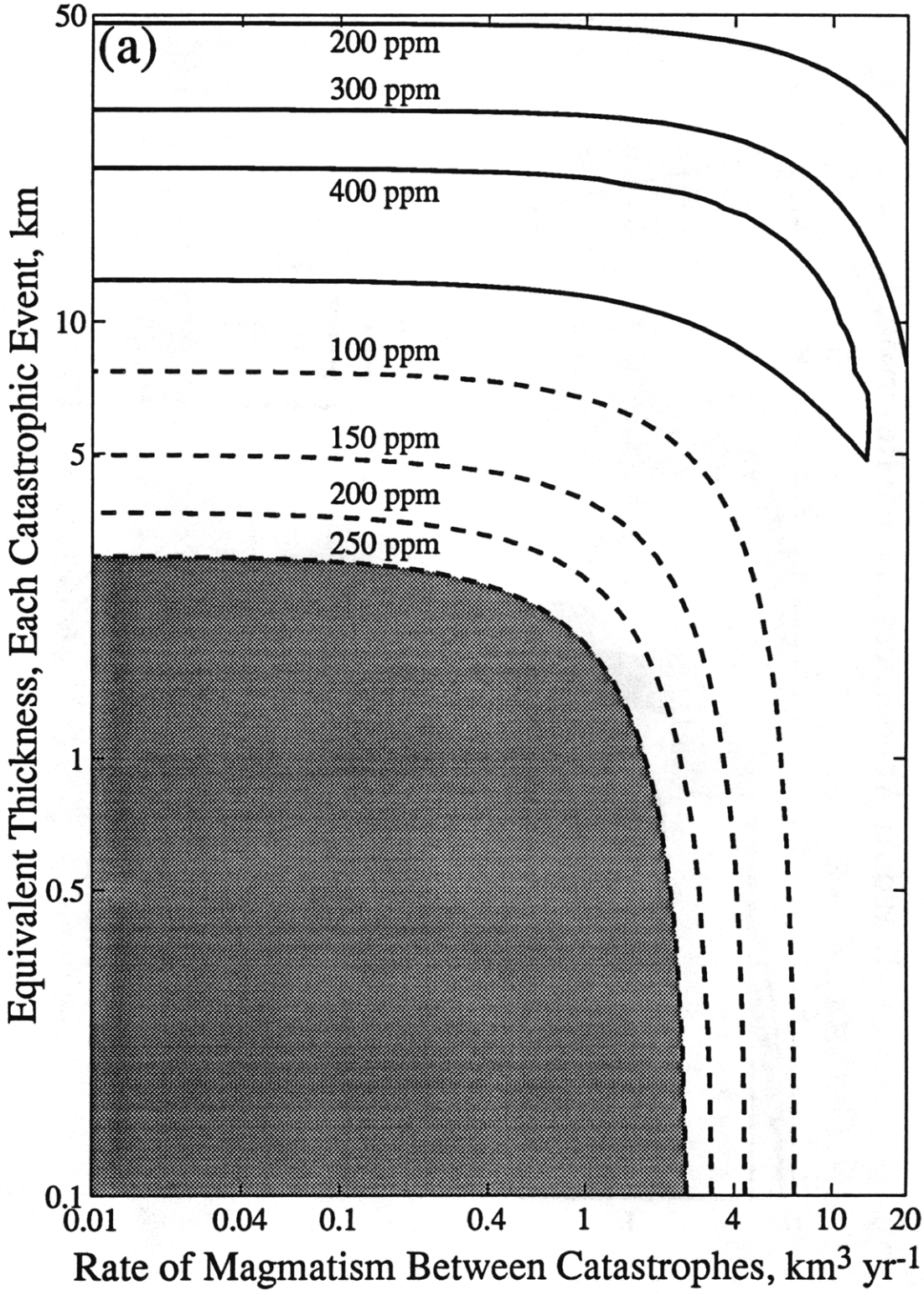
(a)
200 ppm
300 ppm
400 ppm
100 ppm
150 ppm
200 ppm
250 ppm
50
10
5
1
0.5
0.1
0.01
0.04
0.1
0.4
1
4
10
20
Equivalent Thickness, Each Catastrophic Event, km
Rate of Magmatism Between Catastrophes, km3 yr-1

Figure 4.3a

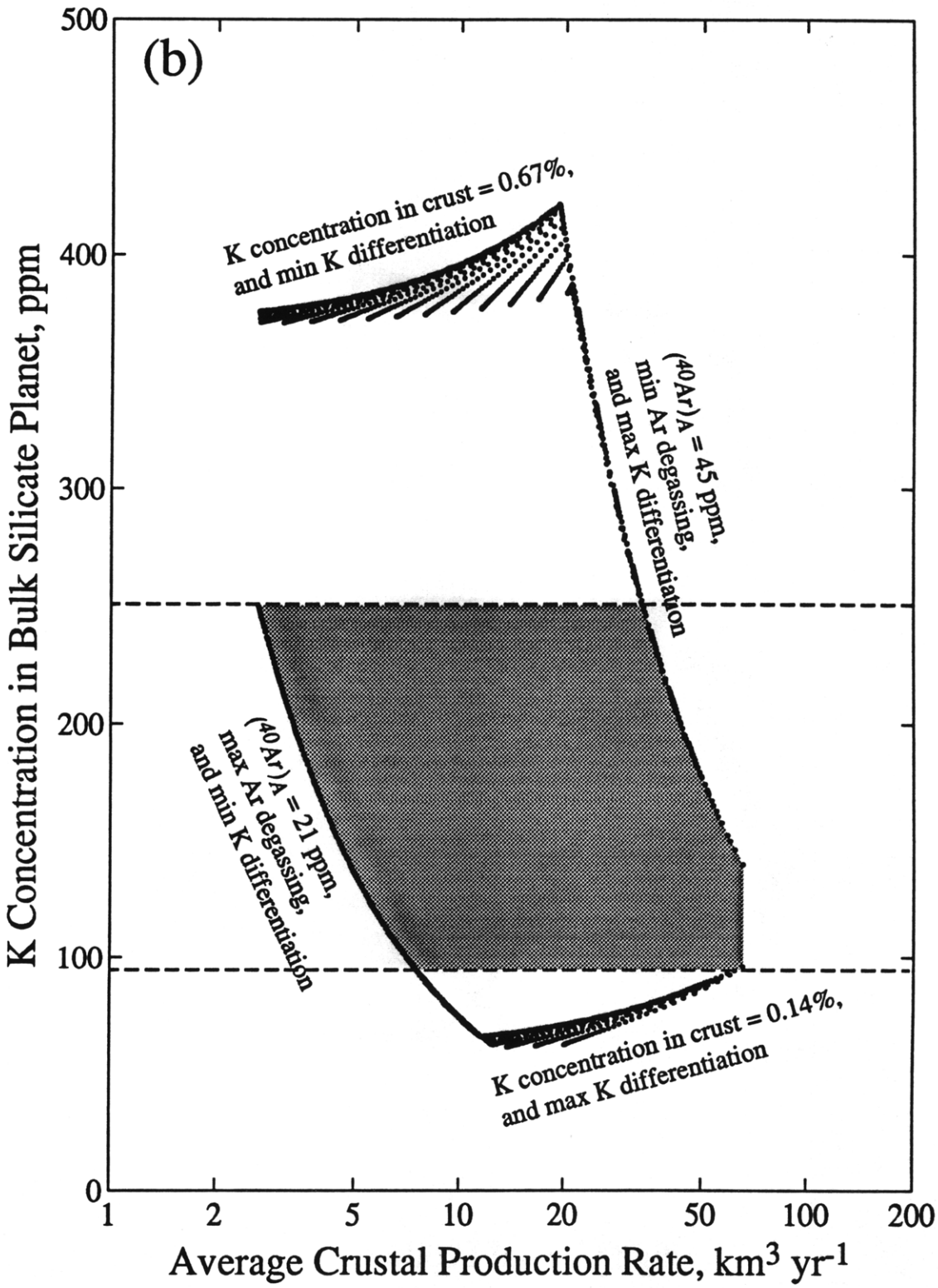
(b)
K concentration in crust = 0.67%,
and min K differentiation
(40Ar/A = 45 ppm,
min Ar degassing,
and max K differentiation
(40Ar/A = 21 ppm,
max Ar degassing,
and min K differentiation
K concentration in crust = 0.14%,
and max K differentiation
K Concentration in Bulk Silicate Planet, ppm
Average Crustal Production Rate, km3 yr-1
500
400
300
200
100
0
1
2
5
10
20
50
100
200

Figure 4.3b

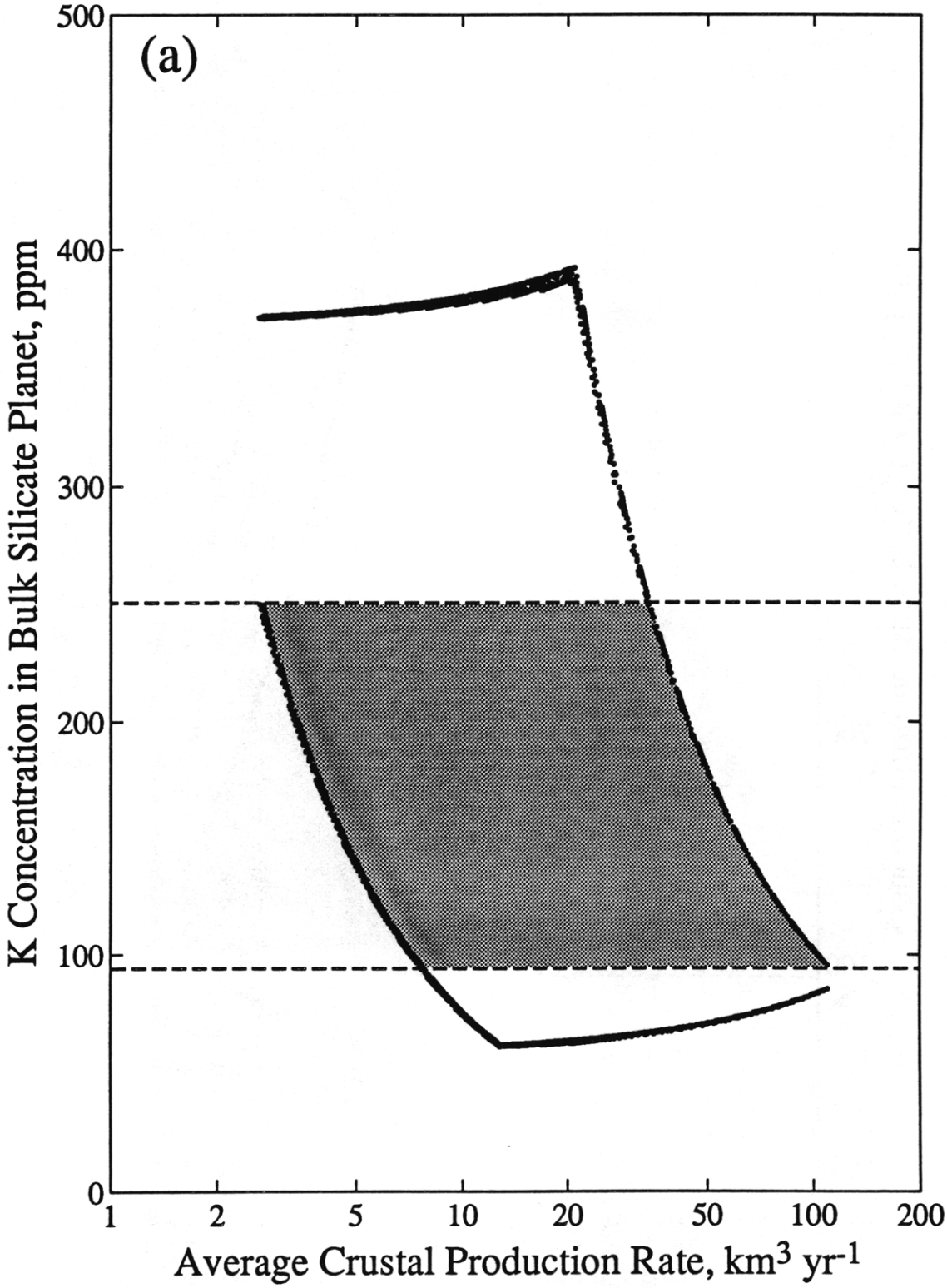
(a)
500
400
300
200
100
0
K Concentration in Bulk Silicate Planet, ppm
1
2
5
10
20
50
100
200
Average Crustal Production Rate, km3 yr-1

Figure 4.4a

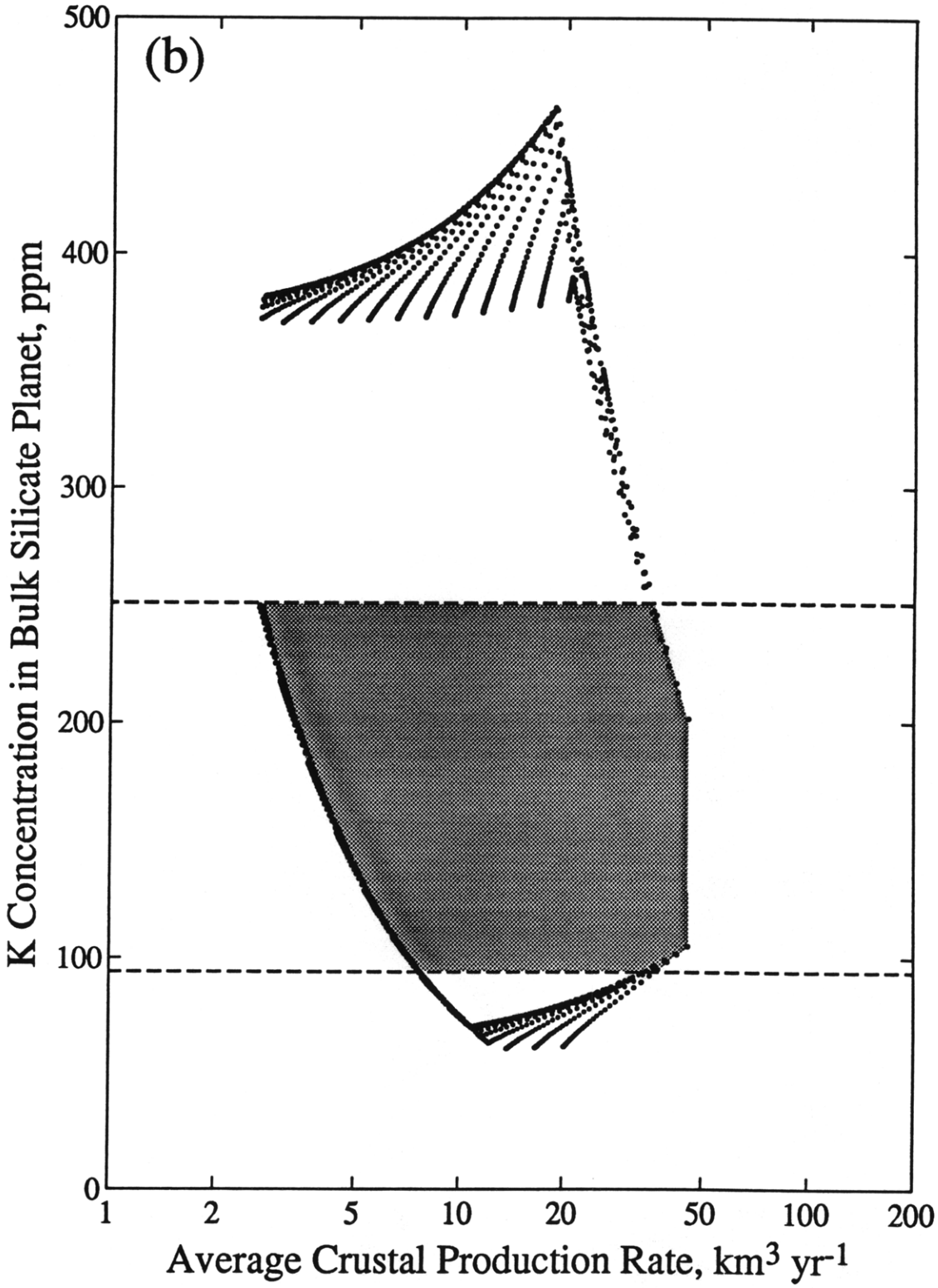
(b)
500
400
300
200
100
0
K Concentration in Bulk Silicate Planet, ppm
1
2
5
10
20
50
100
200
Average Crustal Production Rate, km3 yr-1

Figure 4.4b

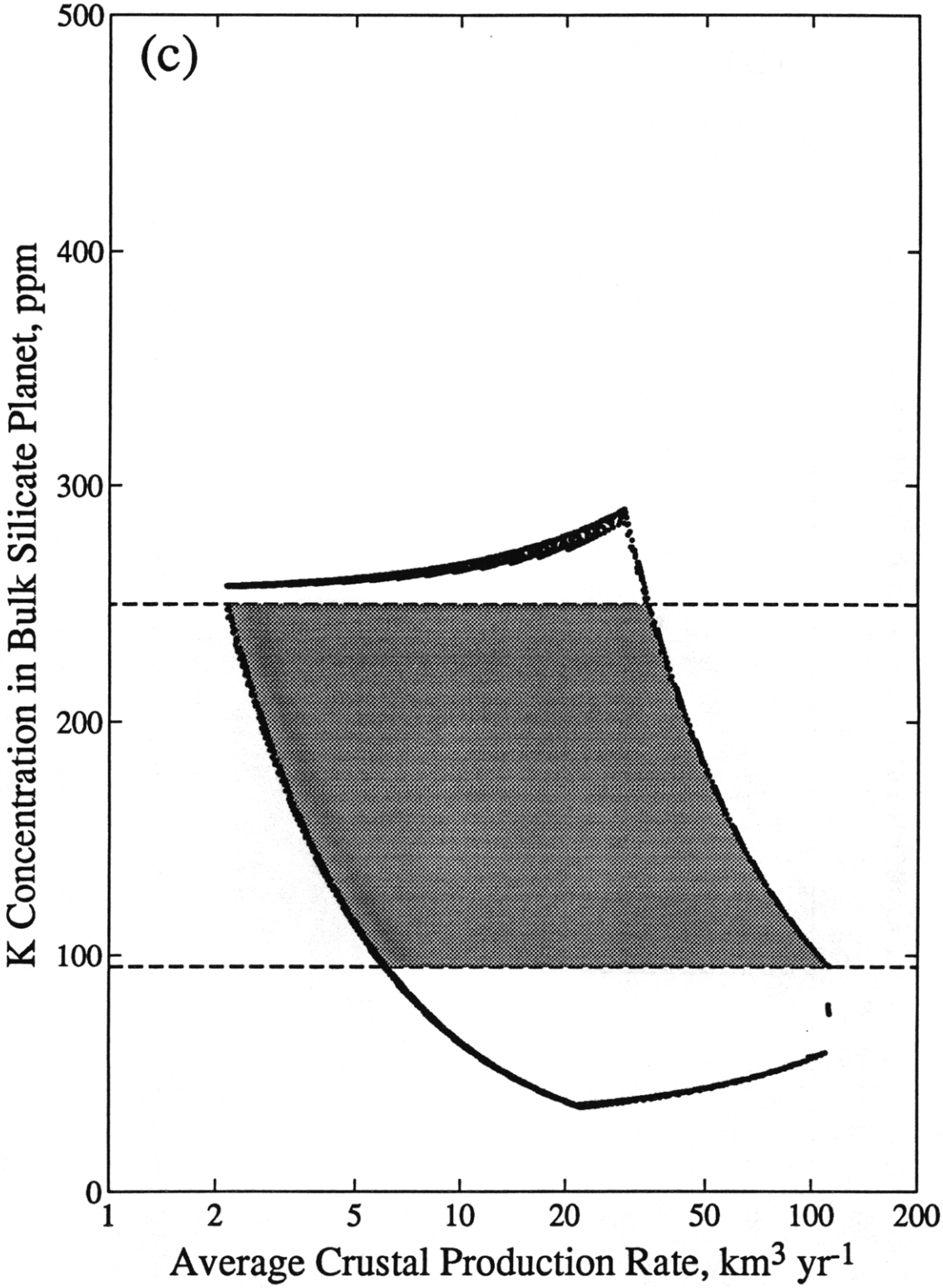
(c)
500
400
300
200
100
0
K Concentration in Bulk Silicate Planet, ppm
1
2
5
10
20
50
100
200
Average Crustal Production Rate, km3 yr-1

Figure 4.4c

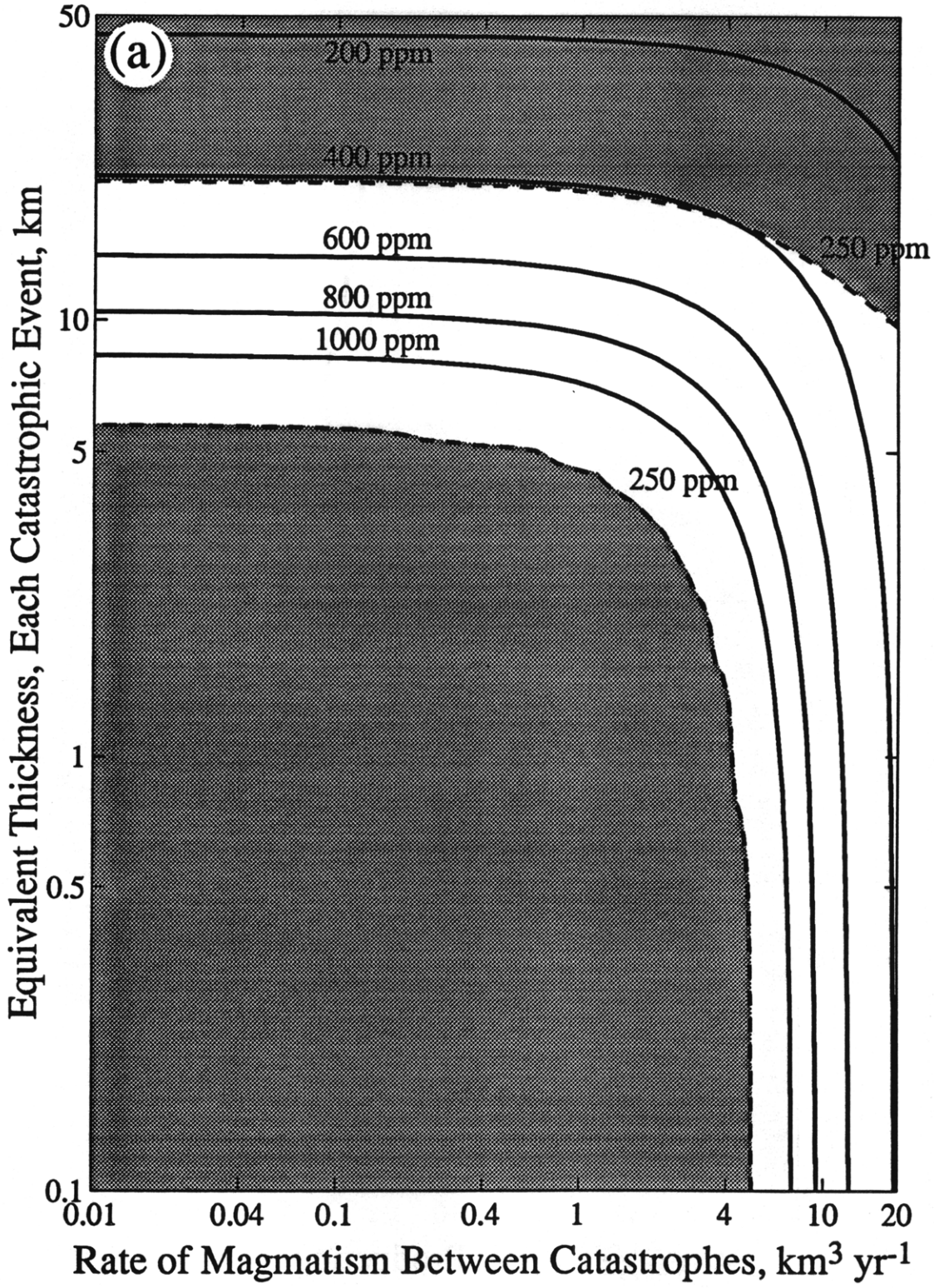
(a)
200 ppm
400 ppm
600 ppm
800 ppm
1000 ppm
250 ppm
250 ppm
50
10
5
1
0.5
0.1
0.01
0.04
0.1
0.4
1
4
10
20
Equivalent Thickness, Each Catastrophic Event, km
Rate of Magmatism Between Catastrophes, km3 yr-1

Figure 4.5a

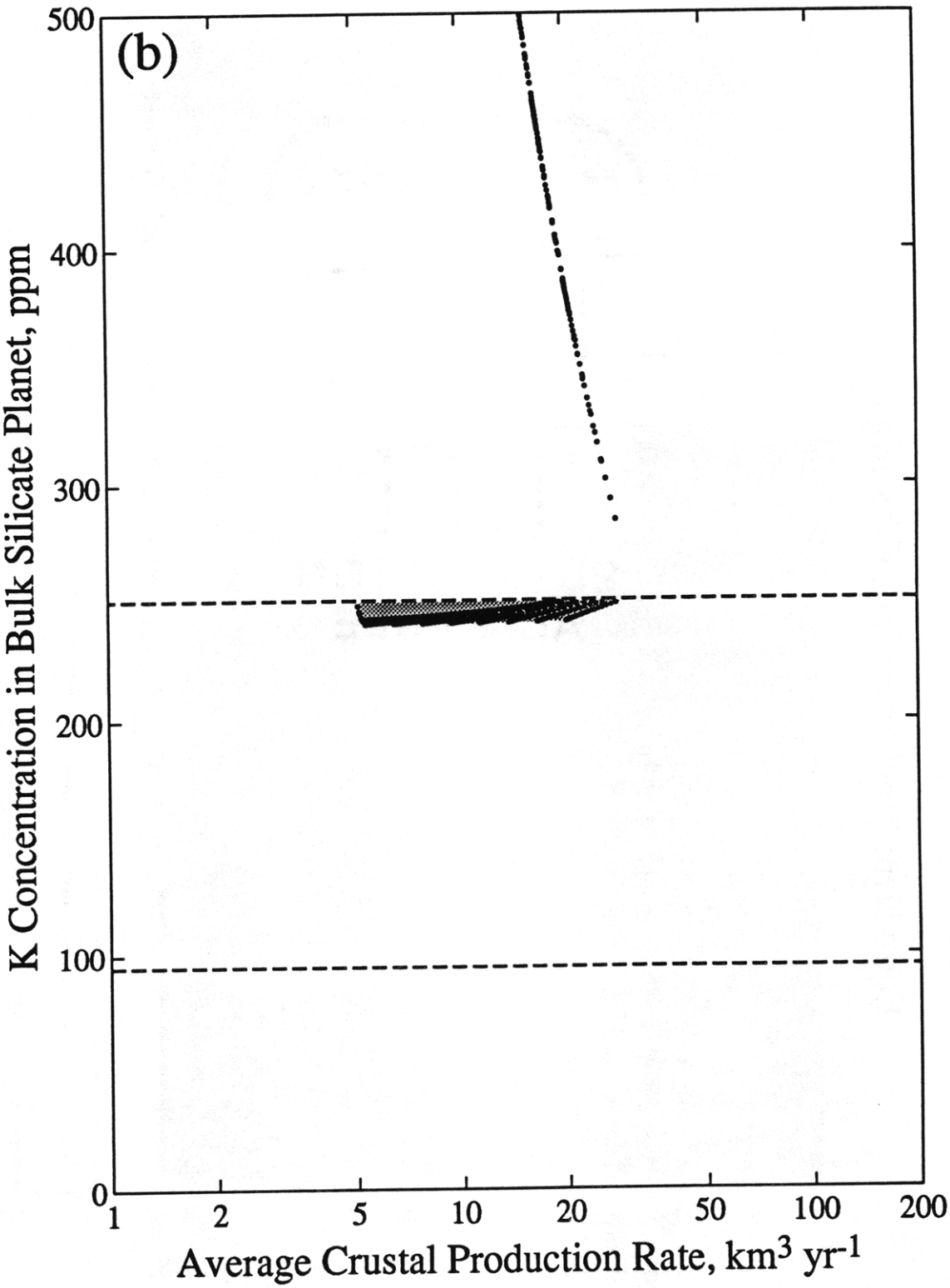
(b)
500
400
300
200
100
0
K Concentration in Bulk Silicate Planet, ppm
1
2
5
10
20
50
100
200
Average Crustal Production Rate, km3 yr-1

Figure 4.5b

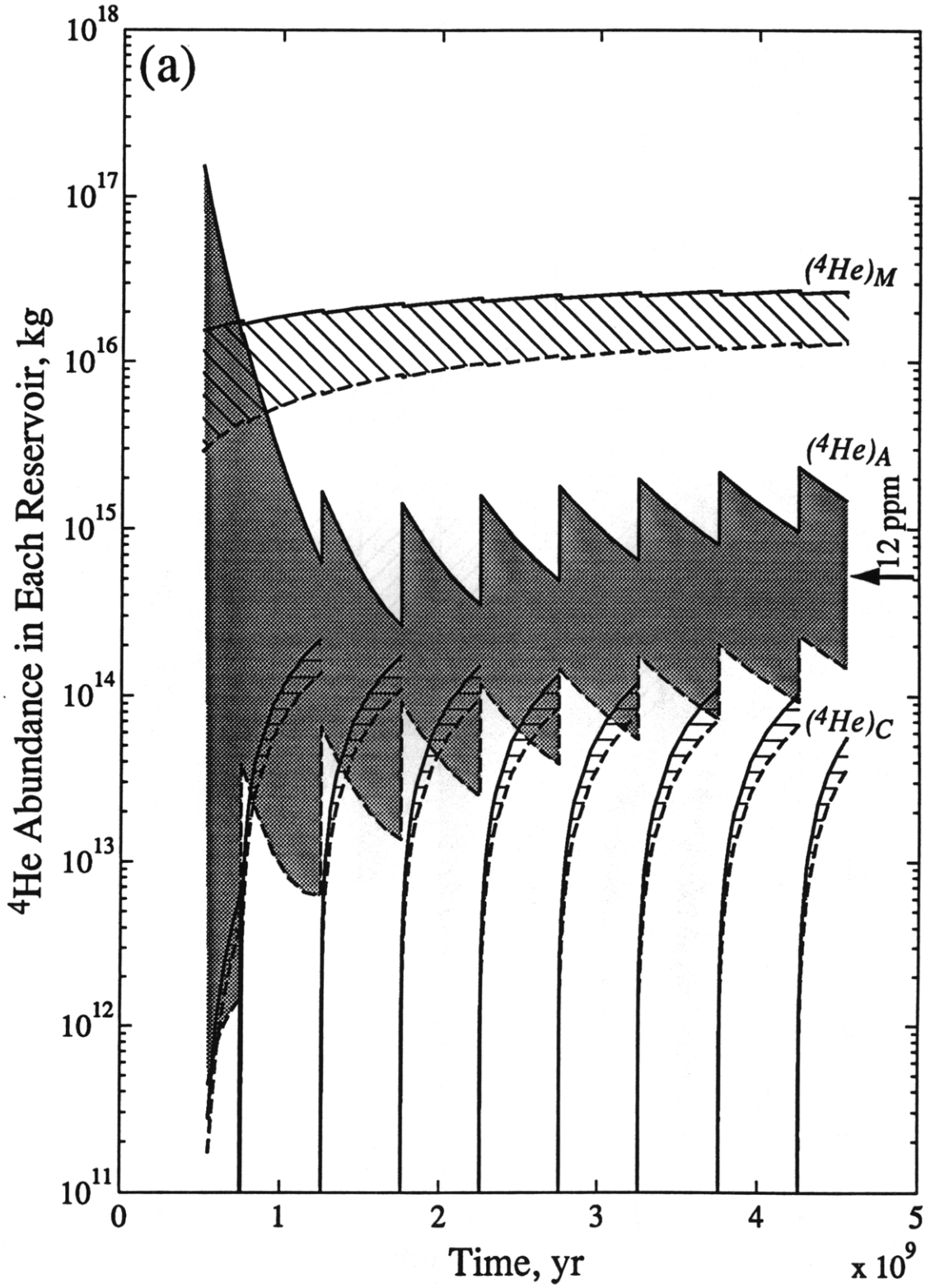
(a)
10^{18}
10^{17}
10^{16}
10^{15}
10^{14}
10^{13}
10^{12}
10^{11}
^{4}He Abundance in Each Reservoir, kg
$(^4He)_M$
$(^4He)_A$
12 ppm
$(^4He)_C$
0
1
2
3
4
5
Time, yr
x 10^9

Figure 4.6a

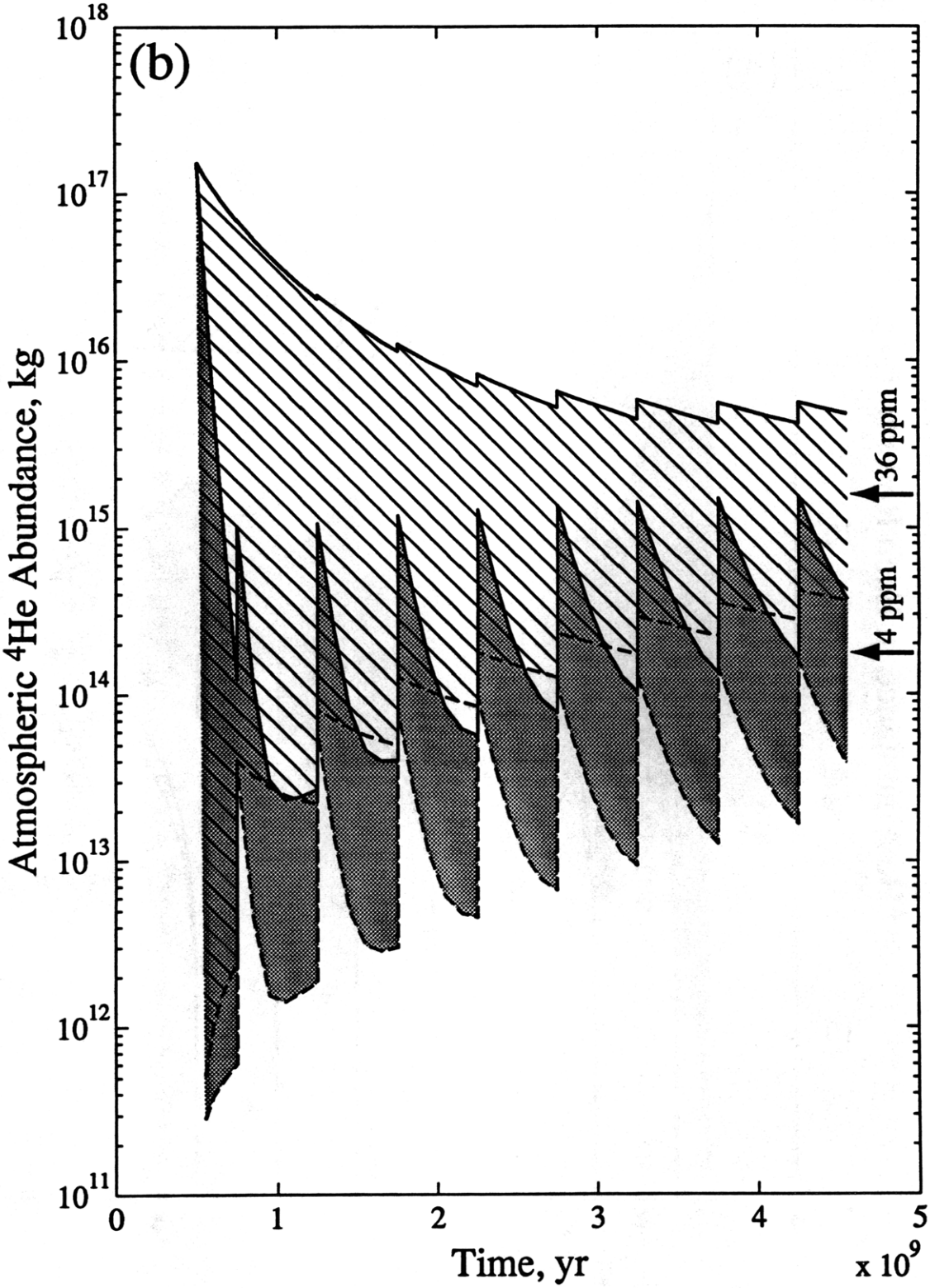
(b)
Atmospheric ^{4}He Abundance, kg
10^{18}
10^{17}
10^{16}
10^{15}
10^{14}
10^{13}
10^{12}
10^{11}
36 ppm
4 ppm
0
1
2
3
4
5
Time, yr
x 10^9

Figure 4.6b

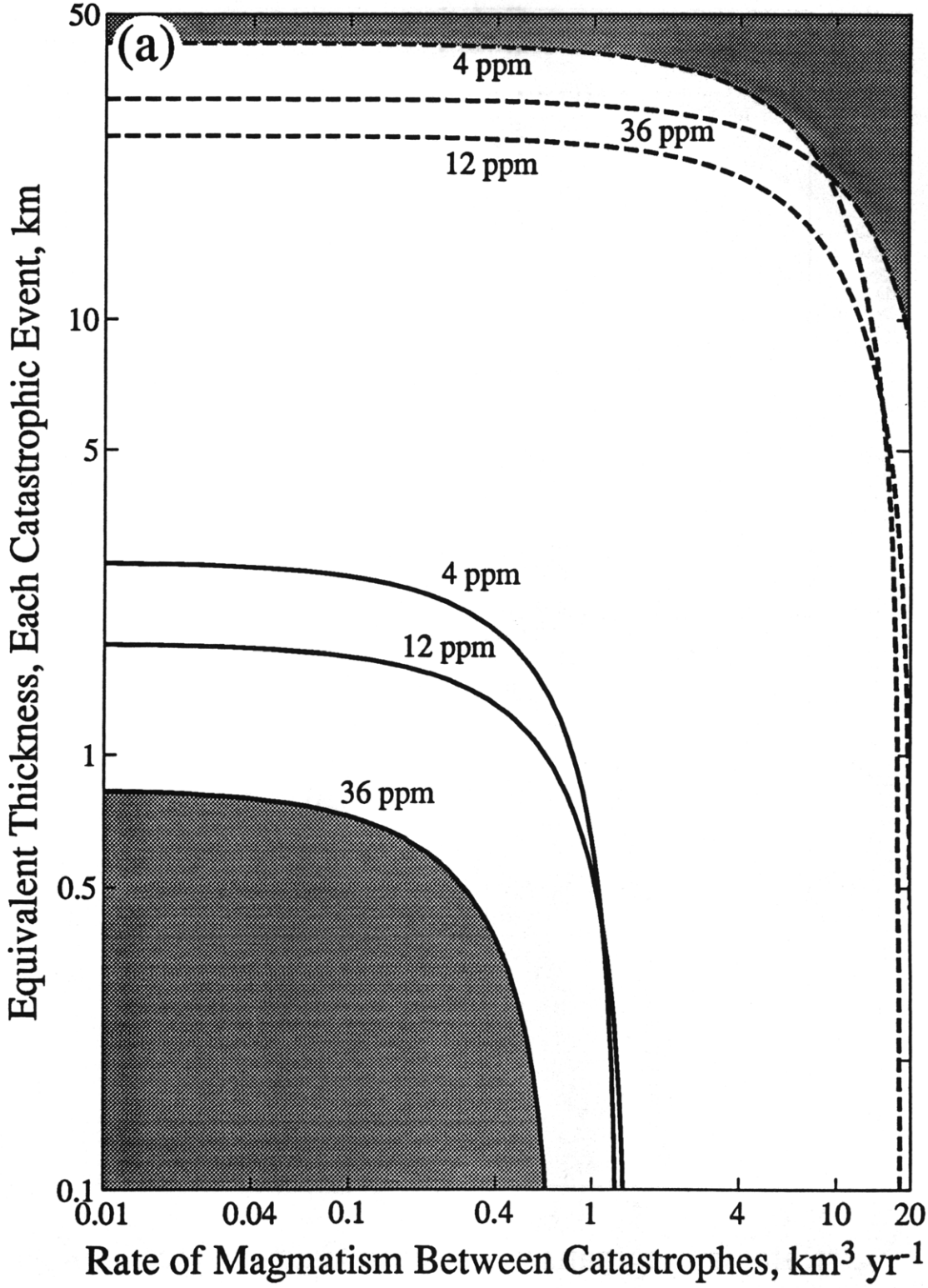
(a)
4 ppm
36 ppm
12 ppm
4 ppm
12 ppm
36 ppm
50
10
5
1
0.5
0.1
0.01
0.04
0.1
0.4
1
4
10
20
Equivalent Thickness, Each Catastrophic Event, km
Rate of Magmatism Between Catastrophes, km3 yr-1

Figure 4.7a

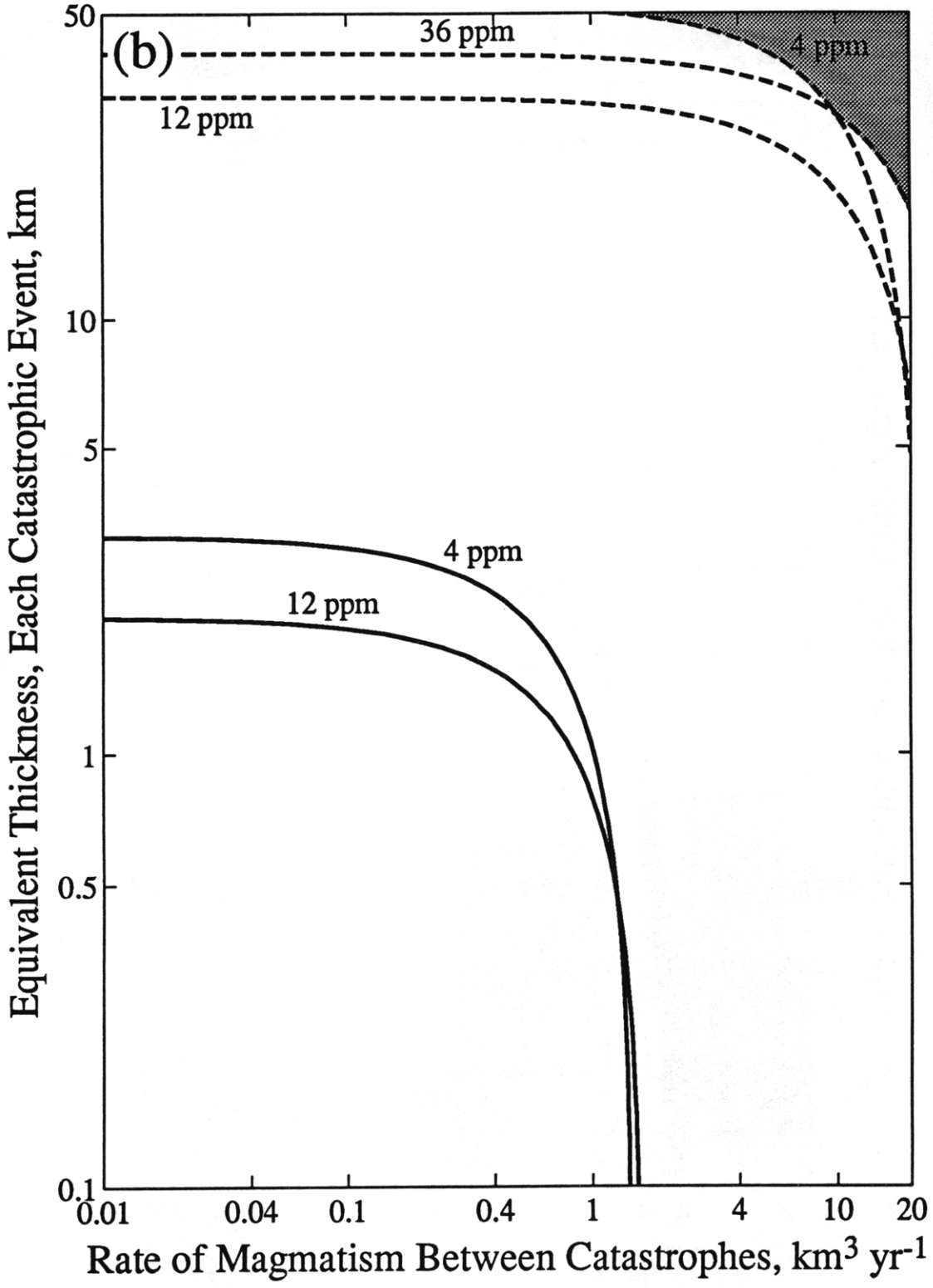
(b)
36 ppm
4 ppm
12 ppm
4 ppm
12 ppm
50
10
5
1
0.5
0.1
0.01
0.04
0.1
0.4
1
4
10
20
Equivalent Thickness, Each Catastrophic Event, km
Rate of Magmatism Between Catastrophes, km3 yr-1

Figure 4.7b

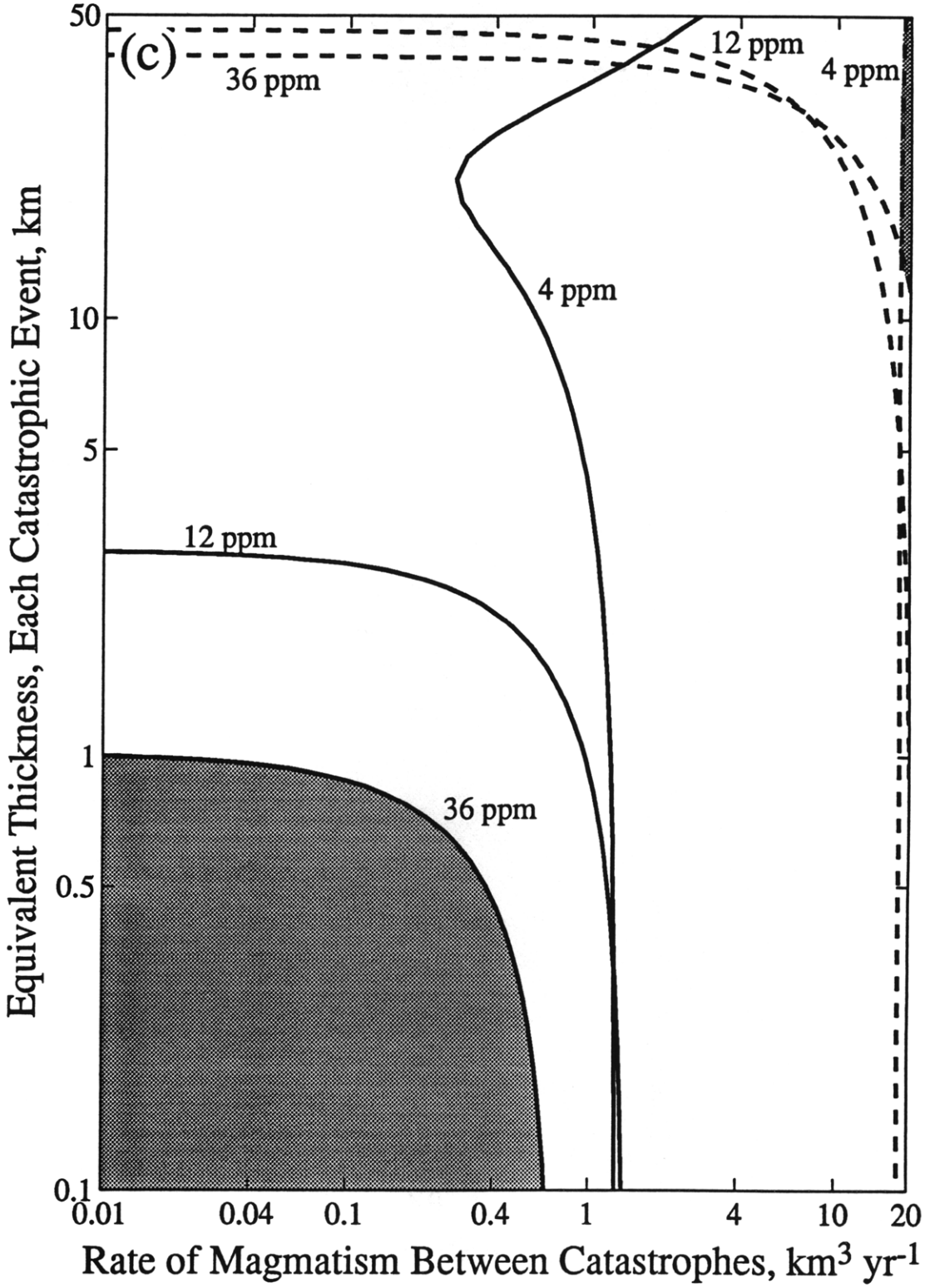
(c)
36 ppm
12 ppm
4 ppm
4 ppm
12 ppm
36 ppm
50
10
5
1
0.5
0.1
0.01
0.04
0.1
0.4
1
4
10
20
Equivalent Thickness, Each Catastrophic Event, km
Rate of Magmatism Between Catastrophes, km3 yr-1

Figure 4.7c

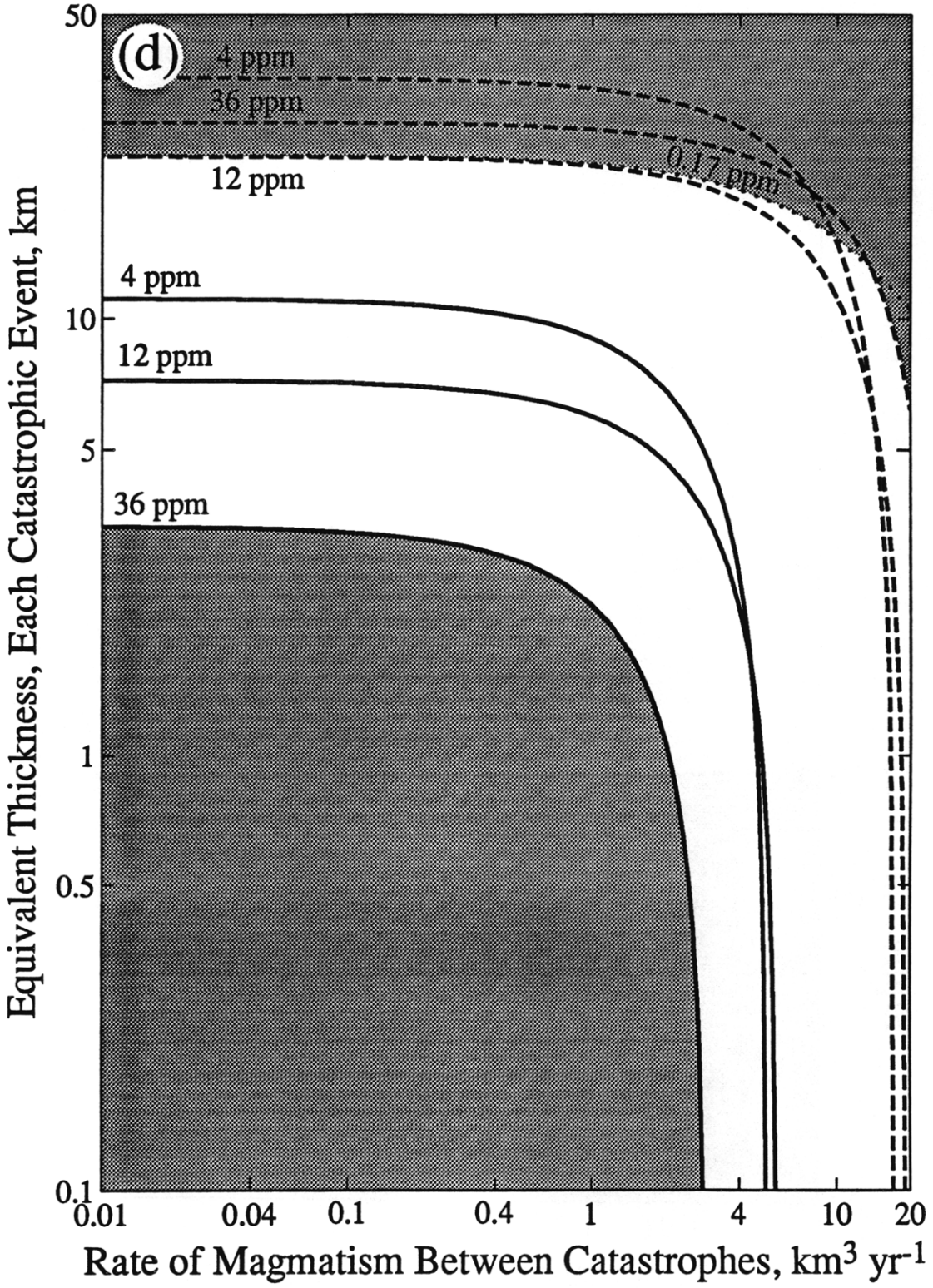
(d)
4 ppm
36 ppm
12 ppm
0.17 ppm
4 ppm
12 ppm
36 ppm
50
10
5
1
0.5
0.1
0.01
0.04
0.1
0.4
1
4
10
20
Equivalent Thickness, Each Catastrophic Event, km
Rate of Magmatism Between Catastrophes, km3 yr-1

Figure 4.7d

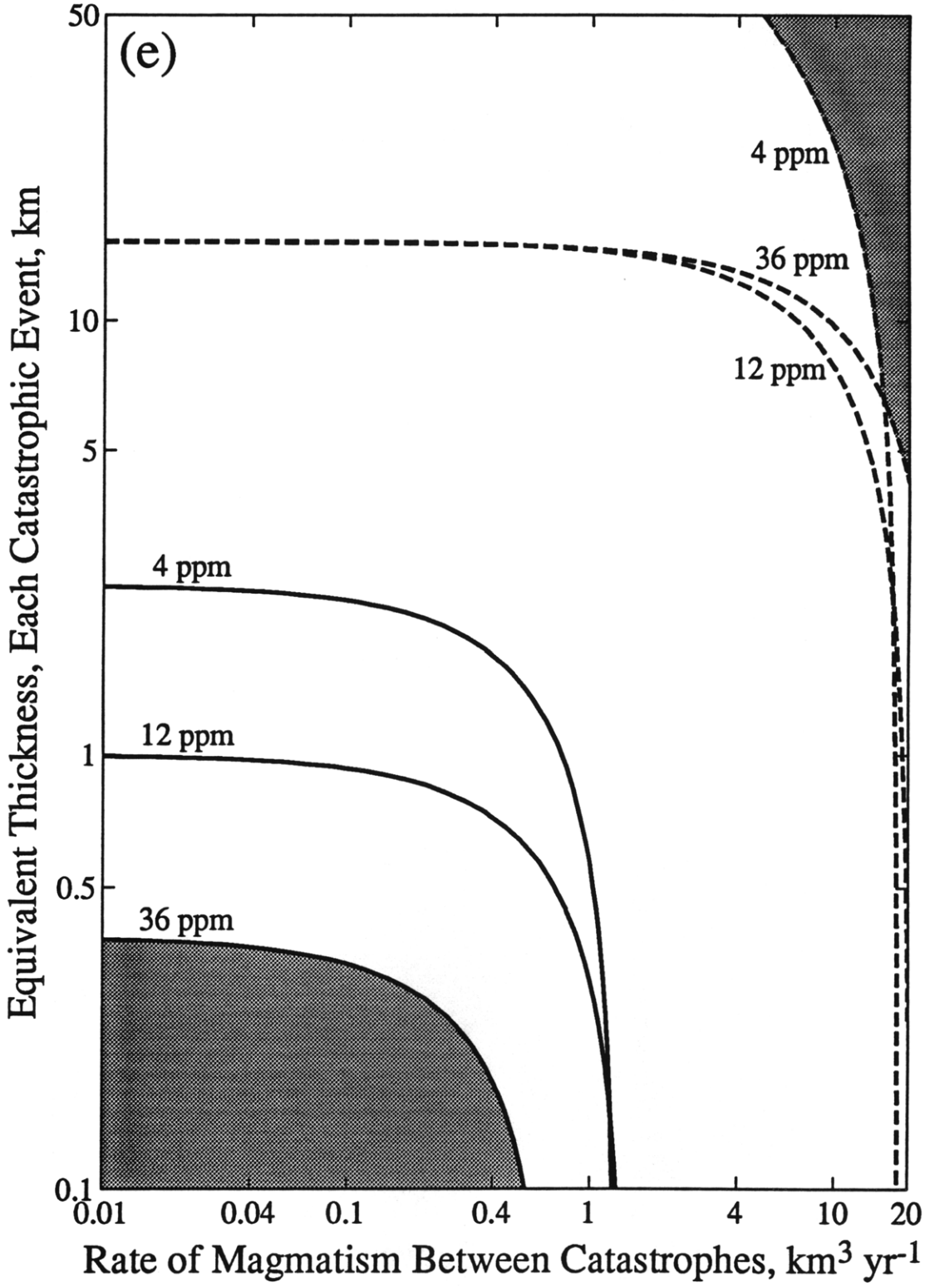
(e)
50
10
5
1
0.5
0.1
4 ppm
36 ppm
12 ppm
4 ppm
12 ppm
36 ppm
0.01
0.04
0.1
0.4
1
4
10
20
Equivalent Thickness, Each Catastrophic Event, km
Rate of Magmatism Between Catastrophes, km3 yr-1

Figure 4.7e

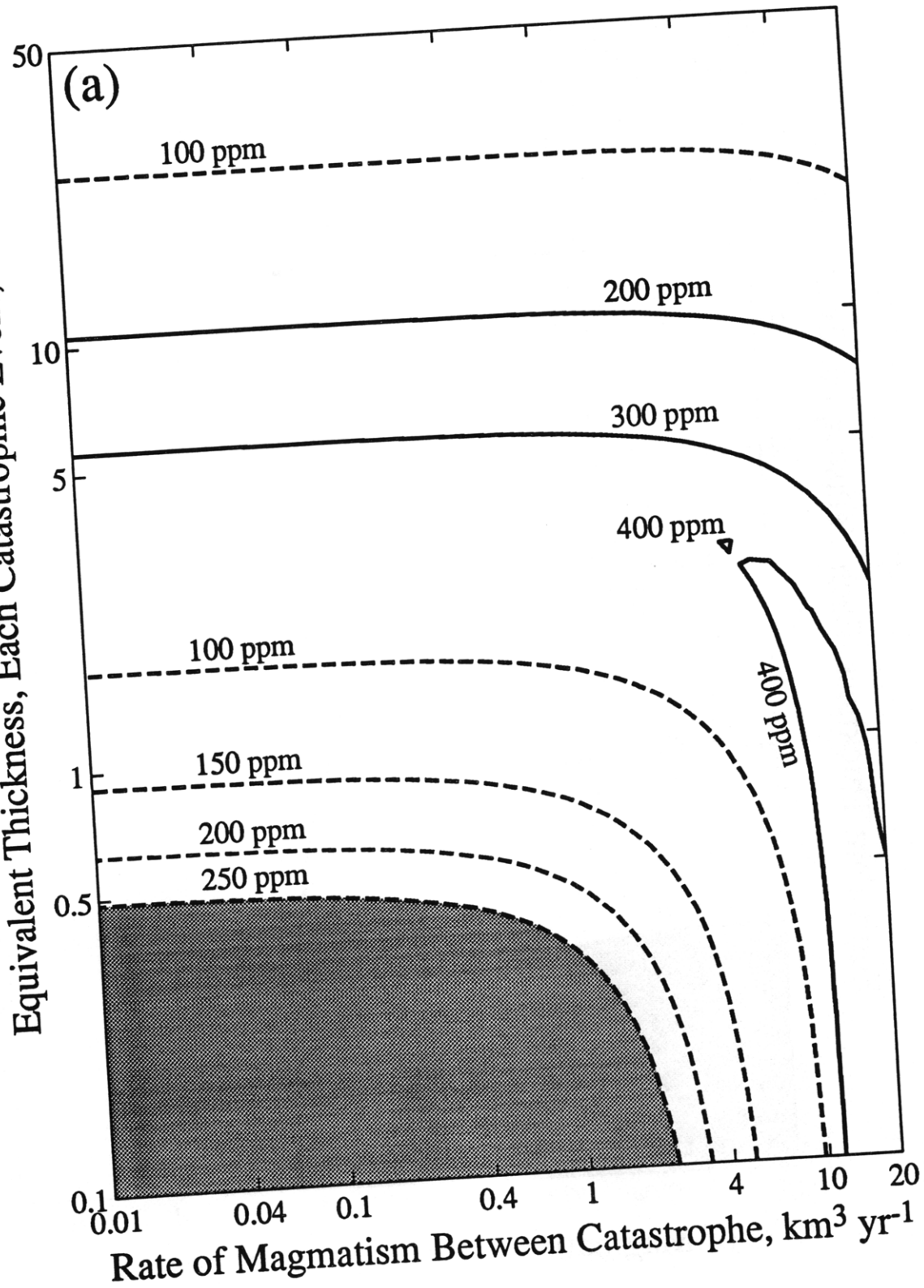
(a)
50
10
5
1
0.5
0.1
100 ppm
200 ppm
300 ppm
400 ppm
100 ppm
150 ppm
200 ppm
250 ppm
400 ppm
0.01
0.04
0.1
0.4
1
4
10
20
Equivalent Thickness, Each Catastrophic Event, km
Rate of Magmatism Between Catastrophe, km3 yr-1

Figure 4.8a

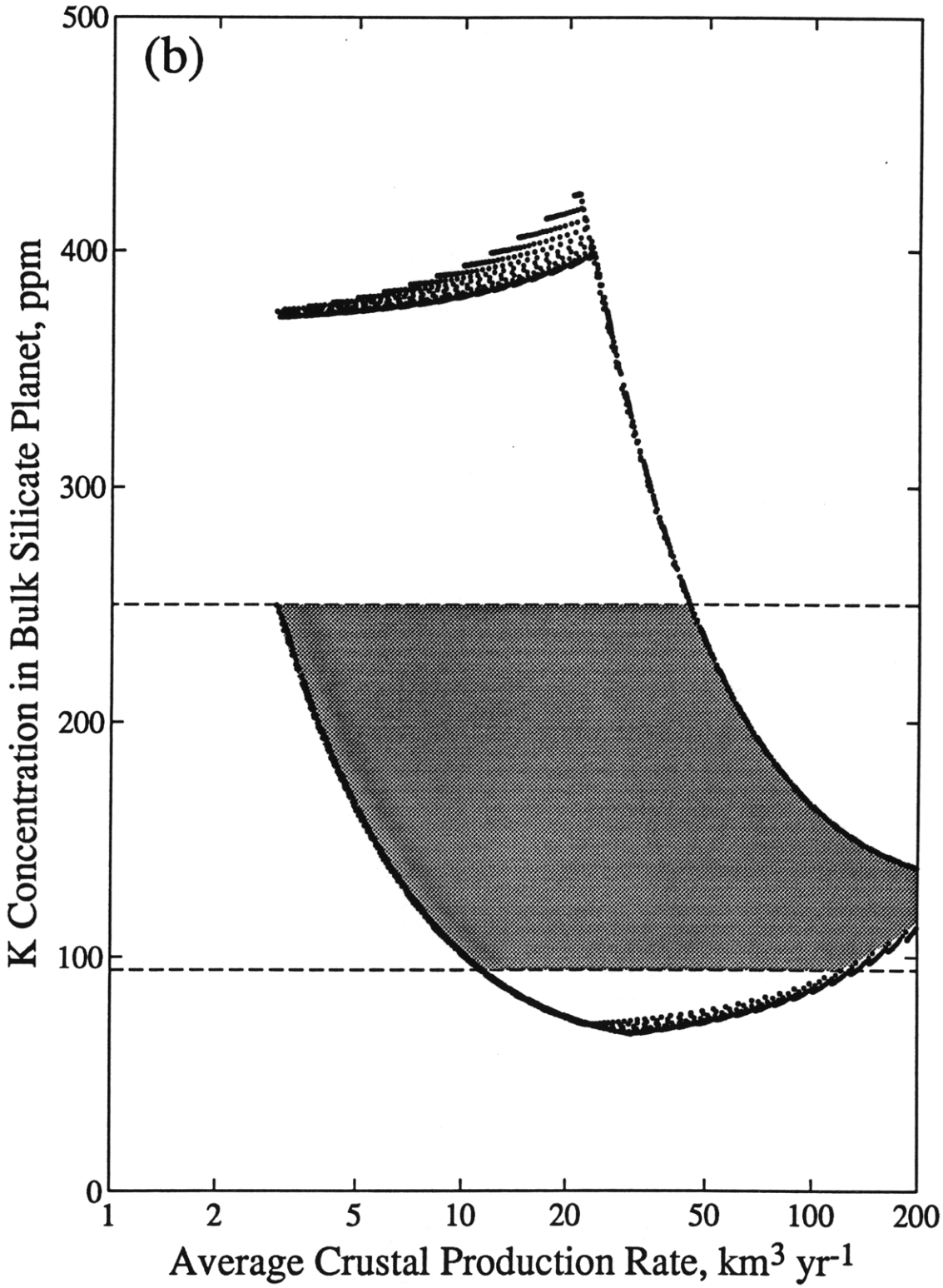
(b)
500
400
300
200
100
0
K Concentration in Bulk Silicate Planet, ppm
1
2
5
10
20
50
100
200
Average Crustal Production Rate, km3 yr-1

Figure 4.8b

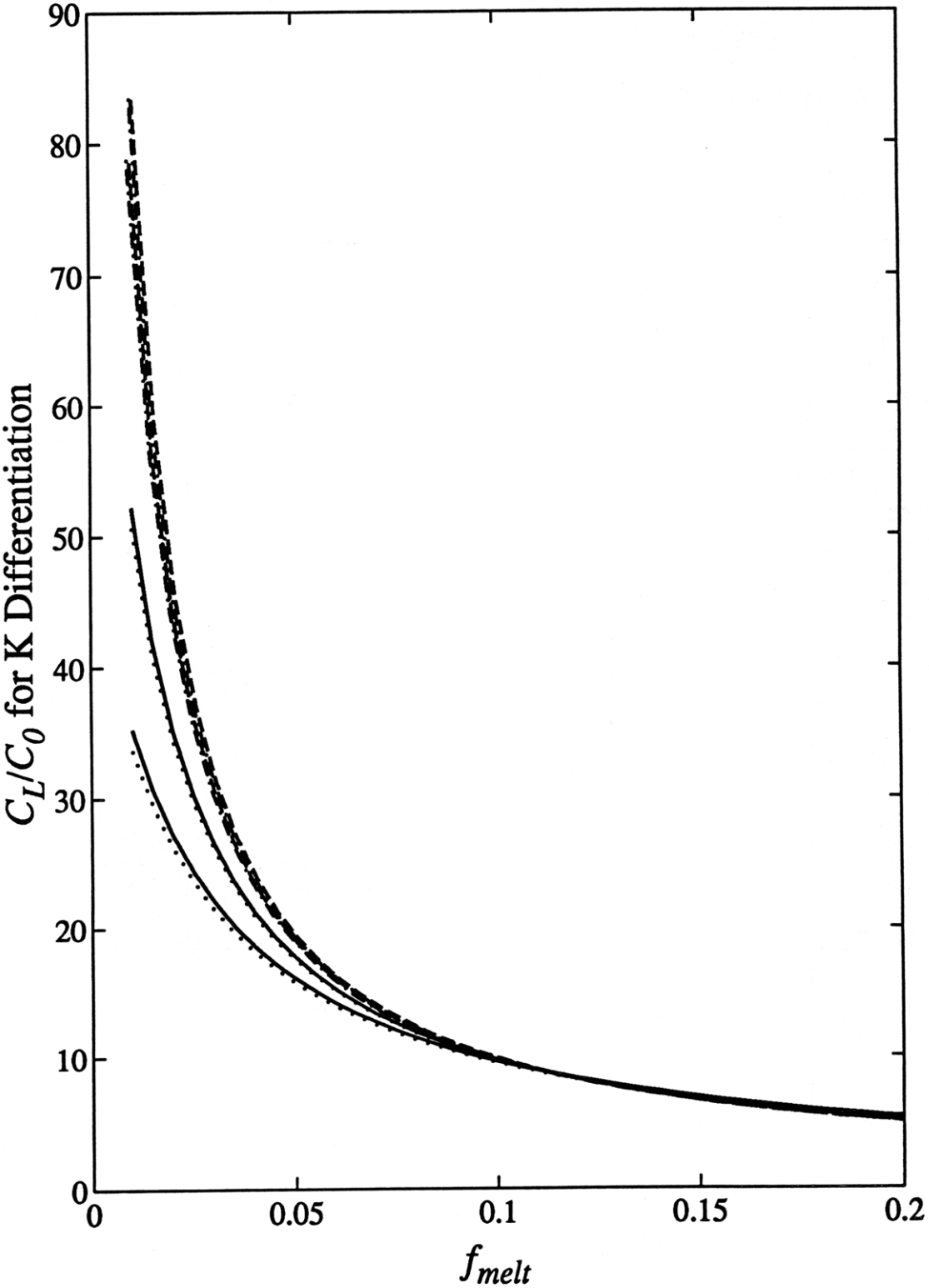
90
80
70
60
50
40
30
20
10
0
0
0.05
0.1
0.15
0.2
C_L/C_0 for K Differentiation
f_{melt}

Figure 4.A1

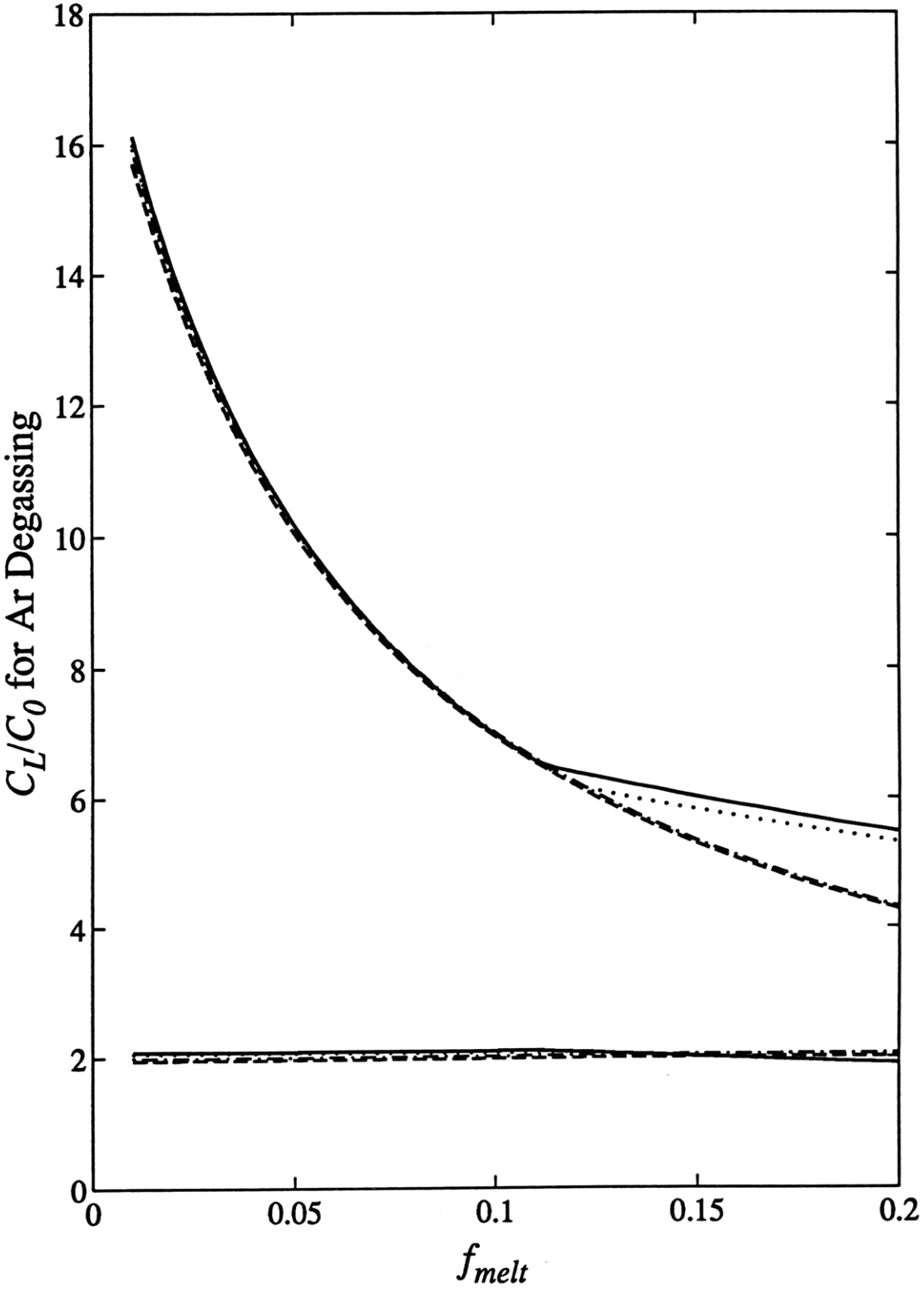

Figure 4.A2

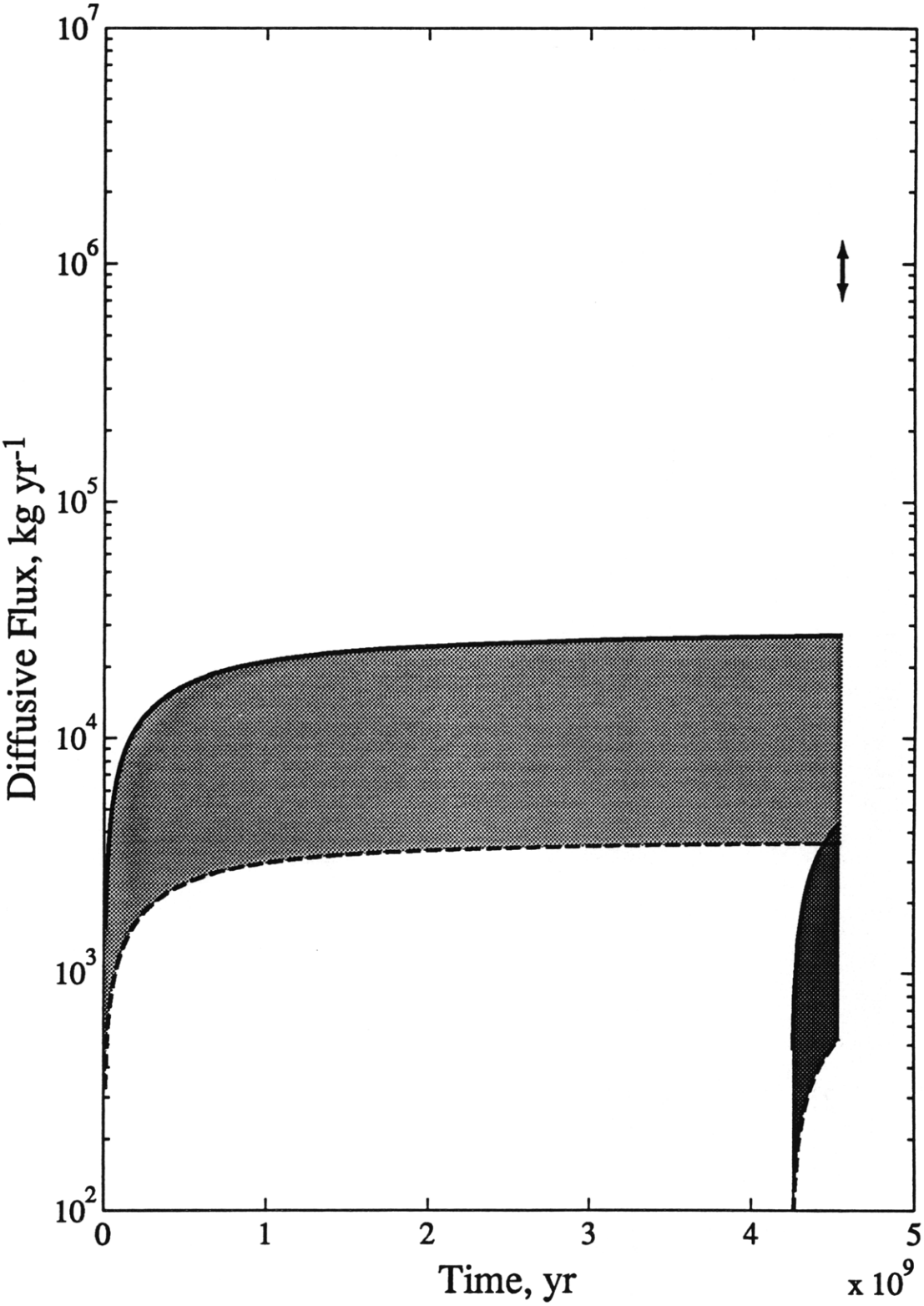
Diffusive Flux, kg yr-1
10^7
10^6
10^5
10^4
10^3
10^2
0
1
2
3
4
5
Time, yr
x 10^9

Figure 4.B1

Chapter 5:

Depletion of Water in the Venus Mantle: A Constraint from Volcanic Degassing of ^{40}Ar and Atmospheric Escape of Hydrogen

INTRODUCTION

Water plays an important role in the rheology of mantle material [*Mackwell et al.*, 1985; *Karato et al.*, 1986; *Karato*, 1989; *McGovern and Schubert*, 1989; *Schubert et al.*, 1989; *Phillips and Hansen*, 1994] and in the large-scale faulting and deformation of the lithosphere [*McKenzie*, 1977; *Mackwell et al.*, 1995; *Schultz and Simons*, 1995]. The interior water budget is of special interest for the history of global tectonics and resurfacing on Venus [*Solomon and Head*, 1982; *Kaula*, 1990; *Phillips and Hansen*, 1994; *Kaula*, 1995]. A global catastrophic resurfacing event ending 300 to 500 Myr ago postulated from the apparently random distribution of impact craters and the small fraction of modified craters [*Phillips et al.*, 1992; *Schaber et al.*, 1992; *Herrick and Phillips*, 1994; *Strom et al.*, 1994] must have had a significant influence on the present atmospheric water abundance and D/H ratio [*Grinspoon*, 1993]. In this chapter we investigate the water concentration in the Venus mantle over the last several hundred million years from models of mantle degassing and the atmospheric evolution of water during and after the last catastrophic resurfacing event. We then extend this inquiry to the mantle water budget over the past several billion years by combining models for water outgassing and hydrogen escape with those for the degassing of ^{40}Ar.

The atmospheric water abundance on Venus is five orders of magnitude less than the mass of the Earth's ocean [*Bell et al.*, 1991; *de Bergh et al.*, 1991; *Drossart et al.*, 1993; *Pollack et al.*, 1993]. The deuterium/hydrogen ratio measured *in situ* [*Donahue et al.*, 1982; *Donahue and Hodges*, 1992] and from the ground [*de Bergh et al.*, 1991] is, in contrast, about 100 times higher than the terrestrial value. The paucity of atmospheric H_2O and the high D/H ratio were first explained as a consequence of the loss of the planet's primordial water endowment, at least 0.14% of a terrestrial ocean, through the atmospheric escape of hydrogen over the planet's history [*Donahue et al.*, 1982]. Hydrogen is lost from the atmosphere as a result of the photodissociation of H_2O and HCl in the middle atmosphere [*von Zahn et al.*, 1983; *Lewis and Prinn*, 1984] and

nonthermal escape mechanisms involving interactions of neutral H atoms with a variety of suprathermal ions in the upper atmosphere [*Kumar et al.*, 1983; *Krasnopolsky*, 1985; *Donahue and Hartle*, 1992; *Hunten*, 1993]. Deuterium is less able to escape than hydrogen and remains in the atmosphere with a considerably longer residence time [*Donahue and Hartle*, 1992; *Gurwell and Yung*, 1993].

These escape processes, as well as a possible rapid loss of hydrogen early in the planet's history by hydrodynamic outflow [*Kasting and Pollack*, 1983; *Pepin*, 1991; *Hunten*, 1993], involve loss rates so high that a primordial endowment of water as great as one Earth ocean can be easily removed over the planet's history, leading to less water and a greater enrichment of deuterium than are currently observed [*Hunten*, 1993]. Thus a regular supply of water by either volcanic outgassing [*Kumar et al.*, 1983; *Krasnopolsky*, 1985] or cometary impact [*Grinspoon*, 1987; *Grinspoon and Lewis*, 1988] is required to satisfy the present atmospheric water abundance and D/H ratio.

The first study of water degassing and atmospheric D/H ratio on Venus that took into account the volcanic resurfacing history as discerned from Magellan observations was that of *Grinspoon* [1993]. Under the assumption of a presently steady balance between atmospheric escape and volcanic degassing, the water content of magmas on Venus is calculated to be 50 ppm by weight, or three orders of magnitude less than that on Earth [*Grinspoon*, 1993]. If instead a catastrophic volcanic resurfacing 500 Myr ago is the cause of the most recent significant supply of water from the mantle to the atmosphere, then an estimated volume of magmatism during the catastrophic resurfacing event of 5×10^9 km^3 yr^{-1} and a total atmospheric water abundance 500 Myr ago of 4500 ppm [*Grinspoon*, 1993] also yield a water concentration in Venus magmas of 50 ppm. Both estimates suggest a great depletion of water on Venus relative to Earth, not only in the atmosphere but also in the planet's interior.

In this chapter we first develop a model for mantle degassing and atmospheric escape of water that incorporates both catastrophic volcanic resurfacing and subsequent

magmatic activity. We calculate the water content of the Venus mantle under a range of physical parameters broader than that considered by *Grinspoon* [1993]. The derived estimates are appropriate for the last several hundred million years.

To extend the inquiry on the mantle water budget on Venus to periods prior to the past several hundred million years, we then couple water degassing and escape to the evolution of atmospheric ^{40}Ar (Chapter 4) [*Pollack and Black*, 1982; *Volkov and Frenkel*, 1993; *Matsui and Tajika*, 1995]. Because the inert nature of argon prevents its return from the atmosphere to the mantle and the escape of Ar to space is negligible, the ^{40}Ar abundance in the present atmosphere can be related directly to degassing and magmatism integrated over the planet's history [e.g., *Ozima and Podosek*, 1983]. The atmospheric ^{40}Ar abundance constrains the total amount of magmatism, while the hydrogen escape flux limits the supply of water from the mantle to the atmosphere. Thus combining ^{40}Ar degassing with water degassing and hydrogen escape allows us to extend previous estimates of the water budget in the Venus interior [*Grinspoon*, 1993] to times prior to the postulated catastrophic resurfacing event that ended 500 Myr ago.

MANTLE DEGASSING AND ATMOSPHERIC ESCAPE OF VOLATILES

An Overview of the Degassing Model

We model the history of crustal production on Venus as three distinct periods of magmatic activity: before, during, and after the postulated catastrophic resurfacing event that ended 300 to 500 Myr ago. The duration of catastrophic resurfacing is essentially unconstrained, because terrains considerably older than the episode of nearly global resurfacing have not yet been unambiguously identified. Global and regional analyses of cratering records have been utilized to address the cessation of global resurfacing, but the time interval for cessation has been variously estimated at anywhere between several and a hundred million years [*Strom et al.*, 1994; *Price*, 1995a]. For simplicity here, we assume that global resurfacing occurred within a geologically short period of time near 500 Myr ago.

Before and after this global resurfacing event, magmatism is assumed to have continued at steady rates that can differ for the two respective periods. If a series of catastrophic resurfacing events preceded the last event [*Parmentier and Hess*, 1992; *Turcotte*, 1993; *Herrick and Parmentier*, 1994], then our derived crustal production rate before the last event should be regarded as an average of a possibly strongly time-dependent magmatic flux. Crater densities on several types of volcanic landforms have been interpreted as an indication of volcanic activity after the last global resurfacing event at a rate that was either indistinguishable from steady in time [*Namiki and Solomon*, 1994] or perhaps increasing with time [*Price and Suppe*, 1994]. For simplicity, we assume that such magmatism took place at a constant rate.

As water and ^{40}Ar degas from the planet's interior, H and D escape from the atmosphere. We extrapolate the estimated escape flux of H and D at present [*Donahue and Hartle*, 1992; *Grinspoon*, 1993] backwards in time on the basis of previous work on escape mechanisms [*Hunten and Donahue*, 1976; *Kumar et al.*, 1983; *Krasnopolsky*,

1985; *Grinspoon and Lewis*, 1988]. We assume that a rapid hydrodynamic outflow phase, or blow-off [*Kasting and Pollack*, 1983; *Pepin*, 1991; *Hunten*, 1993], ended at an arbitrarily chosen time at 500 Myr after planetary formation [*Kasting and Pollack*, 1983; *Pepin*, 1991], and we calculate the subsequent atmospheric and mantle abundances of H and D. Hydrodynamic outflow is not considered for the rest of the planet's history because the total water abundance in the atmosphere remains small relative to major atmospheric components (CO_2 and N_2) [*Kumar et al.*, 1983; *Krasnopolsky*, 1985]. We discuss further below the duration of the hydrodynamic outflow phase, and the atmospheric H abundance and D/H ratio at the end of this phase.

Any exogenous supply of water to the Venus atmosphere by comets and volatile-rich asteroids [*Grinspoon*, 1987; *Grinspoon and Lewis*, 1988; *Owen et al.*, 1992] is ignored. We may make this assumption, because we seek an upper bound on water abundance in the mantle. An exterior source of water reduces the flux required from the interior and hence decreases the mantle water budget. We discuss the effect of the cometary influx of water on the present atmospheric D/H ratio further below.

Abundances of ^{40}Ar and water in the crust are negligible compared with those in the mantle and atmosphere (Chapter 4). Therefore our treatment amounts essentially to a two-reservoir model (mantle and atmosphere) for volatiles. Nevertheless we include the crustal reservoir so that the volume and rate of crustal production during and after the last catastrophic event are explicitly taken into account in our numerical models. The volume of magmatism during the last catastrophic resurfacing event is not well understood. A thickness of a basaltic surface layer is estimated at several hundred meters to a kilometer from a fracturing model of regularly spaced linear fractures in the gridded plains of Guinevere Planitia [*Banerdt and Sammis*, 1992]. An upper bound on the volume of magmatism is constrained by the crustal thickness estimated from gravity/topography admittances to be between 20 and 50 km [*Grimm*, 1994; *Konopliv and Sjogren*, 1994; *Simons et al.*, 1994]. The rate of magmatism after the last catastrophic event has been

estimated to be between 0.4 and 11 $km^3\ yr^{-1}$ on the basis of the rate of reaction of atmospheric SO_2 and surface carbonates [*Fegley and Prinn*, 1989; *Fegley and Treiman*, 1992]. Two- and three-dimensional Monte Carlo models of volcanic resurfacing provide volcanic resurfacing rates over the last 500 Myr of 0.01 - 0.15 and 0.37 $km^3\ yr^{-1}$, respectively [*Bullock et al.*, 1993; *Strom et al.*, 1994]. Because crustal production by intrusions is not taken into account in volcanic resurfacing models, however, these figures should be regarded only as lower bounds on the rate of crustal magmatism after the last catastrophic resurfacing event. Analysis of the cratering record on volcanic terrains also constrain the rate of volcanic resurfacing [*Namiki and Solomon*, 1994; *Price and Suppe*, 1994]. For a terrestrial volumetric ratio of intrusive to extrusive magmatism of between 10 and 17 [*Crisp*, 1984; *Coffin and Eldholm*, 1994], the rate of crustal production over the last several hundred million years is estimated to be 2 $km^3\ yr^{-1}$ [*Price*, 1995b] and less than 7.2 $km^3\ yr^{-1}$ [*Namiki and Solomon*, 1994].

Basic Equations for Mantle Degassing and Atmospheric Evolution

We adopt the set of differential equations for the transfer of K and Ar derived in the previous chapter:

$$\frac{d(^{40}K)_M}{dt} = -\lambda_{40}(^{40}K)_M - \pi^K_{M\to C}(^{40}K)_M \quad (1)$$

$$\frac{d(^{40}Ar)_M}{dt} = y_{40}\lambda_{40}(^{40}K)_M - \pi^{Ar}_{M\to A}(^{40}Ar)_M \quad (2)$$

$$\frac{d(^{40}K)_C}{dt} = -\lambda_{40}(^{40}K)_C + \pi^K_{M\to C}(^{40}K)_M \quad (3)$$

$$\frac{d(^{40}Ar)_C}{dt} = y_{40}\lambda_{40}(^{40}K)_C \quad (4)$$

$$\frac{d(^{40}Ar)_A}{dt} = \pi^{Ar}_{M\to A}(^{40}Ar)_M \quad (5)$$

where $(^{40}K)_M$, $(^{40}Ar)_M$, $(^{40}K)_C$, $(^{40}Ar)_C$, and $(^{40}Ar)_A$ are the mass of the designated isotope in each reservoir (subscript *M*, *C*, and *A* denote mantle, crust, and atmosphere, respectively), *t* is the time since planet formation, λ_{40} and y_{40} are the decay constant and

yield of ^{40}Ar from the radioactive decay of ^{40}K [*McDougall and Harrison*, 1988], and $\pi^{K}_{M\rightarrow C}$ and $\pi^{Ar}_{M\rightarrow A}$ are the degassing coefficients of K and Ar. Degassing coefficients are derived further below from the principles of partial melting of mantle material and partitioning of volatiles between basaltic melt and residuum solid (Chapter 4) [*Ozima and Podosek*, 1983]. We neglect transfer of Ar from mantle to crust and from crust to atmosphere in equations (2), (4), and (5), because the amount of ^{40}Ar retained in igneous rocks immediately after emplacement is minor compared with that degassed during eruption, and because Ar diffusion in the Venus crust is sufficiently slow that the contribution of crustal ^{40}Ar to the atmospheric reservoir is negligible (Chapter 4). The estimated primordial $^{40}Ar/^{36}Ar$ ratio at $t = 0$ is so small that any primordial component to present atmospheric ^{40}Ar may be considered negligible [*Ozima and Podosek*, 1983]. We therefore assume zero primordial ^{40}Ar in both interior and atmospheric reservoirs, i.e., $(^{40}Ar)_M = (^{40}Ar)_C = (^{40}Ar)_A = 0$ at $t = 0$.

For the corresponding equations governing H_2O degassing and escape, there is no radiogenic source term in the mantle evolution equation, but H and D escape fluxes must be included in the equations for the atmosphere:

$$\frac{d(H_2O)_M}{dt} = -\pi^{water}_{M\rightarrow A}(H_2O)_M \tag{6}$$

$$\frac{d(H)_A}{dt} = \frac{2}{18}\times\pi^{water}_{M\rightarrow A}(H_2O)_M - F^H \tag{7}$$

$$\frac{d(D)_A}{dt} = \frac{4}{18}\times\pi^{water}_{M\rightarrow A}(H_2O)_M \times\left(\frac{D}{H}\right)_{prim} - F^D \tag{8}$$

where $(H_2O)_M$ is mass abundance of H_2O in the mantle reservoir, $(H)_A$ and $(D)_A$ are mass abundances of hydrogen and deuterium in the atmosphere, $\pi^{water}_{M\rightarrow A}$ is the degassing coefficient of water from mantle to atmospheric reservoirs, $(D/H)_{prim}$ is the primordial D/H atomic ratio in the Venus mantle, i.e., the D/H ratio of protoplanetary material at $t = 0$, and F^H and F^D are the escape fluxes of H and D from the atmosphere to interplanetary space. The atmospheric H_2O, HDO, and D_2O abundances are expressed

by equivalent atmospheric budgets of H and D in equations (7) and (8) for mathematical convenience. We discuss temporal variations of F^H and F^D below.

D/H ratios measured in terrestrial sea water and in hydrated minerals in meteorites show a good agreement (~1.6 x 10^{-4}), suggesting that $(D/H)_{prim}$ is constant throughout the inner solar system [*Geiss and Reeves*, 1981; *Krasnopolsky*, 1985]. In contrast, the deuterium abundance in the atmosphere of Jupiter, and presumably in the primordial solar nebula, yields a D/H ratio as low as 2 x 10^{-5} [*Geiss and Reeves*, 1981; *Gautier and Owen*, 1983]. We therefore adopt 1.6 x 10^{-4} as a nominal value and 2 x 10^{-5} as a lower bound on $(D/H)_{prim}$. For the present atmospheric D/H ratio, we adopt (1.9 ± 0.6) x 10^{-2}, a value determined from ground-based observations of near-infrared absorption lines of H_2O and HDO [*de Bergh et al.*, 1991] as well as from a recent re-analysis of the Pioneer Venus mass spectrometer data [*Donahue and Hodges*, 1992].

Water is assumed to be a major gas species carrying hydrogen and deuterium in both the mantle and atmospheric reservoirs [*von Zahn et al.*, 1983; *Holland*, 1984], and no isotopic fractionation is assumed during mantle degassing in equation (8). A lower degassing of water from basaltic magma on Venus than on Earth has been suggested on the basis of the high solubility of water in magma [*Holloway*, 1992], but nearly 100% of the H_2O dissolved in terrestrial magma is forced to degas to the atmosphere as magma solidifies following volcanic eruptions and intrusions into shallow reservoirs [*Westrich et al.*, 1988]. The crust as a reservoir for water is thus ignored. Hydrous minerals are unstable at the surface on Venus, at least under current P-T conditions [*Fegley and Treiman*, 1992]. Therefore the return of H_2O to the mantle through crustal recycling is ignored as well in equations (6) to (8).

Degassing Coefficients

The physical mechanisms governing mantle degassing are partial melting of mantle material and partitioning of volatiles between basaltic melt and residuum minerals. The

degassing coefficients, $\pi^{Ar}_{M\to A}$ and $\pi^{water}_{M\to A}$, are derived by assuming equilibrium partitioning between melt and solid, equilibrium batch melting [*Kinzler and Grove*, 1992], and complete degassing from the melt (Chapter 4) [*Ozima and Podosek*, 1983]

$$\pi^{K}_{M\to C} = \frac{1}{K^{K}_{mode} + f_{melt}(1 - K^{K}_{stoi})} \frac{Q_C}{M_M} \tag{9}$$

$$\pi^{Ar}_{M\to A} = \frac{1}{K^{Ar}_{mode} + f_{melt}(1 - K^{Ar}_{stoi})} \frac{Q_C}{M_M} \tag{10}$$

$$\pi^{water}_{M\to A} = \frac{1}{K^{water}_{mode} + f_{melt}(1 - K^{water}_{stoi})} \frac{Q_C}{M_M} \tag{11}$$

where f_{melt} is the fractional degree of partial melting, M_M is the mass of the mantle, Q_C is the rate of crustal production, K_{mode} is an average of mineral partition coefficients weighted by the modal abundances of mantle material prior to partial melting, and K_{stoi} is an average of mineral partition coefficients weighted by the stoichiometric coefficients of the melting reaction [*Kinzler and Grove*, 1992]. The mass of the mantle is determined by subtracting the mass of the crust at the appropriate model time from the mass of the bulk silicate portion of Venus, 3.4 x 10^9 kg (70% of the planetary mass [*Basaltic Volcanism Study Project*, 1981]). The possible existence of an undegassed portion of the Venus mantle (Chapter 4) is considered further below by treating the mass of the degassed mantle as a free parameter. The assumed modal abundances of mantle material, the stoichiometric coefficients, and the mineral partition coefficients for K and Ar are discussed in Chapter 4. We make use of those estimates of partition coefficients to constrain upper and lower bounds on $\pi^{K}_{M\to C}$ and $\pi^{Ar}_{M\to A}$ (Table 5.1). For partitioning of water between basaltic melt and residuum solid, we adopt the bulk partition coefficients of 0.01 for both K^{water}_{mode} and K^{water}_{stoi} (Table 5.1) on the basis of a correlation between water and incompatible elements in MORB rocks [*Dixon et al.*, 1988; *Michael*, 1988; *Bell and Rossman*, 1992].

The value for f_{melt} is estimated to be between 0.02 to 0.16 for the last catastrophic resurfacing event on the basis of U and Th concentrations in Venera and Vega samples [*Surkov et al.*, 1987] and those in the bulk silicate Earth [*Basaltic Volcanism Study*

Project, 1981; *Dreibus and Wänke*, 1989; *McDonough et al.*, 1992; *Kargel and Lewis*, 1993]. Because of a lack of geological information on magmatism significantly predating the most recent global resurfacing, we presume a temporally constant f_{melt}. Q_C is considered to represent a full crustal production rate because both extrusive and intrusive igneous rocks are likely to degas nearly all of the volatiles contained in mantle-derived melts (Chapter 4) [*Westrich et al.*, 1988]. Strictly speaking, however, Q_C represents the supply of magma that releases volatiles to the atmosphere at the surface or from near-surface reservoirs. If there exists a component of the magmatic flux that does not degas, our derived crustal production rate will be an underestimate. Our estimate of water concentration in Venus mantle, on the other hand, will be little affected because such a component of magmatic flux is isolated from the atmospheric evolution of both ^{40}Ar and water.

Hydrogen and Deuterium Escape Mechanisms

The atmospheric escape of hydrogen occurs by three processes: supply of hydrogen from water vapor at the surface to the homopause (presently at about 120 km altitude [*Krasnopolsky*, 1985]), diffusive transfer of hydrogen in the heterosphere (about 120 to 160 km altitude [*Seiff*, 1983]), and loss of hydrogen from the exosphere [*Hunten and Donahue*, 1976; *Houghton*, 1986]. The first process is governed by the water cycle in the homosphere and can be described by a functional relationship between the water vapor volume mixing ratio in the lower atmosphere, X^{water}_{surf}, and the hydrogen mixing ratio at the homopause, X^{H}_{homo}. Because most of the atmospheric mass is concentrated in the lower atmosphere, we treat X^{water}_{surf} as equivalent to a sum of $(H)_A$ and $(D)_A$. The second and third processes are combined and described by another functional relationship between X^{H}_{homo} and the hydrogen escape flux from the exosphere, F^H [*Kumar et al.*, 1983; *Krasnopolsky*, 1985; *Grinspoon and Lewis*, 1988].

Sulfuric Acid Trap and Cold Trap. The quantity X^H_{homo} in an atmosphere that contains as little water as the present Venus atmosphere is controlled by the sulfur cycle in the lower atmosphere. Photochemical reactions between H_2O and SO_2 near the cloud tops (at 62 km altitude [*Krasnopolsky and Pollack*, 1994]) form H_2SO_3 that, in turn, is decomposed to H_2O and SO_3 near the surface [*Lewis and Prinn*, 1984; *Krasnopolsky and Pollack*, 1994]. This sulfur cycle between the clouds and the surface restricts water vapor from regions above 62 km in altitude and thus limits X^H_{homo} at the homopause. This sulfuric acid trap has been extensively studied [*Kumar et al.*, 1983; *Krasnopolsky*, 1985; *Krasnopolsky and Pollack*, 1994]; however, previous workers assumed a value for present X^{water}_{surf} of 200 ppm, a plausible estimate at that time [*von Zahn et al.*, 1983] but more recently shown to be high on the basis of near-infrared observations of the lower atmosphere [*Bell et al.*, 1991; *de Bergh et al.*, 1991; *Drossart et al.*, 1993; *Pollack et al.*, 1993].

Spectroscopic data from ground-based observations [*Bell et al.*, 1991; *de Bergh et al.*, 1991] and from the spectrometer on board the Galileo spacecraft [*Drossart et al.*, 1993] have greatly reduced the uncertainty in the water abundance associated with prior measurements [*von Zahn et al.*, 1983]. Recent analysis of those spectroscopic data show that the H_2O abundance between 10 and 40 km altitude is constant at 30 ± 10 ppm [*Pollack et al.*, 1993]. The present value of X^H_{homo} has been estimated at between 0.42 and 0.6 ppm [*Krasnopolsky and Parshev*, 1981; *Krasnopolsky*, 1985] from a downward extrapolation of the noon hydrogen number density at 165 km [*Brinton et al.*, 1980]. These estimates of present X^{water}_{surf} and X^H_{homo} satisfy a linear relation postulated by *Kumar et al.* [1983]

$$X^H_{homo}(t) = 2 \times 10^{-2} X^{water}_{surf}(t) \tag{12}$$

for small values of $X^{water}_{surf}(t)$.

As $X^{water}_{surf}(t)$ increases, the water vapor mixing ratio above the clouds increases, and water vapor starts to condense at the altitude where temperature is the lowest

[*Henderson-Sellers*, 1983]. $X^H_{homo}(t)$ is then limited by the phase equilibrium between water vaporization and condensation. *Kasting and Pollack* [1983] and *Kumar et al.* [1983] adopt an upper bound on $X^H_{homo}(t)$ of 4×10^{-5} due to this cold trap in Venus' past atmosphere, while *Krasnopolsky* [1985] pointed out that water vapor is likely to supersaturate at the cold trap, so the upper bound should be larger by a factor of 5 to 10 than the above value on the basis of a comparison between mixing and condensation time scales. For our goal of providing an upper bound on the water concentration in the mantle, we assume that the upper bound on $X^H_{homo}(t)$ is a factor of 10 greater than the value for saturation of water at the cold trap [*Krasnopolsky*, 1985]:

$$X^H_{homo}(t) \leq 4.0 \times 10^{-4} \tag{13}$$

Energy and Diffusion Limits. There are four nonthermal processes important for H escape from the present atmosphere of Venus [*Donahue and Hartle*, 1992]: charge exchange between low-temperature H atoms and high-temperature H^+ ions [*Hodges and Tinsley*, 1986; *Brace et al.*, 1987], collisions of H atoms with high-speed hot O atoms produced by dissociative recombination of O_2^+ (termed hot-O impact, or collisional ejection) [*McElroy et al.*, 1982; *Gurwell and Yung*, 1993], outflow of H^+ ions in the plasma tail (termed solar-wind pickup) [*Brace et al.*, 1987], and upward H^+ flow into the solar wind (termed ion escape) [*Donahue and Hartle*, 1992]. Functional relationships between F^H and X^H_{homo} have been examined for charge exchange and hot-O impact processes [*Kumar et al.*, 1983; *Krasnopolsky*, 1985], but similar relations for solar-wind pick up and ion escape processes have not been derived. For simplicity, we assume a linear relationship between F^H and X^H_{homo}. We adopt lower and upper bounds on the present value of F^H of 0.4 and 2.8×10^7 atoms $cm^{-2}\ s^{-1}$, or 0.96 and 6.7×10^6 kg yr^{-1} [*Donahue and Hartle*, 1992; *Grinspoon*, 1993], respectively, and we calculate the present value of X^H_{homo} from equation (12) and a present X^{water}_{surf} of 30 ± 10 ppm [*Bell et al.*, 1991; *de Bergh et al.*, 1991; *Drossart et al.*, 1993; *Pollack et al.*, 1993]. While the

assumed proportionality between F^H and X^H_{homo} is *ad hoc* and perhaps too simplified, our numerical results are not strongly affected by this assumption because an upper bound on F^H is constrained by energy and diffusion limits described below.

The current hydrogen escape from the Venus exosphere is limited by energy input from the solar extreme ultraviolet (EUV) flux. This upper bound on F^H is termed the energy limit [*Hunten et al.*, 1989]. We assume that F^H is proportional to the available EUV flux and that EUV intensity decreases with time [*Zahnle and Walker*, 1982; *Hunten et al.*, 1989]. By combining the temporal variation of the EUV flux given by *Hunten et al.* [1989] with the proportionality assumed above, F^H is given by

$$F^H(t) = F^H(t_P)\frac{X^H_{homo}(t)}{X^H_{homo}(t_P)}\left(\frac{t}{t_P}\right)^{-5/6} \tag{14}$$

where t_P is the age of the planet, 4.55 Gyr. Equation (14) allows H escape to increase indefinitely at the beginning of planetary history. There is a limit on the H escape flux, however, as a result of the slow rate of diffusion of H through the heterosphere [*Hunten*, 1973; *Hunten et al.*, 1989]. This diffusion limit on the H escape flux can be estimated by means of laboratory measurements of the bimolecular diffusion coefficient for H atoms and other gas species. Under the assumption of a background CO_2 atmosphere at an exospheric temperature of 275 K, this upper bound is given by

$$F^H(t) \le 9.6\times10^{12} X^H_{homo}(t) \text{ kg yr}^{-1} \tag{15}$$

[*Kasting and Pollack*, 1983]. From a comparison of equations (14) and (15), the time when the limiting mechanism for hydrogen escape changes from diffusion to energy input, t^H_{diff}, can be immediately calculated

$$t^H_{diff} = \left(\frac{F^H(t_P)}{9.6\times10^{12}\times X^H_{homo}(t_P)}\right)^{6/5} t_P \tag{16}$$

A lower bound on t^H_{diff} is calculated at 380 Myr by adopting a lower bound on $F^H(t_P)$ and an upper bound on $X^{water}_{surf}(t_P)$ (equation (12)). This value of t^H_{diff} is less than the assumed duration of the hydrodynamic outflow phase, i.e., F^H would not be diffusion-

limited for this set of parameters after the end of the hydrodynamic outflow phase at $t = t_{HO}$. On the other hand, an upper bound on $F^H(t_P)$ and a lower bound on $X^{water}{}_{surf}(t_P)$ yield a $t^H{}_{diff}$ larger than t_P because the adopted parameters violate the present diffusion limit (equation (15)). To avoid violating this limit, we assume upper bounds on $F^H(t_P)$ of 3.4, 4.8, and 6.7 x 10^6 kg yr^{-1} for $X^{water}{}_{surf}(t_P)$ equal to 20, 30, and 40 ppm, respectively. The respective upper bounds on $t^H{}_{diff}$ are 4.0, 3.7 and 4.0 Gyr, respectively.

Fractionation of the Atmospheric D/H Ratio. The deuterium escape flux, $F^D(t)$, is scaled relative to $F^H(t)$ by two factors [*Krasnopolsky*, 1985; *Grinspoon*, 1993; *Gurwell and Yung*, 1993]. First, $F^D(t)$ is assumed to be proportional to the D abundance at the homopause and is thus reduced from $F^H(t)$ by the D/H ratio at the homopause. We assume that this ratio is constant with altitude in the homosphere and is given by $(D)_A/(H)_A$. Second, because a D atom is twice heavy as an H atom, it is more resistant to atmospheric escape. $F^D(t)$ is therefore further reduced by an amount termed the fractionation factor, f_{frac}, expected to be different for various escape processes. *Donahue and Hartle* [1992] estimated f_{frac} to be 0.14 at present for an average of the four nonthermal escape processes. On the basis of a more recently published value of f_{frac} for hot-O impact [*Gurwell and Yung*, 1993], their estimate for the present average f_{frac} should be modified slightly to 0.16. Under the assumption that f_{frac} is constant in time, we obtain

$$F^D(t) = 0.16\frac{(D)_A}{(H)_A}F^H(t)$$
$$= 0.16\frac{(D)_A}{(H)_A}F^H(t_P)\frac{X^H_{homo}(t)}{X^H_{homo}(t_P)}\left(\frac{t}{t_P}\right)^{-5/6} \qquad (17)$$

While we assume that both $F^H(t)$ and $F^D(t)$ are proportional to $X^H{}_{homo}(t)$ as stated above, each escape process may have a different functional behavior over a range of $X^H{}_{homo}(t)$ [*Kumar et al.*, 1983]. f_{frac} may also vary with time as the relative importance of each

escape process changes under variations in $X^H_{homo}(t)$. We discuss this point further below.

Deuterium escape is also limited by gas diffusion in the heterosphere for sufficiently high energy input by solar EUV in the past. The diffusion coefficient of an isotope in the heterosphere is proportional to the square root of atomic mass [*Masson and Marrero*, 1970; *Hunten*, 1973]. We use equation (15) to derive a diffusion limit for F^D:

$$F^D(t) \leq \frac{1}{\sqrt{2}} \times 9.6 \times 10^{12} \frac{(D)_A(t)}{(H)_A(t)} X^H_{homo}(t) \text{ kg yr}^{-1} \tag{18}$$

In a manner similar to that used to obtain t^H_{diff} in equation (16), we can derive the time after which diffusion through the heterosphere no longer limits D escape, t^D_{diff}, from equations (17) and (18):

$$\begin{aligned} t^D_{diff} &= \left(\frac{0.16 \times \sqrt{2} \times F^H(t_P)}{9.6 \times 10^{12} \times X^H_{homo}(t_P)} \right)^{6/5} t_P \\ &= \left(0.16 \times \sqrt{2}\right)^{6/5} t^H_{diff} \end{aligned} \tag{19}$$

Thus t^D_{diff} is about a factor of 6 shorter than t^H_{diff}, indicating that F^D is energy-limited over the most of the planet's history subsequent to $t = t_{HO}$ even for upper bounds on t^H_{diff}.

NUMERICAL RESULTS

Mantle Water Abundance Over the Last 500 Myr

We first treat the question of the water abundance in the Venus mantle at the time of and since the last global resurfacing event by adopting equations (6), (7), and (8). In particular, we wish to test the consistency of our results with those of *Grinspoon* [1993] and to extend his conclusion regarding the depletion of water in Venus magmas (relative to terrestrial magmas) over a wider ranges of parameters. Only two conditions are given for the three differential equations with respect to time, namely $(H)_A(t_P)$ and $(D)_A(t_P)$. We therefore assume a value for $(H_2O)_M(t_P)$ in order to integrate the three differential equations backwards in time from the present to the end of the last catastrophic resurfacing event. The values for $(H)_A$, $(D)_A$, and $(H_2O)_M$ at the beginning of the last catastrophic resurfacing event are then calculated by means of finite difference analogues to equations (6) to (8). These calculated values at the beginning of the resurfacing event, of course, must be non-negative. This constraint thus provides an upper bound on $(H_2O)_M(t_P)$, because the contribution to the atmosphere at $t = t_P$ of atmospheric H present before the last global resurfacing event is a minimum when $(H)_A$ at the time immediately before that resurfacing event is zero.

The atmospheric water abundance (the sum of H_2O, HDO, and D_2O abundances), upper bounds on the mantle water concentration, and the atmospheric D/H ratio so calculated are shown as functions of time in Figures 5.1a, 5.1b, and 5.1c, respectively. The present atmospheric abundance is assumed variously to be 20 ppm (dotted lines), 30 ppm (dashed lines), and 40 ppm (solid lines), and the time of the last catastrophic resurfacing is assumed to be either 300 or 500 Myr ago. The present atmospheric D/H ratio and $(D/H)_{prim}$ are taken to be 0.019 [*Donahue et al.*, 1982; *de Bergh et al.*, 1991; *Donahue and Hodges*, 1992] and 1.6×10^{-4} [*Grinspoon*, 1993], respectively, for all six cases. Also assumed are $f_{melt} = 0.04$ both during and after the last catastrophic resurfacing event (Chapter 4), a rate of magmatism after the last catastrophic event of 1

$km^3\ yr^{-1}$ [*Fegley and Treiman*, 1992; *Namiki and Solomon*, 1994; *Price*, 1995], and a volume of magmatism during the last catastrophic event equivalent to an average thickness over the planetary surface of 5 km. The calculated values for $(H_2O)_M(t_P)$ increase as F^H increases. We then adopt the values of $F^H(t_P)$ of 3.4, 4.8, and 6.7 x 10^6 kg yr^{-1} for the cases with $X^{water}_{surf}(t_P)$ of 20, 30, and 40 ppm, respectively, so that the calculated upper bounds on $(H_2O)_M(t_P)$ are the highest permitted for the given set of parameters but respective values for t^H_{diff} do not exceed t_P (equation (16)).

The calculated history of the atmospheric water abundance, for a given value of $X^{water}_{surf}(t_P)$, depends on the age of the last catastrophic resurfacing event (Figure 5.1a), because the calculated value of $(H_2O)_M(t_P)$ depends strongly on that age (Figure 5.1b). The upper bound on $(H_2O)_M(t_P)$ is greatest when upper bounds on $X^{water}_{surf}(t_P)$ and on the age of the last catastrophic resurfacing event are assumed for given values of the volcanic flux and f_{melt} (Figure 5.1b). As shown in Figure 5.1c, the atmospheric D/H ratios at 300 and 500 Myr ago are still significantly greater than $(D/H)_{prim}$, so the value for $(D)_A$ before the last catastrophic event is always positive even though a zero value for $(H)_A$ before the event has been assumed. Because $(D)_A$ is not directly involved in constraining the upper bound on $(H_2O)_M(t_P)$, the results depend little on the assumed values for the present atmospheric D/H ratio or for $(D/H)_{prim}$.

This procedure has been repeated for a series of models parameterized by the volume of magmatism during the last catastrophic resurfacing event and the rate of magmatism after that event. In Figure 5.2a, we show contours of the calculated upper bound on $(H_2O)_M(t_P)$. The $X^{water}_{surf}(t_P)$, $F^H(t_P)$, and the age of the last catastrophic event are assumed to be 40 ppm, 6.7 x 10^6 kg yr^{-1}, and 500 Myr, respectively, to maximize these upper bounds. The value of f_{melt} is assumed to be 0.04 both during and after the last catastrophic resurfacing event (Chapter 4). *Grinspoon* [1993] assumed a rate of steady magmatism of 0.4 $km^3\ yr^{-1}$ to estimate an upper bound on magmatic water concentration of 50 ppm. This figure can be converted to the water content in the mantle of 2.5 ppm by

means of the usual partition coefficient relation (equation (11) in Chapter 4) for an assumed $f_{melt} = 0.04$ and $K^{water}_{mode} = K^{water}_{stoi} = 0.01$ (Table 5.1). The rate of steady magmatism assumed by *Grinspoon* [1993] is denoted by the cross symbol in Figure 5.2a. A good agreement between our results and his is obtained because the upper bound on $(H_2O)_M(t_P)$ is constrained primarily from the near steady balance at present between mantle degassing and atmospheric escape.

The above conversion of magmatic water concentration to mantle water concentration indicates that the calculated upper bound increases as f_{melt} increases. Therefore in Figure 5.2b, we assume an upper bound on f_{melt}, 0.16 (Chapter 4), to constrain allowable maxima of $(H_2O)_M(t_P)$ within the ranges of other parameters. It is clearly illustrated in Figure 5.2 that the maximum $(H_2O)_M(t_P)$ varies over more than three orders of magnitude and depends strongly on the total volume of magmatism during and after the last catastrophic resurfacing event.

Mantle Water Abundance Before the Last Catastrophic Resurfacing Event

The upper bounds on $(H_2O)_M(t_P)$ in Figures 5.2a and 5.2b are not well constrained because the volume of magmatism during and after the last catastrophic resurfacing event have been poorly constrained by geological observations [*Fegley and Prinn*, 1989; *Namiki and Solomon*, 1994; *Strom et al.*, 1994]. However, the total amount of magmatism over the planet's history is constrained by the present atmospheric ^{40}Ar abundance (Chapter 4) [*Pollack and Black*, 1982; *Volkov and Frenkel*, 1993; *Matsui and Tajika*, 1995]. We may thus examine mantle degassing and atmospheric escape over the planet's history by combining ^{40}Ar degassing and H escape, and we may thereby constrain further the upper bound on $(H_2O)_M(t_P)$ as well as explore the temporal variation of the mantle water budget.

The amount of magmatism that occurred before the last catastrophic resurfacing event can be calculated by subtracting the contributions to atmospheric ^{40}Ar degassed during

and after that resurfacing event from $(^{40}Ar)_A(t_P)$. The history of magmatism is difficult to constrain, so for simplicity we assume a constant crustal production rate between $t = 0$ and the time of the last catastrophic event. Because any primordial component of ^{40}Ar is negligible in the present atmosphere and because the radioactive decay of ^{40}K has a half life of 1.25 Gyr, the derived crustal production rate does not depend strongly on the specifics of any extensive period of mantle convection and enhanced degassing in the first several hundred million years after the planet's formation [*Pollack and Black*, 1982]. Our derived crustal production rate thus should be regarded as an average over approximately the last 3.5 Gyr of the planet's magmatic history.

In order to constrain upper bounds on $(H_2O)_M(t_P)$, we calculate a lower bound on crustal production rate from the ^{40}Ar degassing model, because water concentration in magma increases for given $(H)_A$ and $(D)_A$ as the total volume of magmatism decreases. To minimize crustal production rate, we assume a lower bound on $(^{40}Ar)_A(t_P)$ of 21 ppm, parameters appropriate to maximum Ar degassing and minimum K differentiation (Table 5.1), an upper bound on the K concentration in bulk silicate portion of Venus of 250 ppm (Chapter 4), and a lower bound on f_{melt} before the last catastrophic event of 0.02 (Chapter 4). The values for f_{melt} during and after the last catastrophic resurfacing event are assumed to be 0.16, as in Figure 5.2b. In Figure 5.3, we show contours of the lower bound on crustal production rate calculated to satisfy $(^{40}Ar)_A(t_P)$ for a given volume of magmatism during the last catastrophic resurfacing event (ordinate) and a given rate of magmatism after the catastrophe (abscissa). The contour line of zero crustal production rate in Figure 5.3 denotes the amount of magmatism sufficient to account for $(^{40}Ar)_A(t_P)$ solely by activity during and after the last catastrophic event.

The results shown in Figure 5.3 may be used to constrain the history of water degassing and atmospheric escape of H and D. For this calculation we integrate equations (6), (7), and (8) forward in time from the end of the hydrodynamic outflow phase to the present. As discussed above, we are given only two conditions for the three

differential equations with respect to time ($(H)_A(t_P)$ and $(D)_A(t_P)$). So we adopt an atmospheric D/H ratio at $t = t_{HO}$ to provide the third integration constant. The atmospheric D/H ratio at $t = t_{HO}$ is fractionated from $(D/H)_{prim}$ during the hydrodynamic outflow phase [*Kasting and Pollack*, 1983]. Semianalytic models for isotopic fractionation by hydrodynamic outflow have been developed to account for the variable noble gas patterns measured in meteorites and in the atmospheres of the terrestrial planets [*Donahue*, 1986; *Zahnle and Kasting*, 1986; *Hunten et al.*, 1987; *Sasaki and Nakazawa*, 1988; *Zahnle et al.*, 1990; *Pepin*, 1991]. However, the D/H fractionation has not been well constrained because these semianalytic models of fractionation are dependent on the vigor of the hydrogen escape flux, which is not well understood [e.g., *Zahnle et al.*, 1990; *Pepin*, 1991]. So as a lower bound on the D/H ratio in the atmosphere at $t = t_{HO}$, we assume no fractionation during the hydrodynamic outflow phase, i.e., $(D/H)_A(t_{HO}) = (D/H)_{prim}$. In the absence of an upper bound on the D/H ratio in the atmosphere at $t = t_{HO}$, we assume an infinitely high D/H ratio, i.e., $(H)_A(t_{HO}) = 0$. Again, the assumption of zero $(H)_A(t_{HO})$ provides an upper bound on $(H_2O)_M(t_P)$ because the contribution to $(H)_A(t_P)$ of atmospheric H present immediately after the hydrodynamic outflow phase is a minimum. On the other hand, the assumption that the atmospheric D/H ratio at $t = t_{HO}$ equals $(D/H)_{prim}$ provides a lower bound on $(H_2O)_M(t_P)$.

In Figure 5.4a, we show an example of temporal variations in $(H)_A$, $(D)_A$, and $(^{40}Ar)_A$ for the following parameters: a volume of magmatism during the last catastrophic resurfacing event equivalent to an average thickness of 5 km, a rate of magmatism after the last catastrophe of 1 $km^3\ yr^{-1}$ [*Fegley and Treiman*, 1992; *Namiki and Solomon*, 1994; *Price*, 1995], $f_{melt} = 0.16$ during and after the last catastrophic event, and $f_{melt} = 0.02$ before that event (Chapter 4). The present atmospheric D/H ratio and $(D/H)_{prim}$ are assumed to be 0.019 and 1.6×10^{-4}, respectively. Again, a lower bound on $(^{40}Ar)_A(t_P)$, parameters appropriate to maximum Ar degassing and minimum K differentiation (Table 5.1), and an upper bound on the present K abundance in the bulk

silicate portion of Venus are assumed to yield a lower bound on the crustal production rate before the last catastrophic resurfacing event. The present atmospheric water abundance and $F^H(t_P)$ are assumed to be 40 ppm and 6.7 x 10^6 kg yr^{-1}, respectively, but the atmospheric evolution of H and D is not strongly dependent on these assumed values because $F^H(t_P)$ is diffusion-limited over most of the planet's history (t^H_{diff} = 4.0 Gyr).

The effect on $(H)_A$ and $(D)_A$ of adopting the upper and lower bounds on the D/H ratio at $t = t_{HO}$ are shown in Figure 5.4a by solid and dotted lines, respectively. It is clear from the figure that the effect of these alternative conditions for the D/H ratio at $t = t_{HO}$ is negligible by the time of the last catastrophic resurfacing event. Therefore the two conditions result in nearly identical temporal variations of $(H_2O)_M$ (Figure 5.4b). This outcome occurs because we are integrating forward in time in this calculation rather than backwards as in Figure 5.1. In other words, these figures demonstrate that we cannot constrain the composition of the early atmosphere from the present atmospheric H and D abundances (Figure 5.4a) or the present atmospheric D/H ratio (Figure 5.4c). Contributions from the early atmosphere are negligible by about 3 Gyr after planetary formation, and the present atmosphere is dominated by the subsequent degassing during and after the last catastrophic resurfacing event (Figure 5.4a). This result indicates that the upper bounds on $(H_2O)_M(t_P)$ are insensitive to the assumed value for t_{HO}, as long as it is less than 1.5 Gyr. We note that the coincidence of the calculated curves for $(H_2O)_M$ for the two different conditions at $t = t_{HO}$ does not indicate that a lower bound on $(H_2O)_M$ is well determined, because other parameters have been set so as to maximize $(H_2O)_M(t_P)$ and also because any cometary contribution to atmospheric water is not taken into account.

We have repeated the above calculations for a series of models parameterized by the volume of magmatism during the last catastrophic resurfacing event and the rate of magmatism after that event (Figure 5.5a). The value of f_{melt} is assumed to be 0.02 before the last resurfacing event and to be 0.16 during and after that event. The present

atmospheric D/H ratio, $(D/H)_{prim}$, and $(H)_A(t_{HO})$ are again assumed to be 0.019 and 1.6×10^{-4}, and zero, respectively. The shaded area in Figure 5.5a denotes models that result in negative $(D)_A(t_{HO})$, i.e., models that degas too little H by recent volcanic activity to satisfy the present atmospheric D/H ratio. This constraint depends mostly on the assumed present atmospheric D/H ratio and $(D/H)_{prim}$. By adopting an upper bound on the present atmospheric D/H ratio of 0.025 and a lower bound of $(D/H)_{prim}$ of 2.0×10^{-5}, this constraint is removed from Figures 5.5a and 5.5b without changing significantly the calculated upper bounds on $(H_2O)_M(t_P)$. By comparing Figures 5.2b and 5.5a, it is clear that upper bounds on the mantle water budget significantly decrease by considering models that combine H and D escape with ^{40}Ar degassing in an internally consistent manner. The upper bound on $(H_2O)_M(t_P)$ is then 15 ppm (Figure 5.5a).

As shown in Figure 5.4b, the decrease in $(H_2O)_M$ with time is small compared with the absolute abundance (compare Figures 5.5a and 5.5b). Such a near constancy of $(H_2O)_M(t)$ holds because we have assumed a minimum crustal production rate in order to yield an upper bound on $(H_2O)_M(t_P)$. For instance, for Figure 5.4b, we have adopted a crustal production rate of 2.2 $km^3\ yr^{-1}$ and a value for f_{melt} before the catastrophic resurfacing event of 0.02. With the bulk partition coefficients given in Table 5.1 and a mantle mass of 3.4×10^{24} kg, $\pi^{water}_{M \rightarrow A}$ before that event is $5.7 \times 10^{-11}\ yr^{-1}$. Then the characteristic time for mantle water degassing, i.e., the reciprocal of the degassing coefficient, is 17 Gyr, sufficiently high to account for the small temporal variation of $(H_2O)_M$ over 3.5 Gyr.

If instead a higher crustal production rate is assumed prior to the last global resurfacing event, $(H_2O)_M$ in the past may be significantly greater while $(H_2O)_M(t_P)$ is significantly less than in Figure 5.5a. In Figures 5.6a, 5.6b, and 5.6c, we show contours of $(H_2O)_M$ at $t = t_P$, 2 Gyr, and t_{HO}, respectively, for models in which the rate of magmatism before the last catastrophic resurfacing event is taken to be 25 $km^3\ yr^{-1}$. The value of f_{melt} is assumed to be 0.02 before the last catastrophe and to be 0.16 during and

after it, as in Figures 5.5a and 5.5b. The present atmospheric D/H ratio, $(D/H)_{prim}$, and $(H)_A(t_{HO})$ are assumed to be 0.025 and 2×10^{-5}, and zero, respectively. A comparison of Figures 5.5a and 5.6a shows that $(H_2O)_M(t_P)$ decreases as the rate of magmatism before the last event increases. Figures 5.5b and 5.6c illustrate, in contrast, that $(H_2O)_M(t_{HO})$ increases significantly as the rate of magmatism before the last event increases. Such an abundant water reservoir degasses, however, within a few billion years. Again, by taking bulk partition coefficients from Table 5.1 and a mantle mass of 3.4×10^{24} kg, $\pi^{water}_{M \rightarrow A}$ before the catastrophe is calculated at 7.4×10^{-10} yr^{-1}, yielding the characteristic time for mantle water degassing of 1.4 Gyr. In Figure 5.6b, we show $(H_2O)_M$ at $t = 2$ Gyr (1.5 Gyr after Figure 5.6c) to illustrate that the water budget in the mantle indeed decreases considerably over a time period comparable to the characteristic degassing time.

We turn our attention now to the magnitude and duration of this early abundant water budget in the mantle. For an extreme case of a very high crustal production rate before the last catastrophic resurfacing event, for example, nearly 100% of the water budget in the early mantle degasses shortly after t_{HO}, after which $(H)_A$ decreases continuously with time because the degassing flux of water from the mantle is negligible relative to F^H over the rest of the planet's history. For such a case, the amount of water injected into the early atmosphere is constrained by the upper limit on hydrogen escape flux. Here, for simplicity, we assume that F^H is limited by supersaturation of water vapor at the cold trap (equation (13)) and by diffusion of H in the heterosphere (equation (15)). Then a maximum value for F^H of 3.8×10^9 kg yr^{-1} is calculated, allowing escape of 1.5×10^{19} kg of H over 4 Gyr. This figure corresponds to an atmospheric H_2O abundance 4 Gyr ago of 1.4×10^{20} kg. By dividing by a mass of the bulk silicate portion of Venus of 3.4×10^{24} kg, at most 40 ppm of water is allowed to have been present in the early mantle. If only a portion of the mantle has been degassed over the planet's history, then this upper bound on the early water budget increases inversely with the fraction of the mantle that was outgassed. We note, however, that decreasing the mass of the degassed

mantle increases $\pi^{water}_{M\rightarrow A}$ as described in equation (11), so the rate of water loss from the early mantle is increased. An example of degassing from only a portion of the mantle (33%) is shown in Figures 5.7a, 5.7b, and 5.7c ($t = t_P$, 2 Gyr, and t_{HO}, respectively) for a rate of magmatism before the last catastrophic resurfacing event of 15 $km^3\ yr^{-1}$. The value of f_{melt} is assumed to be 0.02 before the last catastrophe and to be 0.16 during and after it, as in Figures 5.5 and 5.6. The present atmospheric D/H ratio, $(D/H)_{prim}$, and $(H)_A(t_{HO})$ are assumed to be 0.025 and 2×10^{-5}, and zero, respectively.

In Figures 5.7a, 5.7b, and 5.7c, models that result in negative $(D)_A(t_{HO})$, i.e., models that overpredict the present atmospheric D/H ratio for any plausible $(D)_A(t_{HO})$, are indicated by the shaded areas. We note that these shaded areas in Figure 5.7 differ from the shaded areas shown in Figure 5.5. Models in the shaded areas in Figure 5.5 are allowed for a higher present atmospheric D/H ratio and a smaller $(D/H)_{prim}$ than assumed for the models shown. In Figure 5.7, in contrast, because an upper bound on the present atmospheric D/H ratio and a lower bound on $(D/H)_{prim}$ are assumed, models in the shaded areas may be rejected.

We use this constraint on model parameters to evaluate the duration of any period of high mantle water abundance. As shown in Figures 5.7a, 5.7b, and 5.7c, $(H_2O)_M$ at each time is highest at the boundary of the shaded area. We therefore can calculate the highest value of $(H_2O)_M$ at each time by assuming zero values for both $(H)_A(t_{HO})$ and $(D)_A(t_{HO})$ for a given rate of magmatism before the last catastrophic resurfacing event and a given mass of the degassed portion of the Venus mantle. While, strictly speaking, there is a highest value of $(H_2O)_M$ along the boundary, we need only to calculate $(H_2O)_M$ at a single point on the boundary because the boundary is nearly parallel to a contour line (Figures 5.7a, 5.7b, and 5.7c). For simplicity, we choose this point such that the volume of magmatism during the last catastrophic resurfacing event is zero. $(H_2O)_M$ and the rate of magmatism after that event are then calculated to satisfy $(H)_A(t_P)$ and $(D)_A(t_P)$. For cases where the degassed portion of the mantle is a large fraction (e.g., Figure 5.6), the

present D/H ratio in the atmosphere does not restrict possible models. For such cases we calculate the highest value of $(H_2O)_M$ by assuming that the volume of magmatism both during and after the last catastrophic resurfacing event is zero, because the contribution to $(H)_A(t_P)$ of $(H_2O)_M$ before that event is maximum when degassing during and after that event is neglected; $(H_2O)_M$ and $(D)_A(t_{HO})$ are then calculated to satisfy $(H)_A(t_P)$ and $(D)_A(t_P)$.

In Figures 5.8a, 5.8b, and 5.8c, the highest values of $(H_2O)_M$ so calculated are shown for $t = t_{HO}$, 2 Gyr, and 3 Gyr, respectively, as functions of the rate of magmatism before the last catastrophic resurfacing event. The mass of the degassed portion of the mantle is variously assumed to be 10% (solid lines), 25% (dot-dash lines), 33% (dashed lines), and 50% (dot-dot-dash lines) of the mass of the bulk silicate fraction of Venus. Two additional constraints are adopted in Figure 5.8 to limit plausible ranges of mantle water concentration. First, models with crustal production rates too low to satisfy the lower bound on the present atmospheric ^{40}Ar abundance within allowable ranges of other parameters (Chapter 4) are rejected. Second, models that require a rate of magmatism after the last global resurfacing event of greater than 20 $km^3\ yr^{-1}$ (Figure 5.8d) are rejected [*Fegley and Prinn*, 1989; *Namiki and Solomon*, 1994]. These rejected models are shown by dotted lines in Figure 5.8.

A comparison of Figures 5.8a and 5.8b shows that an abundant water budget in the mantle at $t = t_{HO}$ degasses within 1.5 Gyr for a rate of magmatism before the last catastrophe of greater than 15 $km^3\ yr^{-1}$. For a rate of magmatism before the last catastrophe of less than 5 $km^3\ yr^{-1}$, in contrast, the abundance at $t = t_{HO}$ is limited and the decrease of mantle water over the period of 0.5 to 2 Gyr is small. Figures 5.8b and 5.8c thus show that the water abundance in the degassed portion of the Venus mantle has been less than 35 ppm over the last 2.5 Gyr and less than 20 ppm over the last 1.5 Gyr. For $(H_2O)_M(t_P)$, degassing subsequent to times depicted in Figure 5.8 constrains the present water abundance in the degassed mantle to be less than 15 ppm, a figure equal to the

upper bound on $(H_2O)_M(t_P)$ obtained for the whole-mantle degassing models shown in Figure 5.5a.

We note that the water concentration in the mantle before $t = t_{HO}$ is unconstrained by our study, because the hydrodynamic outflow process is not included in our calculation. Extensive hydrogen loss can greatly increase the upper bound on water concentration in the mantle during any hydrodynamic outflow phase. It is unlikely, however, that the hydrodynamic outflow phase continued until recently, because any rapid hydrodynamic outflow ceased abruptly once the water vapor mixing ratio in the lower atmosphere became less than about 0.2 [*Kasting and Pollack*, 1983] or about 0.066 [*Kasting et al.*, 1984], depending on whether water existed only in the vapor phase (runaway greenhouse) or condensed as a liquid (moist greenhouse) at the surface, and because at least a few billion years are needed for the atmosphere to lose sufficient H_2O to reach the present abundance from those values by nonthermal escape processes (Figure 5.4a).

DISCUSSION

The existence of an "ocean" on Venus early in the planet's history has been suggested on the basis of a D/H ratio about 100 times greater than the terrestrial value [*Donahue et al.*, 1982]. This inference was challenged by *Grinspoon* [1987] and *Grinspoon and Lewis* [1988] on the grounds that comets could supply atmospheric water over the planet's history. The widespread volcanism observed in Magellan radar images [*Head et al.*, 1992] and a present atmospheric ^{40}Ar abundance on Venus within a factor of 4 of that of Earth [*Ozima and Podosek*, 1983; *von Zahn et al.*, 1983], on the other hand, suggest that volcanic degassing of water by the postulated catastrophic resurfacing event and by magmatism before and after that event was an important contributor to atmospheric H and D abundances.

Following *Grinspoon* [1993], we have estimated the water concentration in the present Venus mantle over a range of assumptions for the volume of magmatism during and after the last catastrophic resurfacing event (Figure 5.5). With the adopted values for the bulk partition coefficients for water (Table 5.1) and f_{melt}, our first set of numerical results for the mantle water concentration before the last catastrophic resurfacing event show good agreement with the water concentration in Venus magma estimated by *Grinspoon* [1993] at his assumed rate of post-catastrophe magmatism (cross symbols in Figures 5.2a and 5.2b).

^{40}Ar degassing provides a lower bound on the crustal production rate before the last catastrophic resurfacing event and decreases the upper bounds on $(H_2O)_M(t_P)$ beyond those given by models treating only H_2O outgassing and H escape, as shown by the second set of our numerical results (Figures 5.4 and 5.5). An example calculation of atmospheric evolution (Figure 5.4a) suggests not only that the present atmospheric H abundance is dominated by degassing during the last catastrophic resurfacing event 500

Myr ago, but also that the H and D abundances in the early atmosphere are not well resolved by the present atmospheric water abundance or D/H ratio.

The calculated water abundance in the present Venus mantle of less than 15 ppm (Figure 5.5a) is considerably less than that for the Earth. Compositional models of the bulk silicate Earth yield water concentrations of 840 to 5600 ppm [*Ringwood*, 1964] and 380 ppm [*Kargel and Lewis*, 1993] A study of chemical interactions between a magma ocean and the early atmosphere on Earth revealed that most of the water in accreting material is trapped in the Earth's interior, as the magma ocean solidified, allowing the water content in the Earth's interior to be as great as 1% depending on the water content of the accreting material [*Abe and Matsui*, 1986; *Matsui and Abe*, 1986; *Liu*, 1987, 1988]. Water abundances in mid-ocean ridge basalt (MORB) glasses reveal correlations with several incompatible elements, in particular, K_2O [*Byers et al.*, 1983; *Byers et al.*, 1985; *Byers et al.*, 1986; *Aggrey et al.*, 1988; *Dixon et al.*, 1988; *Michael*, 1988; *Jambon and Zimmermann*, 1990; *Clague et al.*, 1991]. The water content in the source region of MORB has been estimated on the basis of concentrations of these correlating elements to be between 70 and 550 ppm [*Byers et al.*, 1986; *Dixon et al.*, 1988; *Michael*, 1988; *Jambon and Zimmermann*, 1990; *Bell and Rossman*, 1992]. Interestingly, our estimate of the water content in the present Venus mantle is rather close to the values of between 5 and 35 ppm for residual peridotite after basalt extraction [*Dixon et al.*, 1988; *Bell and Rossman*, 1992].

The existence or absence of water in the Venus mantle has also been argued on the basis of modal compositions estimated from the X-ray analyses at Venera 13 and 14 and Vega 2 landing sites [*Surkov et al.*, 1986; *Barsukov*, 1992], but interpretations are conflicting. *McKenzie et al.* [1992] discuss the existence of water in the Venus mantle on the basis of the similarity of the Venera 13 analysis to terrestrial island arc magmas, while *Kargel et al.* [1993] have inferred the absence of water from the mafic alkaline character of the modal compositions. A strong correlation between gravity and

topography on Venus has been argued to be the result of a high viscosity of the Venus upper mantle, or the absence of an asthenosphere [*Kiefer et al.*, 1986], leading to the hypothesis that the Venus upper mantle lacks water at present [*Kaula*, 1990, 1995].

There are three possible explanations for the apparently marked difference in the interior water budgets of Venus and Earth. First, water on Earth is likely recycled between the hydrosphere and the mantle [e.g., *Kaula*, 1990]. Water is incorporated in oceanic crust by hydrothermal alteration processes and is carried back into the mantle at subduction zones [*Ito et al.*, 1983]. Some of the subducted water is released by metamorphic reactions in the subducting crust and triggers arc magmatism [*Anderson et al.*, 1976; *Peacock*, 1990]. One estimate for the mass of water in the subducting crust and in arc magmas, however, suggests that the subducted H_2O is about an order of magnitude greater than the quantity that degasses from arc magmatism [*Peacock*, 1990]. The estimated net flux of subducting water of 7.3×10^{11} kg yr^{-1} [*Peacock*, 1990] may be balanced by mantle degassing with the above estimate of water content in the MORB source and a present crustal production rate of 26 to 34 km^3 yr^{-1} [*Crisp*, 1984; *Coffin and Eldholm*, 1994], provided that MORB genesis occurs at a low average fractional degree of melting ($f_{melt} \approx 0.02$). On Venus, in contrast, the runaway greenhouse atmosphere maintains a high surface temperature. Water vapor in the lower atmosphere is consequently unable to react with surface materials to form hydrous minerals [*Fegley and Treiman*, 1992], so degassed water can not be recycled into the mantle [*Kaula*, 1990].

A second possibility is that Venus formed dry relative to the Earth [*Lewis and Prinn*, 1984]. Because Venus is closer to the sun than Earth, the temperature in the solar nebula during planetary formation is higher around Venus' present orbit than at 1 AU [*Grossman*, 1972; *Lewis*, 1974]. Therefore, by this argument, water is not incorporated into hydrous minerals in the materials which eventually aggregated to form Venus. The difficulty with this possibility is that current work on solar system formation predicts an intensive mixing of protoplanetary materials throughout the inner solar system during the

growth of the terrestrial planets and suggests that Venus and Earth formed from similar materials [*Wetherill*, 1980, 1994; *Wetherill and Stewart*, 1989]. Our result neither supports nor rejects this possibility, unfortunately, because the formation and evolution of the atmosphere early in the planet's history are not modeled.

A third possibility is that Venus and Earth may have formed with similar water budgets, but most of the water in Venus is retained in an undegassed mantle reservoir. A lower bound on the mass of the degassed mantle is constrained by the present atmospheric ^{40}Ar abundance to be 8% of the mass of the bulk silicate portion of Venus (Chapter 4). Therefore as much as 92% of the mantle may have been undegassed since planetary formation [*Zhang and Zindler*, 1992]. Our results shown in Figure 5.8 constrain the water abundance only in the degassed portion of the Venus mantle, but if $(H_2O)_M(t_{HO})$ in the degassed mantle is taken as a water concentration in the undegassed mantle, 90% of the mantle may still contain at most 310 ppm of water (Figure 5.8a). It should be noted, however, that this possibility is not consistent with some of the mechanistic models postulating that catastrophic global resurfacing is caused by an overturn of the upper and lower mantle [*Steinbach and Yuen*, 1992; *Herrick and Parmentier*, 1994].

A cometary component in the present atmosphere [*Grinspoon*, 1987; *Grinspoon and Lewis*, 1988; *Owen et al.*, 1992] has been neglected in this chapter. Because an additional supply of water to the atmosphere from exogenous sources effectively reduces the amount of mantle degassing, cometary impacts decrease our upper bounds on the mantle water budget. The D/H ratio measured in the gas coma of comet Halley by Giotto [*Balsiger et al.*, 1995] is twice as high as our nominal value for $(D/H)_{prim}$. Because an increase in $(D/H)_{prim}$ tightens the constraint imposed on model parameters by the present D/H ratio (i.e., expands the shaded areas in Figure 5.7), neglect of the effect of comets on the evolution of the D/H ratio is conservative with respect to estimating an upper bound on $(H_2O)_M$.

Temporally variability of the deuterium-to-hydrogen fractionation factor f_{frac} is likely to have an important influence on the atmospheric evolution of the D/H ratio (cf. Figures 5.1c and 5.4c). As stated above, functional relations for solar-wind pickup and ion escape processes over a range of X^H_{homo} have not yet been developed. It has been argued that the charge-exchange process dominates the hot-O impact process as X^H_{homo} becomes greater than 10^{-5} [*Kumar et al.*, 1983]. Because f_{frac} for charge-exchange is an order of magnitude smaller than that for hot-O impact [*Kumar et al.*, 1983; *Krasnopolsky*, 1985; *Gurwell and Yung*, 1993], f_{frac} is likely to decrease as X^H_{homo} increases. A decrease of f_{frac} tightens the constraint from the present D/H ratio (i.e., expands the shaded areas in Figure 5.7), because a small f_{frac} promotes atmospheric D/H fractionation. Therefore our assumption of constant f_{frac} is likely to yield conservative upper bounds on the mantle water abundance.

We have ignored the degassing of Ar from the crust in equations (4) and (5) on the basis of the very slow diffusion of Ar expected under anhydrous conditions (Chapter 4) [*Freer*, 1981; *Zeitler*, 1987]. This assumption, however, is yet to be tested geologically or in the laboratory. If most of the present atmospheric ^{40}Ar is derived from the crust [*Turcotte and Schubert*, 1988], then there is no need for water to degas from the planet's interior. However, we have shown that even a small amount of water degassing can considerably influence the present atmospheric water abundances (cf. Figures 5.4a and 5.4c). Therefore, if the Venus mantle contains as much water as the MORB source region on Earth, then the Venus mantle must have been shielded from degassing to the atmosphere. If so, the extensive magmatic activity observed in Magellan radar images must have resulted from remelting of crustal materials. This scenario, however, is inconsistent with geologic interpretations of the surface composition from the morphology of volcanic flows and the nature of volcanic constructs [*Head et al.*, 1992], as well as with direct measurements of surface composition at Venera and Vega landing sites [*Surkov et al.*, 1986; *McKenzie et al.*, 1992; *Kargel et al.*, 1993].

CONCLUSIONS

The present Venus mantle has been shown to be depleted in water by more than an order of magnitude relative to the Earth's upper mantle. The amount of water degassed from the planetary interior over the last 4 Gyr is constrained by the hydrogen escape flux, and the present atmospheric ^{40}Ar abundance yields a lower bound on magmatic activity over the planet's history of 2 $km^3\ yr^{-1}$. By combining these two constraints, the water concentration in the present Venus mantle has been shown to be less than 15 ppm, much less than that in Earth's MORB mantle but close to that in the residual peridotite after basalt extraction. For crustal production rates greater than the lower bound given by ^{40}Ar degassing, the present water abundance in the mantle decreases further while the water abundance early in the planet's history increases. Any enrichment of water in the early mantle disappears, however, within a characteristic degassing time that is inversely proportional to the crustal production rate and proportional to the mass of the degassed portion of the mantle. The water content in the Venus mantle has been less than 35 ppm for the last 2.5 Gyr and has been less than 20 ppm for the last 1.5 Gyr.

REFERENCES

Abe, Y., and T. Matsui, Early evolution of the Earth: Accretion, atmosphere formation, and thermal history, *Proc. Lunar Planet. Sci. Conf. 17th, J. Geophys. Res., 91*, E291-E302, 1986.

Aggrey, K. E., D. W. Muenow, and R. Batiza, Volatile abundances in basaltic glasses from seamounts flanking the East Pacific Rise at 21° N and 12-14° N, *Geochim. Cosmochim. Acta, 52*, 2115-2119, 1988.

Anderson, R. N., S. Uyeda, and A. Miyashiro, Geophysical and geochemical constraints at converging plate boundaries–part I: Dehydration in the downgoing slab, *Geophys. J. R. Astron. Soc., 44*, 333-357, 1976.

Balsiger, H., K. Altwegg, and J. Geiss, D/H and $^{18}O/^{16}O$ ratio in the hydronium ion and in neutral water from in situ ion measurements in comet Halley, *J. Geophys. Res., 100*, 5827-5834, 1995.

Banerdt, W. B., and C. G. Sammis, Small-scale fracture patterns on the volcanic plains of Venus, *J. Geophys. Res., 97*, 16,149-16,166, 1992.

Barsukov, V. L., Venusian igneous rocks, in *Venus Geology, Geochemistry, and Geophysics*, edited by V. L. Barsukov, A. T. Basilevsky, V. P. Volkov, and V. N. Zharkov, pp. 165-176, Univ. Arizona Press, Tucson, 1992.

Basaltic Volcanism Study Project, *Basaltic Volcanism on the Terrestrial Planets*, 1286 pp., Pergamon, New York, 1981.

Bell, D., and G. R. Rossman, Water in Earth's mantle: The role of nominally anhydrous minerals, *Science, 255*, 1391-1397, 1992.

Bell, J. F., III, D. Crisp, P. G. Lucey, T. A. Ozoroski, W. M. Sinton, S. C. Willis, and B. A. Campbell, Spectroscopic observations of bright and dark emission features on the night side of Venus, *Science, 252*, 1293-1296, 1991.

Brace, L. H., W. T. Kasprzak, H. A. Taylor, R. F. Theis, C. T. Russel, A. Barnes, J. D. Mihalov, and D. M. Hunten, The iontail of Venus: Its configuration and evidence for ion escape, *J. Geophys. Res.*, *92*, 15-26, 1987.

Brinton, H. C., H. A. Taylor, H. B. Niemann, H. G. Mayr, A. F. Nagy, T. E. Cravens, and D. F. Strobel, Venus nighttime hydrogen bulge, *Geophys. Res. Lett.*, *7*, 865-868, 1980.

Bullock, M. A., D. H. Grinspoon, and J. W. Head III, Venus resurfacing rates: Constraints provided by 3-D Monte Carlo simulation, *Geophys. Res. Lett.*, *19*, 2147-2150, 1993.

Byers, C. D., D. W. Muenow, and M. O. Garcia, Volatiles in basalts and andesites from Garapagos spreading center, 85° to 86° W., *Geochim. Cosmochim. Acta*, *47*, 1551-1558, 1983.

Byers, C. D., M. O. Garcia, and D. W. Muenow, Volatiles in pillow rim glasses from Loihi and Kilawea volcanoes, Hawaii, *Geochim. Cosmochim. Acta*, *49*, 1887-1896, 1985.

Byers, C. D., M. O. Garcia, and D. W. Muenow, Volatiles in basaltic glasses from the East Pacific Rise at 21° N: Implications for MORB sources and submarine lava flow morphology, *Earth Planet. Sci. Lett.*, *79*, 9-20, 1986.

Clague, D. A., W. S. Weber, and J. E. Dixon, Picritic glasses from Hawaii, *Nature*, *353*, 553-556, 1991.

Coffin, M. F., and O. Eldholm, Large igneous provinces: Crustal structure, dimensions, and external consequences, *Rev. Geophys.*, *32*, 1-36, 1994.

Crisp, J. A., Rates of magma emplacement and volcanic output, *J. Volcan. Geotherm. Res.*, *20*, 177-211, 1984.

de Bergh, C., B. Bézard, T. Owen, D. Crisp, J.-P. Malliard, and B. L. Lutz, Deuterium on Venus: Observations from Earth, *Science*, *251*, 547-549, 1991.

Dixon, J. E., E. Stolper, and J. R. Delaney, Infrared spectroscopic measurements of CO_2 and H_2O in Jun de Fuca Ridge basaltic glasses, *Earth Planet. Sci. Lett.*, *90*, 87-104, 1988.

Donahue, T. M., Fractionation of noble gases by thermal escape from accreting planetesimals, *Icarus*, *66*, 195-210, 1986.

Donahue, T. M., and R. E. Hartle, Solar cycle variations in H^+ and D^+ densities in the Venus ionosphere: Implications for escape, *Geophys. Res. Lett.*, *12*, 2449-2452, 1992.

Donahue, T. M., and R. R. Hodges, Past and present water budget of Venus, *J. Geophys. Res.*, *97*, 6083-6091, 1992.

Donahue, T. M., J. H. Hoffman, R. R. Hodges, Jr. , and A. J. Watson, Venus was wet: A measurement of the ratio of deuterium to hydrogen, *Science*, *216*, 630-633, 1982.

Dreibus, G., and H. Wänke, Supply and loss of volatile constituents during the accretion of terrestrial planets, in *Origin and Evolution of Planetary and Satellite Atmospheres*, edited by S. K. Atreya, J. B. Pollack, and M. S. Matthews, pp. 268-288, Univ. Arizona Press, Tucson, 1989.

Drossart, P., B. Bezard, T. Encrenaz, E. Lellouch, M. Ross, F. W. Taylor, A. D. Collard, S. B. Calcutt, J. Pollack, D. H. Grinspoon, R. W. Carlson, K. H. Baines, and L. W. Kamp, Search for spatial variations of the H_2O abundance in the lower atmosphere of Venus from NIMS-Galileo, *Planet. Space Sci.*, *41*, 495-504, 1993.

Fegley, B., Jr., and R. G. Prinn, Estimation of the rate of volcanism on Venus from reaction rate measurements, *Nature*, *337*, 55-58, 1989.

Fegley, B., Jr., and A. H. Treiman, Chemistry of atmosphere - surface interactions on Venus and Mars, in *Venus and Mars: Atmospheres, Ionospheres, and Solar Wind Interactions*, edited by J. G. Luhmann, M. Tatrallyay, and R. O. Pepin, *Geophysical Monograph*, *66*, pp. 7-71, Am. Geophys. Union, Washington, D. C., 1992.

Freer, R., Diffusion in silicate minerals and glasses: A data digest and guide to the literature, *Contrib. Mineral. Petrol.*, *76*, 440-454, 1981.

Gautier, D., and T. Owen, Cosmological implications of helium and deuterium abundances on Jupiter and Saturn, *Nature*, *302*, 215-218, 1983.

Geiss, J., and H. Reeves, Deuterium in the solar system, *Astron. Astrophys.*, *93*, 189-199, 1981.

Grimm, R. E., The deep structure of Venusian plateau highlands, *Icarus*, *112*, 89-103, 1994.

Grinspoon, D. H., Was Venus wet? Deuterium reconsidered, *Science*, *238*, 1702-1704, 1987.

Grinspoon, D. H., Implications of the high D/H ratio for the sources of water in Venus' atmosphere, *Nature*, *363*, 428-431, 1993.

Grinspoon, D. H., and J. S. Lewis, Cometary water on Venus: Implications of stochastic impacts, *Icarus*, *74*, 21-35, 1988.

Grossman, L., Condensation in the primitive solar nebula, *Geochim. Cosmochim. Acta*, *36*, 597-619, 1972.

Gurwell, M. A., and Y. L. Yung, Fractionation of hydrogen and deuterium on Venus due to collisional ejection, *Planet. Space Sci.*, *41*, 91-104, 1993.

Head, J. W., L. S. Crumpler, J. C. Aubele, J. E. Guest, and R. S. Saunders, Venus volcanism: Classification of volcanic features and structures, associations, and global distribution from Magellan data, *J. Geophys. Res.*, *97*, 13,153-13,197, 1992.

Henderson-Sellers, A., *The Origin and Evolution of Planetary Atmospheres*, 240 pp., Adam Hilger, Bristol, 1983.

Herrick, D. L., and E. M. Parmentier, Episodic large-scale overturn of two-layer mantles in terrestrial planets, *J. Geophys. Res.*, *99*, 2053-2062, 1994.

Herrick, R. R., and R. J. Phillips, Implications of a global survey of Venusian impact craters, *Icarus*, *111*, 387-416, 1994.

Hodges, R. R., Jr., and B. A. Tinsley, The influence of charge exchange on the velocity distribution of hydrogen in the Venus exosphere, *J. Geophys. Res.*, *91*, 13,649-13,658, 1986.

Holland, H. D., *The Chemical Evolution of the Atmosphere and Oceans*, 582 pp., Princeton Univ. Press, 1984.

Holloway, J. A., Volcanic degassing under thick atmospheres: Consequences for magmatic volatiles on Venus (abstract), *Lunar Planet. Sci.*, *23*, 545-546, 1992.

Houghton, J. T., *The Physics of Atmospheres*, 271 pp., Cambridge Univ. Press, 1986.

Hunten, D. M., The escape of light gases from planetary atmospheres, *J. Atmos. Sci.*, *30*, 1481-1494, 1973.

Hunten, D. M., Thermal and nonthermal escape mechanisms for terrestrial bodies, *Planet. Space Sci.*, *8*, 773-783, 1982.

Hunten, D. M., Atmospheric evolution of the terrestrial planets, *Science*, *259*, 915-920, 1993.

Hunten, D. M., and T. M. Donahue, Hydrogen loss from the terrestrial planets, *Ann. Rev. Earth Plant. Sci.*, *4*, 265-292, 1976.

Hunten, D. M., T. M. Donahue, J. C. G. Walker, and J. F. Kasting, Escape of atmospheres and loss of water, in *Origin and Evolution of Planetary and Satellite Atmospheres*, edited by S. K. Atreya, J. B. Pollack, and M. S. Matthews, pp. 386-422, Univ. Arizona Press, Tucson, 1989.

Hunten, D. M., R. O. Pepin, and J. C. G. Walker, Mass fractionation in hydrodynamic escape, *Icarus*, *69*, 532-549, 1987.

Ito, E., D. M. Harris, and A. T. Anderson Jr., Alteration of oceanic crust and geologic cycling of chlorine and water, *Geochim. Cosmochim. Acta*, *47*, 1613-1624, 1983.

Jambon, A., and J. L. Zimmermann, Water in oceanic basalts: Evidence for dehydration of recycled crust, *Earth Planet. Sci. Lett.*, *101*, 323-331, 1990.

Karato, S., Defects and plastic deformation in olivine, in *Rheology of solids and of the Earth*, edited by S. Karato and M. Toriumi, pp. 176-208, Oxford Univ. Press, 1989.

Karato, S., M. S. Paterson, and J. D. FitzGerald, Rheology of synthetic olivine aggregates: Influence of grain size and water, *J. Geophys. Res.*, *91*, 8151-8176, 1986.

Kargel, J. S., and J. S. Lewis, The composition and early evolution of Earth, *Icarus*, *105*, 1-25, 1993.

Kargel, J. S., G. Komatsu, V. R. Baker, and R. G. Strom, The volcanology of Venera and VEGA landing sites and the geochemistry of Venus, *Icarus*, *103*, 253-275, 1993.

Kasting, J. F., and J. B. Pollack, Loss of water from Venus. I. Hydrodynamic escape of hydrogen, *Icarus*, *53*, 479-508, 1983.

Kasting, J. F., J. B. Pollack, and T. P. Ackerman, Response of Earth's atmosphere to increases in solar flux and implications for loss of water from Venus, *Icarus*, *57*, 335-355, 1984.

Kaula, W. M., Venus: A contrast in evolution to Earth, *Science*, *247*, 1191-1196, 1990.

Kaula, W. M., Venus reconsidered, *Science*, submitted, 1995.

Kiefer, W. S., M. A. Richards, B. H. Hager, and B. G. Bills, A dynamic model of Venus's gravity field, *Geophys. Res. Lett.*, *13*, 14-17, 1986.

Kinzler, R. J., and T. L. Grove, Primary magmas of mid-ocean ridges basalts 1. Experiments and methods, *J. Geophys. Res.*, *97*, 6885-6906, 1992.

Konopliv, A. S., and W. L. Sjogren, Venus spherical harmonic gravity model to degree and order 60, *Icarus*, *112*, 42-54, 1994.

Krasnopolsky, V. A., Total injection of water vapor into Venus atmosphere, *Icarus*, *62*, 221-229, 1985.

Krasnopolsky, V. A., and V. A. Parshev, Chemical composition of the atmosphere of Venus, *Nature*, *292*, 610-613, 1981.

Krasnopolsky, V. A., and J. B. Pollack, H_2O-H_2SO_4 system in Venus' clouds and OCS, CO, and H_2SO_4 profiles in Venus' troposphere, *Icarus*, *109*, 58-78, 1994.

Kumar, S., D. M. Hunten, and J. B. Pollack, Nonthermal escape of hydrogen and deuterium from Venus and implications for loss of water, *Icarus*, *55*, 369-389, 1983.

Lewis, J. S., The temperature gradient in the solar nebula, *Science*, *186*, 440-443, 1974.

Lewis, J. S., and R. G. Prinn, *Planets and their Atmospheres: Origin and Evolution*, 470 pp., Academic Press, Orlando, Fla., 1984.

Liu, L.-G., Effects of H_2O on the phase behavior of the forsterite–enstatite system at high pressures and temperatures and implications for the Earth, *Phys. Earth Planet. Int.*, *49*, 142-167, 1987.

Liu, L.-G., Water in the terrestrial planets and the Moon, *Icarus*, *74*, 98-107, 1988.

Mackwell, S. J., D. L. Kohlstedt, and M. S. Paterson, The role of water in the deformation of olivine single crystals, *J. Geophys. Res.*, *90*, 11,319-11,333, 1985.

Mackwell, S. J., M. E. Zimmermann, D. L. Kohlstedt, and D. S. Scherber, Experimental deformation of dry Columbia diabase: Implications for tectonics on Venus, *Proc. 35th U.S. Symp. Rock Mechanics,* in press, 1995.

Masson, E. A., and T. R. Marrero, The diffusion of atoms and molecules, in *Advances in Atomic and Molecular Physics*, edited by D. R. Bates and I. Esterman, *6*, pp. 155-232, Academic Press, New York, 1970.

Matsui, T., and Y. Abe, Evolution of an impact-induced atmosphere and magma ocean of the accreting Earth, *Nature*, *319*, 303-305, 1986.

Matsui, T., and E. Tajika, Comparative study of crustal production rates of Mars, Venus, and the Earth (abstract), *Lunar Planet. Sci., 26*, 909-910, 1995.

McDonough, W. F., S.-S. Sun, A. E. Ringwood, E. Jagoutz, and A. W. Hofmann, Potassium, rubidium, and cesium in the Earth and Moon and the evolution of the mantle of the Earth, *Geochim. Cosmochim. Acta*, *56*, 1001-1012, 1992.

McDougall, I., and T. M. Harrison, *Geochronology and Thermochronology by the $^{40}Ar/^{39}Ar$ Method*, 212 pp., Oxford University Press, New York, 1988.

McElroy, M. B., M. J. Prather, and J. M. Rodriguez, Escape of hydrogen from Venus, *Science, 215*, 1614-1615, 1982.

McGovern, P. J., and G. Schubert, Thermal evolution of the Earth: Effects of volatile exchange between atmosphere and interior, *Earth Planet. Sci. Lett., 96*, 27-37, 1989.

McKenzie, D., P. G. Ford, C. Johnson, B. Parsons, D. Sandwell, S. Saunders, and S. C. Solomon, Features on Venus generated by plate boundary processes, *J. Geophys. Res., 97*, 13,533-13,544, 1992.

McKenzie, D. P., The initiation of trenches: A finite amplitude instability, in *Island Arcs, Deep Sea Trenches, and Back-Arc Basins*, edited by M. Talwani and W. C. Pitman, III, *Maurice Ewing Ser., 1*, pp. 57-61, Am. Geophys. Union., Washington, D. C., 1977.

Michael, P. J., The concentration, behavior and storage of H_2O in the suboceanic upper mantle: Implications for mantle metasomatism, *Geochim. Cosmochim. Acta, 52*, 555-566, 1988.

Namiki, N., and S. C. Solomon, Impact crater densities on volcanoes and coronae on Venus: Implications for volcanic resurfacing, *Science, 265*, 929-933, 1994.

Owen, T., A. Bar-Nun, and I. Kleinfeld, Possible cometary origin of heavy noble gases in the atmospheres of Venus, Earth and Mars, *Nature, 358*, 43-46, 1992.

Ozima, M., and F. A. Podosek, *Noble Gas Chemistry*, 367 pp., Cambridge Univ. Press, 1983.

Parmentier, E. M., and P. C. Hess, Chemical differentiation of a convective planetary interior: Consequences for a one plate planet such as Venus, *Geophys. Res. Lett., 20*, 2015-2018, 1992.

Peacock, S. M., Fluid processes in subduction zones, *Science, 248*, 329-337, 1990.

Pepin, R. O., On the origin and early evolution of terrestrial planet atmospheres and meteoritic volatiles, *Icarus, 92*, 2-79, 1991.

Phillips, R. J., and V. L. Hansen, Tectonic and magmatic evolution of Venus, *Ann. Rev. Earth Planet. Sci., 22*, 597-654, 1994.

Phillips, R. J., R. F. Raubertas, R. E. Arvidson, I. C. Sarkar, R. R. Herrick, N. Izenberg, and R. E. Grimm, Impact craters and Venus resurfacing history, *J. Geophys. Res.*, *97*, 15,921-15,948, 1992.

Pollack, J. B., and D. C. Black, Noble gases in planetary atmospheres: Implications for the origin and evolution of atmospheres, *Icarus*, *51*, 169-198, 1982.

Pollack, J. B., J. B. Dalton, D. Grinspoon, R. B. Wattson, R. Freedman, D. Crisp, D. A. Allen, B. Bézard, C. de Bergh, L. P. Giver, Q. Ma, and R. Tipping, Near-infrared light from Venus' nightside: A spectroscopic analysis, *Icarus*, *103*, 1-42, 1993.

Price, M., Resurfacing history of the Venusian plains based on distribution of impact craters (abstract), *Lunar Planet. Sci.*, *26*, 1143-1144, 1995a.

Price, M. H., Estimates of global magmatic flux on Venus based on geologic mapping and dating of volcanism (abstract), *Eos Trans. AGU*, *76*, S190-S191, 1995b.

Price, M., and J. Suppe, Mean age of rifting and volcanism on Venus deduced from impact crater densities, *Nature*, *372*, 756-759, 1994.

Ringwood, A. E., The chemical composition and origin of the Earth, in *Advances in Earth Sciences*, edited by P. M. Hurley, *Contributions to the International Conference on the Earth Sciences*, pp. 287-356, M.I.T. Press, Cambridge, Mass., 1964.

Sasaki, S., and K. Nakazawa, Origin of isotopic fractionation of terrestrial Xe: Hydrodynamic fractionation during escape of the primordial H_2-He atmosphere, *Earth Planet. Sci. Lett.*, *89*, 323-334, 1988.

Schaber, G. G., R. G. Strom, H. J. Moore, L. A. Soderblom, R. L. Kirk, D. J. Chadwick, D. D. Dawson, L. R. Gaddis, J. M. Boyce, and J. Russell, Geology and distribution of impact craters on Venus: What are they telling us?, *J. Geophys. Res.*, *97*, 13,257-13,301, 1992.

Schubert, G., D. L. Turcotte, S. C. Solomon, and N. H. Sleep, Coupled evolution of the atmospheres and interiors of planets and satellites, in *Origin and Evolution of Planetary*

and Satellite Atmospheres, edited by S. K. Atreya, J. B. Pollack, and M. S. Matthews, pp. 450-483, Univ. Arizona Press, Tucson, 1989.

Schultz, R. A., and M. Simons, Water, rock strength, and tectonics on Venus, *Science*, submitted, 1995.

Seiff, A., Thermal structure of the atmosphere of Venus, in *Venus*, edited by D. M. Hunten, L. Colin, T. M. Donahue, and V. I. Moroz, pp. 215-279, Univ. Arizona Press, Tucson, 1983.

Simons, M., B. H. Hager, and S. C. Solomon, Global variations in the geoid/topography admittance of Venus, *Science, 264*, 798-803, 1994.

Solomon, S. C., and J. W. Head, Mechanisms for lithospheric heat transport on Venus: Implications for tectonics and volcanism, *J. Geophys. Res., 87*, 9236-9246, 1982.

Steinbach, V., and D. A. Yuen, The effects of multiple phase transitions on venusian mantle convection, *Geophys. Res. Lett., 19*, 2243-2246, 1992.

Strom, R. G., G. G. Schaber, and D. D. Dawson, The global resurfacing of Venus, *J. Geophys. Res., 99*, 10,899-10,926, 1994.

Surkov, Yu. A., L. P. Moskalyova, V. P. Kharyukova, A. D. Dudin, G. G. Smirnov, and S. Y. Zaitseva, Venus rock composition at the Vega 2 landing site, *Proc. Lunar Planet. Sci. Conf. 17th, J. Geophys. Res., 91*, E215-218, 1986.

Surkov, Yu. A., F. F. Kirnozov, V. N. Glazov, A. G. Dunchenko, L. P. Tatsy, and O. P. Sobornov, Uranium, thorium, and potassium in the Venusian rocks at the landing sites of Vega 1 and 2, *Proc. Lunar Planet. Sci. Conf. 17th, J. Geophys. Res., 92*, E537-E540, 1987.

Turcotte, D. L., An episodic hypothesis for Venusian tectonics, *J. Geophys. Res., 98*, 17,061-17,068, 1993.

Turcotte, D. L., and G. Schubert, Tectonic implications of radiogenic noble gases in planetary atmospheres, *Icarus, 74*, 36-46, 1988.

Volkov, V. P., and M. Y. Frenkel, The modeling of Venus' degassing in terms of K-Ar system, *Earth Moon Planets*, *62*, 117-129, 1993.

von Zahn, U., S. Kumar, H. Niemann, and R. Prinn, Composition of the Venus atmosphere, in *Venus*, edited by D. M. Hunten, L. Colin, T. M. Donahue, and V. I. Moroz, pp. 299-430, Univ. Arizona Press, Tucson, 1983.

Westrich, H. R., H. W. Stockman, and J. C. Eichelberger, Degassing of rhyolitic magma during ascent and emplacement, *J. Geophys. Res.*, *93*, 6503-6511, 1988.

Wetherill, G. W., Numerical calculations relevant to the accumulation of the terrestrial planets, in *The Continental Crust and Its Mineral Deposits*, edited by D. W. Strangway, pp. 3-24, Geol. Assoc. Can. Spec. Pap. 20, 1980.

Wetherill, G. W., Provenance of the terrestrial planets, *Geochim. Cosmochim. Acta*, *58*, 4513-4520, 1994.

Wetherill, G. W., and G. R. Stewart, Accumulation of a swarm of small planetesimals, *Icarus*, *77*, 330-357, 1989.

Zahnle, K., J. F. Kasting, and J. B. Pollack, Mass fractionation of noble gases in diffusion-limited hydrodynamic hydrogen escape, *Icarus*, *84*, 502-527, 1990.

Zahnle, K. J., and J. F. Kasting, Mass fractionation during transonic escape and implications for loss of water from Mars and Venus, *Icarus*, *68*, 462-480, 1986.

Zahnle, K. J., and J. C. G. Walker, The evolution of solar ultraviolet luminosity, *Rev. Geophys. Space Phys.*, *20*, 280-292, 1982.

Zeitler, P. K., Argon diffusion in partially outgassed alkali feldspars: Insights for $^{40}Ar/^{39}Ar$ analysis, *Chem. Geology*, *65*, 167-181, 1987.

Zhang, Y., and A. Zindler, Outgassing history of Venus and the absence of water on Venus (abstract), in *International Colloquium on Venus*, edited by *International Colloquium on Venus*, pp. 135-137, Lunar and Planetary Institute, Houston, Tex., 1992.

Table 5.1. Bulk partition coefficients for maximum and minimum degassing models (Chapter 4) [after *Dixon et al.*, 1988; *Bell and Rossman*, 1992].

		f_{melt}	K_{mode}	K_{stoi}
K	max		0.002	0.0024
	min	≤ 0.121	0.021	0.16
		> 0.121	0.011	0.073
Ar	max	≤ 0.112	0.053	0.098
		> 0.112	0.12	0.68
H_2O			0.01	0.01

FIGURE CAPTIONS

Figure 5.1. Evolution of (a) the atmospheric water abundance, (b) mantle water concentration, and (c) atmospheric D/H ratio after the last catastrophic resurfacing event of 300 or 500 Myr ago. The values for $X^{water}_{surf}(t_P)$ and escape flux $F^H(t_P)$ are assumed to be 20 ppm and 3.4 x 10^6 kg yr^{-1} (dotted lines), 30 ppm and 4.8 x 10^6 kg yr^{-1} (dashed lines), and 40 ppm and 6.7 x 10^6 kg yr^{-1} (solid lines), respectively. The D/H ratios for the case with 40 ppm water and $F^H(t_P)$ = 6.7 x 10^6 kg yr^{-1} (solid lines) and those for the case of 20 ppm water and $F^H(t_P)$ = 3.4 x 10^6 kg yr^{-1} (dotted lines) are almost identical in (c).

Figure 5.2. Contours of upper bounds on $(H_2O)_M(t_P)$ calculated from mantle degassing and atmospheric escape models parameterized by the volume of magmatism during the last catastrophic event averaged over the planetary surface (ordinate) and the rate of magmatism after that event (abscissa). The value of f_{melt} is assumed to be (a) 0.04 and (b) 0.16 during and after the last catastrophic resurfacing event. The mixing ratio $X^{water}_{surf}(t_P)$ and the escape flux $F^H(t_P)$ are assumed to be 40 ppm and 6.7 x 10^6 kg yr^{-1}, respectively. The cross symbol denotes the rate of steady volcanism assumed by *Grinspoon* [1993].

Figure 5.3. Minimum crustal production rate before the last catastrophic resurfacing event calculated from ^{40}Ar degassing.

Figure 5.4. An example of a model for the evolution of (a) atmospheric hydrogen, deuterium, and ^{40}Ar abundances, (b) the mantle water abundance, and (c) the atmospheric D/H ratio. The volume of magmatism during the last catastrophic resurfacing event is assumed to be 2.3 x 10^9 km^3 (equivalent to an average thickness over the planet's surface of 5 km) and the rate of magmatic activity after the last catastrophic resurfacing event is assumed to be 1 km^3 yr^{-1}. Cases for zero $(H)_A(t_{HO})$ and for an atmospheric D/H ratio at $t = t_{HO}$ of $(D/H)_{prim}$ are shown by solid and dotted lines, respectively; the two cases result in nearly identical values

of $(H_2O)_M$, so the solid and dotted lines are indistinguishable in (b). Also shown in (a) are t^H_{diff}, t^D_{diff}, and the time at which supersaturation of the cold trap ends for the second case (thin dashed lines), as well as the time of the last catastrophic resurfacing event (arrows).

Figure 5.5. Contours of upper bounds on $(H_2O)_M$ at (a) $t = t_P$ and (b) $t = t_{HO}$. The value of f_{melt} is assumed to be 0.02 before the last catastrophic resurfacing event and to be 0.16 during and after the event. The shaded area denotes models that fail to satisfy a present D/H ratio of 0.019 and a $(D/H)_{prim}$ of 1.6×10^{-4}.

Figure 5.6. Contours of upper bounds on $(H_2O)_M$ at t = (a) t_P, (b) 2 Gyr, and (c) t_{HO}. A crustal production rate before the last catastrophic resurfacing event of 25 $km^3\ yr^{-1}$ is assumed.

Figure 5.7. Contours of upper bounds on $(H_2O)_M$ in the degassed portion of the mantle at t = (a) t_P, (b) 2 Gyr, and (c) t_{HO}. A crustal production rate before the last catastrophic resurfacing event of 15 $km^3\ yr^{-1}$ and a mass of the degassed portion of the mantle equal to 33% of the mantle mass are assumed. Models within the shaded area fail to match a present atmospheric D/H ratio less than 0.025 or a $(D/H)_{prim}$ higher 2.0×10^{-5} and may be rejected.

Figure 5.8. Maximum water abundance in the degassed portion of the mantle at t = (a) t_{HO}, (b) 2 Gyr, and (c) 3 Gyr, and (d) the corresponding rate of volcanism after the last catastrophic resurfacing event, calculated as functions of the rate of magmatism before that event. The mass of the degassed portion of the mantle is assumed to be 10% (solid lines), 25% (dot-dash lines), 33% (dashed lines), and 50% (dot-dot-dash lines). Models that either do not satisfy the lower bound on $(^{40}Ar)_A(t_P)$ or require a rate of magmatism after the catastrophe of greater than 20 $km^3\ yr^{-1}$ may be rejected (dotted lines).

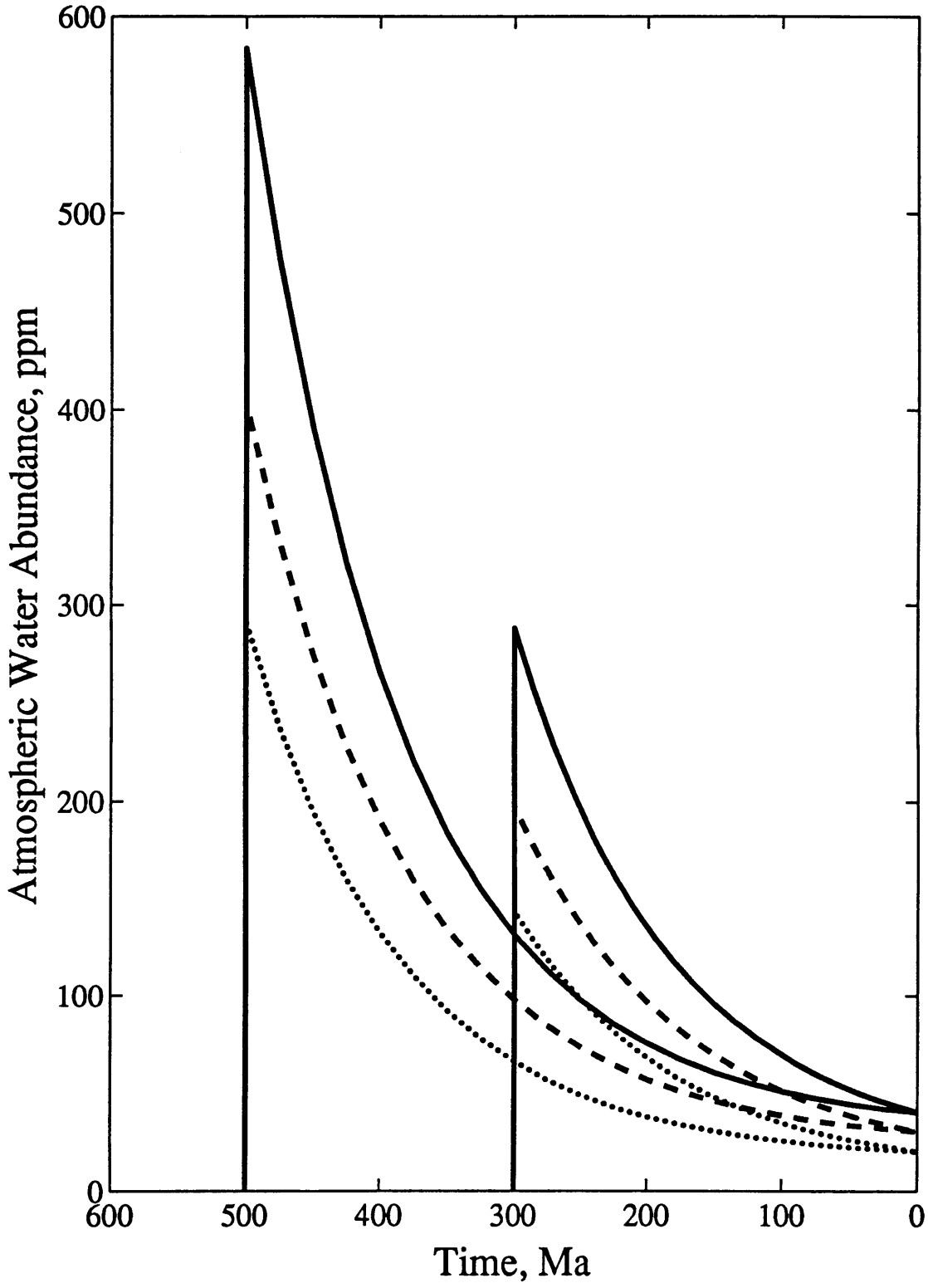
600
500
400
300
200
100
0
Atmospheric Water Abundance, ppm
600
500
400
300
200
100
0
Time, Ma

Figure 5.1a

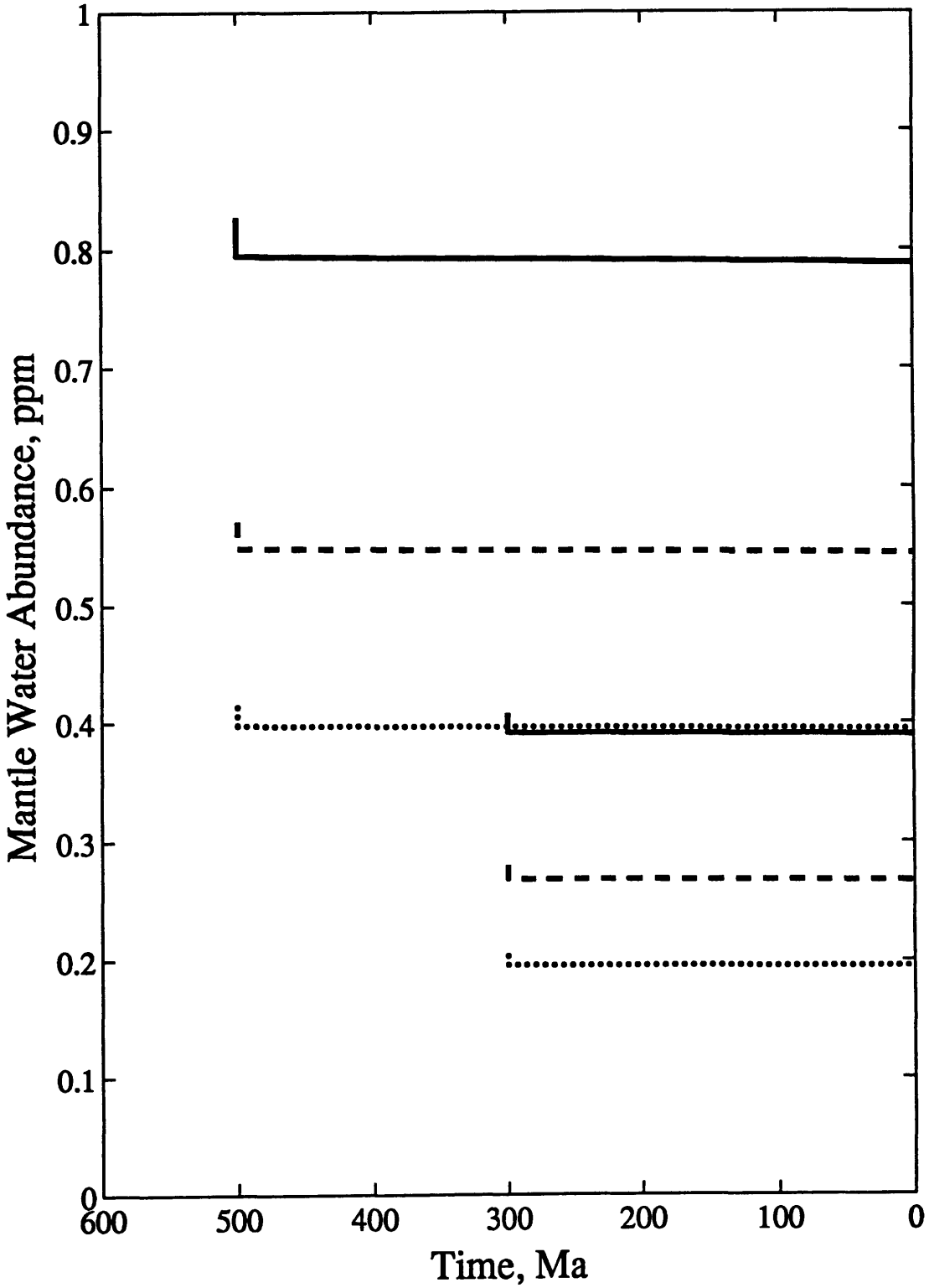
Mantle Water Abundance, ppm
1
0.9
0.8
0.7
0.6
0.5
0.4
0.3
0.2
0.1
0
600
500
400
300
200
100
0
Time, Ma

Figure 5.1b

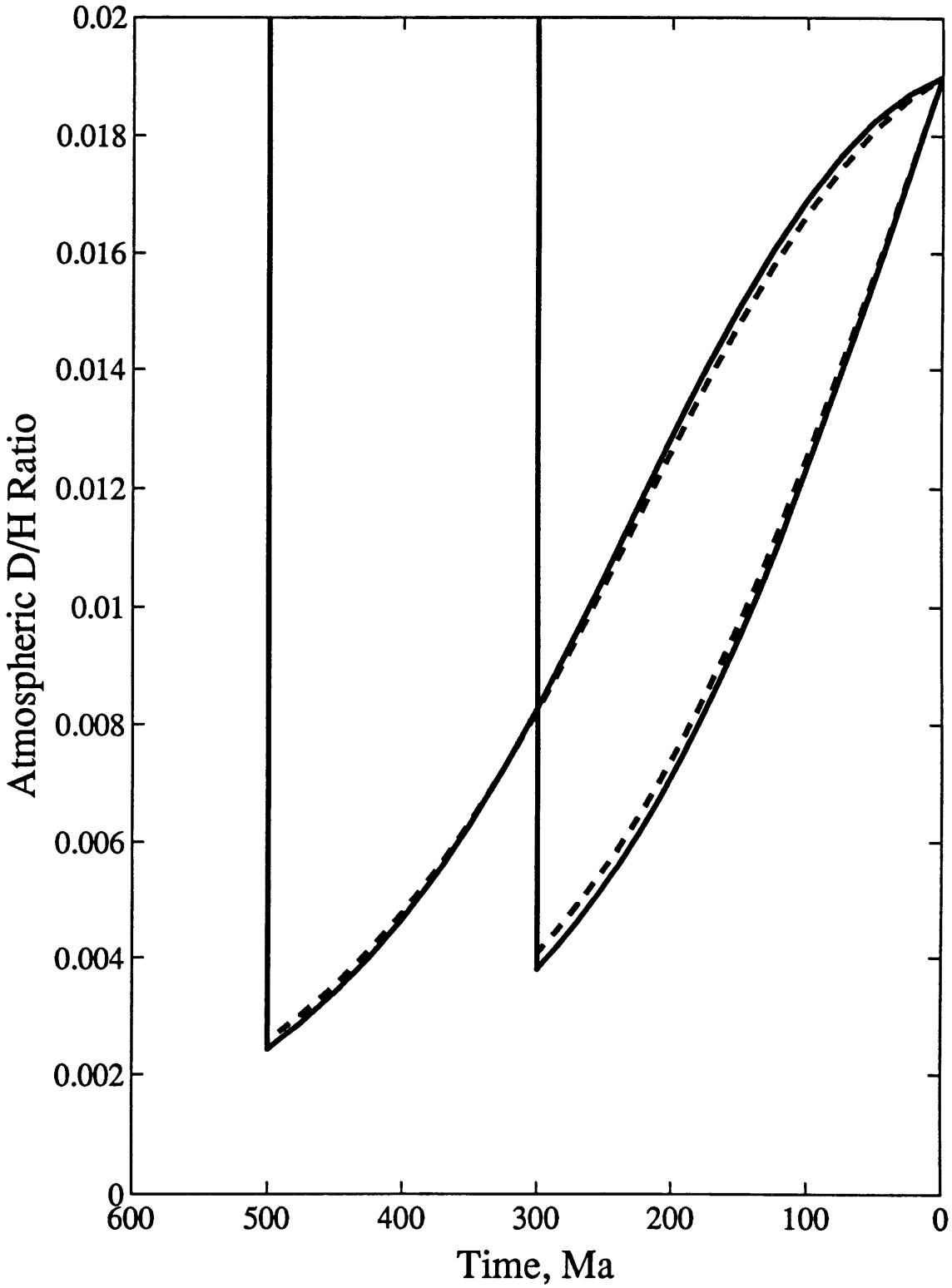
0.02
0.018
0.016
0.014
0.012
0.01
0.008
0.006
0.004
0.002
0
Atmospheric D/H Ratio
600
500
400
300
200
100
0
Time, Ma

Figure 5.1c

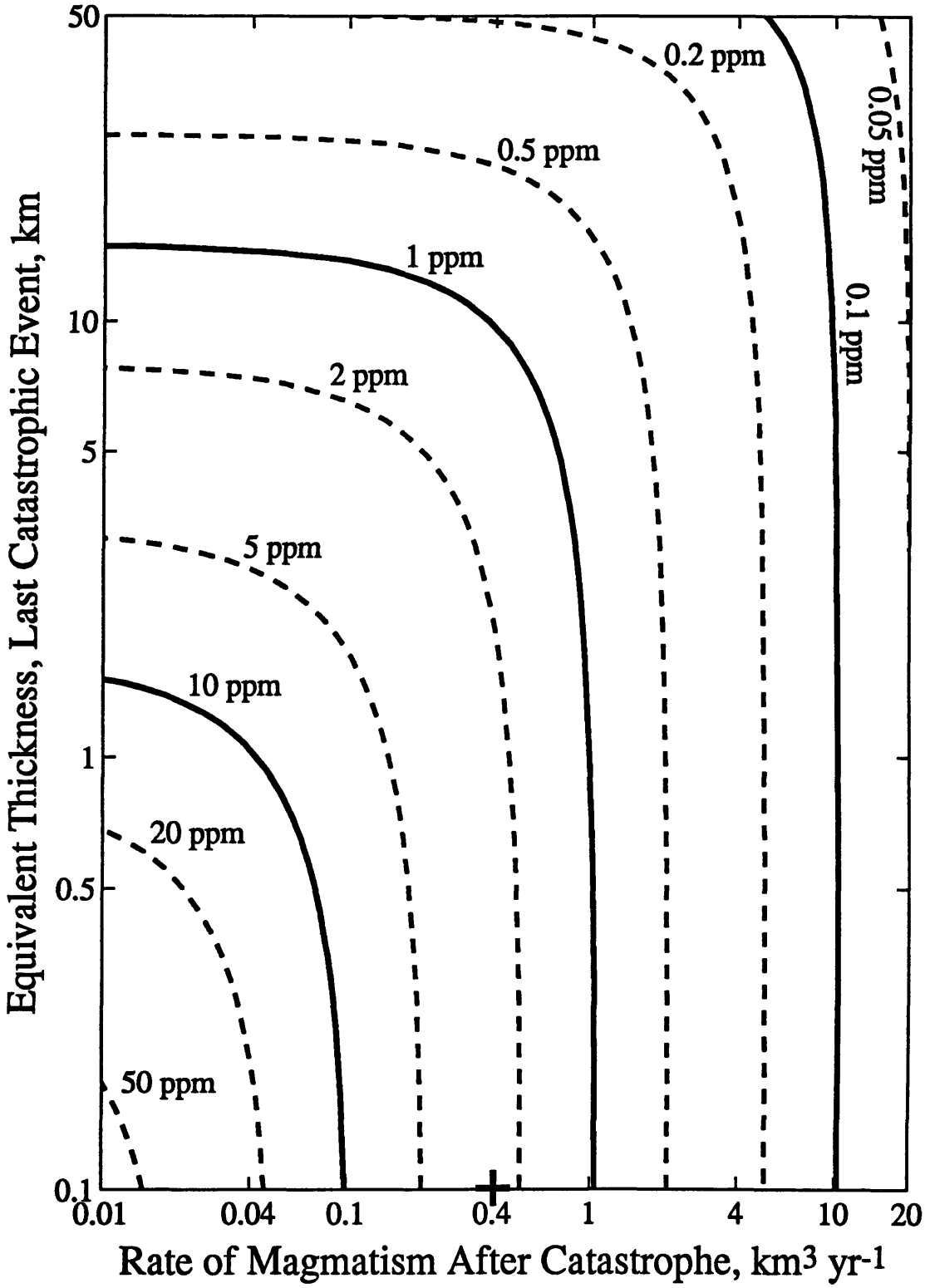
50
10
5
1
0.5
0.1
0.01
0.04
0.1
0.4
1
4
10
20
0.2 ppm
0.5 ppm
1 ppm
2 ppm
5 ppm
10 ppm
20 ppm
50 ppm
0.05 ppm
0.1 ppm
Equivalent Thickness, Last Catastrophic Event, km
Rate of Magmatism After Catastrophe, km3 yr-1

Figure 5.2a

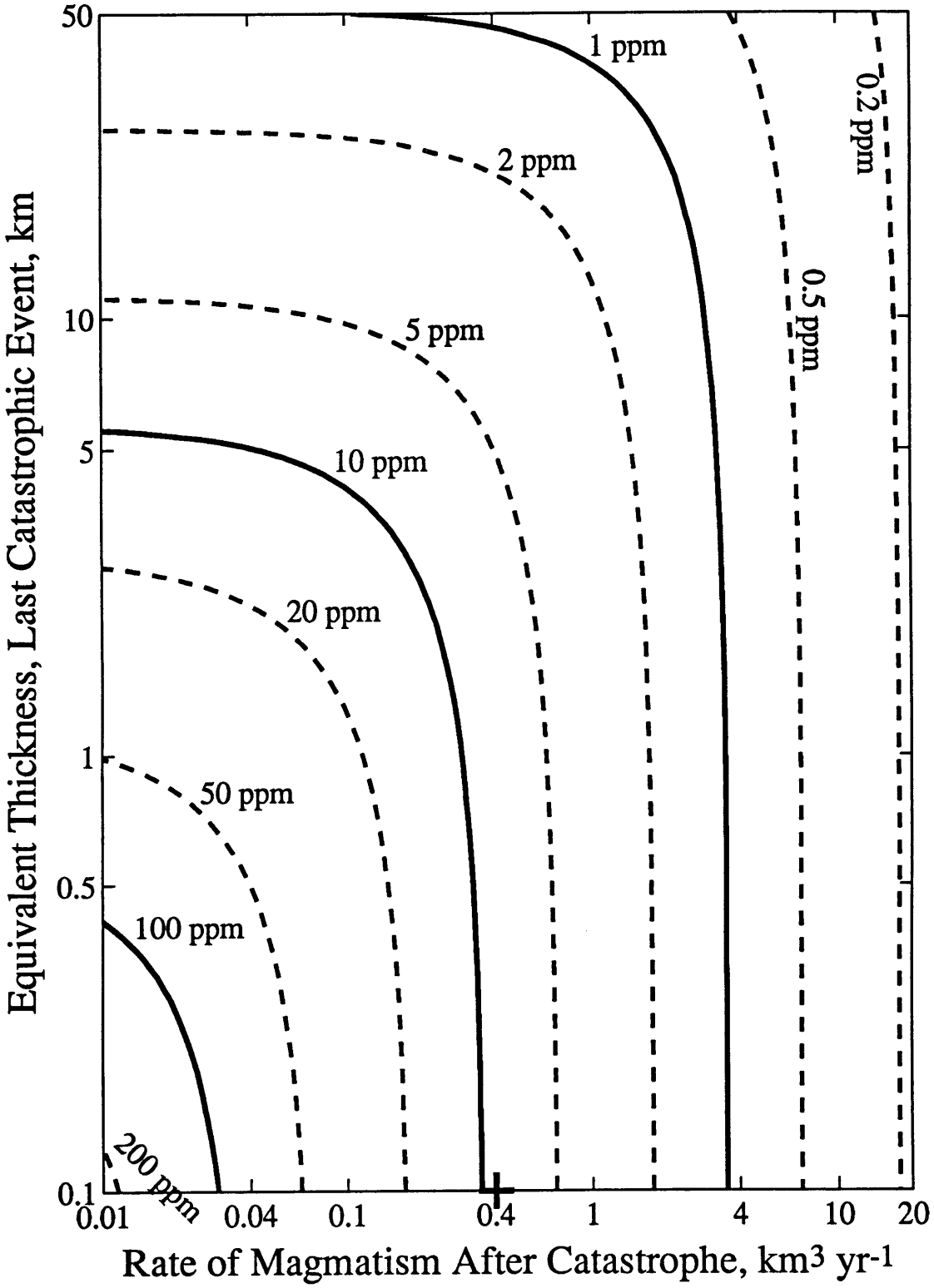
Equivalent Thickness, Last Catastrophic Event, km
50
10
5
1
0.5
0.1
1 ppm
2 ppm
5 ppm
10 ppm
20 ppm
50 ppm
100 ppm
200 ppm
0.2 ppm
0.5 ppm
0.01
0.04
0.1
0.4
1
4
10
20
Rate of Magmatism After Catastrophe, km3 yr-1

Figure 5.2b

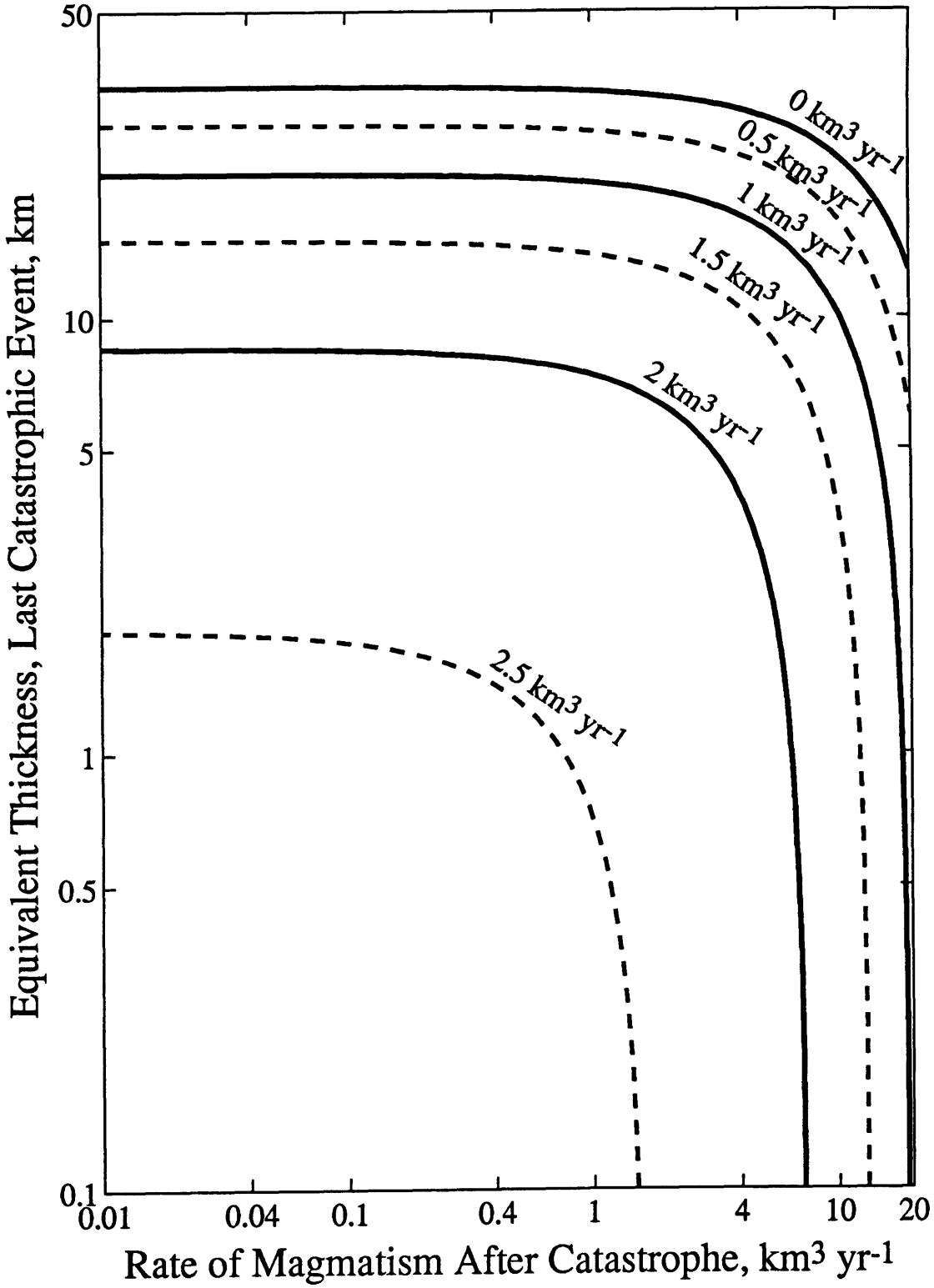
50
10
5
1
0.5
0.1
0.01
0.04
0.1
0.4
1
4
10
20
0 km3 yr-1
0.5 km3 yr-1
1 km3 yr-1
1.5 km3 yr-1
2 km3 yr-1
2.5 km3 yr-1
Equivalent Thickness, Last Catastrophic Event, km
Rate of Magmatism After Catastrophe, km3 yr-1

Figure 5.3

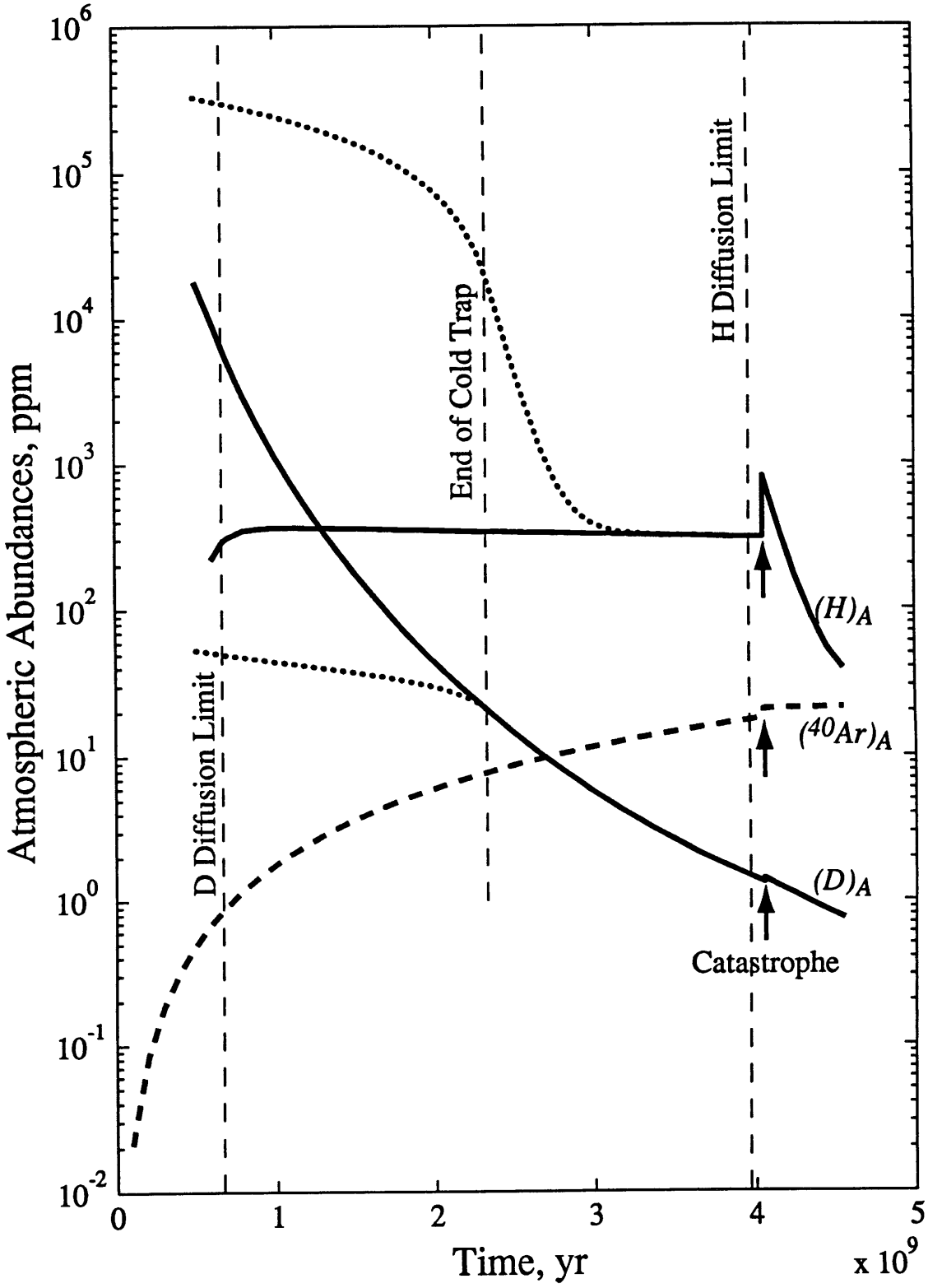
Atmospheric Abundances, ppm
Time, yr
x 10^9
End of Cold Trap
H Diffusion Limit
D Diffusion Limit
(H)A
(40Ar)A
(D)A
Catastrophe

Figure 5.4a

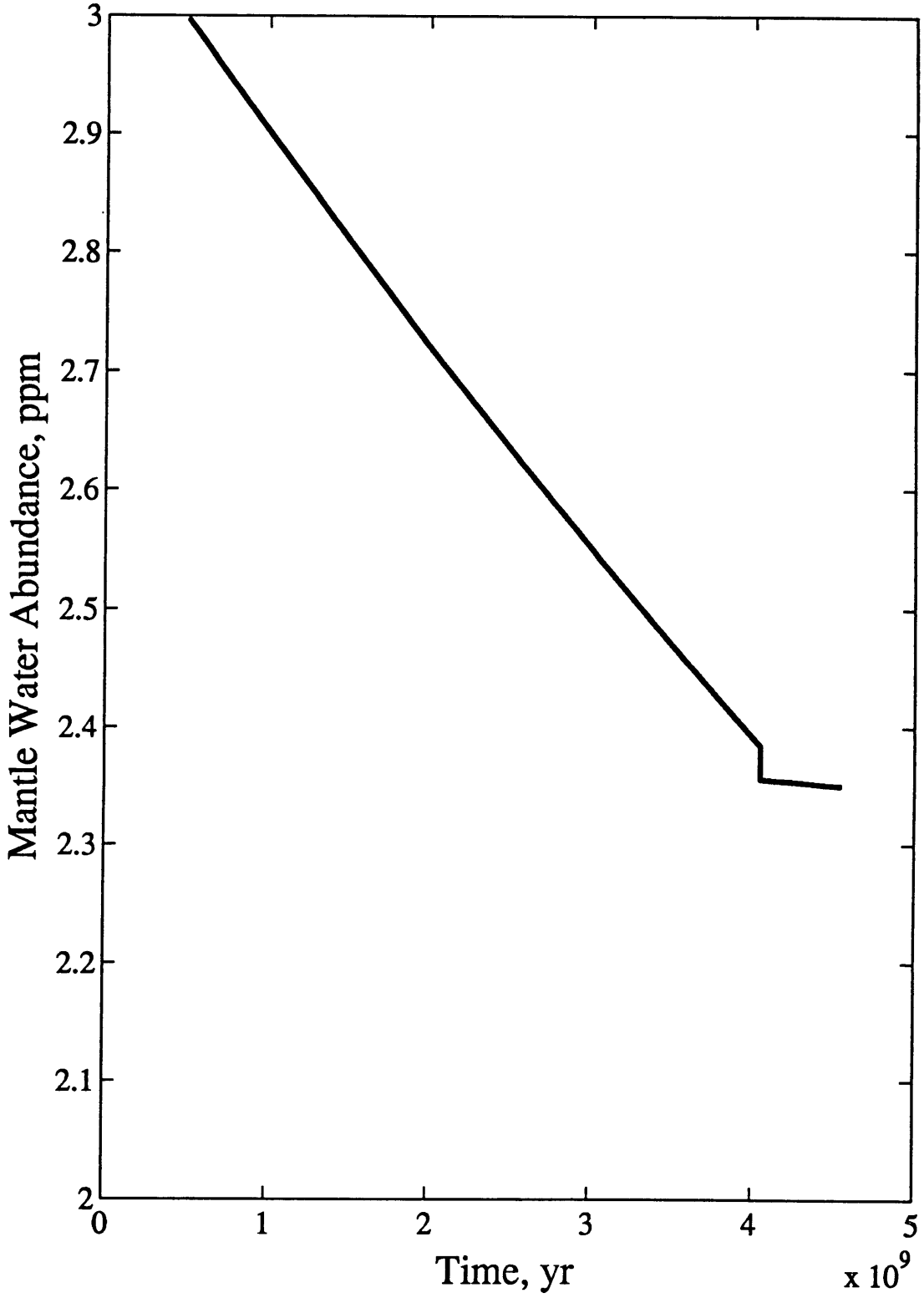
Mantle Water Abundance, ppm
3
2.9
2.8
2.7
2.6
2.5
2.4
2.3
2.2
2.1
2
0
1
2
3
4
5
Time, yr
x 10^9

Figure 5.4b

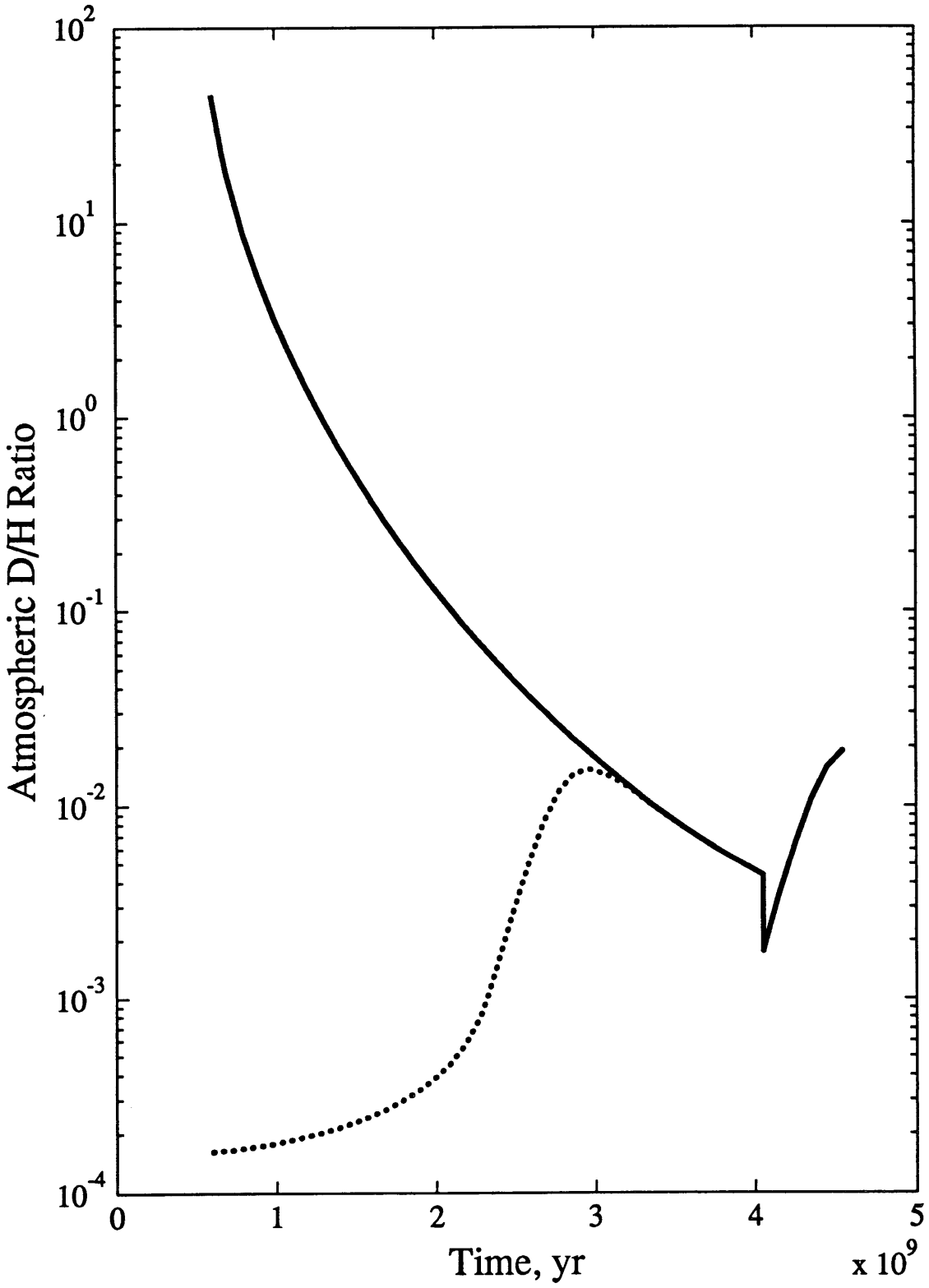
Atmospheric D/H Ratio
10^{2}
10^{1}
10^{0}
10^{-1}
10^{-2}
10^{-3}
10^{-4}
0
1
2
3
4
5
Time, yr
x 10^{9}

Figure 5.4c

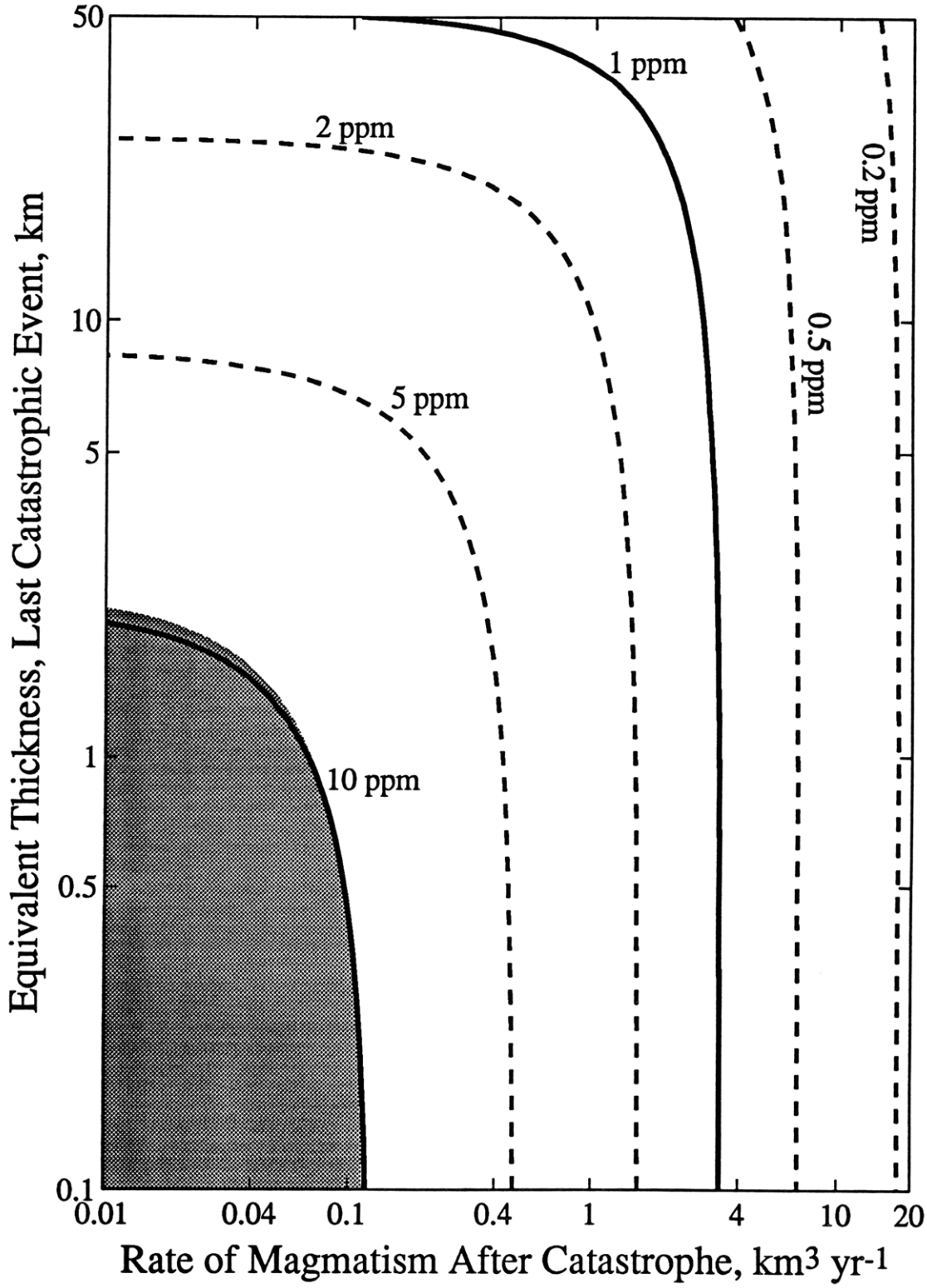
50
10
5
1
0.5
0.1
1 ppm
2 ppm
5 ppm
10 ppm
0.2 ppm
0.5 ppm
0.01
0.04
0.1
0.4
1
4
10
20
Equivalent Thickness, Last Catastrophic Event, km
Rate of Magmatism After Catastrophe, km3 yr-1

Figure 5.5a

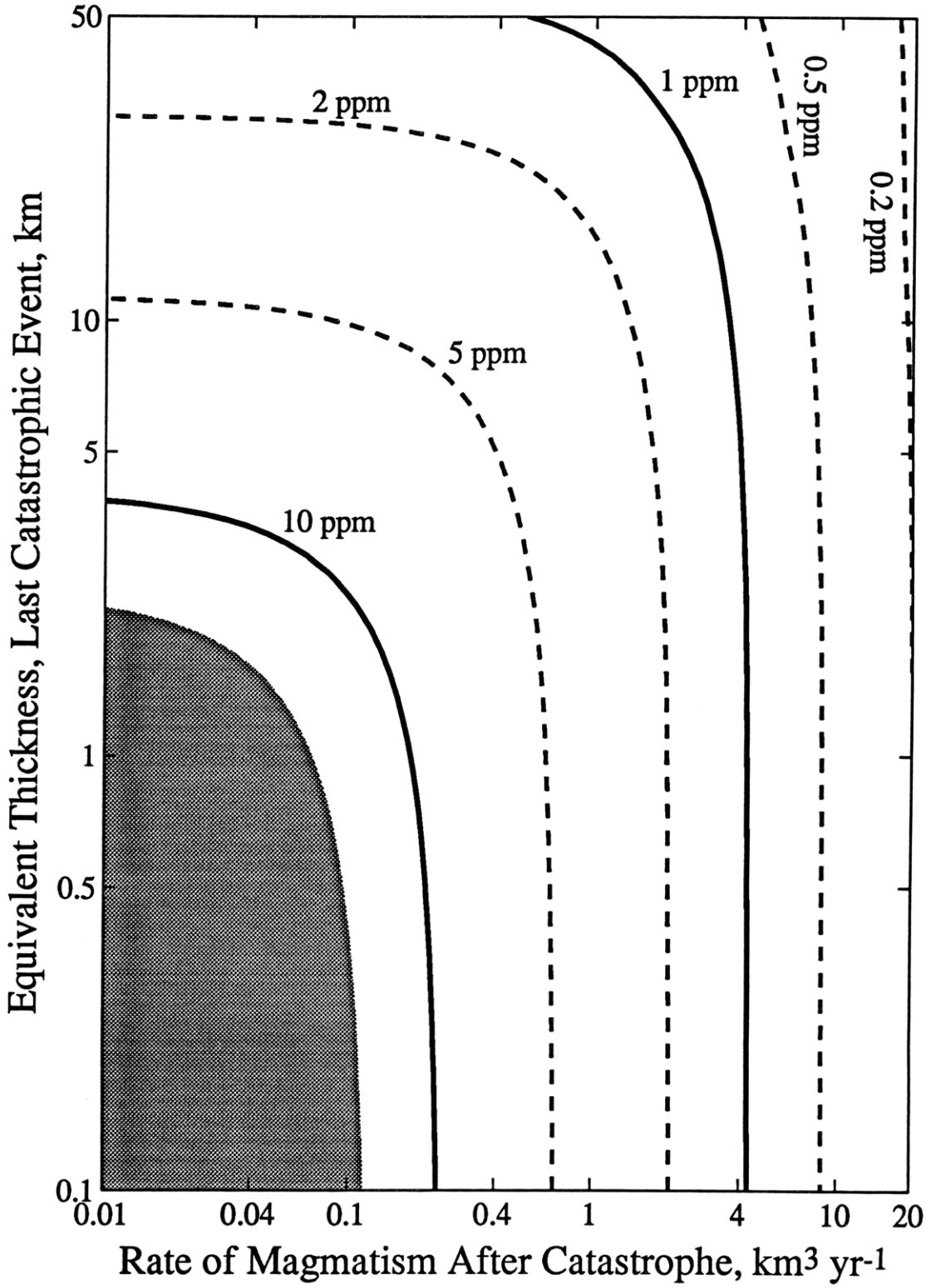
50
10
5
1
0.5
0.1
Equivalent Thickness, Last Catastrophic Event, km
2 ppm
1 ppm
0.5 ppm
0.2 ppm
5 ppm
10 ppm
0.01
0.04
0.1
0.4
1
4
10
20
Rate of Magmatism After Catastrophe, km3 yr-1

Figure 5.5b

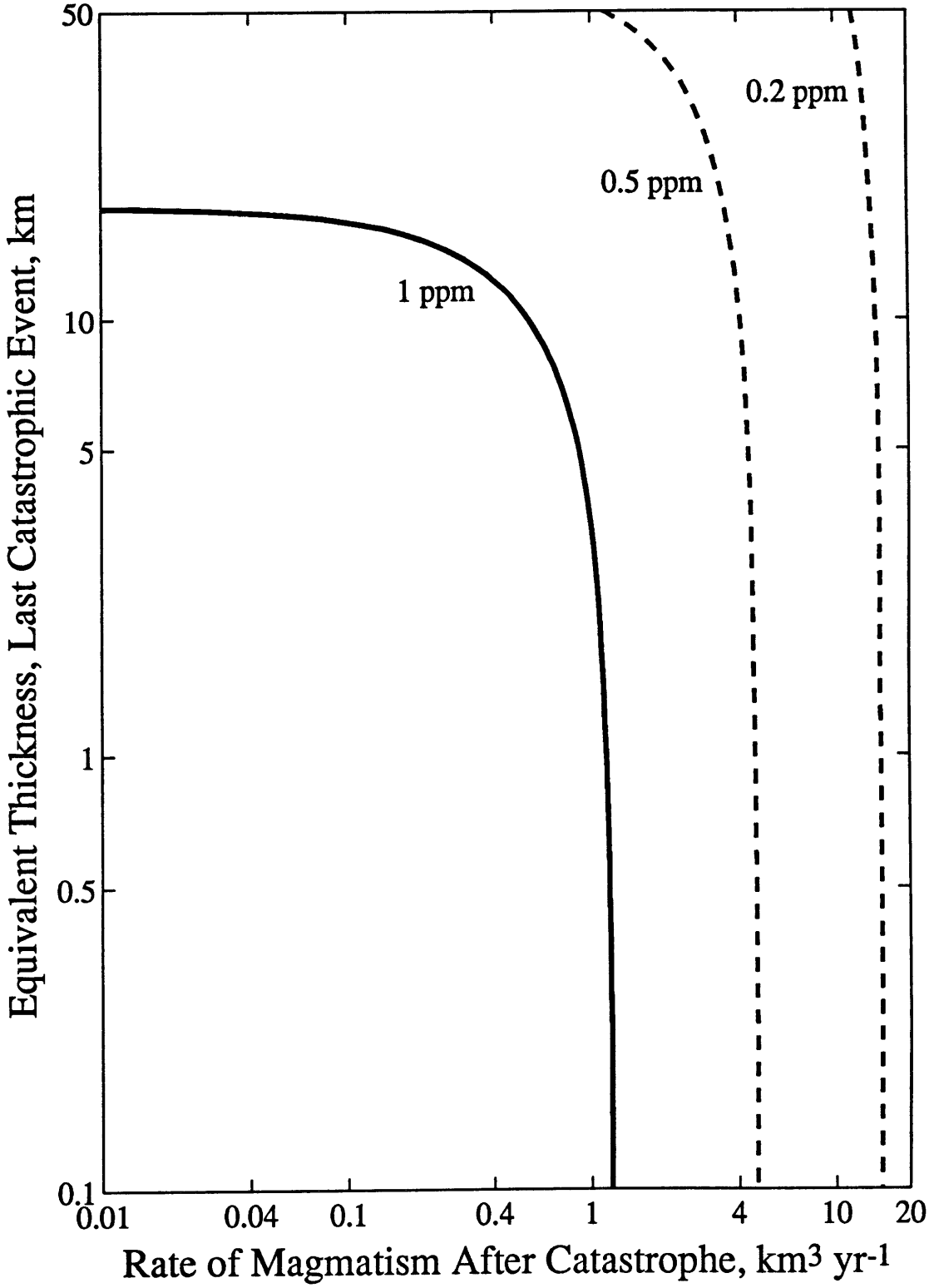
50
10
5
1
0.5
0.1
0.01
0.04
0.1
0.4
1
4
10
20
0.2 ppm
0.5 ppm
1 ppm
Equivalent Thickness, Last Catastrophic Event, km
Rate of Magmatism After Catastrophe, km3 yr-1

Figure 5.6a

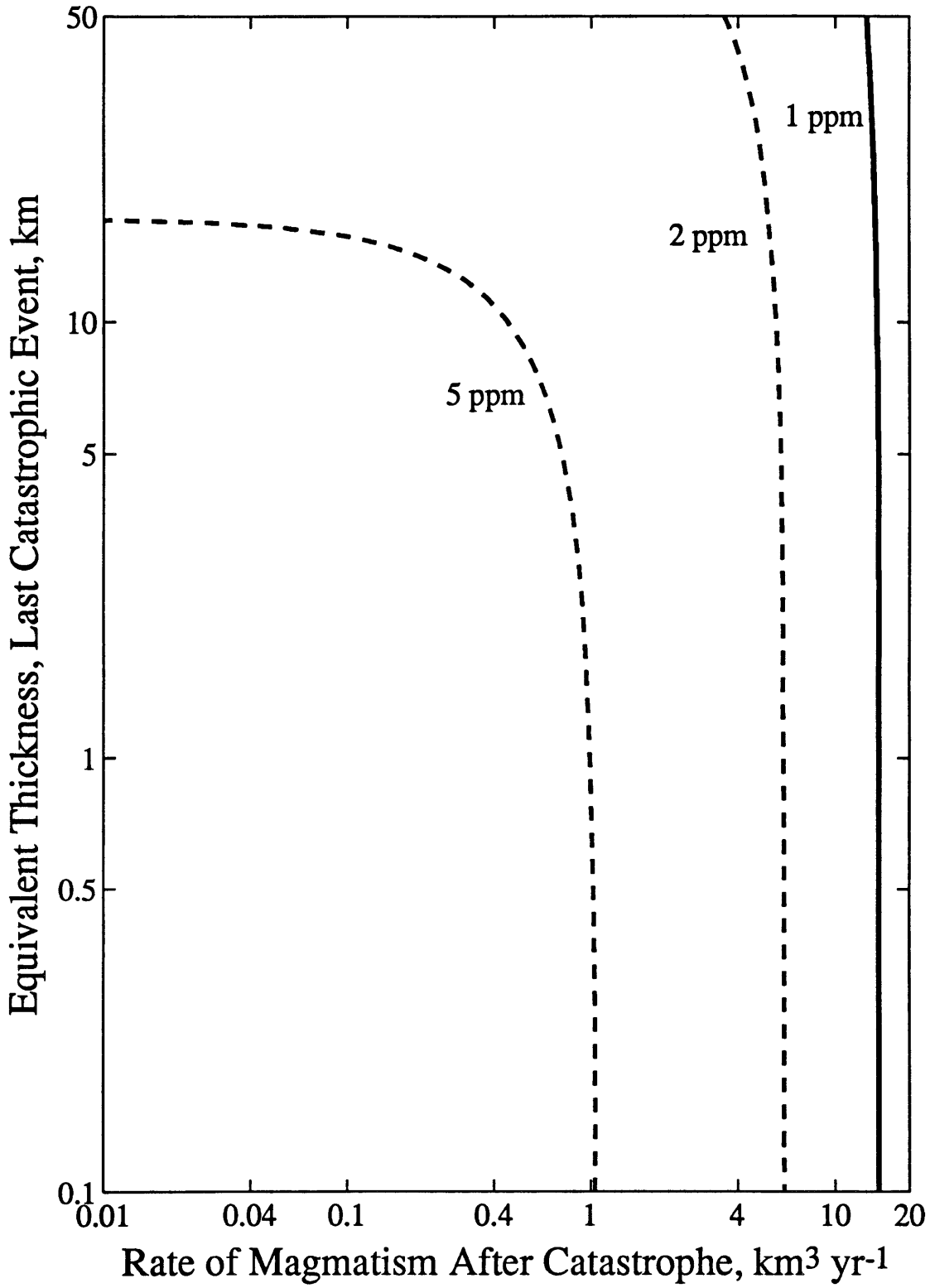
50
10
5
1
0.5
0.1
Equivalent Thickness, Last Catastrophic Event, km
1 ppm
2 ppm
5 ppm
0.01
0.04
0.1
0.4
1
4
10
20
Rate of Magmatism After Catastrophe, km3 yr-1

Figure 5.6b

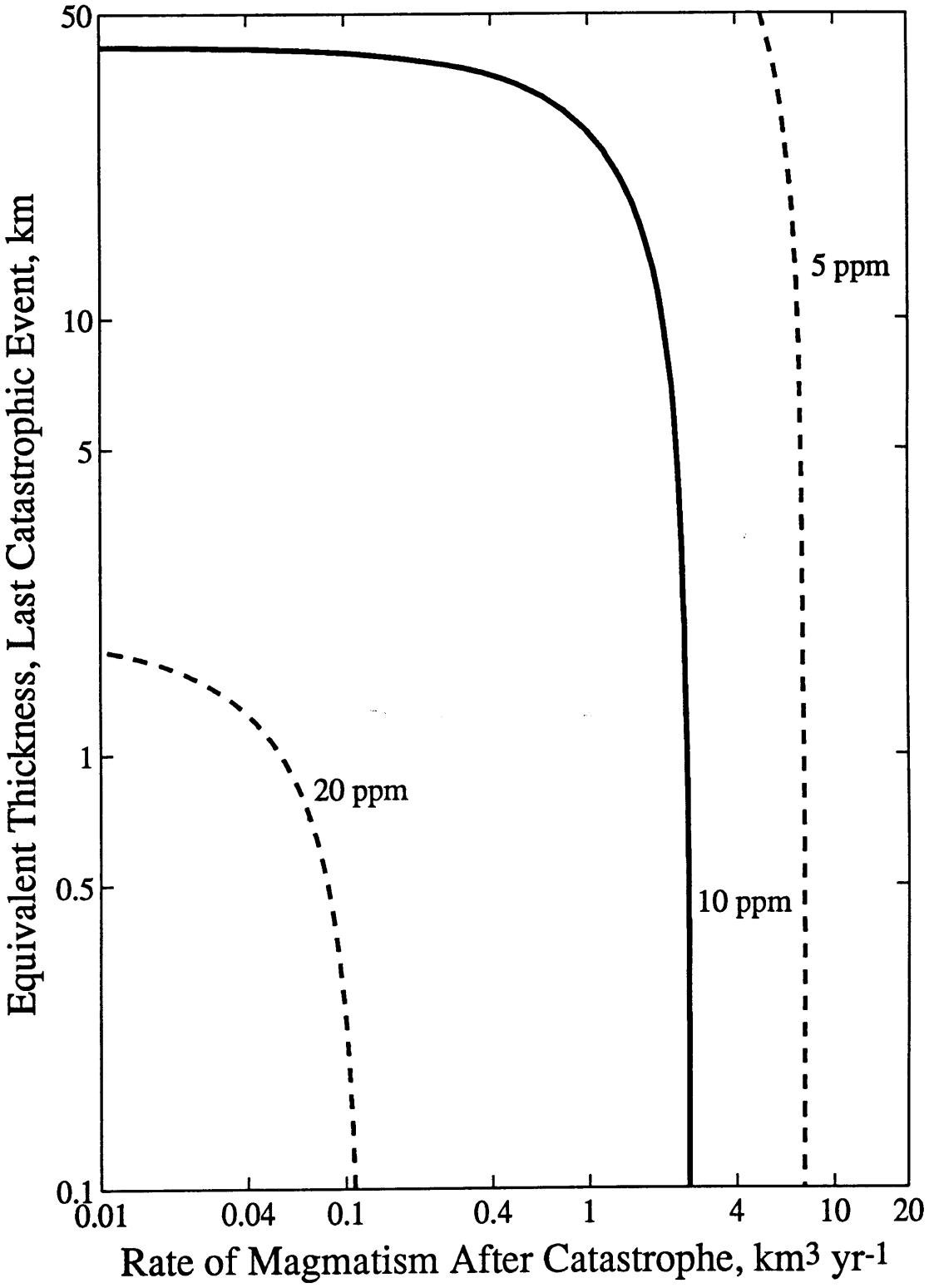
50
10
5
1
0.5
0.1
Equivalent Thickness, Last Catastrophic Event, km
5 ppm
20 ppm
10 ppm
0.01
0.04
0.1
0.4
1
4
10
20
Rate of Magmatism After Catastrophe, km3 yr-1

Figure 5.6c

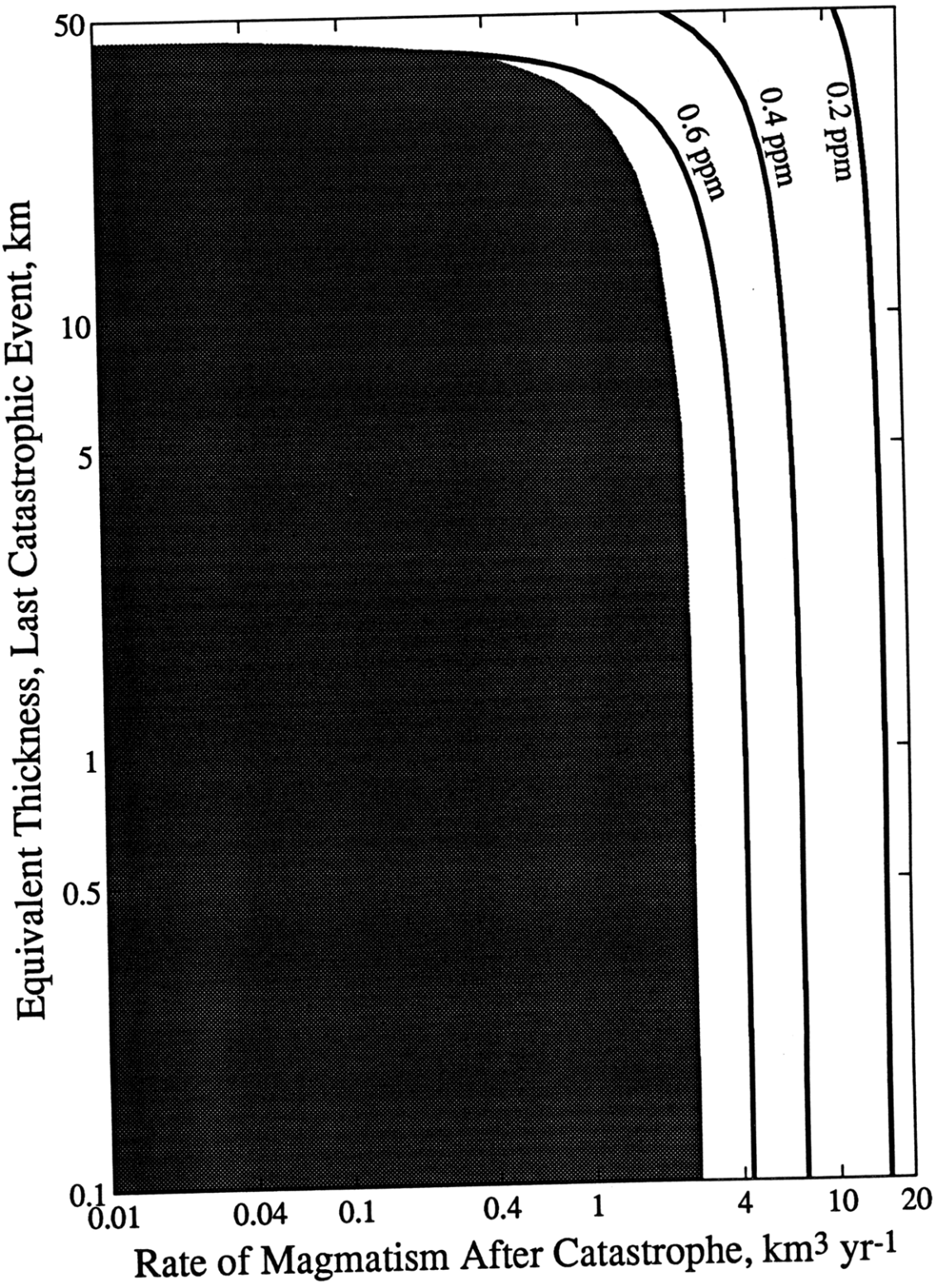
50
10
5
1
0.5
0.1
Equivalent Thickness, Last Catastrophic Event, km
0.6 ppm
0.4 ppm
0.2 ppm
0.01
0.04
0.1
0.4
1
4
10
20
Rate of Magmatism After Catastrophe, km3 yr-1

Figure 5.7a

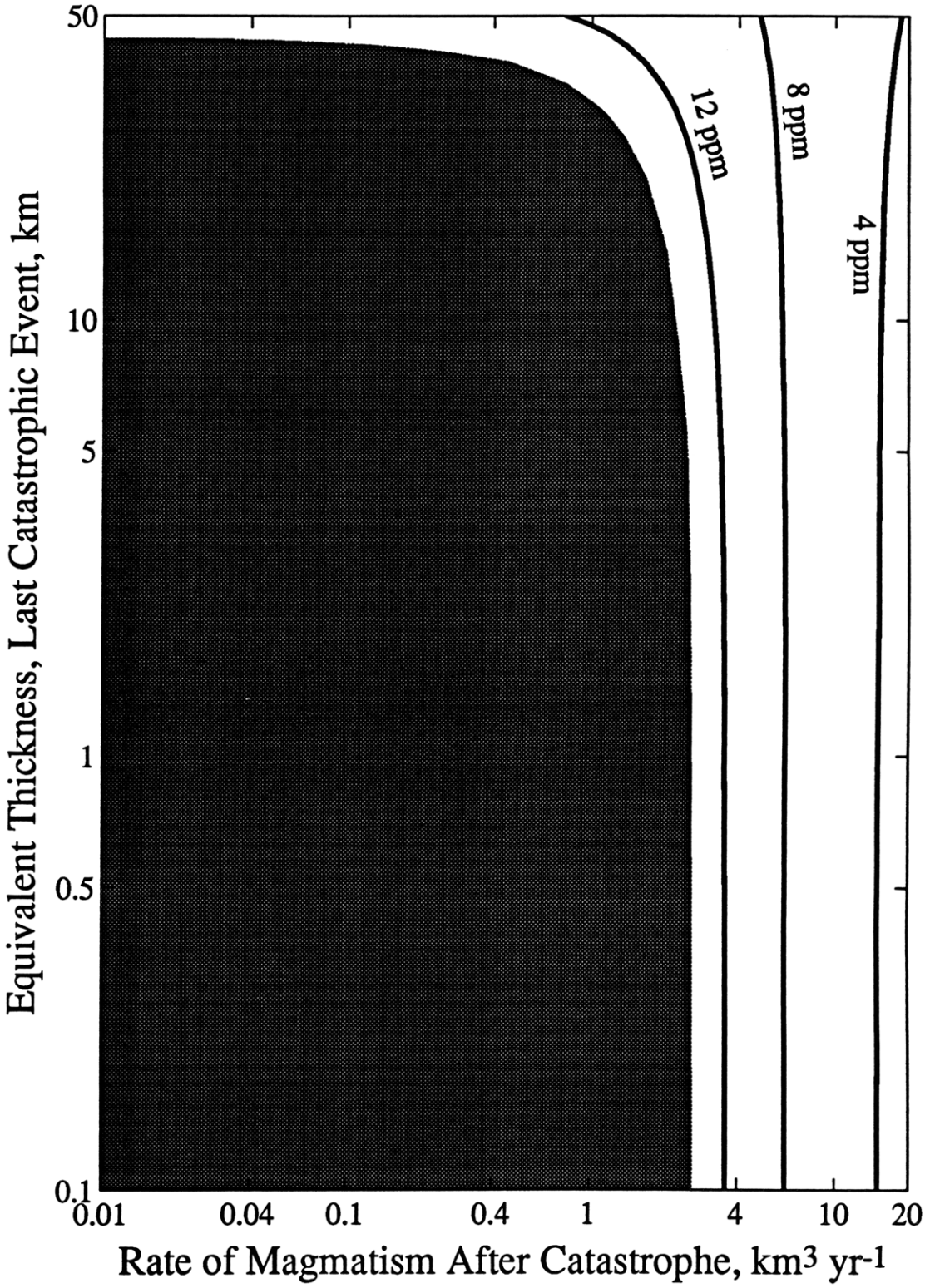
50
10
5
1
0.5
0.1
Equivalent Thickness, Last Catastrophic Event, km
12 ppm
8 ppm
4 ppm
0.01
0.04
0.1
0.4
1
4
10
20
Rate of Magmatism After Catastrophe, km3 yr-1

Figure 5.7b

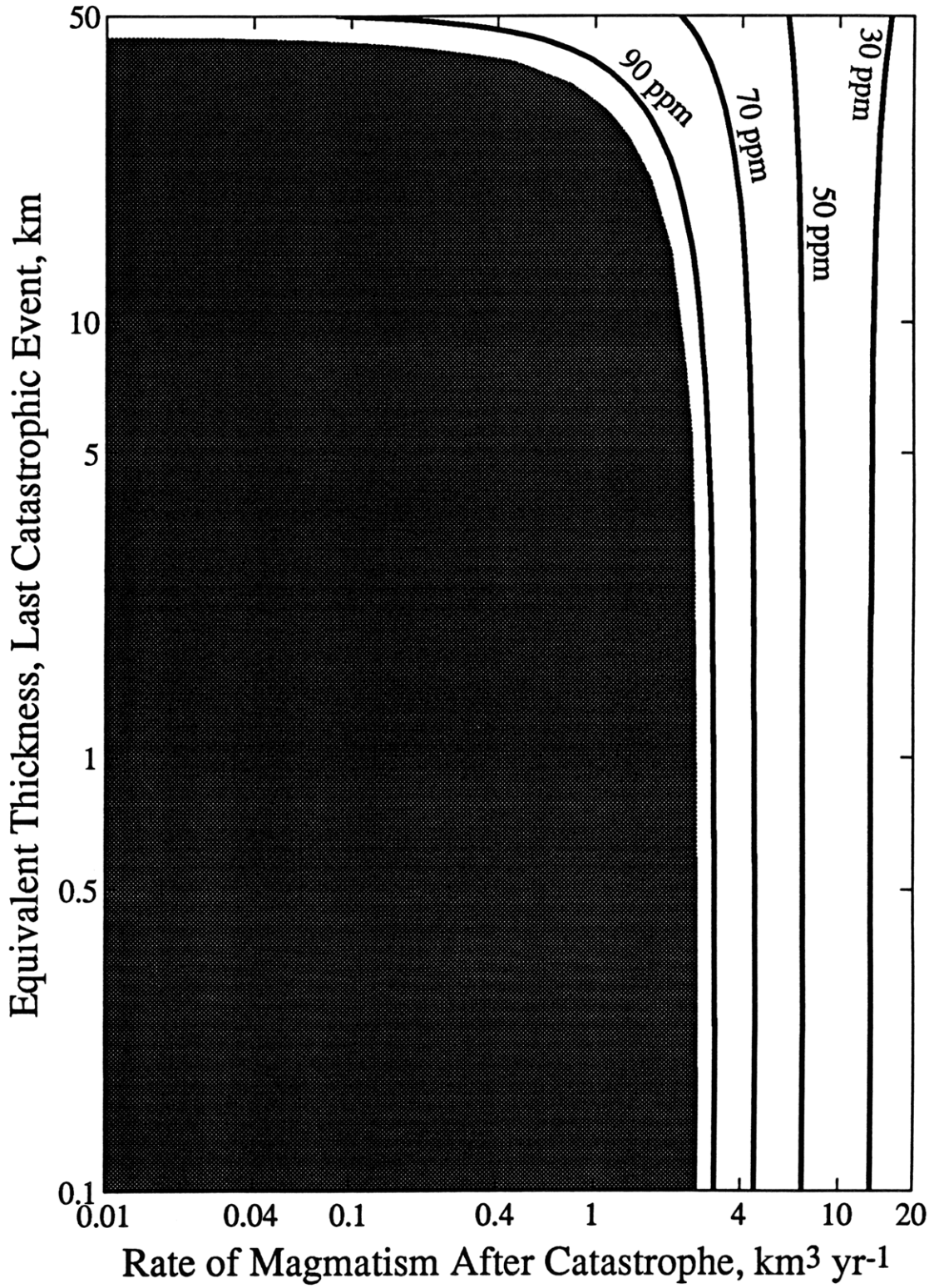
Equivalent Thickness, Last Catastrophic Event, km
50
10
5
1
0.5
0.1
90 ppm
70 ppm
50 ppm
30 ppm
0.01
0.04
0.1
0.4
1
4
10
20
Rate of Magmatism After Catastrophe, km3 yr-1

Figure 5.7c

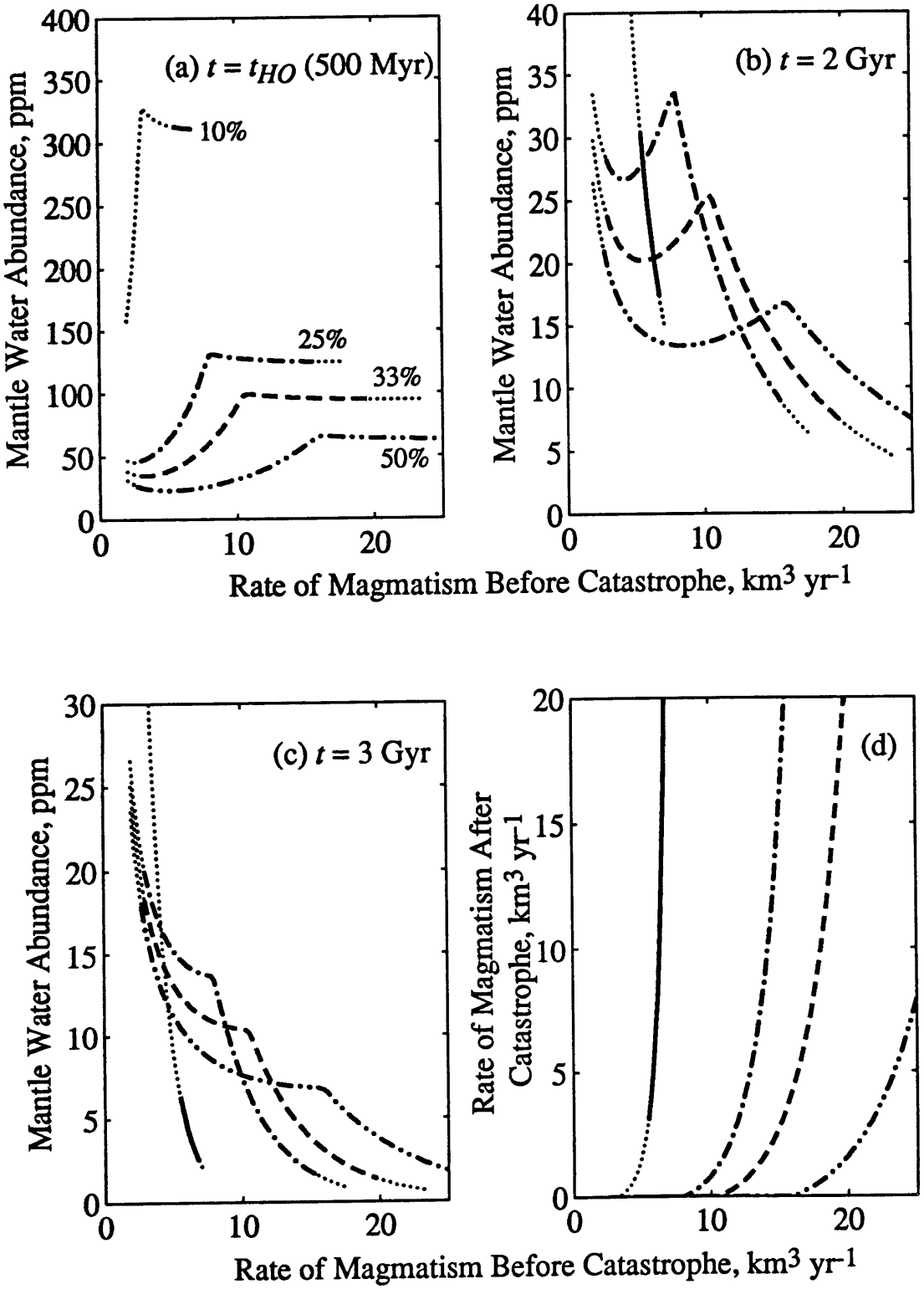
(a) $t = t_{HO}$ (500 Myr)
10%
25%
33%
50%
Mantle Water Abundance, ppm
(b) t = 2 Gyr
(c) t = 3 Gyr
(d)
Rate of Magmatism After Catastrophe, km^3 yr^{-1}
Rate of Magmatism Before Catastrophe, km^3 yr^{-1}

Figure 5.8

Chapter 6:

Concluding Remarks

Constraints on the tectonic and thermal history of Venus have been investigated in this thesis on the basis of topographic relief, the impact cratering record, and atmospheric abundances of volcanic gasses. In Chapter 2, it is concluded that formation of mountain belts in Ishtar Terra occurred at a strain rate at least of order 10^{-15} s^{-1}. A further suggestion is that Maxwell Montes are likely to be comparatively young, of order 50 My.

Subsequent to the writing of that chapter, the assumption of Airy isostatic compensation of the topographic relief of the mountain belts has received support from analyses of the high-latitude gravity field of Venus after the Magellan spacecraft achieved a nearly circular orbit [*Konopliv and Sjogren*, 1994; *Simons et al.*, 1994]. Several recent developments, however, have challenged the view that the mountain belts are relatively young. First, it has been argued from measurements of crater density in tessera terrain that the deformation preserved in tessera terrain occurred dominantly at times comparable to [*Herrick*, 1994] or greater than [*Ivanov and Basilevsky*, 1993] the average age of the planet's surface. These results include the large blocks of tessera in Ishtar Terra. Second, an apparent depth of compensation of about 40 km obtained from recent gravity data indicates that a dynamic component is unnecessary to support the long-wavelength topography in Ishtar Terra [*Simons et al.*, 1994]. Further, that geoid/topography admittance values are positive everywhere on Venus constitutes an argument that tessera terrain and compressively deformed plateau highlands are relics of an earlier era of deformable crust [*Simons et al.*, 1994]. Finally, recently reported measurements of the creep strength of dry diabase support much more creep resistant flow laws than those used in previous models of crustal deformation on Venus [*Mackwell et al.*, 1995].

It should be noted that there is a difference between the definitions of the age of the mountain belts as used in Chapter 2 and those addressed above. In Chapter 2, the time of formation of mountain belts has been referred to as the age, while the above arguments constrain the time following mountain belt formation. I have shown that the time of formation is likely limited by the reaction rate of the gabbro-eclogite phase transition

(Chapter 2). The subsequent relaxation of the high topographic relief has been discussed by others on the basis of crustal flow models and observations of post-orogenic crustal deformation [e.g., *Smrekar and Solomon*, 1992], but the effects of phase changes in the lower crust were ignored.

The 7-km elevation of Maxwell Montes above the adjacent plateaus and the inferred time since the orogeny of 500 Myr pose the problem that the crustal root beneath the mountains must be metastable for times much longer than the maximum formation time of 50 Myr calculated in Chapter 2. From a careful examination of the assumptions adopted in Chapter 2, four explanations for this apparent contradiction are possible. First, crustal material in the mountain belts may not be basaltic in composition. The gabbro-eclogite phase transition would then not limit the elevation of Maxwell Montes. The assumption of a basaltic composition for at least the uppermost crust on Venus is generally supported by the X-ray measurements by the Venera 14 and Vega 2 landers [*Surkov et al.*, 1984, 1987] and the γ-ray measurements by the Venera 9 and 10 and Vega 1 landers [*Surkov et al.*, 1986], but several other rock types including more silica-rich varieties have been considered on the basis of the K_2O content and high K, U, and Th concentrations at the Venera 13 and 8 landing sites, respectively [*Barsukov*, 1992; *Kargel et al.*, 1993]. Any rock types less dense than mantle material can afford the isostatic support necessary for the observed elevation of Maxwell Montes. This possibility is difficult to explore until geochemical analyses of crustal materials in the mountain belts are carried out in the course of future exploration.

A second possibility is that the adopted phase boundaries of the gabbro-garnet granulite-eclogite stability fields are incorrect. Different sets of boundaries have indeed been proposed for the gabbro-eclogite phase transition than the one adopted in Chapter 2 [*Yoder and Tilley*, 1963; *Ringwood*, 1975]. However, the differences are not so significant that the results in Chapter 2 would change considerably through the use of such other determinations of the phase boundaries.

A third explanation is that the rate of the phase transition may be significantly slower (i.e., by at least one order of magnitude) than assumed in Chapter 2. Diffusion rates much lower than the adopted lower bound were mentioned in Chapter 2, although these rates are not well-determined and arguments against their adoption were made. It is also possible that processes other than the volume diffusion of cations (e.g., nucleation of product crystals) may limit the reaction rate. While the precise laboratory measurement of the rate of the phase transition under different pressures and temperatures would be a formidable task, upper bounds on the reaction rate may nonetheless be derivable experimentally.

A fourth option is that temperatures in the crust beneath the mountain belts are lower than those calculated in Chapter 2. Possible mechanisms for producing lower temperature include underthrusting of the crust [*Head*, 1990] and currently active downwelling beneath the mountain belts [*Kiefer and Hager*, 1991; *Lenardic et al.*, 1993]. While the dynamic support of topography in Ishtar Terra is not necessary [*Simons et al.*, 1994], present downwelling in the mantle beneath Maxwell Montes cannot be excluded by Magellan gravity data [*Konopliv and Sjogren*, 1994]. Both crustal underthrusting and mantle downwelling would reduce the rate of increase in temperature in the lower crust beneath the mountains and render gabbro metastable for periods longer than 50 Myr. This option can be investigated quantitatively by numerical models that incorporate both mantle flow and crustal deformation [*Lenardic et al.*, 1993]. The evolution and the support mechanisms of the mountain belt should thus be regarded as open questions until these various possibilities are tested.

Recent volcanic activity on the planet was studied in Chapter 3 from the impact crater density on volcanoes and coronae. The crater density on large volcanoes is about half of the global average. From the measured area of large volcanoes and the population of embayed craters, I have estimated the volcanic resurfacing rate and the maximum volumetric magmatic flux as 0.2 $km^2\ yr^{-1}$ and 7 $km^3\ yr^{-1}$, respectively. The crater density on coronae, on the other hand, is not significantly different from the global average.

Detailed study of crater densities by corona class, however, suggests that coronae associated with extensive volcanic deposits have surfaces resolvably younger than the global average. These results suggest that volcanoes and coronae with associated volcanism have been active over the past 500 My. The resurfacing history consistent with all of the cratering record involves nearly global resurfacing followed by modest levels of subsequent volcanic resurfacing over as much as 20% of the planet area.

In Chapter 4 and 5, volcanic degassing and atmospheric escape of ^{40}Ar, ^{4}He, and water were investigated. The γ-ray measurements of U, Th, and K by Venera and Vega landers [*Surkov et al.*, 1987] constrain the present K abundance in the bulk silicate portion of Venus to be between 100 and 250 ppm. This result then yields a lower bound on the average crustal production rate over the planet's history of 2 $km^3\ yr^{-1}$. By combining this lower bound with the upper limit on the hydrogen escape flux, an upper bound on the water content in the Venus mantle is obtained. It is shown in Chapter 5 that the Venus mantle has been at least an order of magnitude dryer than the upper mantle beneath the Earth's mid-ocean ridges. Because water plays a significant role in the rheology of mantle, the marked difference in the interior water budgets of Venus from Earth is likely to have influenced strongly the thermal and tectonic evolution of the planet [*McKenzie*, 1977; *Kaula*, 1990; *Phillips and Hansen*, 1994; *Kaula*, 1995; *Schultz and Simons*, 1995].

The studies in this thesis have developed new insights into the tectonic and thermal evolution of Venus, but available constraints are so few that an unambiguous picture of the evolution of our neighboring planet has yet to emerge. Efforts to exploit the full range of results from the Magellan mission will continue to be of importance for a better understanding of the planet and will provide an informed basis for future exploration.

REFERENCES

Barsukov, V. L., Venusian igneous rocks, in *Venus Geology, Geochemistry, and Geophysics*, edited by V. L. Barsukov, A. T. Basilevsky, V. P. Volkov, and V. N. Zharkov, pp. 165-176, Univ. Arizona Press, Tucson, 1992.

Head, J. W., III, Formation of mountain belts on Venus: Evidence for large-scale convergence, underthrusting, and crustal imbrication in Freyja Montes, Ishtar Terra, *Geology*, *18*, 99-102, 1990.

Herrick, R. R., Resurfacing history of Venus, *Geology*, *22*, 703-706, 1994.

Ivanov, M. A., and A. T. Basilevsky, Density and morphology of impact craters on tessera terrain, Venus, *Geophys. Res. Lett.*, *20*, 2579-2582, 1993.

Kargel, J. S., G. Komatsu, V. R. Baker, and R. G. Strom, The volcanology of Venera and VEGA landing sites and the geochemistry of Venus, *Icarus*, *103*, 253-275, 1993.

Kaula, W. M., Venus: A contrast in evolution to Earth, *Science*, *247*, 1191-1196, 1990.

Kaula, W. M., Venus reconsidered, *Science*, submitted, 1995.

Kiefer, W. S., and B. H. Hager, Mantle downwelling and crustal convergence: A model for Ishtar Terra, Venus, *J. Geophys. Res.*, *96*, 20,967-20,980, 1991.

Konopliv, A. S., and W. L. Sjogren, Venus spherical harmonic gravity model to degree and order 60, *Icarus*, *112*, 42-54, 1994.

Lenardic, A., W. M. Kaula, and D. L. Bindschadler, A mechanism for crustal recycling on Venus, *J. Geophys. Res.*, *98*, 18,697-18,705, 1993.

Mackwell, S. J., M. E. Zimmermann, D. L. Kohlstedt, and D. S. Scherber, Experimental deformation of dry Columbia diabase: Implications for tectonics on Venus, *Proc. 35th U.S. Symp. Rock Mechanics,* in press, 1995.

McKenzie, D. P., The initiation of trenches: A finite amplitude instability, in *Island Arcs, Deep Sea Trenches, and Back-Arc Basins*, edited by M. Talwani and W. C. Pitman III, *Maurice Ewing Ser.*, *1*, pp. 57-61, Am. Geophys. Union., Washington, D. C., 1977.

Phillips, R. J., and V. L. Hansen, Tectonic and magmatic evolution of Venus, *Ann. Rev. Earth Planet. Sci.*, *22*, 597-654, 1994.

Ringwood, A. E., *Composition and Petrology of the Earth's Mantle*, 618 pp., McGraw-Hill, New York, 1975.

Schultz, R. A., and M. Simons, Water, rock strength, and tectonics on Venus, *Science*, submitted, 1995.

Simons, M., B. H. Hager, and S. C. Solomon, Global variations in the geoid/topography admittance of Venus, *Science*, *264*, 798-803, 1994.

Smrekar, S. E., and S. C. Solomon, Gravitational spreading of high terrain in Ishtar Terra, Venus, *J. Geophys. Res.*, *97*, 16,121-16,148, 1992.

Surkov, Yu. A., V. L. Barsukov, L. P. Moskalyeva, V. P. Kharyukova, and A. L. Kemurdzhian, New data on the composition, structure, and properties of Venus rock obtained by Venera 13 and Venera 14, *Proc. Lunar Planet. Sci. Conf. 14th, J. Geophys. Res.*, *89*, B393-B402, 1984.

Surkov, Yu. A., L. P. Moskalyova, V. P. Kharyukova, A. D. Dudin, G. G. Smirnov, and S. Y. Zaitseva, Venus rock composition at the Vega 2 landing site, *Proc. Lunar Planet. Sci. Conf. 17th, J. Geophys. Res.*, *91*, E215-218, 1986.

Surkov, Yu. A., F. F. Kirnozov, V. N. Glazov, A. G. Dunchenko, L. P. Tatsy, and O. P. Sobornov, Uranium, thorium, and potassium in the Venusian rocks at the landing sites of Vega 1 and 2, *Proc. Lunar Planet. Sci. Conf. 17th, J. Geophys. Res.*, *92*, E537-E540, 1987.

Yoder, H. S., Jr., and C. E. Tilley, Origin of basalt magmas, *J. Petrol.*, *3*, 342-532, 1963.

19?-37